How dark is dark matter? Robust limits on dark matter - radiation interactions from cosmological observations

JULIA STADLER

How dark is dark matter?

Robust limits on dark matter - radiation interactions from cosmological observations.

Julia Johanna Stadler

A Thesis presented for the degree of
Doctor of Philosophy

Institute for Particle Physics Phenomenology
Department of Physics
Durham University
United Kingdom

October 2019

How dark is dark matter?

Robust limits on dark matter - radiation interactions from cosmological observations.

Julia Johanna Stadler

Submitted for the degree of Doctor of Philosophy
October 2019

Abstract: Extensions to the canonical ΛCDM model which incorporate elastic scattering between dark matter and Standard Model radiation predict the suppression of matter perturbations on small scales and modifications to the cosmic microwave background anisotropies. Studying these scenarios not only allows us to constrain the particle physics properties of dark matter, it also reveals if they can alleviate remaining tensions in cosmological data sets. In this context, the present thesis considers several aspects of dark matter-photon and dark matter-neutrino interactions.

One central aspect of our work is the accurate description of additional scattering terms in the numerical solutions. In the context of dark matter-photon interactions, we demonstrate the robustness of earlier studies with respect to inconsistencies in the tight coupling approximation and to the negligence of the dark matter sound speed. Accounting for the latter, however, potentially tightens limits from large-scale structure observations for light dark matter candidates. Our updated constraints, derived from the Planck 2015 data release, are about 20% tighter than previous CMB limits in the most conservative case.

We further extend dark matter-photon interactions to a mixed dark matter scenario in which two components, one collisional and one collisionless, contribute to the relic abundance. In particular a small fraction of interacting dark matter impacts the matter power spectrum in a fashion very similar to massive neutrinos. In this case, CMB data only imposes weak constraints on the interaction strength, and our Fisher forecast for the DESI survey predicts notably larger error margins on the neutrino mass.

Dark matter-neutrino interactions alter the initial conditions and cause inconsistencies in the ultra-relativistic fluid approximation, which impact the matter power spectrum on small scales. Still, we can reinforce the validity of previous studies that neglected those effects. In addition to the canonical collisional damping, dark matter-neutrino interactions imply the suppression of structure by mixed damping. Indeed, our exploration of the parameter space reveals the relevance of mixed damping for observational constraints. To provide insight into the underlying physical processes, we derive an analytical approximation to the evolution of dark matter perturbations in the mixed damping regime, which accomplishes to capture all qualitative features of our full numerical results.

To Reini.

Acknowledgements

Foremost I want to thank my supervisors, Céline Bœhm and Silvia Pascoli, for their guidance and support, for all the great opportunities I enjoyed and for the freedom to explore who I want to be as a physicist.

I am grateful to Olga Mena for our friendly and fruitful collaboration and to my colleagues at Durham, who became friends, Andres Olivares, Matheus Hostert and Andrew Cheek. A special thanks goes to Jakub Scholtz, who let me abuse his house as a storage facility, and to Jessica Turner and Holger Schulz for their kind hospitality.

Visiting the Max Planck Institute for Astrophysics was always a great pleasure, and I want to thank the IFT group for the welcoming atmosphere, the open discussions and their help with all my small and big questions. Torsten Enßlin had the right advice when I needed it, without his support my path would probably be a different one now.

I gratefully acknowledge the financial support, the travel opportunities and the possibilities for physics discourse I enjoyed as a member of the Elusives network, supported from the European Union's Horizon 2020 research and innovation programme under the Marie Sklodowska-Curie grant agreement No 674896.

The Durham Mountain Sports Club really is Durham's friendliest outdoor club. It is mostly for the people I met there the North East started feeling like a home, and it always is a great pleasure to climb, walk and drink a pint with them.

I am fortunate to have Christine, Reinhard, Maria and Stephan in my life.

Declaration

The work in this thesis is based on research carried out in the Department of Physics at Durham University. No part of this thesis has been submitted elsewhere for any degree or qualification.

The following chapters have been published in the form of papers:

- Section 3.6, Section 4.1, Section 4.2 and Chapter 5 are based on [1]

  J. Stadler and C. Bœhm, *Constraints on γ-CDM interactions matching the Planck data precision*, *JCAP* **1810** (2018) 009, [1802.06589]

- Section 3.5, Section 4.3, Section 4.4 and Chapter 7 are based on [2]

  J. Stadler, C. Bœhm and O. Mena, *Comprehensive Study of Neutrino-Dark Matter Mixed Damping*, *JCAP* **2019** (2020) 014, [1903.00540]

- Chapter 6 is based on [3]

  J. Stadler, C. Bœhm and O. Mena, *Is it Mixed dark matter or neutrino masses?*, [1807.10034]. submitted to JCAP

Contents

List of Figures

List of Tables

Chapter 1

The ΛCDM cosmological standard model

The standard model of cosmology, the so-called ΛCDM model, is hugely successful in describing observations over a vast range of scales, reaching from the present-day Hubble radius, at the largest, down to the size of galaxies. Yet, it remains an effective description, as the physical nature of two central elements, that of the dark energy Λ and of cold dark matter (CDM), is unknown. Despite a dedicated program, aiming for the detection of dark matter in the laboratory, the only evidence for its existence to date derives from cosmological and astrophysical observations. These also provide most of the current knowledge about the properties of dark matter.

In this situation, a possibility to better understand one of the universe's most fundamental constituents is to consider alternatives to the vanilla assumptions of cold, non-interacting dark matter, and to study how successfully these can describe the cosmological and astrophysical data. This approach is highly complementary to direct detection efforts and to laboratory searches for dark matter. The past decades have seen vast progress in the area of observational cosmology, and by now the field has clearly entered the realm of a data driven precision science. In the future, an ambitious program aims for more precise measurements of the cosmic microwave background (CMB) polarisation and of the CMB anisotropies on small scales. In addition, galaxy surveys and lensing measurements aspire to determine the matter power spectrum at an increased accuracy.

To fully exploit present and future data sets requires precise theory predictions not only for the canonical ΛCDM model but also for alternative scenarios. The present thesis is intended to contribute precisely at this theory frontier. It studies dark matter interactions with Standard Model radiation, concretely with neutrinos and photons, and thereby primarily considers the evolution of cosmological perturbations in the linear regime.

This work is outlined as follows. In the remainder of this first Chapter we present the main aspects of the ΛCDM model and discuss its observational status in the following Chapter 2. Cosmological perturbations in the linear regime are described by the coupled, linearised Boltzmann Einstein equations, which we derive in Chapter 3 for the cases of ΛCDM, dark matter-photon interactions and dark matter-neutrino interactions. In scenarios with non-standard dark matter interactions, several approximation schemes, derived under the assumption of a ΛCDM evolution, have to be reconsidered. These rather technical

aspects are presented in Chapter 4. Having established the formalism, Chapter 5 deals with interactions between dark matter and photons, examines the numerical accuracy and derives updated constraints on the parameter space from Planck CMB observations. Chapter 6 extends dark matter-photon interactions to a scenario with two dark matter components, one of them interacting, the other collisionless. We constrain the parameter space from CMB observations and put special emphasis on forecasting the sensitivity of future galaxy surveys to such a scenario. Finally, interactions between dark matter and neutrinos and the numerical accuracy of theory predictions in this context are the topic of Chapter 7. In scenarios with dark matter-neutrino interactions, there is an alternative damping mechanism to the usually considered collisional damping, called mixed damping. We investigate its parameter space and derive an analytical approximation to the evolution of dark matter perturbations in the mixed damping regime. Finally, in Chapter 8, we summarise our results.

1.1 The metric of the universe

Modern cosmology, and in particular its theoretical foundations, rest upon two major premises: the theory of general relativity and the cosmological principle. The Einstein equation [10]

$$G_{\mu\nu} = \frac{8\pi}{m_{\rm P}^2}\, T_{\mu\nu}\,, \tag{1.1.1}$$

connects the evolution of the space-time metric, described by the Einstein tensor $G_{\mu\nu}$, to the matter distribution characterised by the stress-energy tensor $T_{\mu\nu}$ (c.f. Sec 3 for a more detailed discussion). The Planck mass $m_{\rm P}$ appearing in Eq. (1.1.1) is related to the gravitational constant by $m_{\rm P} = G^{-1/2} = 1.22 \times 10^{19}\,\text{GeV}$. If, as stated by the cosmological principle, the stress-energy tensor is spatially isotropic and homogeneous, there exist only three geometries which solve the Einstein equations [11–14]. All of them are described by the Friedmann-Robertson-Walker (FRW) metric

$$ds^2 = c\,dt^2 - a^2(t)\left(\frac{dr^2}{1-k\,r^2} + r^2\,d\theta^2 + r^2\,\sin^2\theta\,d\phi^2\right)\,, \tag{1.1.2}$$

and reflected by the choice of the curvature parameter $k \in \{-1, 0, 1\}$. A universe of negative curvature exhibits an open geometry, one of positive curvature is closed, and the intermediate case of $k = 0$ corresponds to a spatially flat universe. The spherical coordinates r, θ, ϕ in Eq. (1.1.2) are referred to as comoving coordinates. An observer who is at rest with respect to the comoving frame will remain so and he will measure the proper time, t. The absolute value of the scale factor a has no physical importance and is commonly fixed to equal one at the current time, i.e. $a_0 = 1$. Physically meaningful, however, is the time dependence of a, which determines how the proper distance between two comoving observers evolves. The time evolution of the scale factor is quantified by the Hubble rate

$$H \equiv \frac{da/dt}{a} = \frac{\dot{a}}{a}\,, \tag{1.1.3}$$

and evolves according to the Friedmann equations

$$H^2 = \frac{8\pi}{3\,m_{\mathrm{P}}^2}\,\rho - \frac{k}{a^2}\,, \tag{1.1.4}$$

$$\frac{\ddot{a}}{a} = -\frac{4\pi}{3m_{\mathrm{P}}^2}\,(\rho + 3p)\;, \tag{1.1.5}$$

where ρ is the energy density and p the pressure. Especially the first Friedmann equation makes the connection between the energy density in the universe and its geometry very explicit and allows to define the critical energy density

$$\rho_{\mathrm{crit}} = \frac{3m_{\mathrm{P}}^2}{8\pi}\,H_0^2\,. \tag{1.1.6}$$

A universe of sub-critical energy density is open and a universe with $\rho > \rho_{\mathrm{crit}}$ is closed. Recent measurements strongly suggest a flat spatial geometry, i.e. $\rho = \rho_{\mathrm{crit}}$ [4,15]. Also the inflationary paradigm (c.f. Sec. 1.2.1), an integral component of the cosmological standard model, predicts a flat geometry, and hence we assume that $k = 0$ throughout this thesis.

Having fixed the geometry of the universe, the evolution of the scale factor still depends on the universe's energy density and its equation of state $w = p/\rho$. Distinct contributions to the energy density come to dominate at different cosmological epochs, these are radiation in the form of massless or highly relativistic particles ρ_{r} ($w_{\mathrm{r}} = 1/3$), non-relativistic matter ρ_{m} ($w_{\mathrm{m}} = 0$), and vacuum energy ρ_Λ with $w_\Lambda = -1$. While the latter is mathematically accounted for easily – the Einstein equation (1.1.1) is invariant under the addition of a constant – insight into its physical origin is not that obvious. The second Friedmann equation (Eq. 1.1.4) predicts a different evolution of the scale factor, depending whether the universe is dominated by matter, radiation or dark energy

$$a(t) \propto \begin{cases} t^{1/2} & \text{matter domination}\,, \\ t^{2/3} & \text{radiation domination}\,, \\ \exp\left(\sqrt{\Lambda/3}\,t\right) & \text{dark energy domination}\,, \end{cases} \tag{1.1.7}$$

where $\Lambda = (8\pi)/m_{\mathrm{P}}^2\,\rho_\Lambda$. Finally, energy conservation (see Sec. 3.2.3 for a derivation)

$$\dot{\rho} = -3H\,(\rho + p)\;, \tag{1.1.8}$$

determines how each individual component evolves with the scale factor. Namely,

$$\rho_{\mathrm{m}} \propto a^{-3}\,, \quad \rho_{\mathrm{r}} \propto a^{-4} \quad \text{and} \quad \rho_\Lambda = \mathrm{const}\,. \tag{1.1.9}$$

Obviously from Eq. (1.1.7), a flat universe populated by matter, radiation or dark energy is expanding, and the expansion is decelerating if matter or radiation are the dominant components but accelerating for dark energy domination. The expansion implies that the universe must have been denser and hotter at an earlier time. Extrapolation to very early times reveals a singularity, where the scale factor is infinitely small, which coined the name Big Bang model. Initial acceptance of the Big Bang model rooted on three

observational pillars. First, the direct observation of the expansion [16, 17], whose current status is summarised in Sec. 2.1. Further, the thermal conditions in the early universe allow to predict the abundances of light elements from Big Bang nucleosynthesis (BBN, c.f. Sec 1.2.3) and the presence of a thermal photon population remaining of a hotter and denser epoch, the cosmic microwave background (CMB) radiation (c.f. Sec. 1.2.5 and Sec. 2.3).

The expansion causes distant galaxies to recede from Earth and hence their spectra are redshifted by the Doppler effect. Light observed today from faraway objects at wavelength λ_{obs} was emitted at a shorter wavelength λ_{emit}, determining the redshift z as

$$1 + z \equiv \frac{\lambda_{\text{obs}}}{\lambda_{\text{emit}}} = \frac{1}{a_{\text{emit}}} \,. \tag{1.1.10}$$

Because it is closely related to the scale factor at the time of emission a_{emit}, the redshift is simultaneously used as a time and a distance measure. For objects which are close to the Earth, the Hubble rate approximately remained constant between the emission and detection of their light and is given by the present-day value H_0. Then indeed, the redshift is a linear function of the physical distance d

$$z = H_0 \, d \,. \tag{1.1.11}$$

The linear relation holds for $d \lesssim 50\,\text{Mpc}$ [18], but to compute the distance to the the oldest observed astrophysical objects requires the integration of the full expression in Eq. (1.1.4).

Several different species add to the total matter and radiation densities, which affect the expansion history. From the Standard Model, photons, neutrinos and baryons are the most important contributions, where the latter summarise electrons, protons and light nuclei. In addition, observations strongly support the presence of dark matter, a non-relativistic species which only interacts gravitationally. Finally, the energy density of vacuum energy is particularly important for the late time evolution. A practical parameterisation, to keep track of all individual species, is to express their present-day abundance as a fraction of the critical density

$$\Omega_i = \frac{\rho_{i,0}}{\rho_{\text{crit}}} \,, \quad \text{where} \quad i = \gamma,\, \nu,\, \text{b},\, \text{dm},\, \Lambda,\, \ldots \,. \tag{1.1.12}$$

Interactions between the individual species and departures from thermal equilibrium are described by the laws of thermodynamics, but their presence renders the prediction of each individual component's energy density a non-trivial task. In the following subsection we discuss the particle content of the universe in more detail. Eventually, the combination of general relativity, which determines the metric, and thermodynamics culminates in the ΛCDM cosmological standard model, which is summarised in Sec. 1.3.

1.2 Cosmological history

1.2.1 Inflation

As mentioned previously, the observed cosmological energy density is very close to the critical value Eq. (1.1.6), yet a priori there is no theoretical preposition for a flat universe. Observations also indicate a remarkable smoothness of the universe on very large scales, the so called horizon problem. Inflation addresses these two fine-tuning issues and, in addition, provides an origin for small initial density perturbations from which the present large-scale structure of galaxies, clusters, filaments and voids grew by gravitational collapse.

The scales over which physical processes are in causal contact are given by the comoving Hubble radius $(aH)^{-1}$. It measures the distance a particle can travel at the speed of light in one expansion time, that is roughly the time over which the scale factor doubles. The Hubble radius at CMB decoupling is about $\sim 100\,\mathrm{Mpc}$, subtending an angle of about 1° on today's sky. The horizon problem marks the surprising smoothness of the CMB on much larger scales [19, 20], which by far exceeds the level one would expect if these regions had never been in causal contact. There is, however, a subtle difference between the comoving Hubble radius, determining if two points are currently in causal contact, and the comoving horizon χ, which indicates if two points have ever been in causal contact [21],

$$\chi = \int_0^t \frac{dt'}{a(t')} = \int_0^a \frac{da'}{a'} \, \frac{1}{a'H(a')} \,. \tag{1.2.1}$$

During the radiation and the matter-dominated epoch, the universe's expansion decelerates, i.e. aH decreases, and the largest contributions to χ arise at late times. If, however, the universe undergoes an early era of accelerated expansion during which aH grows rapidly, significant contributions to χ arise from this era. Hence, distances separated by more than a Hubble radius in the radiation and matter-dominated epoch might have been in causal contact at the beginning of inflation. Typical inflationary models solve the horizon problem by postulating an era of exponential growth, during which the scale factor increases by at least 60 e-folds, i.e. by a factor of e^{60} [21, 22].

The accelerated expansion in these most common models originates from a scalar field φ, called inflaton, which evolves slowly in a flat potential [23, 24]. During the slow-roll phase, the inflaton's potential energy $V(\varphi)$ is nearly constant and much less than the kinetic energy, hence the field acts like a cosmological constant $p_\varphi = -\rho_\varphi = \text{const}$. If ρ_φ dominates the energy density, the Hubble rate is a constant H_i, and the Friedmann equation (1.1.4) is solved by

$$a(t) = a_\mathrm{e}\, e^{H_\mathrm{i}(t-t_\mathrm{e})} \quad t < t_\mathrm{e}\,, \tag{1.2.2}$$

where the subscript e refers to values at the end of the inflationary epoch. Irrespective of its initial magnitude, the curvature term in the Friedmann equation (1.1.4) is suppressed by the exponential increase of the scale factor, explaining why the current energy density is so close to the critical value.

Inflation terminates when the condition of a slowly rolling inflaton field is no longer valid, e.g. because the inflaton field approaches the minimum of its potential [19, 25]. Subsequently, during reheating [26, 27], a hot Big Bang cosmology is recovered as the inflaton field decays into the particles of the Standard Model, possibly via intermediate exotic states. Typically inflationary models associate reheating with temperatures of $\sim 10^{15}\,\mathrm{GeV}$, but stringent observational constraints only provide a much weaker bound, $T_{\mathrm{rh}} > 4\,\mathrm{MeV}$ at 95% C.L. [28].

During the rapid expansion, small quantum fluctuations in the inflaton field are stretched to exceed the Hubble radius. While causally disconnected, perturbations remain frozen. However, as the Hubble radius increases in the radiation and the matter-dominated era, fluctuations regain their causal connection and grow by gravitational instability. Eventually, they evolve into the observed large-scale structure. The random initial fluctuations are Gaussian distributed in the baseline models of inflation and fully characterised by their two-point correlation function, the power spectrum $P(k)$,

$$\left\langle \delta(\boldsymbol{k})\delta(\boldsymbol{k'})\right\rangle = (2\pi)^3\,\delta_{\mathrm{D}}\left(\boldsymbol{k}-\boldsymbol{k'}\right)P(k)\,,\quad \Delta^2_{\mathrm{s}}(k) = \frac{k^3\,P(k)}{2\pi^2}\,. \tag{1.2.3}$$

The scale-invariant power spectrum $\Delta^2_{\mathrm{s}}(k)$ is often a convenient quantity to work with. Further, $\boldsymbol{k}$ denotes a mode in Fourier space and k its modulus, angular brackets indicate expectation values and the subscript "D" discriminates the Dirac delta-distribution δ_{D} from density fluctuations $\delta = (\rho - \langle\rho\rangle)/\langle\rho\rangle$.

Cosmological perturbations can be classified into adiabatic or curvature perturbations and isocurvature perturbations. While the latter are relevant in more exotic inflationary models, the former are rather prevalent. Adiabatic perturbations can be characterised as fluctuations in the local curvature, where all components of the energy density contribute to the perturbation [29]. They subdivide further, according to their properties under a gauge transformation, into scalar, vector and tensor modes. Only scalar perturbations couple to matter perturbations and are the most important for structure formation [21,30,31]. In its vanilla form, inflation predicts a nearly scale-invariant white noise spectrum for adiabatic scalar perturbations

$$\Delta^2_{\mathrm{s,p}}(k) = A_{\mathrm{s}}\left(\frac{k}{k_{\mathrm{s}}}\right)^{n_{\mathrm{s}}-1}\,. \tag{1.2.4}$$

The reference scale k_{s} is arbitrary a priori and usually adapted to the experimental region of sensitivity if a specific observation is considered. Gravitational instability alters the simple power law shape of Eq. (1.2.4), and the additional subscript "p" discriminates primordial perturbations against the processed spectra at lower redshifts. Near scale invariance means that the spectral index n_{s} is very close to one. Departures from unity permit insight into the dynamics of the inflaton field. Namely, given the slow-roll parameters

$$\epsilon = \frac{m_{\mathrm{P}}^2}{16\pi}\left(\frac{\partial V/\partial\varphi}{V}\right)^2\,,\quad \eta = \frac{m_{\mathrm{P}}^2}{8\pi}\left(\frac{\partial^2 V/\partial\varphi^2}{V}\right)\,, \tag{1.2.5}$$

the spectral index is

$$n_{\mathrm{s}} = 1 - 6\epsilon + 2\eta\,. \tag{1.2.6}$$

The evolution of scalar, vector and tensor perturbations decouples according to the decomposition theorem, and can be described independently [21]. In particular the production of tensor perturbations is predicted by inflation, and these are observable via their effect on anisotropies in the CMB at large scales [32–35]. While scalar modes dominate, the ratio between the scalar and the tensor power spectrum $\Delta^2_{\rm t}$, is sensitive to the inflationary scale. It is parameterised by

$$r\ (k) = \frac{\Delta^2_{\rm t}(k)}{\Delta^2_{\rm s}(k)}\,, \tag{1.2.7}$$

and usually given at some fiducial scale. The predictions for the tensor-to-scalar ratio by different models of inflation cover several orders of magnitude, such that a measurement of r would allow to constrain possible inflationary scenarios [36]. At the present, however, there are only upper limits on r (see Sec. 2.3).

1.2.2 The hot thermal universe

After the end of inflation, reheating restores the conditions of a hot Big Bang cosmology, meaning that the universe is filled with a hot plasma of radiation and heavier species, which are kept in equilibrium by frequent interactions. At temperature T_i, the phase space distribution of a species i in kinetic equilibrium follows a Fermi-Dirac or a Bose-Einstein statistic, respectively for fermions and bosons [29]

$$f_i = \left[\exp\left(\frac{E_i - \mu_i}{T_i}\right) \pm 1\right]^{-1}\,, \tag{1.2.8}$$

where $E_i = \sqrt{p_i^2 + m_i}$ is the energy and μ_i refers to the chemical potential. The latter is much smaller than the temperature for almost all species and at all times [21] and can be neglected to good approximation. The phase-space distribution in Eq. (1.2.8) describes the smooth universe at zeroth order and hence is independent of the spatial position and the direction of the momentum p_i. First order perturbations around the smooth background evolution are considered in Sec. 3.

The energy density of a species ρ_i can be expressed as an integral over its phase space distribution as

$$\rho_i = \frac{g_i}{(2\pi)^3}\int d^3p\ E_i(\boldsymbol{p})\, f_i(\boldsymbol{p})\,, \tag{1.2.9}$$

where g_i counts the internal degrees of freedom. In the ultra-relativistic limit this integral evaluates to

$$\rho_i \xrightarrow{T_i \gg m} \begin{cases} \frac{\pi^2}{30}\, g_i\, T_i^4 & \text{bosons} \\ \frac{7}{8}\,\frac{\pi^2}{30}\, g_i\, T_i^4 & \text{fermions} \end{cases}\,. \tag{1.2.10}$$

On the other hand, in the non-relativistic limit the energy density is proportional to the number density, $\rho_i = m_i\, n_i$, and becomes exponentially suppressed

$$\rho_i \xrightarrow{T_i \ll m} g_i m_i \left(\frac{m_i T_i}{2\pi}\right)^{3/2} e^{-\frac{m_i}{T_i}}\,. \tag{1.2.11}$$

At the high temperatures associated with the very early universe, pair production and

annihilation of Standard Model particles maintain thermal equilibrium. Then, $T_i = T_\gamma$, and, because the energy density of non-relativistic species is exponentially suppressed, the total energy density of the plasma is to good approximation given by

$$\rho = \left(\sum_{i=\text{bosons}} g_i + \frac{7}{8} \sum_{i=\text{fermions}} g_i \right) \frac{\pi^2}{30} T_\gamma^4 \quad (m_i \gg T_\gamma). \tag{1.2.12}$$

In a similar fashion, the pressure p_i of a species is determined by an integral over the phase space distribution

$$p_i = \frac{g_i}{(2\pi)^3} \int d^3p \; f_i(\boldsymbol{p}) \, \frac{p_i^2}{3\, E_i(\boldsymbol{p})} \longrightarrow \begin{cases} \rho_i/3 & \text{for } T_i \gg m_i \\ n_i\, T_i & \text{for } T_i \ll m_i \end{cases} . \tag{1.2.13}$$

Finally, the entropy density can be defined as

$$s_i = \frac{\rho_i + p_i}{T_i} \,, \tag{1.2.14}$$

and its sum over all species in thermal equilibrium is conserved [29].

There are several, notable departures from thermal equilibrium which significantly affected the evolution of the universe. Some of the most important, the production of light elements during Big Bang nucleosynthesis, and the production of dark matter, are discussed in the subsequent Secs. 1.2.3 and 1.2.4. Here, we consider the decoupling of neutrinos. A species with interaction rate Γ_i is in equilibrium with the plasma if it interacts repeatedly while the scale factor doubles. That is

$$\Gamma_i = \sum_j \Gamma_{i-j} \gg H \,, \tag{1.2.15}$$

where Γ_{i-j} refers to all individual interaction rates in the plasma. For neutrinos the dominant reactions are with electrons, and the interaction rate evolves as $\Gamma_\nu \simeq G_\text{F}^2\, T_\gamma^5$ [29]. Neutrinos decouple from the plasma at a temperature of $T_\gamma \simeq 1\,\text{MeV}$, and by then all three neutrino species are highly relativistic. After the decoupling, the neutrino temperature is only affected by the cosmological redshift and scales as $T_\nu \propto a^{-1}$. Shortly after, the temperature drops below the electron mass and the annihilation of $e^\pm$ pairs releases entropy to the photons, reheating them. The ratio between the electron and neutrino temperature is determined by the conservation of entropy (1.2.14) within the photon plasma. Before the annihilation, the photon temperature equals the neutrino temperature and both, relativistic electrons with $g_e = 4$ and photons with $g_\gamma = 2$ contribute. Equating $\sum_i s_i$ before and after the electron annihilation gives

$$\left(2 + \frac{7}{8} \times 4\right) T_\nu^3 = 2 \times T_\gamma^3 \,, \tag{1.2.16}$$

and therefore $T_\nu = (4/11)^{1/3}\, T_\gamma$.

Even after neutrinos have decoupled, their energy density contributes in the Friedmann equation (1.1.4) and increases the Hubble rate. Hypothetical additional light decoupled

states beyond the standard model have the same impact. The combined effect of decoupled radiation is parameterised by the effective number of neutrinos, $N_{\rm eff}$, and the total radiation density after electron decoupling is given by

$$\rho_{\rm rad} = \left[N_{\rm eff} \times \frac{7}{8} \left(\frac{4}{11} \right)^{4/3} + 1 \right] \rho_\gamma \,. \tag{1.2.17}$$

In the Standard Model, there are three light neutrino species and [37–39]

$$N_{\rm eff}^{\Lambda{\rm CDM}} = 3.046 \,. \tag{1.2.18}$$

The value is slightly larger than 3, because electron annihilation occurs shortly after neutrino decoupling and affects the high-energy neutrino tail, and because quantum electrodynamic effects at finite temperature cause the plasma properties to deviate from the ideal gas description.

Although the Standard Model of particle physics presumes massless neutrinos, this is contradicted by the observation of neutrino oscillations [40–42]. These are sensitive to the mass differences between states and can provide a lower bound on the absolute neutrino mass scale [43]

$$\left(\sum m_\nu \right)^{\rm osc.} \gtrsim 0.06\,{\rm eV} \,. \tag{1.2.19}$$

Neutrino oscillations indicate that at least two neutrino species become non-relativistic during the late-time evolution of the universe. We postpone a detailed discussion of the implications to Sec. 6.2.3.

Accounting for the possibility of decoupled, radiative species with a temperature other than T_γ, Eq. (1.2.12) generalises to

$$\rho = g_* \frac{\pi^2}{30} \, T_\gamma^4 \,, \tag{1.2.20}$$

where the effective radiative degrees of freedom g_* are defined as

$$g_* = \sum_{i={\rm bosons}} g_i \left(\frac{T_i}{T_\gamma} \right)^4 + \frac{7}{8} \sum_{i={\rm fermions}} g_i \left(\frac{T_i}{T_\gamma} \right)^4 \,. \tag{1.2.21}$$

For temperatures well in the excess of 300 GeV all species of the Standard Model contribute to the sum and $g_* = 106.75$. Subsequently, the effective degrees of freedom decline through confinement and the annihilation of heavy species, and in the temperature range $100\,{\rm MeV} \gtrsim T_\gamma \gtrsim 1\,{\rm MeV}$ Standard Model contributions arise from photons, electrons and positrons and neutrinos and amount to 10.75. Finally, at $T \ll 1\,{\rm MeV}$, after neutrinos have decoupled and electrons have annihilated with positrons, $g_* = 3.36$. A similarly compact notation can be introduced for the entropy density,

$$g_{*{\rm s}} = \sum_{i={\rm bosons}} g_i \left(\frac{T_i}{T_\gamma} \right)^3 + \frac{7}{8} \sum_{i={\rm fermions}} g_i \left(\frac{T_i}{T_\gamma} \right)^3 \,. \tag{1.2.22}$$

such that

$$s = \frac{2\pi^2}{45}\, g_{*\mathrm{s}}\, T_\gamma^3 \,. \tag{1.2.23}$$

1.2.3 Big Bang nucleosynthesis

The synthesis of light elements commences when the photon temperature falls to about 1 MeV. At this stage, the reaction rates between photons, electrons, protons and neutrons are large enough to maintain equilibrium. Pair annihilation would have extinguished the neutrons and protons by then, if there was not a small initial asymmetry between the baryon and anti-baryon abundances. The amount of leftover baryons is described by the baryon-to-photon ratio,

$$\eta_\mathrm{b} \equiv \frac{n_\mathrm{b}}{n_\gamma} = 5.5 \times 10^{-10} \left(\frac{\Omega_\mathrm{b} h^2}{0.020}\right) , \tag{1.2.24}$$

which remains constant as the universe expands. Although essential to establish the presently observed conditions in the universe, the origin of the baryon/anti-baryon asymmetry is obscure. Baryon-number violation is required for the production of a net asymmetry as well as $\mathcal{C}$ and $\mathcal{CP}$ violation and a departure from thermal equilibrium [44]. These three requirements, the Sakharov conditions, are achieved at some high energy scale by the most common models of baryogenesis, such as electroweak baryogenesis [45] or leptogenesis [46]. Still, the baryon asymmetry of the universe needs to be generated at a lower scale than that of inflation, otherwise it would be washed out. Here, we plainly presume the existence of a baryon/anti-baryon asymmetry, but its precise origin is beyond the scope of this work.

Helium is the most abundant element after hydrogen and produced from the fusion of deuterium and tritium. The bottleneck for this process is the creation of deuterium via $\mathrm{p} + \mathrm{n} \leftrightarrow \mathrm{D} + \gamma$. In nuclear statistical equilibrium, the deuterium density is approximately

$$\frac{n_\mathrm{D}}{n_\mathrm{b}} \sim \eta_\mathrm{b} \left(\frac{T_\gamma}{m_\mathrm{p}}\right) \mathrm{e}^{B_\mathrm{D}/T_\gamma} \,, \tag{1.2.25}$$

where $m_\mathrm{p} = 938.27\,\mathrm{MeV}$ is the proton mass and $B_\mathrm{D} = 2.22\,\mathrm{MeV}$ the deuterium binding energy. Thus, while $T_\gamma \gtrsim B_\mathrm{D}$, the deuterium abundance is suppressed by the smallness of η_b. Deuterium production becomes effective, i.e. $n_\mathrm{D}/n_\mathrm{b} \sim 1$, at T_nuc,

$$\ln\left(\eta_\mathrm{b}\right) + \frac{3}{2} \ln\left(\frac{T_\mathrm{nuc}}{m_\mathrm{p}}\right) \sim -\frac{B_\mathrm{D}}{T_\mathrm{nuc}} \,, \tag{1.2.26}$$

which numerically evaluates to $T_\mathrm{nuc} \simeq 0.07\,\mathrm{MeV}$. However, the amount of deuterium produced by then depends on the availability of free neutrons.

At temperatures larger than T_nuc, only free protons and neutrons exists, which interact by the weak process $\mathrm{p} + \mathrm{e}^- \leftrightarrow \nu + \mathrm{n}$. In nuclear statistical equilibrium (indicated here by the "(0)" superscript) the proton to neutron ratio is

$$n_\mathrm{p}^{(0)} / n_\mathrm{p}^{(0)} = \exp\left(\frac{m_\mathrm{n} - m_\mathrm{p}}{T_\gamma}\right) , \tag{1.2.27}$$

where $m_\mathrm{n} - m_\mathrm{p} = 1.293\,\mathrm{MeV}$. If weak interactions were rapid enough to maintain the equilibrium distribution until T_nuc, neutrons would have been completely deteriorated, and no light elements could form. However, the annihilation rate being $\Gamma_{\mathrm{p+e}\to\mathrm{n}+\nu} \sim G_\mathrm{F}^2 T_\gamma^5$, the interactions freeze out at a temperature around 0.5 MeV, when neutrons contribute about 15% to the total baryon abundance. Subsequently, the neutron abundance is affected by neutron decay, $\mathrm{n} \to \mathrm{p} + \mathrm{e}^- + \nu$, with lifetime $\tau_\mathrm{n} = 886.7\,\mathrm{s}$ and decreases by an additional factor of e^{-t/τ_n}. The time elapsed between weak decoupling and T_nuc is determined by

$$\frac{1}{T_\gamma}\frac{dT_\gamma}{dt} = -H = -\sqrt{\frac{8\,\pi}{3\,m_\mathrm{P}^2}\rho}\,, \tag{1.2.28}$$

where ρ is given by Eq. (1.2.20) and we used that the universe is dominated by radiation at the time of Big Bang nucleosynthesis. Taking $N_\mathrm{eff} = 3.046$ (c.f. Eq. (1.2.17)), the neutron abundance $X_\mathrm{n} \equiv n_\mathrm{n}/(n_\mathrm{p} + n_\mathrm{n})$ is

$$X_\mathrm{n}\,(T_\mathrm{nuc}) = 0.11\,. \tag{1.2.29}$$

The binding energy of ^{4}He is much larger than that of deuterium, and helium is fused immediately after deuterium production starts. Eventually, almost all neutrons available are processed into ^{4}He and the resulting helium mass fraction is [47–51]

$$X_4 \equiv \frac{4\,n\,(^4\mathrm{He})}{n_\mathrm{b}} = 2X_\mathrm{n}(T_\mathrm{nuc})\,. \tag{1.2.30}$$

Because the reactions which fuse deuterium and ^{3}He are not completely efficient, small traces of the respective isotopes remain unburnt, each at a level of about 10^{-5} when compared to the hydrogen abundance. Some ^{7}Li is synthesised as well, at a level of $\sim 10^{-10}$ [19]. However, when the deuterium abundance becomes significant, the Coulomb barrier to synthesise heavier elements is already large compared to thermal energies. This and the lack of stable isotopes with mass numbers 5 and 8 prevents the nucleosynthesis of heavier elements. Those are produced in stellar nucleosynthesis at a later time.

Big Bang nucleosynthesis gives direct, observational insights into the thermal conditions in the early universe. In particular, the light element abundances are sensitive to the baryon density, because it determines T_nuc, and to the number of relativistic degrees of freedom at temperatures around 1 MeV, which affect the Hubble rate and therefore the neutron abundance at T_nuc. Importantly, the observed isotope abundances agree well with the predictions of BBN [52].

1.2.4 Dark matter production

There is a plethora of observational evidence supporting the existence a species with small velocity dispersion, which interacts with the Standard Model sector predominantly through gravity – cold dark matter (CDM). Amongst this evidence are galactic rotation curves, the dynamics of galaxy clusters and gravitational lensing. Perturbations in the baryon density only can grow after baryons and photons have decoupled, too late to explain the oldest

observed galaxies or anisotropies in the CMB [19, 21, 29]. The X-ray emission from galaxy clusters [53, 54] and fluctuations in the CMB [15], independently indicate that baryons only contribute 16% to the total matter abundance.

Observations impose that dark matter has to be a stable particle with neither electric nor colour charge and a small velocity dispersion. No candidate from the Standard Model can meet all requirements. However, there is a multitude of extensions to the Standard Model, which provide suitable options. Those candidates often experience some weak, non-gravitational interactions with the Standard Model, which can enable their production in the early universe and their experimental detection at the present.

The most prominent mechanism to generate the dark matter relic abundance is the freeze out of a weakly coupled, massive particle (WIMP) [21, 29, 55]. At high temperatures $T_\gamma \gg m_{\rm dm}$, dark matter production from Standard Model collisions and dark matter annihilation proceed at equal rates. When the plasma temperature drops below the dark matter mass, production becomes less efficient than annihilation, and the dark matter abundance gets suppressed exponentially (c.f. Eq. (1.2.11)). Soon after, the rate for dark matter annihilation drops below the Hubble rate. At this time, dark mater chemically decouples, and henceforth the comoving dark matter density remains fixed.

In the most simple case, where the dark matter particle is stable, symmetric and has no significant self interactions, the Boltzmann equation (c.f. Eq. (3.4.8)), can be integrated to [56, 57]

$$\frac{d\,n_{\rm dm}}{dt} + 3H\,n_{\rm dm} = \langle\sigma_{\rm dm} v\rangle \left[(n_{\rm dm}^{\rm eq})^2 - n_{\rm dm}^2\right] , \tag{1.2.31}$$

where $\langle\sigma_{\rm dm} v\rangle$ is the thermally averaged annihilation cross section [58], $n_{\rm dm}$ the dark matter number density and $n_{\rm dm}^{\rm eq} = \int d^3p f_{\rm dm}^{\rm eq}$ the number density in chemical equilibrium. For convenience, the integrated Boltzmann equation is further rewritten in terms of the dimensionless variables $Y \equiv n_{\rm dm}/s$ and $x = m_{\rm dm}/T_\gamma$,

$$\frac{x}{Y_{\rm eq}}\,\frac{dY}{dx} = \frac{\Gamma_{\rm dm}}{H}\left[\left(\frac{Y}{Y_{\rm eq}}\right)^2 - 1\right] , \tag{1.2.32}$$

with the effective interaction rate $\Gamma_{\rm dm} = n_{\rm dm}^{\rm eq}\,\langle\sigma_{\rm dm} v\rangle$. With this parameterisation, Y is proportional to the comoving number density and remains constant if $n_{\rm dm} \propto a^{-3}$. Numerical integration of Eq. (1.2.32) reveals that for $H \ll \Gamma_{\rm dm}$ and $x \ll 1$ the dark matter number density follows the equilibrium distribution and $Y \sim$ const.. When $\Gamma_{\rm dm} \sim H$, Y starts to decrease. Eventually, in the $H \ll \Gamma_{\rm dm}$ regime, Y approaches a constant again, marking the freeze out of dark matter. If the temperature at freeze out is $T_{\rm f} \sim m_{\rm dm}/20$, the predicted dark matter relic abundance,

$$\Omega_{\rm dm} h^2 = 5.36 \times 10^9\,\frac{\sqrt{g_*}}{g_{*\rm s}}\,\frac{m_{\rm dm}}{T_{\rm f}}\,\frac{(n+1)\,{\rm GeV}^{-1}}{m_{\rm P}\,\langle\sigma_{\rm dm} v\rangle} , \tag{1.2.33}$$

roughly matches observations [21, 29]. Here, g_*, $g_{*\rm s}$ and $\langle\sigma_{\rm dm} v\rangle$ are evaluated at $T_{\rm f}$ and n characterises the temperature dependence of the annihilation cross section, i.e. $n = 0$ for s-wave and $s = 1$ for p-wave annihilation.

Famously, Eq. (1.2.33) predicts the correct relic abundance for a particle with $m_{\rm dm} \sim 100\,\text{GeV}$ and weak-scale interactions, a circumstance referred to as the WIMP miracle [59]. Nevertheless, freeze out production of dark matter is viable over a broad mass range. Owing to the fact that freeze out creates a dark matter population with a thermal distribution and that the freeze out time decreases for smaller dark matter masses, light thermal dark matter candidates are often referred to as warm dark matter. The free streaming of warm dark matter suppresses initial perturbations in the matter power spectrum and prohibits the formation of structures on scales smaller than the free streaming length. Small-scale density fluctuations observed in the Ly-α forest (c.f. Sec. 2.2.3) impose the constraint [60]

$$m_{\rm dm} \gtrsim 3.3\,\text{keV}\,. \tag{1.2.34}$$

In addition to freeze out, there are plenty alternative dark matter production mechanism, which have gained popularity in view of collider and direct detection null results. Among them is the possibility that dark matter is a feebly interacting massive particle (FIMP), produced from the thermal plasma by freeze in [55, 61]. In this scenario, the dark matter particle never reaches chemical equilibrium with the heat bath. Instead, some particle σ in the plasma decays into dark matter. The process $\sigma \to \text{dm} + \text{dm}$ continues to increase the dark matter abundance until the temperature drops to $T_\gamma \simeq m_\sigma$ and n_σ becomes Boltzmann suppressed. Assuming that the initial dark matter density is negligible and that back reactions are insignificant due to the smallness of $n_{\rm dm}$, the relic abundance is given by [61]

$$\Omega_{\rm dm}h^2 = 4.48 \times 10^8 \, \frac{g_\sigma}{g_{*\rm s}\sqrt{g_*}} \, \frac{m_{\rm dm}}{\text{GeV}} \, \frac{m_{\rm P}\,\Gamma_{\sigma\to\text{dm}+\text{dm}}}{m_\sigma^2}\,, \tag{1.2.35}$$

where g_σ counts the intrinsic degrees of freedom of the field σ, g_* and $g_{*\rm s}$ are evaluated at $T_\gamma \simeq m_\sigma$ and $\Gamma_{\sigma\to\text{dm}+\text{dm}}$ is the decay width. The FIMP couplings required to produce the correct relic abundance are $\mathcal{O}(8)$ magnitudes smaller than the weak-scale couplings of WIMPs [55]. Indeed, these couplings are sufficiently small to be compatible with the central freeze in assumption, that is that dark matter has not thermalised with the visible sector at $T_\gamma > m_\sigma$. Alternatively, freeze in can proceed via annihilation, i.e. by the process $\sigma + \sigma \to \text{dm} + \text{dm}$. In this case, the relic abundance is established when $\max\left(m_{\rm dm}, m_\sigma\right)/T_\gamma \sim \mathcal{O}(1)$.

Yet another option is the entirely non-thermal production of a very light scalar or pseudo-scalar particle from the misalignment mechanism [62–64]. In the early universe, the equation of motion for such a field φ with mass m_φ is [65, 66]

$$\ddot{\varphi} + 3H\,\dot{\varphi} + m_\varphi^2\,\varphi = 0\,, \tag{1.2.36}$$

and its solution breaks into two regimes. At early times, when $H \gg m_\varphi$, φ is constant. Later, when the Hubble rate and m_φ become of the same order, Eq. (1.2.36) describes a damped, harmonic oscillator. In this regime, the energy density stored in the coherent

oscillations of φ precisely behaves like dark matter

$$\rho_\varphi(a) \simeq \frac{m_\varphi^2\,\varphi_{\rm ini}^2}{2}\left(\frac{a_{\rm osc}}{a}\right)^3\,, \quad \text{for} \quad a > a_{\rm osc}\,, \tag{1.2.37}$$

where $a_{\rm osc}$ is defined from $m_\varphi = H(a_{\rm osc})$. The dark matter abundance depends on the initial value $\varphi_{\rm ini} \simeq \varphi(a_{\rm osc})$ which, in many cases, is a random value between 0 and 2π. Dark matter production from misalignment is entirely non-thermal and does not rely on any couplings between dark matter and the visible sector. The canonical example for such a dark matter candidate is the QCD axion [67–69], whose mass exhibits an extra temperature dependence such that oscillations in the axion field commence when $T_\gamma \sim 1\,\text{GeV}$. Axions with masses in the ballpark of $\mathcal{O}(1)\,\mu\text{eV}$ to $\mathcal{O}(100)\,\mu\text{eV}$ could naturally account for all observable dark matter [19]. For more general models of axion like particles and fuzzy dark matter [70], masses as low as $10^{-21}\,\text{eV}$ are viable [71]. Because the misalignment effect produces a dark matter population with extremely small velocity dispersion, the warm dark matter mass bound of Eq. (1.2.34) does not apply in this case.

Beyond the baseline mechanism outlined here, a large variety of more complex scenarios exists. So are the freeze out predictions modified if the dark matter particle has significant self-couplings [72–74]. In dark freeze out, as another example, an extended dark sector is populated in a freeze in manner, thermalises within itself and, eventually, dark matter freezes out from the dark sector [75, 76]. The similarity between the baryon and dark matter abundances motivate to consider the production of dark matter from an initial asymmetry [77, 78]. Sterile neutrinos in the keV mass range can be produced either by freeze in or freeze out and explain the small neutrino masses observed in the Standard Model simultaneously with the dark matter abundance [79]. Alternatively, there is the possibility that dark matter emerges during reheating from inflaton decay [80].

1.2.5 Recombination

Compton scattering between photons and electrons is effective while the photon temperature exceeds the binding energy of hydrogen, $B_{\rm H} = 13.6\,\text{eV}$, and the large photon to baryon ratio (c.f. Eq. 1.2.24) ensures that every neutral hydrogen atom is immediately ionised by a high energy proton. Meanwhile, electrons and the other baryons, namely protons, helium and small abundances of other light isotopes, are tightly coupled by Coulomb interactions. Only when the temperature has decreased sufficiently, neutral hydrogen can form during the epoch of recombination. As the abundance of free electron decreases, Compton scattering becomes less effective and photons decouple from baryons.

To predict the time of recombination, we neglect helium, which contributes about one in ten nuclei. Charge neutrality of the universe implies that the number densities of free electrons and protons equal each other. Thus, the free electron fraction is [21]

$$X_{\rm e} \equiv \frac{n_{\rm e}}{n_{\rm e} + n_{\rm H}} = \frac{n_{\rm p}}{n_{\rm p} + n_{\rm H}}\,. \tag{1.2.38}$$

While the process of hydrogen formation, $e^- + p \leftrightarrow H + \gamma$, is in thermal equilibrium, the free electron fraction obeys the Saha equation [21, 29]

$$\frac{1 - X_e^{eq}}{(X_e^{eq})^2} = \frac{4\sqrt{2}\,\zeta(3)}{\sqrt{\pi}}\,\eta_b \left(\frac{T_\gamma}{m_e}\right)^{3/2} e^{\frac{B_H}{E_\gamma}} . \tag{1.2.39}$$

The Saha equation correctly predicts the temperature at recombination T_* by which an $\mathcal{O}(1)$ fraction of electrons is confined in neutral hydrogen. The smallness of η_b in Eq. (1.2.39) leads to a significant delay of recombination, and $T_* \simeq 0.3\,\text{eV}$ is much smaller than the hydrogen binding energy. However, the equilibrium assumption eventually breaks down and Eq. (1.2.39) can not reliably evolve X_e further. Rather, the Boltzmann equations for the coupled system of baryons and photons need to be solved numerically [81–83]. The full numerical treatment shows that the free electron fraction drops very quickly from unity to 10^{-3}, implying a steep decrease in the rate for photon-electron scattering,

$$\Gamma_{\gamma-b} = n_e\,\sigma_T\,, \tag{1.2.40}$$

where $\sigma_T = 1708.36\,\text{GeV}^2$ is the Thomson cross section [19, 29]. As a consequence, the photon scattering rate drops below the Hubble rate and the universe becomes transparent to radiation. The free streaming photons have an almost perfect black body spectrum, which is redshifted by the expansion of the universe [51, 84], and comprise the cosmic microwave background [85, 86]. The COBE/FIRAS measurement of the CMB temperature [87] determines its present-day value as

$$T_{CMB} = (2.7255 \pm 0.0006)\ \text{K}\,, \tag{1.2.41}$$

and confirm the black body nature of the CMB spectrum. The CMB temperature is remarkably uniform over the whole sky and exhibits only small anisotropies at the level of $\Delta T/T \sim 10^{-5}$ [20], which originate from inflationary perturbations. Temperature and polarisation anisotropies in the CMB are a powerful test of the ΛCDM model [15] and further discussed in Sec. 2.3.

1.2.6 Structure formation

The cosmic large-scale structure, the galaxies, clusters, voids and filaments, originates from small inflationary density perturbations. After inflation, their wavelength exceeds the Hubble radius and fluctuations are frozen, but they start to evolve as they regain causal contact during the matter- and radiation-dominated epoch. Then, pressure and the cosmic expansion act to decrease δ, while it is enhance by self-gravity [21]. The combination of these competing forces determines the evolution of density perturbations, which differs considerably between species.

Scales which enter the horizon before electroweak decoupling are observationally not accessible. Thus, in the context of structure formation, neutrinos are described as relativistic, free streaming particles at early times. At late times, the neutrino mass has to be accounted for, we postpone the discussion of its effect to Sec. 6.2.3. Their large velocity dispersion

enables free streaming neutrinos to escape from overdense regions, and perturbations in the neutrino density decrease by free streaming damping [29, 88].

Dark matter is completely collisionless as well and, under standard ΛCDM assumptions, has a negligible velocity dispersion. Only the cosmological expansion and gravity affect the evolution of its perturbations. At early times, when radiation dominates the gravitational potentials and determines the Hubble rate, their growth is slowed down, but it accelerates during matter domination [89]. While a perturbation is in the linear regime, that is $\delta \lesssim 0.1$ [90], it evolves according to [21]

$$\delta_{\mathrm{dm}} \propto \begin{cases} \ln a & \text{radiation domination} \\ a & \text{matter domination} \end{cases} . \tag{1.2.42}$$

Matter-radiation equality, marking the transition between both regimes, occurs slightly before CMB decoupling at a temperature and redshift of

$$T_{\mathrm{eq}} = 0.77\,\mathrm{eV} \left(\frac{\Omega_{\mathrm{m}} h^2}{0.142}\right) , \tag{1.2.43a}$$

$$z_{\mathrm{eq}} = 3.3 \times 10^3 \left(\frac{\Omega_{\mathrm{m}} h^2}{0.142}\right) . \tag{1.2.43b}$$

Photons and baryons, finally, are tightly coupled before the epoch of recombination. The pressure support from photons prevents baryon perturbations from growing, even though baryons are fully non-relativistic. Diffusion between photons and baryons at the time of last scattering further damps their perturbations, this process is called collisional or Silk damping [91]. The coupling of baryons and photons, as well as diffusion damping, have important observable consequences for the CMB anisotropy spectrum and the matter power spectrum. We further discuss these in Sec. 2.3.1 and Sec. 2.2.1, respectively. After decoupling, photons free stream, while baryons fall into the potential wells created by dark matter.

Dark matter overdensities continue to grow until they reach the non-linear regime, $\delta \sim 1$. At this point an overdense region separates out from the cosmological expansion, collapses and virializes to eventually form a halo. Smaller structures enter the Hubble radius earlier and are the first objects to collapse. As larger scales enter the non-linear regime, the small halos are merged, and partly destroyed, into bigger ones, and the formation of the cosmological large-scale structure proceeds in a hierarchical bottom-up way.

The evolution of perturbations in the linear regime, is formally described by the linearised Einstein and Boltzmann equations, which we derive in Chapter 3. In the non-linear regime, n-body simulations are a powerful tool, to predict the formation of large-scale structure. They follow the self-gravitational evolution of a large number of test particles on a comoving grid. By the time perturbations grow non-linear, their size is much smaller than the Hubble radius and the gravitational dynamics can be approximated as Newtonian [90].

1.2.7 The universe at late times

After recombination, when the pressure support from the thermal plasma ceases, neutral atoms fall in the potential wells of dark matter perturbations and condense. The formation of early stars requires halo masses around $(10^5 - 10^7)\,M_\odot$, where $M_\odot$ refers to the solar mass. Only halos above this threshold can incarcerate gas at temperatures in excess of $1,000\,\mathrm{K}$ [92,93], and therefore star formation is suspended until a redshift of ~ 70. After decoupling, the CMB is soon redshifted to near infrared wavelength, and the universe enters the so-called dark ages, where there is no source of light in the visible spectrum in the universe.

The modest energy injection from early stars reionises only a small fraction of the cosmological helium abundance [94,95]. The first galaxies, formed abundantly in halos of masses $\gtrsim 10^8\,M_\odot$ around $z \sim 10$, can harbour more substantial star formation rates [96,97]. They most likely drove the ionisation of the intergalactic medium (IGM), the non-virialized matter residing in the voids between galaxies and larger collapsed structures [97,98]. This late-time reionisation is evident from the CMB, where it suppresses temperature fluctuations but generates polarisation anisotropies at small scales. A simple, one parameter description suffices to characterise the effect of reionisation, it is given by the optical depth to Thomson scattering from reionisation [4,98]

$$\tau_\mathrm{re} = (n_{\mathrm{H},0} + n_{\mathrm{p},0})\; c\,\sigma_\mathrm{T} \int_0^{z_\mathrm{max}} dz\; X_\mathrm{e}(z)\,\frac{(1+z)^2}{H(z)}\,, \tag{1.2.44}$$

where $(n_{\mathrm{H},0} + n_{\mathrm{p},0})$ is the total number density of hydrogen nuclei today and z_max labels some early time, before the onset of reionisation, when the free electron fraction X_e is negligible.

Measurements of the spectra of very distant supernovae [99–101] allow to extend the Hubble diagram beyond the simple proportionality law of Eq. (1.1.11). They reveal that the expansion of the universe is accelerating. Furthermore, the CMB anisotropy spectrum strongly favours a flat universe [102,103], yet the mass inferred from gravitational lensing [104] and X-ray surveys [53,54] only accounts for $\sim 30\%$ of ρ_crit [19]. A straightforward way to explain the accelerated expansion and the missing energy density is the introduction of a dark energy component with constant energy density ρ_Λ $w_\Lambda = -1$ as in Eq. (1.1.7). This assumption, comprised in the ΛCDM model, implies that the transition from matter to dark energy domination occurred very recently, at a redshift of

$$z_\Lambda = 0.764\,\left(\frac{\Omega_\Lambda}{0.962}\right)^{1/3}\left(\frac{\Omega_\mathrm{m}}{0.308}\right)^{-1/3} - 1\,, \tag{1.2.45}$$

where Ω_m is the fractional energy density of all non-relativistic matter. However, the required value of ρ_Λ is hard to motivate, and at least 10^{15} times smaller the vacuum energy density predicted from Standard Model quantum effects [19,105]. There is also room for a time-varying dark energy component, any equation of state with $w < -1/3$ results in an accelerated expansion according to Eq. (1.1.5). Alternatively, modifications to general relativity can accommodate the acceleration [106].

1.3 The cosmological standard model

The ΛCDM model summarises the cosmological history outlined in the previous section and successfully describes the observational data available at present. It is based on the presumption that general relativity is an adequate description of gravity, that the universe is spatially homogeneous and isotropic and that it has negligible curvature. Accordingly, the Friedmann-Robertson-Walker metric (Eq. (1.1.2)) with $k = 0$ describes the universe's geometry and its evolution is governed by the Friedmann equations (1.1.4) and (1.1.5). Several different species contribute to the total energy density, and those relevant to describe current observations are:

- Dark energy, with a constant equation of state.
- Dark matter, which is stable, pressureless and has only gravitational interactions.
- Baryonic matter, to which electrons, protons, neutrons and nuclei contribute, with the primordial helium fraction set by Big Bang Nucleosynthesis.
- The CMB photons. Their temperature can be measured directly to accurate precision and without dependence on any further cosmological parameters [87]. In the baseline scenario it is fixed to $T_{\rm CMB} = 2.2755\,\mathrm{K}$.
- Three light Standard Model neutrino species. At first order, cosmology is only sensitive to the sum of their masses [107, 108]. In the baseline scenario this is fixed to the minimum value required by neutrino oscillations, which, assuming a normal hierarchy, is $\sum m_\nu = 0.06\,\mathrm{eV}$.

An early inflationary epochs provides small, adiabatic, Gaussian density perturbations with a near scale-invariant primordial spectrum. The cosmic large-scale structure grows from these fluctuations by gravitational instability. Inflation also predicts the existence of tensor perturbations, but at the present a scalar-to-tensor ratio of $r = 0$ provides an excellent fit to the data available. After inflation, reheating restores thermal conditions, and light elements form during Big Bang nucleosynthesis. Neutrinos decouple from the thermal plasma when $T_\gamma \sim 1\,\mathrm{MeV}$ and at $T_* \simeq 0.3\,\mathrm{eV}$ neutral hydrogen forms and photons decouple. At later times the first galaxies reionise the intergalactic medium.

Notably, under the assumption of a ΛCDM cosmology, six free parameters suffice to characterise cosmological observations. For many purposes it is convenient to introduce the dimensionless Hubble constant h

$$H_0 = 100 \times h \, \frac{\mathrm{km}}{\mathrm{Mpc\,s}} \,. \tag{1.3.1}$$

A common set of parameters, convenient in the description of observations, is [4]

$$\Omega_{\rm dm} h^2 \,, \quad \Omega_{\rm b} h^2 \,, \quad \ln\left(10^{10} A_{\rm s}\right) \,, \quad n_{\rm s} \,, \quad \tau_{\rm re} \,, \quad 100\,\theta_* \,, \tag{1.3.2}$$

where $\Omega_{\rm dm}$ and $\Omega_{\rm b}$ refer to the energy density in baryons and dark matter normalised to $\rho_{\rm crit}$, c.f. Eq. (1.1.12). Two parameters, A_s and n_s, describe the spectrum of inflationary perturbations as defined in Eq. (1.2.4), and $\tau_{\rm re}$ gives the optical depth to Thomson scattering from reionisation (1.2.44). Finally, θ_* is the angular scale of the acoustic oscillations, which specifies the position of the CMB acoustic peaks. It is determined by the comoving sound horizon at recombination $r_{\rm s}(z_*)$ and the comoving angular diameter distance to recombination $D_{\rm M}(z_*)$ [109]

$$\theta_* = \frac{r_{\rm s}(z_*)}{D_{\rm M}(z_*)}\,, \tag{1.3.3}$$

where z_* is the redshift of recombination. The sound horizon follows from the sound speed of the baryon-photon plasma $c_{\rm pl}$ (see Eq. (2.2.2))

$$r_{\rm s}(z) \simeq \int_0^{t(z)} dt\; c_{\rm pl}(t)\,. \tag{1.3.4}$$

The angular diameter distance relates the size of an object at redshift z to the sky angle it subtends

$$D_{\rm M}(z) = \int_{a(z)}^{1} \frac{da'}{a'^2\, H(a')}\,. \tag{1.3.5}$$

Further cosmological quantities of interest, e.g. H_0, Ω_Λ or the redshift of reionisation $z_{\rm re}$, are completely determined by the parameters in Eq. (1.3.2). Another derived parameter, important in the context of structure formation, is the root mean square of density fluctuations today on a scale of $R = 8\,{\rm Mpc}/h$, defined as [109]

$$\sigma_8^2 = \int \frac{dk}{k}\; \Delta_{\rm s}^2(k) \left(\frac{3 j_1(k\,R)}{k\,R}\right)^3\,, \tag{1.3.6}$$

where $\Delta_{\rm s}^2$ is the dimensionless, linear matter power spectrum at $z = 0$ and j_1 refers to the spherical Bessel function of first order.

The baseline ΛCDM scenario, outlined here, is the same as assumed by the Planck collaboration [4, 109]. Its underlying assumptions have been extensively scrutinised. Amongst the most familiar extensions to the ΛCDM model are:

- Departures from the dynamics predicted by general relativity.
- Modifications to the spectrum of inflationary perturbations, such as non-Gaussianities, isocurvature perturbations and a running of the spectral index $n_{\rm s}$. Actually, latter is implied by slow-roll inflation, but, due the smallness of $n_{\rm s}$, present data is well described assuming an entirely scale-invariant spectrum.
- The introduction of spatial curvature, parameterised by $\Omega_{\rm k} = 1 - \sum_i \Omega_i$, where i labels matter, radiation and vacuum energy.
- Modifications to the dark energy equation of state, i.e. $w_\Lambda \neq 1$, or a time varying equation of state $w_{\rm de}(a) = w_{\rm de,0} + (1-a)\; w_{{\rm de},a}$ [4].
- Non-minimal neutrino masses, i.e. $\sum m_\nu \neq 0.06\,{\rm eV}$.

- Additional radiative degrees of freedom, that is $N_{\rm eff} \neq 3.046$.
- Relaxing the assumption that dark matter has zero pressure. This is, for example, the case for warm dark matter or fuzzy dark matter.
- Allowing for dark matter self-interactions, dark matter annihilation, extended dark matter sectors or scattering between dark matter and Standard Model particles.

In the following Chapter, we summarise the observational status of the ΛCDM model, discuss how the baseline parameters are determined from observations, and what freedom remains on possible extensions of the ΛCDM scenario.

Chapter 2

Observational status of the cosmological standard model

The past decades have seen a tremendous progress in observational cosmology, and to date five of the six free parameters in Eq. (1.3.2) are measured to better than 1% accuracy [15]. Importantly, cosmological observations cover a wide range of redshifts and scales, so that complementary probes allow for consistency checks and can reveal potential tensions. Here, we give a brief overview of the observational status of the ΛCDM model.

2.1 Direct measurements of the Hubble constant

The Hubble diagram [16] provides the most direct evidence of the cosmic expansion. For its determination, the luminosity distance and the redshift of distant astrophysical sources, such as galaxies, clusters, supernovae and quasars need to be measured. While the latter – an accurate determination of the redshift – is rather straightforward [21], distance measures are challenging and often afflicted with systematics. In the following we explain three possibilities to directly measure the expansion rate, the distance ladder, time delay strong lensing and from gravitational waves.

2.1.1 The distance ladder

One of the most reliable methods to measure the Hubble constant directly is by the distance ladder, which was key motivation for the NASA/ESA Hubble Space Telescope (HST) [110]. The approach uses Cepheid variable stars, whose intrinsic brightness is tightly related to their luminosity period [111], to calibrate secondary distance measures. Amongst these are the lightcurves of type Ia and type II supernovae (SN), the Tully-Fisher relation and surface-brightness fluctuations. Relying on brighter sources, the secondary distance measures can extend further out in the Hubble flow [110].

For the most recent study along these lines [112], the SH0ES team uses SN Ia as secondary distance measurements. Their intrinsic brightness is calibrated from Cepheids in the supernova's host halos, observed at distances up to 40 Mpc. At the near end, the ladder is

completed by establishing the distance to Cepheids in the Large Magellanic Cloud from measurements of 20 detached eclipse binaries (DEBs) [113]. This yields, as best estimate of the Hubble constant [112],

$$H_0^{\mathrm{SNIa}} = (74.03 \pm 1.42)\ \mathrm{km\,Mpc^{-1}\,s^{-1}}\,, \tag{2.1.1}$$

and reduces uncertainties by 15% with respect to the previous best estimate [114] based on the distance ladder.

2.1.2 Time delay strong lensing

An alternative approach for the determination of H_0, completely independent of the distance ladder, is to measure the time-delay of strongly lensed images [115]. The lensed image of a source β experiences a time delay with respect to the unperturbed path, which depends on the redshift of the deflector z_{d} and the time delay distance $D_{\Delta t}$. The rays which create multiple lensed images, θ_i, experience different path lengths and gravitational potentials $\Phi\left(\theta_i\right)$, hence there is a net difference between the image's time delay

$$\Delta t_{ij} = \frac{D_{\Delta t}}{c}\left[\left(\frac{(\theta_i-\beta)^2}{2} - \Phi(\theta_j)\right) - \left(\frac{(\theta_j-\beta)^2}{2} - \Phi(\theta_j)\right)\right]. \tag{2.1.2}$$

This difference can be measured, for a variable source, by time monitoring the individual image's brightness [116]. The time delay distance is a combination of angular diameter distances to the deflector D_{d}, to the source D_{s} and between the source and the deflector D_{ds},

$$D_{\Delta t} = (1+z_{\mathrm{d}})\ \frac{D_{\mathrm{d}}\,D_{\mathrm{s}}}{D_{\mathrm{ds}}}\,. \tag{2.1.3}$$

Because $D_{\Delta t} \propto H_0^{-1}$ [117], the Hubble constant can be inferred from measurements of the time delay.

Quasars are suitable sources for time delay strong lensing due to their brightness and variability. To establish accurate time delays requires the long-term monitoring of a sufficiently sized sample. Further, deep, high resolution imaging of the lens is needed for a reliable model of the deflector, as well as a measurement of the lens galaxy's velocity dispersion. Finally, the mass distribution along the line of sight needs to be characterised [117, 118].

For the most resent H0LiCOW result [118], six strongly lensed quasars are analysed. A substantial data set provides the required information to characterise the systems, it contains time delay measurements of the COSMOSMOGRAIL collaboration [119], radio monitoring of the source, deep imaging by the Hubble Space Telescope and with ground based adaptive optics, spectroscopic data of the lens galaxy to estimate its velocity dispersion along with deep wild field spectroscopy to characterise the line of sight. The data allows for a 2.4% determination of the Hubble constant

$$H_0^{\mathrm{TDSL}} = \left(73.3^{+1.7}_{-1.8}\right)\ \mathrm{km\,Mpc^{-1}\,s^{-1}}\,, \tag{2.1.4}$$

Time delay strong lensing is primarily sensitive to H_0, but can, considering departures from the ΛCDM baseline model, also constrain the spatial curvature or the dark energy equation of state. In combination with other data sets, in particular with the CMB and baryon acoustic oscillations discussed below, its high complementarity allows to break degeneracies [118]. Finally, a sample of ~ 40 strongly lensed quasars would allow to determine H_0 to $\sim 1\%$ accuracy, which is feasible in the near future [118].

2.1.3 Gravitational waves as standard sirens

Gravitational waves, detected recently by LIGO [120] and VIRGO [121], can serve as standard sirens, and it is possible to extract the distance to an event directly from the gravitational wave signal [122–126]. Still, for a determination of H_0, the event's redshift is required. In the case of the neutron star merger GW 170817 [127], the observation of its electromagnetic counter-part allowed to identify NGC 4493 as host galaxy of the event. Black hole mergers, on the other hand, are not accompanied by an electromagnetic signal. Even without the unique identification of the host halo, H_0 can be determined statistically, considering a potential set of hosts from galaxy catalogues [122]. Such an approach requires ~ 100 gravitational wave events for a $\sim 5\%$ measurement of the Hubble constant [128].

The combined analysis of GW 170817 and 5 black hole mergers from the first and second LIGO/VIRGO observing run gives [129]

$$H_0^{\mathrm{GW}} = \left(68^{+14}_{-7}\right)\ \mathrm{km\,Mpc^{-1}\,s^{-1}}\,, \tag{2.1.5}$$

and improves the result based on GW 170817 only [18] by about 7%. Although consistent with the distance ladder and time delay strong lensing, the measurement exhibits considerably larger error margins. However, gravitational wave measurements of H_0 are still at an early stage, and upcoming observing runs, with improved detector sensitivity and higher event rates, are expected to improve the constraint [129].

2.2 The universe's large-scale structure

While the observations discussed previously probe the homogeneous universe, perturbations around this background contain a wealth of information. In this section, we consider perturbations in the matter content – the large-scale structure of the universe – from which cosmological parameters can be inferred and the ΛCDM mode can be checked for its consistency. Anisotropies in the CMB are then considered in Sec. 2.3

2.2.1 Cosmological matter distribution

Density perturbations remain Gaussian while they evolve in the linear regime and then are fully characterised by their two-point correlation function. We derive the formalism

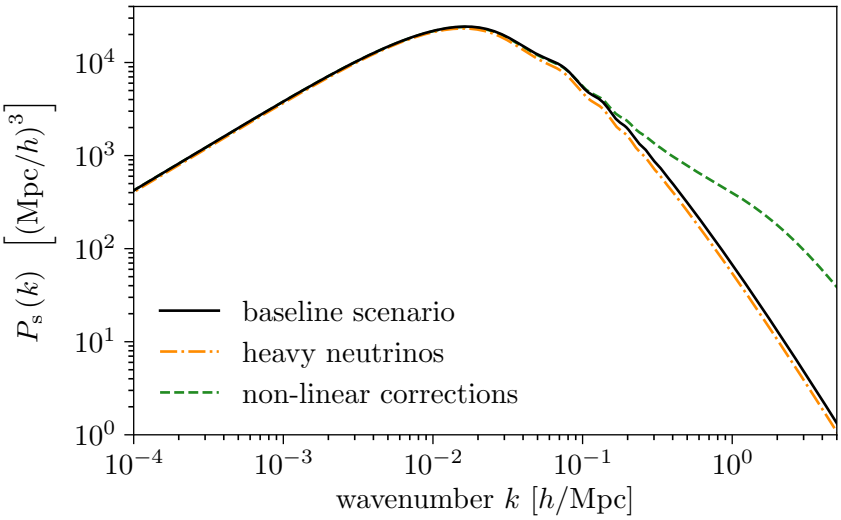

Figure 2.1: The power spectrum of density perturbations at $z = 0$. The baseline scenario assumes a ΛCDM cosmology and $\sum m_\nu = 0.06\,\mathrm{eV}$, while the heavy neutrino example considers $\sum m_\nu = 0.40\,\mathrm{eV}$. Non-linear corrections are shown for the baseline scenario only.

to predict the matter power spectrum in the linear regime – the linearised Boltzmann-Einstein equations – in Chapter 3. Importantly, within the baseline ΛCDM model, the matter power spectrum is entirely determined by the six free parameters of Eq. (1.3.2). One realisation, which assumes the Planck 2018 central values from Tab. 2.1, is shown in Fig. 2.1. Scales smaller than $\sim 10\,\mathrm{Mpc}$ have entered the non-linear regime and non-linear corrections are represented by the green, dashed line in Fig. 2.1. However, the accurate predictions of non-linearities requires numerically-expensive n-body simulations. Often, it is practical to extrapolate the linear evolution until the present epoch, and to work in terms of the linear matter power spectrum at $z = 0$, represented by the black line in Fig 2.1. Observations at different scales and redshift can then be projected onto the extrapolation [130]. Several features in the matter power spectrum, detailed below, are sensitive to cosmological parameters and the properties of dark matter.

Large scales enter the Hubble radius after matter-radiation equality and then grow proportional to the scale factor. Here, the primordial spectrum is translated into an approximate $P(k) \propto k$ scaling at the present epoch. Before matter-radiation equality, however, the growth of perturbations is retarded according to Eq. (1.2.42), and a mode receives the more suppression, the earlier it enters the Hubble radius. Consequently, on small scales the matter power spectrum is a decaying function of the wavenumber [21]. The presence of these two regimes is called Meszaros effect [89], and a turnover in the matter power spectrum marks the transition between them. It occurs precisely at the scale which entered the horizon at matter-radiation equality,

$$k_{\mathrm{eq}} = \sqrt{2}\,\pi\,H_0\,\frac{\Omega_{\mathrm{m}}}{\sqrt{\Omega_{\mathrm{r}}}} = 0.032\,\left(\frac{\Omega_{\mathrm{m}}\,h^2}{0.1408}\right)\,\mathrm{Mpc}^{-1}\,, \tag{2.2.1}$$

where Ω_{r} refers to the total contribution of radiation to the critical energy density.

The baryon contribution to the total matter density imprints a distinct feature on the

matter power spectrum, called baryon acoustic oscillations (BAO). Prior to recombination, baryons and photons form a tightly coupled plasma. Density perturbations excite sound waves in the baryon-photon plasma, which propagate at the plasma's sound speed [131],

$$c_{\mathrm{pl}}^2 = \left[3\left(1+\frac{3\,\rho_{\mathrm{b}}}{4\rho_{\gamma}}\right)\right]^{-1} . \tag{2.2.2}$$

The phase of the oscillations at the time of decoupling is frozen into the baryon perturbations as well as the CMB anisotropies, for the latter see Sec. 2.3. The baryon scattering rate is

$$\Gamma_{\mathrm{b}-\gamma} = R_{\gamma\mathrm{b}}\,\Gamma_{\gamma-\mathrm{e}} = \frac{3\,\rho_{\mathrm{b}}}{4\,\rho_{\gamma}}\,n_{\mathrm{e}}\,\sigma_{\mathrm{T}}\,, \tag{2.2.3}$$

and differs from the photon scattering rate by a momentum conserving factor $R_{\gamma\mathrm{b}} = (3\,\rho_{\mathrm{b}})\,/\,(4\,\rho_{\gamma})$. Thus, baryon decoupling at a redshift of z_{drag} is slightly delayed with respect to recombination [132]. Close to last scattering, photons diffuse from overdense regions and later free stream, dragging along the baryons. This process, called Silk damping [91], decreases the magnitude of baryon perturbations on small scales. After the end of the drag epoch, baryons evolve as non-relativistic matter, and their oscillations lead to a contrast in the present-day matter power spectrum at the level of 10% [133, 134].

The observation of baryon acoustic oscillations on top of a smooth spectrum affirms the growth of density perturbations prior to recombination, and is a further indicator for the existence of dark matter [133]. The characteristic scale of the oscillations is set by the sound horizon (1.3.4) at baryon decoupling $r_{\mathrm{s}}\,(z_{\mathrm{drag}})$, and provides a "standard ruler", a sharp length scale whose comoving size is known accurately [135]. The baryon sound horizon can be obtained to good precision from the CMB, current observations giving $r_{\mathrm{s}} = (144.43 \pm 0.26)$ Mpc [4], and is well separated from non-linear scales [136]. This makes theory predictions very robust, but extracting the weak BAO signal at such a large scale requires huge survey volumes [137]. From measurements of the acoustic scales at varying redshifts one can infer the angular diameter distance $D_{\mathrm{A}}(z)$ and the Hubble rate $H(z)$ and hence track the expansion history of the universe. Considering the Ly-α forest (Sec. 2.2.3) and galaxy clustering (Sec. 2.2.2), the BAO feature can be tracked over a redshift range of $0 < z < 2.5$ [15], with the best current measurements of the BAO feature being given by the BOSS survey [138]. At low redshifts, $z \lesssim 0.5$, the BAO probe of the expansion history is complementary to SN type Ia observations. At larger redshifts, however, the technique is especially powerful in probing the cosmic geometry and the nature of dark energy. In particular, BAO observations break degeneracies when analysed jointly with CMB data sets [15].

Proceeding to small scales, a cut-off of non-gravitational origin is expected in the matter power spectrum [90]. Its observation would advance the understanding of the particle nature of dark matter significantly but is difficult due to the small scales involved. For example suppresses the free streaming of warm dark matter perturbations below the free streaming scale [139, 140] and imposes the bound in Eq. (1.2.34). WIMP dark matter remains kinetically coupled the the Standard Model plasma even after chemical decou-

pling established the relic abundance via the freeze out mechanism. In this case, elastic scattering and, after kinetic decoupling, free streaming prevents the growth of small scale perturbations [141]. For neutralino dark matter, a candidate motivated by supersymmetry, the possible cut-off scale ranges from $10^{-11}\,M_\odot$ to a few times $10^{-4}\,M_\odot$ [142]. The cut-off can be even smaller if dark matter is produced by the misalignment mechanism and set by the Hubble radius when the field commences to oscillate. For the classical QCD axion, halos as small as $10^{-12}\,M_\odot$ are viable [143–146]. Very light misalignment candidates, on the other hand, experience a suppression of perturbations below their present-day de Broglie wavelength [70].

Heavy neutrinos, finally, imprint a characteristic cut-off scale (c.f. Eq. (6.2.6)) on the matter power spectrum as well, followed by a small suppression of power with respect to the case of massless neutrinos. The decrease, whose physical origin is discussed in Sec. 6.2.3, can lie between a factor of 0.04 to 0.08 for viable neutrino masses.

2.2.2 Galaxy surveys

Because the bulk of cosmic matter is dark and not directly observable by telescopes, probing the matter distribution observational is not straightforward. One approach is to infer the total matter power spectrum from the clustering of luminous tracers, such as galaxies. However, galaxies do not follow the underlying matter distribution perfectly [147], but experience a so-called galaxy bias [19, 148].

On the largest cosmological scales, where perturbations are linear, a scale-independent, deterministic bias model applies. The number density of tracers, n_t, follows the distribution of matter except for a constant linear bias parameter b_t and

$$\delta_\mathrm{t}\left(\boldsymbol{x}\right) \equiv \frac{n_\mathrm{t}\left(\boldsymbol{x}\right)}{\langle n_\mathrm{t}\rangle} - 1 = b_\mathrm{t}\,\delta\left(\boldsymbol{x}\right)\,. \tag{2.2.4}$$

In general, however, the bias is scale dependent and stochastic. If not accounted for correctly, it can introduce systematic effects in the determination of cosmological parameters from redshift surveys [149]. In comparison to cosmologies with massless neutrinos, neutrino masses introduce and additional, scale dependent bias [150]. This scale dependence can be neglected in the analysis of current surveys, but it is important for future observations [151], especially when the signatures of non-zero neutrino masses are targeted [152–154].

The halo bias is important for the comparison between galaxy surveys and n-body simulations, and without it the two produce inconsistent results [155]. It can be studied theoretically from simulations of galaxy formation [156]. For its experimental determination, modern surveys consider higher order correlation functions [157–160] and observations of weak lensing [161].

2.2.3 The Lyman-α forest

The light emitted by distant quasars traverses neutral hydrogen clouds along the line of sight. Ly-α absorption in these clouds and the subsequent redshift of the spectrum

produce a set of absorption lines blueward of $121.6\,(1+z_\mathrm{s})$ nm, where z_s is the source's redshift. Because the gas largely traces the underlying matter distribution [162], the so-called Ly-α forest is sensitive to the matter power spectrum.

The probability for Ly-α absorption at redshift z, $P = \exp\left(-\tau_{\text{Ly-}\alpha}\right)$, is determined by the optical depth [98]

$$\tau_{\text{Ly-}\alpha} = 1.3\,\Delta_\mathrm{b}\left(\frac{X_\mathrm{HI}}{10^{-5}}\right)\left(\frac{1+z}{4}\right)^{3/2}\left(\frac{dv/dz}{H(z)/(1+z)}\right)^{-1}, \tag{2.2.5}$$

where Δ_b is the baryon density in units of the cosmic mean, X_HI the neutral hydrogen fraction and dv/dz the line of sight velocity gradient of the gas. Ly-α observations are particularly sensitive for $2 \lesssim z \lesssim 5$. In this range, the line has redshifted to the optical range and a large abundance of bright quasars permits high signal to noise observations. Further, the density and ionisation state of the intergalactic medium at those times provide ideal sensitivity for gas densities close to the cosmic mean [98].

The Ly-α forest probes smaller scales than galaxy surveys and the CMB. These are of a few Mpc and fall into the mildly non-linear regime, where no reliable analytic models are available. Instead, cosmological simulations are used to predict the matter power spectrum and to relate the baryon distribution to inhomogeneities in the total matter abundance [98]. Analyses commonly consider the Ly-α line of sight power spectrum

$$P_{\text{Ly-}\alpha}(k) \equiv L_\mathrm{LOS}^{-1}\,|\delta_\mathrm{F}(k)|^2 \tag{2.2.6}$$

where L_LOS is the length of the sight line and $\delta_\mathrm{F}(k)$ the Fourier transform of the transmission overdensity at a position x, i.e. $\delta_\mathrm{F}(x) = (F(x)/\langle F(x)\rangle) - 1$. At high wavenumbers $P_{\text{Ly-}\alpha}(k)$ is sensitive to the small-scale smoothing of the gas and can probe the gas temperature or constrain models of warm dark matter [60]. Low wavenumbers, on the other hand, are complementary to probes at larger scales and sensitive to the large-scale structure of dark matter. The Ly-α power spectrum alone constraints Ω_m, n_s and σ_8 to better than 10% precision [163]. The BAO feature can also be extracted from the correlation of Ly-α absorption lines. Assuming a ΛCDM cosmology, the BAO measurement of eBOSS at $z = 2.34$ is consistent with results from the CMB [164].

2.2.4 Cosmic shear

Associated with the cosmic large-scale structure is a tidal field, which acts as gravitational lens on the light emitted by distant galaxies and distorts their shapes. In contrast to galaxy surveys and Ly-α observations, gravitational lensing is sensitive to the total mass along the line of sight. Thus, it directly probes the total matter distribution, rather than inferring it from baryons [147, 165]. Because the distortions caused by lensing are small, on the order of a few percent, and the intrinsic shape and size of the lensed galaxy are unknown, the effect is measured statistically, from the correlation between galaxy shapes. This technique is called "cosmic shear" or "weak cosmological lensing" [166].

Major complications in the cosmological interpretation of the lensing signal arise because the bulk of statistical power stems from significantly non-linear scales [4], and because not only weak lensing affects the galaxy correlation function but also the intrinsic alignment between galaxies and their surrounding potentials [167]. The modelling of this shape noise, for example, significantly affects the results of the Kilo-Degree Survey (KiDS) survey [168].

Cosmic shear is sensitive to the clustering of matter over a wide range of scales, from the highly non-linear sub-Mpc regime to several hundreds of Mpc [166]. Further, it probes the time evolution of perturbations if the source galaxies are divided into redshift bins [169]. In the context of the canonical ΛCDM model, weak lensing is sensitive to Ω_m and σ_8, and in particular to the combination $\sigma_8\,\Omega_\mathrm{m}^\alpha$ where $\alpha \simeq 0.5 - 0.7$. It constrains the gravitational potentials at a lower redshift than the CMB and hence offers a complementary probe. Further, CMB lensing and cosmic shear probe orthogonal directions in the Ω_m-σ_8 plane, and the combination of both significantly reduces degeneracies [170]. Beyond the ΛCDM model, weak lensing is of particular importance studies of to the dark energy equation of state and models of modified gravity, both of which predict modifications to the late-time growth of matter perturbations [171].

The Hubble Space Telescope Cosmic Evolution Survey (COSMOS) [172] obtained the shapes of half a million galaxies, whose analysis reveals overdense regions, which are insufficiently dense to generate X-ray emission. The observed filaments, objects which have gravitationally collapsed along two axes [173], resemble very well the predictions from n-body simulations of structure formation [174]. More recently, the Dark Energy Survey (DES) [175] observed 26 million galaxies at redshift $0.2 \leq 1.3$ over a sky area of 1321 deg^2. Cosmic shear alone constrains the amplitude of matter perturbations, parameterised by $S_8 \equiv \sigma_8\ (\Omega_\mathrm{m}/0.3)^{0.5}$, to [176]

$$S_8^{\mathrm{DES-shear}} = 0.782 \pm 0.027 \quad \text{at } 68\%\ \text{C.L.}\,, \tag{2.2.7}$$

assuming a ΛCDM cosmology with unknown neutrino masses. To tightly constrain the dark energy equation of state, DES considers several additional probes, namely the lightcurves of type Ia supernovae, baryon acoustic oscillations and galaxy clustering. Their combination, again not assuming a specific value for $\sum m_\nu$, yields [177]

$$S_8^{\mathrm{DES,wCDM}} = 0.786^{+0.029}_{-0.019}\,, \quad w_\Lambda^{\mathrm{DES,wCDM}} = -0.80^{+0.09}_{-0.11} \quad \text{at } 68\%\ \text{C.L.} \tag{2.2.8}$$

2.2.5 Discrepancies at small scales

The ΛCDM model describes the distribution of matter in the universe remarkably well over a wide range of scales, from the cosmic horizon ($\sim 15,000\,\mathrm{Mpc}$) at largest down to the typical spacing between galaxies ($\sim 1\,\mathrm{Mpc}$) [155, 178]. The lower end of this range already is deeply in the non-linear regime, where predictions are obtained from numerical n-body simulations. Proceeding to even smaller scales, high resolution simulations of Milky Way sized halos [179–183] predict the existence of dark matter clumps at all resolved masses. Comparing the abundance and structure of these predicted small-scale halos to observed

dwarf galaxies reveals several discrepancies, which are commonly summarised as small scale crisis [178]. Amongst these issues are the missing satellite problem [184, 185], the cusp-vs-core problem [186, 187] and the too-big-to-fail problem [188].

The missing satellite problem addresses a mismatch in the abundance of substructures in Milky Way sized halos. While simulations predict the existence of $\mathcal{O}(10^3)$ subhalos with masses in principle large enough to support stellar cooling, only ~ 50 satellite galaxies are known in the Milky Way and only ~ 30 for Andromeda [189]. Investigating the structure of small dark matter halos itself, the cusp-vs-core problem arises. In simulations, their density profiles are of the form $\rho(r) \propto r^{-\gamma}$ with $\gamma \simeq 0.8 - 1.4$ [190] and display a central cusp. In contrast, most galaxies in low-mass, dark matter-dominated halos with well measured rotation curves prefer a cored profile with $\gamma \simeq 0 - 0.5$, see e.g. [191]. As a closely related issue, simulations also prefer a lower central density as observed in satellite galaxies [192,193]. The mismatch in the total mass of dwarf galaxies and its first derivative, the density profile, might likely be of common origin and is often discussed jointly [178]. Finally, the most massive subhalos in simulations have systematically higher central density than the brightest Milky Way dwarf galaxies [188, 194]. Although subhalos with masses matching the brightest Milky Way dwarfs exist in simulations, these never are amongst the ~ 10 most massive [178]. Why those less massive halos should have formed galaxies when the heavier ones failed to is unclear. The mismatch, dubbed too-big-to-fail-problem, has also been observed for Andromeda satellites [195], dwarf galaxies in the Local Group [196] and more isolated low-mass galaxies [197, 198].

The small scale problems provide motivation to consider alternatives to the paradigm of collisionless, pressureless dark matter. However, given the huge success of ΛCDM on large scales, any viable solution should behave as cold dark matter there. For example, the matter power spectrum of warm dark matter exhibits a cut-off at small scales. Because structure formation proceeds in a hierarchical, bottom-up manner, the truncation's impact extends to halos which are 2 - 3 orders of magnitude heavier than the free streaming scale. These exhibit a reduced central density, which helps to alleviate the too-big-to-fail problem [199]. Dark matter scattering with Standard Model particles beyond the kinetic decoupling time implied by WIMP models has a similar effect [200–202]. And dark matter self-interactions in virialized halos can transfer kinetic energy from high- to low-velocity particles, which heats the central part of the halo and reduces the density [203,204]. Simulations with self-interacting dark matter (SIDM) [205–208] suggest an interaction cross section around $\sigma_{\mathrm{dm-dm}}/m_{\mathrm{dm}} = (0.5 - 10)\ \mathrm{cm}^2/\mathrm{g}$ to alleviate the cusp-vs-core and the too-big-to-fail problem [178], but substructure counts remain nearly identical to collisionless dark matter [209]. In contrast to this value, the high central density of galaxy clusters limits the dark matter self interaction cross section to $\sigma_{\mathrm{dm-dm}} \lesssim 0.5\,\mathrm{cm}^2/\mathrm{g}$. One possibility to solve small scale discrepancies with self interacting dark matter and simultaneously accommodate the constraints from clusters, are models with an velocity dependent cross section, which decreases for higher velocities.

Despite the existence of many beyond-ΛCDM solutions to the small scale problems, it is noteworthy that hard to model baryonic processes can significantly alter predictions

for the shape and observability of dark matter halos. Indeed, there exist well motivated solutions to the small scale problems, which require no modifications to the ΛCDM premise. The heating of the intergalactic medium by reionisation can inhibit galaxy formation in small mass halos [210–212], and these truly dark objects would go undetected in surveys. In combination with a careful consideration of the luminosity bias [213], this mechanism settles the missing satellite problem [178, 214]. Baryonic feedback can erase central cusps and create cored density profiles in halos with suitable star formation [215, 216]. If the star formation rate is too low, there is not enough energy release from supernovae to significantly alter the density profile. In contrast, for a too high star formation rate, the excess central mass can compensate outflows and drag dark matter back in [217, 218]. Several groups' simulations indicate that baryonic feedback is efficient in producing cores in halos with a viral mass above $10^{10}\,M_\odot$ (or a stellar mass above $10^6\,M_\odot$). Still, these solutions are not ab initio ΛCDM predictions and depend on various adopted parameters for the modelling of galaxy formation [178]. The situation is more complicated in case of the too-big-to-fail problem. Only about half the observed dwarfs are above the threshold where baryonic feedback induces cores. Several environment dependent feedback mechanism, e.g., tidal stripping, disk shocking and ram pressure stripping, can be effective within a few viral radii of the host galaxy. If those are key factors in setting the central density of small halos, satellites should differ systematically from field galaxies [219–226], but no such dependence has been detected yet [196]. Other environmental effects, like cosmic web stripping, are effective over larger distances but still can not explain the too-big-to-fail problem in field galaxies [227]. Finally, the discrepancy could be afflicted by observational systematics, and there is a number of factors which affects the conversion between the observed HI line width and the underlying gravitational potential [228].

At present, the question to what extent small scale discrepancies challenge the ΛCDM paradigm is still open. Further progress is possible from a more complete understanding of the observational samples, searches for dark matter halos with masses below the threshold for galaxy formation or the characterisation of central structures in very faint objects. Meanwhile, given the absence of a dark matter signal in direct detection, indirect, astrophysical evidence provides the strongest clues about the nature of dark matter. It seems important to take astrophysical discrepancies seriously and explore all possible theoretical solutions [178].

2.3 The cosmic microwave background

Thermal relic photons, which free stream from the epoch of recombination, constitute the cosmic microwave background. Historically, the CMB discovery [85, 86] played key role in establishing acceptance for the hot Big Bang model. Its temperature (1.2.41) and spectrum was measured precisely, most recently by the COBE/FIRAS experiment [87], and closely follows the expected black body shape. The absence of spectral distortions [229] puts tight constraints on energy injection into the photons, e.g. from dark matter annihilation or decay, at redshifts $z \lesssim 2 \times 10^6$ [230].

Beyond the homogeneous background distribution, small anisotropies in the CMB temperature and polarisation enable precision tests of cosmology. The fluctuations probe larger scales and relate to higher redshifts, around the epoch of recombination, than the previously discussed large-scale structure observations. Governed by linear perturbation theory, the CMB spectrum can be predicted very precisely, such that five of the six ΛCDM parameters are constrained with a precision better than 1% from the latest Planck data release [15].

2.3.1 The temperature autocorrelation spectrum

The CMB exhibits temperature anisotropies on the 10^{-5} level, which emerge from the random inflationary perturbations. As for matter inhomogeneities, the Gaussian fluctuations are fully characterised by their two point correlation, which diagonalises over the harmonic domain. To make the transition, the CMB temperature, observed on a sphere as function of the direction $\hat{n}$, is expanded in terms of spherical harmonics $Y_{l,m}$ [19]

$$T\left(\hat{n}\right) = \sum_{l=0}^{\infty} \sum_{m=-l}^{m} a_{l,m}^{\mathrm{T}} \, Y_{l,m}\left(\hat{n}\right) \, . \tag{2.3.1}$$

For a given multipole l, all coefficients $a_{l,m}^{\mathrm{T}}$ are statistical independent, and drawn from a Gaussian with zero mean and variance [21]

$$\left\langle a_{l,m}^{\mathrm{T}} \left(a_{l',m'}^{\mathrm{T}}\right)^{*} \right\rangle = \delta_{l,l'} \delta_{m,m'} \, C_{l}^{\mathrm{TT}} \, . \tag{2.3.2}$$

The angular power spectrum C_l^{TT} encodes all theoretical knowledge about the CMB anisotropies in a given cosmological model. Considering observations, the average over all coefficients, $\left\langle \left| a_{l,m}^{\mathrm{T}} \right|^2 \right\rangle$, provides an estimator for C_l^{TT}. However, for a given multipole l, at most $(2l+1)/2$ independent coefficients $a_{l,m}^{\mathrm{T}}$ can be observed in an all-sky survey. This imposes an intrinsic limit on the accuracy to which the angular power spectrum can be determined,

$$\frac{\Delta C_l^{\mathrm{TT}}}{C_l^{\mathrm{TT}}} = \sqrt{\frac{2}{2l+1}} \, , \tag{2.3.3}$$

which is called the cosmic variance and can not be overcome by experimental accuracy. For example, the uncertainty of the temperature auto-correlation spectrum from the Planck 2015 data release is dominated by cosmic variance up to $l \simeq 1586$ [231].

The angular power spectrum inferred from the Planck all-sky maps [15] is shown in Fig. 2.2, alongside with the best-fit theory spectrum. The peculiar pattern of peaks and toughs in the multipole range $100 \lesssim l \lesssim 1000$ emerges from the oscillations of the photon-baryon plasma, which also generate the BAO pattern in the matter power spectrum. Its characteristic scale is set by the sound horizon at recombination $r_{\mathrm{s}}\left(z_*\right)$, when photons decouple [232,233]. The first peak corresponds to the mode which went through 1/4 of an oscillation between entering the Hubble radius and decoupling and signifies a maximal overdensity. It is followed by a peak at the mode which completed 1/2 of an oscillation period and exhibits

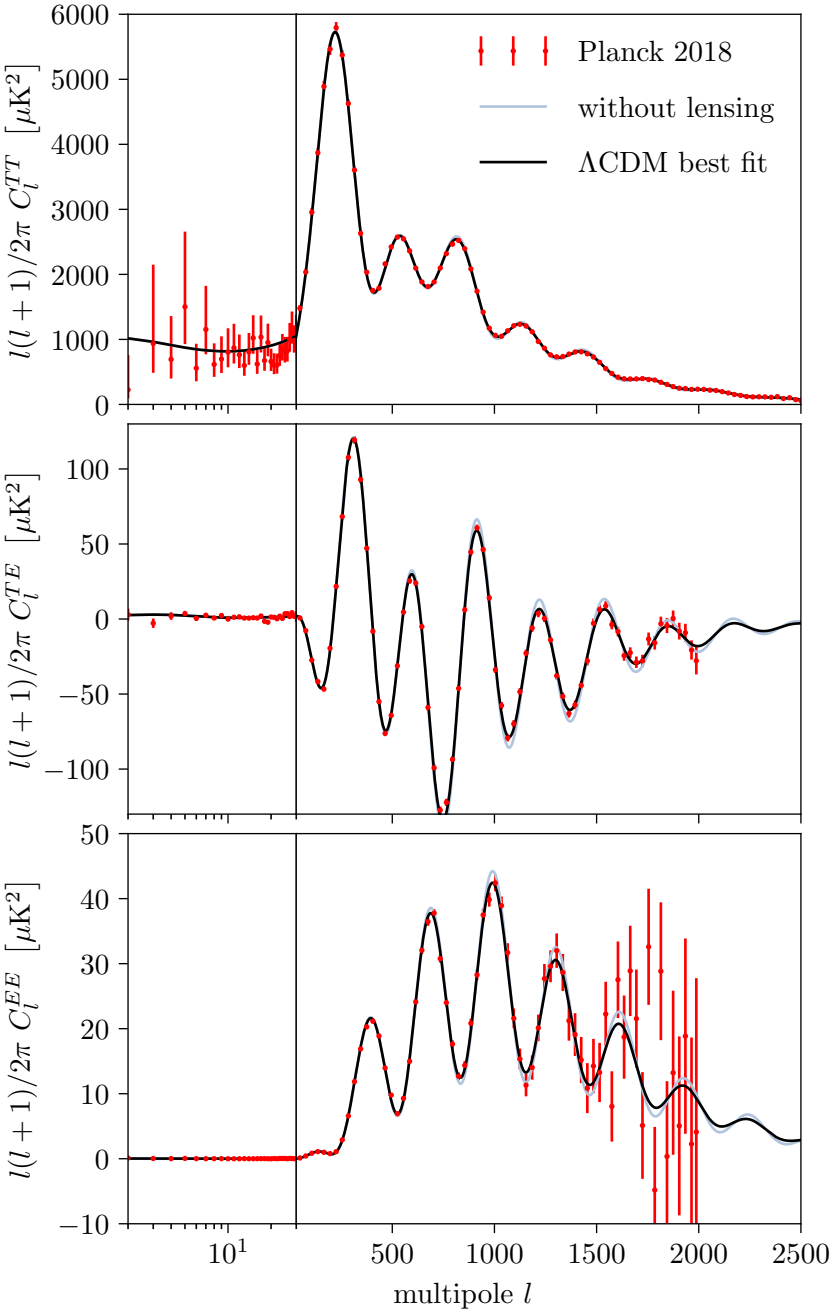

Figure 2.2: CMB angular power spectra as measured by the Planck satellite [4] in comparison with the best-fit ΛCDM predictions. The theory spectra are shown with and without secondary corrections induced by weak lensing.

maximal underdensities. The pattern continues as the multipole moment increases, with odd peaks representing maximal overdensities and even peaks maximal underdensities. The oscillations of the baryon-photon plasma are driven by the gravitational potentials, photon pressure acts as restoring force and baryons provide some inertia. The latter has to be overcome in the rebound of oscillations, hence odd peaks are higher than the even ones. The height ratio between odd and even peaks is directly sensitive to the baryon density. A larger baryon fraction also decreases the plasma's sound speed and oscillation frequency, which shifts the acoustic peaks to higher multipoles [19, 21]

After recombination, the height of the CMB acoustic peaks is proportional to the amplitude of primordial perturbations A_s. Later, when reionisation increases the free electron abundance, isotropic photon scattering partially erases fluctuations. The present-day peak height is determined by the combination of both effects and sensitive to $A_\mathrm{s}\, e^{-2\tau_\mathrm{re}}$ where the optical depth to reionisation, τ_re, is defined in Eq. (1.2.44).

At high multipoles, $l \gtrsim 1000$, The CMB acoustic peaks become increasingly suppressed. Recombination does not occur instantaneously, but there is a finite width to the surface of last scattering, and photon diffusion from overdense regions damps fluctuations. The damping scale is set by the distance a photon can random walk prior to decoupling [21]

$$\lambda_\mathrm{diff} \sim (n_\mathrm{e}\, \sigma_\mathrm{T}\, H)^{-1/2} \,, \tag{2.3.4}$$

and increases if the baryon density is small. Therefore, for models with a small baryon abundance, the damping sets in at a larger scale. The effect of diffusion damping [91] handicaps the measurement of the anisotropy spectrum at high multipoles significantly.

The oscillatory pattern of CMB anisotropies does not continue to the largest scales, $l \lesssim 100$, which enter the Hubble radius after recombination. Here, the temperature anisotropies directly reflect primordial perturbations [19,21], and $l\,(l+1)\,C_l$ is approximately constant, which is called the Sachs-Wolf effect [234]. At late times, the Sachs Wolf effect is modified by the presence of dark energy. Free streaming CMB photons experience a blueshift when entering an overdense region, and, upon escaping it, are redshifted. If the gravitational potential remains constant in the meantime, as is the case in a matter-dominated universe, the net effect cancels. The contribution of vacuum energy to the expansion rate causes the decay of gravitational potentials and leads to an increase of temperature anisotropies at low multipoles, called the Integrated Sachs-Wolf effect [235]. The presence of this increase has been confirmed from the correlation of large-scale structure and CMB anisotropies at low multipoles [236]. If the dark energy equation of state deviates from unity, it further modifies the Integrated Sachs-Wolf effect. However, cosmic variance seriously affects observations at large scales and usually prevents the deviation of significant constraints [19].

Reionisation and the decay of gravitational potentials in the dark energy dominated epoch impose secondary effects on the CMB, which modify the primordial spectrum established at recombination. Of further importance along these lines is the weak gravitational lensing of CMB photons by non-linear structures at low redshifts [237]. The deflections primarily arise from structures at redshifts between 0.5 and 10, are of order 2-3 arcsecond and

coherent over patches of a few degrees [15]. In spectrum of temperature anisotropies, lensing slightly smooths the peak/tough structure. Because lensing couples adjacent multipoles, it introduces non-Gaussianities to the CMB perturbations [238], to which higher order correlations of temperature maps, polarisation maps and their derivatives are sensitive [239, 240]. The effect of gravitational lensing has been detected with more than 40σ significance from Planck data [241]. The reconstruction of lensing potentials permits an independent estimate of A_s and helps to break the $A_\mathrm{s}\, e^{\tau_\mathrm{re}}$ degeneracy. The combination of lensing potentials, BAO data and CMB anisotropies tightly constraints Ω_m, σ_8 and H_0. In particular σ_8 is determined to better than 1% accuracy as $\sigma_8 = 0.811 \pm 0.006$ [241].

2.3.2 CMB polarisation

The polarisation dependence of Thomson scattering causes the CMB to be linearly polarised at a level of $\sim 5\%$ of the temperature anisotropies [242]. The differential cross section is,

$$\frac{d\sigma}{d\Omega} = \frac{3\sigma_\mathrm{T}}{8\pi} \left|\hat{\boldsymbol{\epsilon}}_1 \cdot \hat{\boldsymbol{\epsilon}}_2\right|^2 , \tag{2.3.5}$$

where $\hat{\boldsymbol{\epsilon}}_1$ and $\hat{\boldsymbol{\epsilon}}$ are the directions of the incident and the scattered polarisation. Photons polarised transversely to the outgoing direction pass unimpeded, while parallelly polarised radiation is blocked. Still, for isotropic incident radiation, the outgoing radiation is unpolarised due to the superposition of individual scatterings. A net linear polarisation can only be generated from quadrupole anisotropies. Before recombination, when Thomson scattering is effective, the tight coupling between baryons and photons suppresses the quadrupole moment (c.f. Sec 4.2). Hence the small polarisation signal directly probes the thickness of the last scattering surface [19, 21].

Linear polarisation can be decomposed in several ways. While the Stokes parameters Q and U are a convenient description for the evolution of perturbations, the decomposition into curl free E-modes and divergence free B-modes is practical to discuss physical implications. Analogous to temperature fluctuations (2.3.1), the Stokes parameter in the direction $\hat{n}$ can be expanded in terms of spin-2 spherical harmonics [243, 244]

$$(Q + iU)(\hat{n}) = \sum_{l=2}^{\infty} \sum_{m=-l}^{l} {}_2a_{l,m}\ {}_2Y_{l,m} , \tag{2.3.6}$$

$$(Q - iU)(\hat{n}) = \sum_{l=2}^{\infty} \sum_{m=-l}^{l} {}_{-2}a_{l,m}\ {}_{-2}Y_{l,m} . \tag{2.3.7}$$

A linear combination of the respective expansion coefficients connects the Stokes parameters to the E- and B-mode description,

$$a^\mathrm{E}_{l,m} = -\frac{1}{2}\left({}_2a_{l,m} + {}_{-2}a_{l,m}\right) \tag{2.3.8}$$

$$a^\mathrm{B}_{l,m} = \frac{i}{2}\left({}_2a_{l,m} - {}_{-2}a_{l,m}\right) , \tag{2.3.9}$$

from which the rotationally-invariant, scalar quantities $E(\hat{n})$ and $B(\hat{n})$ are defined as

$$E(\hat{n}) = \sum_{l=2}^{\infty} \sum_{m=-l}^{l} a^{\mathrm{E}}_{l,m}\, Y_{l,m}(\hat{n}) \tag{2.3.10}$$

$$B(\hat{n}) = \sum_{l=2}^{\infty} \sum_{m=-l}^{l} a^{\mathrm{B}}_{l,m}\, Y_{l,m}(\hat{n})\,. \tag{2.3.11}$$

B-modes have opposite parity than temperature anisotropies and E-mode polarisation, therefore the cross-correlation between the $a^{\mathrm{B}}_{l,m}$ coefficients and $a^{\mathrm{T/E}}_{l,m}$ vanishes. In total, there are four angular power spectra which can be observed in the CMB

$$\left\langle a^{\mathrm{E}}_{l,m} \left(a^{\mathrm{E}}_{l',m'}\right)^{*} \right\rangle = \delta_{l,l'}\delta_{m,m'}\, C^{\mathrm{EE}}_{l}\,, \tag{2.3.12}$$

$$\left\langle a^{\mathrm{E}}_{l,m} \left(a^{\mathrm{T}}_{l',m'}\right)^{*} \right\rangle = \delta_{l,l'}\delta_{m,m'}\, C^{\mathrm{ET}}_{l}\,, \tag{2.3.13}$$

$$\left\langle a^{\mathrm{B}}_{l,m} \left(a^{\mathrm{B}}_{l',m'}\right)^{*} \right\rangle = \delta_{l,l'}\delta_{m,m'}\, C^{\mathrm{BB}}_{l}\,, \tag{2.3.14}$$

alongside with the C^{TT}_{l} coefficients of Eq. (2.3.2).

The CMB E-mode polarisation was first measured by the DASI experiment [245]. More recent results from the Planck satellite [15] are displayed in the lower two panels of Fig. 2.2, which show the E-mode autocorrelation spectrum (EE) and the cross-correlation with temperature anisotropies (TE). Like the temperature spectrum, the polarisation spectra show a characteristic structure of peaks and thoughts, which also originates from acoustic oscillations in the baryon-photon plasma. There is no polarised Sachs-Wolff effect, and at high multipoles the polarisation spectra become zero. Photon scattering after reionisation introduces a small bump in the polarisation spectra at low multipoles. This signature, particularly visible in the EE-spectrum, partially breaks the degeneracy in $A_{\mathrm{s}}\, e^{\tau_{\mathrm{re}}}$. The observed CMB polarisation agrees well with expectations based on the temperature spectrum – a further support for the consistency of the ΛCDM model. Its primary merit is a tighter constraint on the reionisation optical depth [15, 19], while errors on further ΛCDM parameters do not reduce by much with the addition of polarisation data [15, 19].

The Thomson scattering of scalar perturbations only sources E-mode polarisation. Tensor perturbations, in contrast, produce roughly equal amounts of B- and E-modes [246, 247]. A measurement of the CMB B-mode polarisation would determine the tensor-to-scalar ratio (1.2.7) and provide insight into the inflationary scale [35, 36], but imposes severe experimental challenges. At small angular scales, gravitational lensing transforms some E-mode polarisation into B-modes [238, 248], and this secondary effect contaminates the primordial B-mode signal. Even more severe limitations are imposed by foreground effects [36]. Interstellar dust grains align with the galactic magnetic field and produce thermal emission with a degree of linear polarisation [249]. No dust free windows, at the level required for future CMB polarisation, exist on the sky [4,250], such that a correct modelling of foregrounds is essential. So showed the combined analysis of Planck and BICEP data that the formerly announced detection of B-modes at the level $r = 0.20^{+0.07}_{-0.05}$ [251] is

	Planck 2015 results		Planck 2018 results	
	best-fit	68% C.L.	best-fit	68% C.L.
$\Omega_{\rm b}h^2$	0.022242	0.02226 ± 0.00023	0.022383	0.02237 ± 0.00015
$\Omega_{\rm dm}h^2$	0.11977	0.1186 ± 0.0020	0.12011	0.1200 ± 0.0012
$100\,\theta_*$	1.040862	1.04103 ± 0.00046	1.040909	1.04092 ± 0.00031
$\tau_{\rm re}$	0.0781	0.066 ± 0.016	0.0543	0.0544 ± 0.0073
$\ln\left(10^{10}A_{\rm s}\right)$	3.0904	3.062 ± 0.029	3.0448	3.044 ± 0.014
$n_{\rm s}$	0.9658	0.9677 ± 0.0060	0.96605	0.9649 ± 0.0042
H_0	$--$	67.8 ± 0.9	$--$	67.36 ± 0.54
Ω_Λ	$--$	0.692 ± 0.012	$--$	0.6847 ± 0.0073
σ_8	$--$	0.8149 ± 0.0093	$--$	0.8111 ± 0.0060

Table 2.1: Parameters of the ΛCDM cosmological standard model estimated from Planck CMB measurements at 68% C.L.. The 2015 results are based on the temperature power spectrum and polarisation at low multipoles [7], while the 2018 baseline data set also contains polarisation at larger multipoles and the autocorrelation of lensing potentials [4].

actually consistent with polarised dust foregrounds [36].

2.3.3 Cosmological parameters and constraints

Since their initial discovery by the COBE satellite [20], the CMB anisotropies have been mapped with increasing accuracy by the WMAP [252] and the Planck [15] space missions and, in addition, by a variety of ground- and balloon-based experiments. The final Planck data release provides high-fidelity maps of the temperature fluctuations, E-mode polarisation and the lensing potentials as well as the corresponding correlation spectra [15]. Ground-based experiments measure the CMB at high resolution, extending the angular correlation spectra to larger multipoles. While the focus of BICEP/KECK [253] and POLARBEAR [254] is on the detection of B-modes, measurements of temperature and E-mode polarisation with the South Pole Telescope (SPT) and the Atacama Cosmology Telescope (ACT) provide information which is complementary to Planck's results. Due to the wider survey area, the Planck spectra are statistically more powerful than ACT and SPT measurements [15]. Still, data from the latter experiments is used to constrain low-amplitude foregrounds in the Planck analysis. The Planck observations are in good agreement with ACT and SPT temperature maps [255] and with the ACT polarisation results. The inclusion of ACT polarisation spectra [256] in the analysis has little impact on ΛCDM parameters, but slightly improves extended scenarios which modify the CMB's damping tail. The SPT collaboration found a moderate tension between their polarisation data and the ΛCDM model preferred by Planck, especially at larger multipoles [257]. This could hint at the need for extensions beyond the ΛCDM model, but systematics in $A_{\rm s}\,e^{-2\tau_{\rm re}}$ might contribute to this discrepancy as well [4]. The consistency between the Planck ΛCDM model and polarisation spectra at high multipoles should become clearer as ACTPol and SPTpol accumulate more data.

The baseline ΛCDM model provides an excellent fit to the Planck data, which puts stringent constrains on all six free parameters simultaneously. These results are summarised in Tab. 2.1. Most precisely measured is the angular scale of acoustic oscillations θ_* with an accuracy of 0.03%, while limits on the optical depth to reionisation are the weakest. BBN allows to infer the baryon density from the deuterium to helium ratio observed in the Ly-α forest [258]. The constraint,

$$0.021 \leq \left(\Omega_\mathrm{b} h^2\right)^\mathrm{BBN} \leq 0.024\,, \tag{2.3.15}$$

is consistent with Planck observations [19], but exhibits considerably larger errors.

Because CMB anisotropies and matter perturbations share a common, inflationary origin, an interesting consistency check for the ΛCDM paradigm is the comparison of the matter power spectrum derived from either kind of observation. This is, for example, presented in Fig. 19 of Ref. [15], which projects the individual measurements on the present-day linear matter power spectrum. CMB temperature anisotropies probe the largest scales and relate to high redshifts, around recombination. On intermediate scales, the CMB polarisation provides additional high-redshift information. The high-redshift constraints overlap with probes at later times, such as CMB lensing, sensitive around $0.5 \lesssim z \lesssim 10$, and galaxy clustering, which assesses the recent state of the universe. At smaller scales, cosmic shear and the Ly-α forest become relevant. The latter probes redshifts in the range $z \simeq 2 - 3$, and the former those redshifts intermediate between the CMB and the Ly-α observations. Overall, the consistency of observations, spanning the entire redshift range between recombination and today and covering three orders in length scale is rather remarkable. In the context of CMB analyses, BAO observations are particularly important. The associated scales are largely unaffected by non-linear physics, making the measurements very robust, and their inclusion breaks degeneracies in the CMB data and often tightens parameter constraints. In this context, the Planck collaboration considers data sets from the 6dF galaxy survey [259], an estimate of the acoustic scale from the SDSS DR7 galaxy sample [260] and the SDSS DR12 data release [261].

The tighter limits permitted by the combination of CMB and BAO data are also of importance to many extensions beyond the 6-parameter ΛCDM model, like those outlined at the end of Sec. 1.3. To date, there is no compelling evidence for any of them [4], and we summarise the constraints in the following.

- The fluctuations observed in the CMB are consistent with purely adiabatic, scalar curvature perturbations. Detected non-Gaussianities agree with expectations from secondary effects in the ΛCDM framework, like lensing, the integrated Sachs-Wolf effect and foregrounds [4].

- The running of the spectral index is constrained by the combination of Planck temperature, polarisation and lensing data with BAO observations [4],

$$\left(\frac{d\, n_\mathrm{s}}{d\, \ln k}\right)^\mathrm{CMB+BAO} = -0.0045 \pm 0.0067 \quad \text{at } 68\% \text{ confidence.} \tag{2.3.16}$$

- The Planck measurement of B-mode polarisation is limited by noise and systematics [4]. Tighter limits on the tensor-to-scalar ratio (1.2.7), evaluated at a fiducial scale of $0.05\,\mathrm{Mpc}^{-1}$, are obtained from BICEP2/Keck measurements, using Planck data to clean dust foregrounds [253],

$$r\left(0.05\,\mathrm{Mpc}^{-1}\right) < 0.06 \quad \text{at } 95\% \text{ confidence}\,. \tag{2.3.17}$$

- Concerning the spatial curvature, CMB data alone suffers from a geometric degeneracy between Ω_m and Ω_Λ, which BAO data can lift. The tight constraints on the curvature density,

$$\Omega_k^{\mathrm{CMB+BAO}} = 0.0007 \pm 0.0019 \quad \text{at } 68\% \text{ confidence}\,, \tag{2.3.18}$$

  suggest that the universe is flat to 0.2% accuracy [4].

- Modifications to the dark energy equation of state mainly cause late time effects in the growth of structure and the cosmological expansion rate. Combining BAO data, Planck temperature, polarisation and lensing spectra and the Pantheon Sample of 1048 type Ia supernovae [262] yields for the dark energy equation of state [4]

$$w_\Lambda^{\mathrm{CMB+BAO+SNa}} = -1.028 \pm 0.032 \quad \text{at } 68\% \text{ confidence}\,. \tag{2.3.19}$$

  The previously discussed DES constraint (2.2.8), on the other hand, is completely independent of CMB data.

- The impact of neutrino masses on CMB anisotropies is small and primarily arises from the early Integrated Sachs-Wolf effect. Close to recombination, radiation significantly contributes to the energy density, which causes the cosmic equation of state to deviate from zero and hence a decay of the gravitational potentials. Analogously, the late Integrated Sachs-Wolf effect, discussed in Sec. 2.3.1, emerges from the late-time dark energy contribution. For neutrino masses of $\sum m_\nu \sim \mathcal{O}\,(1\,\mathrm{eV})$, the transition from the relativistic to the non-relativistic regime impacts the equation of state close to recombination [263]. The matter power spectrum, however, is more sensitive to the neutrino mass scale, and the tightest constraints are obtained when the CMB spectra are analysed in combination with lensing potentials and BAO measurements, yielding [4]

$$\left(\sum m_\nu\right)^{\mathrm{CMB+BAO}} < 0.12\,\mathrm{eV} \quad \text{at } 95\% \text{ confidence}\,. \tag{2.3.20}$$

  While cosmology provides the tightest upper bound on the neutrino mass scale at present [264], the constraint is model dependent and can weaken considerably in extended cosmological scenarios with additional free parameters [265].

- The presence of additional thermal relics at the epoch of recombination increases the Hubble rate for fixed θ_* and z_eq. The resulting increase of the photon diffusion scale (2.3.4) is noticeable in the CMB anisotropy spectra, as well as from baryon acoustic

oscillations [19]. Current bounds,

$$N_{\rm eff}^{\rm CMB+BAO} = 2.99^{+0.34}_{-0.33} \quad \text{at } 95\% \text{ confidence}\,, \tag{2.3.21}$$

mildly disfavour a thermal relic which froze out after the QCD phase transition and would contribute $\delta N_{\rm eff} = 0.3$ per degree of freedom [4].

2.3.4 Discrepancies with other data sets

The baseline ΛCDM scenario describes CMB observations remarkably well [4], and in general there is good agreement between the CMB and other data sets. Still, some discrepancies exist. These could be statistical fluctuations, hints for underestimated systematics or they might also point to need for extension beyond the ΛCDM paradigm.

First, there is a moderate tension in the amplitude of matter perturbations, parameterised here by S_8, and the matter density, $\Omega_{\rm m}$. Planck data in combination with BAO determines these as [4]

$$\left.\begin{aligned} S_8^{\rm CMB+BAO} &= 0.8102 \pm 0.0060\,, \\ \Omega_{\rm m}^{\rm CMB+BAO} &= 0.3111 \pm 0.0056\,, \end{aligned}\right\} \quad \text{at } 68\% \text{ confidence}\,. \tag{2.3.22}$$

An analysis of the combined DES likelihood for weak lensing and galaxy clustering [266] under the assumption $\sum m_\nu = 0.06\,\text{eV}$, on the other hand, yields [4]

$$\left.\begin{aligned} S_8^{\rm DES} &= 0.792 \pm 0.024\,, \\ \Omega_{\rm m}^{\rm DES} &= 0.257^{+0.023}_{-0.031}\,, \end{aligned}\right\} \quad \text{at } 68\% \text{ confidence}\,. \tag{2.3.23}$$

Similarly, the KiDS data set implies a smaller perturbation amplitude and a lower matter density [267,268] than the Planck data. At the moment it is unclear whether the discrepancy is a statistical fluctuation, caused by systematics or an indicator of physics beyond ΛCDM.

A second, more severe, discrepancy exists in the determinations of the Hubble constant. From Planck temperature, polarisation and lensing data the Hubble constant today is determined as [4]

$$H_0^{\rm CMB} = (67.36 \pm 0.54)\ \text{km}\,\text{Mpc}^{-1}\,\text{s}^{-1} \quad \text{at } 68\% \text{ confidence}\,. \tag{2.3.24}$$

Further, the combination of weak lensing, galaxy clustering, baryon acoustic oscillations and measurements of Big Bang nucleosynthesis is completely independent of the CMB results and yields [269]

$$H_0^{\rm DES+BAO+BBN} = \left(67.2^{+1.2}_{-1.0}\right)\ \text{km}\,\text{Mpc}^{-1}\,\text{s}^{-1} \quad \text{at } 68\% \text{ confidence}\,. \tag{2.3.25}$$

In contrast, the distance ladder approach (2.1.1) and time delay strong lensing (2.1.4), favour considerably larger values. Their tension with the CMB estimate amounts to $4.4\,\sigma$ and $3.1\,\sigma$, individually, or to $5.3\,\sigma$, when combined [112,118]. CMB and BAO measurements depend on the sound horizon at recombination, $r_{\rm s}\,(z_*)$, and at baryon decoupling $r_{\rm s}\,(z_{\rm drag})$, respectively, which provide a characteristic scales in either observation. The presence of

such a well known scale allows to determine the angular diameter distance and hence offers sensitivity to the Hubble rate. In either case, the sound horizon is determined at a high redshift at or close to recombination. Thus, the discrepancy in H_0 is often understood in terms of a tension between early and late-time determinations of the Hubble rate, as e.g. in Fig. 4 of [112]. Gravitational waves provide yet another independent measurement of H_0 at low redshifts, but have not yet reached the required sensitivity to clarify the situation.

By now, the discrepancy between early- and late-time measurements of the Hubble constant seems rather significant. It might be caused by systematics in either analysis, but dedicated studies [270–276] have not identified any obvious problems. On the other hand, high-redshift probes do not measure H_0 directly, but assume a specific cosmological model to infer it from the data. In particular would the preferred value change if ΛCDM can not predict the sound horizon accurately. In this regard, it is intriguing to consider modifications to the cosmological baseline scenario. No simple, one-parameter extensions, like changes to the dark energy equation of state, an increase in $N_{\rm eff}$ or non-zero spatial curvature, can alleviate the problem [15]. Interactions between dark matter and neutrinos [277] or an early ($z \gtrsim 3000$) dark energy component [278], which decays like radiation at later times, manage to ease the tension without fully resolving it [112]. Another possibility are neutrino self-interactions [279], for which the CMB data prefers a larger H_0 and a smaller σ_8 value. These scenarios also imply a rather large effective number of neutrinos, $N_{\rm eff} = 4.02 \pm 0.29$. Finally, a local underdensity could explain the discrepancy [280], without modifications to the ΛCDM model.

Chapter 3

The evolution of linear cosmological perturbations

Overall, the ΛCDM scenario provides an excellent description of cosmological observations. Yet, discrepancies remain and the particle physics nature of dark matter is not addressed. Both shortcomings motivate to consider extensions the the ΛCDM paradigm. Either, these help to lift degeneracies, or, by imposing consistency with the data, the properties of dark matter can be constrained. In this context, we abandon the premise that dark matter is collisionless at all times and scales of interest and, in particular study dark matter interactions with Standard Model radiation. These have been evoked to resolve small scale problems [200, 281, 282], and the scattering between dark matter and neutrinos can ease the Hubble tension [277]. The existence of precise theory predictions is crucial for a meaningful comparison to observations. In the context of CMB observations and the matter distribution in the linear regime, these are provided by the linearised Boltzmann-Einstein equations. We review their derivation under ΛCDM assumptions in this section, closely following Ref. [283], before updating the formalism carefully to include dark matter-photon and dark matter-neutrino interactions, respectively.

3.1 Notations and conventions

We treat the evolution of perturbations in the linear regime in terms of comoving coordinates, $x^\mu = (\tau, \boldsymbol{x})$. The comoving time τ is related to the proper time t by $d\tau = dt/a(t)$, and unperturbed FRW line element (1.1.2) takes the form

$$ds^2 = a^2(\tau)\left(-d\tau^2 + dx_i dx^i\right) , \tag{3.1.1}$$

where we also assumed spatial flatness. Greek indices denote the four space-time coordinates x^μ, $\mu \in (0, 1, 2, 3)$, while Latin letters indicate spatial vectors $\boldsymbol{x} = x^i$, $i \in (1, 2, 3)$. Repeated indices are summed over according to the Einstein sum convention.

While an overdot represents derivatives with respect to proper time, derivatives with respect to conformal time are indicated by a prime. Working in terms of conformal time, it is practical to define reduced Hubble rate

$$\mathcal{H} \equiv \frac{a'}{a} = a\,H\,. \tag{3.1.2}$$

Quantities which concern the homogeneous background are indicated by an overbar and perturbations around that homogeneous background by an δ, such that e.g. the energy density can be written as $\rho = \bar{\rho} + \delta\rho$. On the whole, our notation follows closely that of Ref. [283].

To distinguish the interacting scenarios, we label dark matter with photon interactions by a subscript "γdm" and dark matter with neutrino interactions by a subscript "νdm". The label "cdm" emphasises a truly collisionless component in the sense of ΛCDM, while "dm" is used to summarise all aforementioned possibilities.

3.2 The perturbed Einstein equations

Two aspects are important in the evolution of cosmological perturbations. First, the Einstein equation (1.1.1) describes the metric evolution, which depends on the collective cosmological energy density, represented by the stress-energy tensor. Second, several different species contribute to the stress-energy tensor, and their individual evolution is governed by the Boltzmann equation (3.4.1). We discuss the latter in the subsequent sections and here focus on metric perturbations.

3.2.1 Perturbed Einstein tensor

The evolution of cosmological perturbations commences when their size is comparable to the Hubble radius and requires a fully-relativistic treatment in the terms of general relativity. Yet, the smallness of fluctuations permits a perturbative solution in powers of small departures from the homogeneous background. Different gauges exist to represent perturbations to the FRW metric, the most common are synchronous gauge [284] and the conformal Newtonian gauge [30]. Coordinates in the former are defined with respect to a freely falling observer, and, in the absence of interactions, the gauge is comoving with dark matter. The gauge condition is fixed by requiring that the dark matter velocity divergence vanishes at all times. Interactions of dark matter with other species introduce a coupling between the respective velocity divergences and necessitate modifications to the gauge fixing [285]. Instead, we choose to work in Newtonian gauge, where the perturbed line element to describe scalar perturbations is

$$ds^2 = a^2(\tau)\left[-(1+2\psi)\,d\tau^2 + (1-2\phi)\,dx_i dx^i\right]. \tag{3.2.1}$$

Being related to the metric tensor, $ds^2 = g_{\mu\nu}g^{\mu\nu}$, the line element determines the Einstein tensor,

$$G_{\mu\nu} = R_{\mu\nu} - \frac{1}{2}\,g_{\mu\nu}\,R\,, \tag{3.2.2}$$

where the Ricci tensor is defined as contraction of the curvature tensor, $R_{\mu\nu} = R^{\lambda}{}_{\mu\lambda\nu}$, and the Ricci scalar is given by $R = R^{\mu}{}_{\mu}$. The curvature tensor itself can be computed from

the metric's Christoffel symbols

$$R^{\lambda}{}_{\kappa\mu\nu} = \partial_\nu \Gamma^{\lambda}{}_{\kappa\mu} - \partial_\mu \Gamma^{\lambda}{}_{\kappa\nu} + \Gamma^{\beta}{}_{\kappa\mu}\Gamma^{\lambda}{}_{\beta\nu} - \Gamma^{\beta}{}_{\kappa\nu}\Gamma^{\lambda}{}_{\beta\mu}\,. \tag{3.2.3}$$

Finally, the Christoffel symbols follow from the metric tensor

$$\Gamma^{\lambda}{}_{\mu\nu} = \frac{1}{2}\, g^{\lambda\rho}\, \left(\partial_\nu\, g_{\rho\nu} + \partial_\mu\, g_{\rho\nu} - \partial_\rho\, g_{\mu\nu}\right)\,. \tag{3.2.4}$$

Expanded to first order in metric perturbations, the Christoffel symbols of the perturbed line element in Newtonian (3.2.1) gauge are

$$\Gamma^{0}{}_{00} = \mathcal{H} + \psi'\,, \tag{3.2.5a}$$
$$\Gamma^{0}{}_{0i} = \partial_i\,\psi\,, \tag{3.2.5b}$$
$$\Gamma^{i}{}_{00} = \delta^{ij}\,\partial_j\,\psi\,, \tag{3.2.5c}$$
$$\Gamma^{0}{}_{ij} = \mathcal{H}\,\delta_{ij} - \left[\phi' + 2\mathcal{H}\,(\phi+\psi)\right]\,\delta_{ij}\,, \tag{3.2.5d}$$
$$\Gamma^{i}{}_{j0} = \left(\mathcal{H} - \phi'\right)\,\delta^{i}_{j}\,, \tag{3.2.5e}$$
$$\Gamma^{i}{}_{jk} = -\delta^{i}_{j}\,\partial_k\,\phi - \delta^{i}_{k}\,\partial_j\,\phi + \delta^{j}_{k}\,\partial_i\,\phi\,. \tag{3.2.5f}$$

Taken all together, the components of the Einstein tensor (3.2.2), expanded to first order in perturbations, are given by

$$G_{00} = 3\,\mathcal{H}^2 + 2\,\nabla^2\phi - 6\,\mathcal{H}\,\phi'\,, \tag{3.2.6a}$$
$$G_{0i} = 2\,\partial_i\,\left(\phi' + \mathcal{H}\psi\right)\,, \tag{3.2.6b}$$
$$\begin{aligned} G_{ij} = &-\left(2\,\mathcal{H}' + \mathcal{H}^2\right)\,\delta_{ij} + \Big[\nabla^2\,(\psi-\phi) + 2\phi'' + 2\left(2\,\mathcal{H}' + \mathcal{H}^2\right)\,(\phi+\psi) \\ &+ 2\,\mathcal{H}\,\psi' + 4\,\mathcal{H}\,\phi'\Big]\,\delta_{ij} + \partial_i\,\partial_j\,\left(\phi-\psi\right)\,. \end{aligned} \tag{3.2.6c}$$

3.2.2 Perturbed stress-energy tensor

For a perfect fluid of energy density ρ pressure P the stress-energy tensor, appearing on right hand side of the Einstein equation (1.1.1), is [283]

$$T^{\mu}_{\nu} = P\,g^{\mu}_{\nu} + (\rho + P)\,U^{\mu}U_{\nu}\,, \tag{3.2.7}$$

and $U^{\mu} = dx^{\mu}/\sqrt{-ds^2}$ denotes the fluid's four-velocity. In the fluids rest frame, defined by the condition $U^{i} = 0$, we find

$$U^{\mu}U_{\mu} = -1 = g_{00}U^0U^0 = -a^2\,\left(1+2\psi\right)\,\left(U^0\right)^2\,, \tag{3.2.8}$$

which implies that, to first order in metric perturbations, the zero component of the four-velocity is given by

$$U^0 = a^{-1}\,(1-\psi)\,. \tag{3.2.9}$$

Next, we consider a small coordinate velocity of the fluid $v^i \equiv dx^i/d\tau$, which can be regarded as a perturbation of the same order as the metric perturbations. From the definition of the coordinate velocity it follows that

$$\boldsymbol{v} = \frac{d\,\boldsymbol{x}}{d\tau} = \frac{d\,x^i}{d\tau}\,\hat{\boldsymbol{e}} = \frac{dx^i/\sqrt{-ds^2}}{d\tau/\sqrt{-ds^2}} = \frac{U^i}{U_0}\,\hat{\boldsymbol{e}}\,, \tag{3.2.10}$$

where $\hat{\boldsymbol{e}}$ is a unit vector in the direction of $\boldsymbol{v}$. Finally, the fluid's four-velocity at first order in perturbations is given by

$$U^\mu = a^{-1}\left(1-\psi, v^i\right)\,. \tag{3.2.11}$$

A full first-order expression of the stress-energy tensor is obtained by expressing the energy density and the pressure in terms of fluctuations around the homogeneous background, i.e. $\rho = \bar{\rho} + \delta\rho$ and $P = \bar{P} + \delta P$. Here, $\delta\rho$ and δP are perturbations of the same order as the metric perturbations, ψ and ϕ, and as the coordinate velocity $\boldsymbol{v}$. With this definition we obtain

$$T^0{}_0 = -(\bar{\rho}+\delta\rho)\,, \tag{3.2.12a}$$

$$T^0{}_i = \left(\bar{\rho}+\bar{P}\right)v_i\,, \tag{3.2.12b}$$

$$T^i{}_0 = -\left(\bar{\rho}+\bar{P}\right)v^i\,, \tag{3.2.12c}$$

$$T^i{}_j = \left(\bar{P}+\delta P\right)\delta^i{}_j + \Pi^i{}_j\,. \tag{3.2.12d}$$

The anisotropic shear, $\Pi^i{}_j$, in Eq. (3.2.12d), is added by hand to describe departures from a perfect fluid [283]. Any trace of $\Pi^i{}_j$ can be absorbed in δP, and thus it is practical to define the anisotropic shear as the traceless component of $T^i{}_j$, imposing $\Pi^i{}_i = 0$.

The linear perturbations are most conveniently evolved in Fourier space, where individual $\boldsymbol{k}$-modes decouple. There, denoting unit vector by a hat, the notation simplifies by defining the velocity divergence θ and the shear stress σ as

$$\theta \equiv i\,k^i v_j\,, \tag{3.2.13}$$

$$\left(\bar{\rho}+\bar{P}\right)\sigma \equiv -\left(\hat{k}_i\hat{k}_j - \frac{1}{3}\delta_{ij}\right)\Pi^{ij}\,. \tag{3.2.14}$$

3.2.3 Zeroth order evolution: the Friedmann equations

The Friedmann equations (1.1.4) and (1.1.5), anticipated in Sec. 1.1, follow directly from the Einstein equation under the assumption of an unperturbed FRW metric. Evidently from Eq. (3.2.6a) and Eq. (3.2.12a) the time-time component to zeroth order in perturbations

$$\mathcal{H}^2 = a^2\,\frac{8\pi}{3m_{\rm P}^2}\,\bar{\rho}\,, \tag{3.2.15}$$

gives the first Friedmann equation. The trace over spatial components of the Einstein and the stress-energy tensor is $G^i{}_i = 3\,a^{-2}\left(2\mathcal{H}' + \mathcal{H}^2\right)$ and $T^i{}_i = 3\bar{P}$, respectively, to zeroth

order in perturbations. Both expressions combine to the second Friedmann equation

$$\mathcal{H}' = \frac{8\pi}{3m_{\mathrm{P}}^2}\left(\bar{\rho} + 3\,\bar{P}\right) . \tag{3.2.16}$$

3.2.4 The Einstein equations at first order in perturbations

With the expansions of the Einstein tensor (3.2.6) and the stress-energy tensor (3.2.12) to first order in perturbations, we have all ingredients in place to write down the first-order evolution equations for metric perturbations. In Fourier space, using the zeroth order results, these are [30, 283, 284, 286, 287]

$$k^2\phi + 3\mathcal{H}\,\left(\phi' + \mathcal{H}\,\psi\right) = -\frac{4\pi}{m_{\mathrm{P}}^2}\,a^2\,\delta\rho\,, \tag{3.2.17a}$$

$$k^2\,\left(\phi' + \mathcal{H}\psi\right) = \frac{4\pi}{m_{\mathrm{P}}^2}\,a^2\,(\bar{\rho} + \bar{P})\,\theta\,, \tag{3.2.17b}$$

$$\phi'' + \mathcal{H}\,\left(\psi' + 2\phi'\right) + \left(2\frac{a''}{a} - \mathcal{H}^2\right)\psi + \frac{k^2}{3}\,(\phi - \psi) = \frac{4\pi}{m_{\mathrm{P}}^2}\,a\,\delta P\,, \tag{3.2.17c}$$

$$k^2\,(\phi - \psi) = \frac{12\pi}{m_{\mathrm{P}}^2}\,a^2\,\left(\bar{\rho} + \bar{P}\right)\sigma\,. \tag{3.2.17d}$$

The first two equations correspond to the time-time and the time-space components of the Einstein equations, the latter two are obtained from the trace and the trace-free part of the space-space component. The set provides redundant information, only two equations are needed for a complete description of the metric perturbations. A common choice in numerical codes [288] is to obtain ϕ from the integration of Eq. (3.2.17b) and ψ by solving Eq. (3.2.17d) algebraically.

3.3 Evolution of non-relativistic species

In general, the Boltzmann equation determines the phase space distribution of each individual species. However, in the case of non-relativistic, collisionless matter, energy momentum conservation suffices to characterise the evolution of perturbations. We exploit this relation here, to determine the equations governing dark matter perturbations and also extend the results to baryons.

3.3.1 Stress-energy conservation

The conservation of energy and momentum in general relativity is expressed by the vanishing covariant derivative ∇_μ of the stress-energy tensor, i.e.

$$\nabla_\mu T^\mu_{\ \nu} = \partial_\mu T^\mu_{\ \nu} + \Gamma^\mu_{\ \mu\alpha}\,T^\alpha_{\ \nu} - \Gamma^\alpha_{\ \mu\nu}\,T^\mu_{\ \alpha} = 0\,. \tag{3.3.1}$$

The Christoffel symbols of the perturbed metric are given in Eq. (3.2.5), and the conservation equation is straightforwardly applied to the perturbed stress-energy tensor (3.2.12).

To zeroth order in perturbations, the $\nu = 0$ component of the conservation equation reduces to Eq. (1.1.8), while, keeping first and second order terms, we obtain

$$\bar{\rho}' + \delta\rho' + \left(\bar{\rho} + \bar{P}\right) \partial_i v^i + 3\mathcal{H}\left(\bar{\rho} + \delta\rho\right) - 3\phi'\left(\bar{\rho} + \bar{P}\right) + 3\mathcal{H}\left(\bar{P} + \delta P\right) = 0\,. \tag{3.3.2}$$

By using the zeroth-order result, the definition of the density contrast $\delta \equiv \delta\rho/\rho$, of the equation of state $w = \delta P/\delta\rho$ and of the adiabatic sound speed of the fluid $c_\mathrm{s} = dP/d\rho = w + \rho\, dw/d\rho$, the this expression further simplifies to

$$\delta' = -3\,\mathcal{H}\,\left(c_s^2 - w\right)\,\delta - (1+w)\,(\theta - 3\phi')\ . \tag{3.3.3}$$

In the same manner we consider the $\nu = i$ component of Eq. (3.3.1), which simplifies to

$$v_i' = -\frac{\bar{P}'\,v_i}{\bar{\rho} + \bar{P}} - \frac{\partial_j\,\Pi_i^j}{\bar{\rho} + \bar{P}} - \frac{\partial_i\,\delta P}{\bar{\rho} + \bar{P}} - \mathcal{H}\,v_i - \partial_i\,\psi\,, \tag{3.3.4}$$

and finally, after Fourier transformation and contraction with k^i, becomes

$$\theta' = -\mathcal{H}\,(1 - 3w)\,\theta - \frac{w'}{1+w}\,\theta + \frac{\delta P/\delta\rho}{1+w}\,k^2\,\delta - k^2\,\sigma + k^2\psi\,. \tag{3.3.5}$$

The conservation equations for δ (3.3.3) and for θ (3.3.5) are valid for a single, uncoupled fluid. If several, coupled species a are considered, the stress-energy tensor in Eq. (3.3.1) is replaced by the sum over all individual contributions, $\sum_a T_a^{\mu\nu}$. In this case the zeroth-order conservation equation of the energy density becomes

$$\sum_a \bar{\rho}_a' = -3\mathcal{H} \sum_a \left(\bar{\rho} + \bar{P}\right)\ . \tag{3.3.6}$$

In many cases one type of energy, e.g., matter, radiation or a cosmological constant, dominates the energy density by several orders of magnitude. Then, the respective one-component equation (1.1.8) suffices to compute the universe's expansion rate.

In the following subsections, we consider several scattering processes, such as Thomson scattering between photons and electrons and elastic dark matter scattering with photons or neutrinos. The elastic processes do not couple the energy densities and Eq. (3.3.3) remain valid for each individual δ. The same is not given for the velocity dispersion, instead the combined conservation equation for several species applies

$$\begin{aligned}\sum_a \left(\bar{\rho}_a + \bar{P}_a\right)\theta_a' = &-\mathcal{H}\sum_a \bar{\rho}_a\,(1+w_a)\,(1-3w_a)\,\theta_a - \sum_a w_a'\,\bar{\rho}_a\,\theta_a + k^2\sum_a \frac{\delta P_a}{\delta\rho_a}\,\bar{\rho}_a\delta_a \\ &- k^2\sum_a \bar{\rho}_a\,(1+w_a)\,\sigma_a + k^2\psi\sum_a \bar{\rho}_a\,(1+w_a)\ .\end{aligned} \tag{3.3.7}$$

The two equations provided by stress-energy conservation contain a total of three unknown parameters, δ, θ and σ, to characterise perturbations in the fluid. As such, the problem is under-constrained. Because the anisotropic stress of a non-relativistic component can be neglected, stress-energy conservation suffices to evolve the specie's perturbations in this case, but not for partially or fully relativistic particles. Within the ΛCDM particle content, dark matter and baryons can be regarded as non-relativistic at all epochs and

scales relevant for the computation of CMB anisotropies and the large-scale structure. We discuss their respective evolution equations in the following.

3.3.2 Dark matter evolution equations

The evolution of dark matter perturbations is particularly simple. The ΛCDM model postulates that dark matter is a collisionless, pressureless, perfect fluid, which interacts with other species only through gravity. Hence the single-species equations Eq. (3.3.3) and Eq. (3.3.5) are directly applicable with $c_{\rm cdm} = w_{\rm cdm} = w'_{\rm cdm} = \sigma_{\rm cdm} = 0$, and give

$$\delta'_{\rm cdm} = -\theta_{\rm cdm} + 3\phi' \,, \tag{3.3.8a}$$

$$\theta'_{\rm cdm} = -\mathcal{H}\,\theta_{\rm cdm} + k^2\,\psi \,. \tag{3.3.8b}$$

3.3.3 Baryon evolution

Baryons behave as a non-relativistic fluid with $\sigma_{\rm b}\,,\ w_{\rm b} \ll 1$. Thomson scattering causes a non-zero baryon sound speed, which can affect the velocity divergence of large-k modes [283], but is negligible elsewhere. Hence, the baryon density perturbations evolve according to

$$\delta'_{\rm b} = -\theta_{\rm b} + 3\,\phi' \,. \tag{3.3.9}$$

The combined conservation equation for the velocity divergence of baryons and photons (3.3.7) yields

$$\begin{aligned}
&\frac{4}{3}\rho_\gamma\,\theta'_\gamma + \rho_{\rm b}\,\theta'_{\rm b} = \\
&\quad = \frac{1}{3}\,k^2\,\rho_\gamma\,\delta_\gamma - \frac{4}{3}\,k^2\,\rho_\gamma\,\sigma_\gamma + \frac{4}{3}\,\rho_\gamma\,k^2\,\psi - \mathcal{H}\,\rho_{\rm b}\,\theta_{\rm b} + k^2\,c_{\rm b}^2\ \ \rho_{\rm b}\delta_{\rm b} + k^2\,\rho_{\rm b}\psi \\
&\quad = \frac{4}{3}\,k^2\,\rho_\gamma\,\frac{\delta_\gamma}{4} - \frac{4}{3}\,k^2\,\rho_\gamma\,\sigma_\gamma + \frac{4}{3}\,k^2\rho_\gamma\,\psi + \frac{4}{3}\,\rho_\gamma\kappa'_{\gamma{\rm b}}\,(\theta_{\rm b} - \theta_\gamma) + \rho_{\rm b}\,\theta'_{\rm b} \,.
\end{aligned} \tag{3.3.10}$$

In the last line, we already anticipated the photon evolution equation (3.4.36), which is derived independently, from the Boltzmann equation, in Sec. 3.4.3. The comoving rate for Thomson scattering is

$$\kappa'_{\gamma{\rm b}} = a\,n_{\rm e}\,\sigma_{\rm T} \,. \tag{3.3.11}$$

From the comparison of the last latter two lines we obtain

$$\theta'_{\rm b} = -\mathcal{H}\,\theta_{\rm b} + k^2\,c_{\rm b}^2\,\delta_{\rm b} + k^2\,\psi - R_{\gamma{\rm b}}\,\kappa'_{\gamma{\rm b}}\,(\theta_{\rm b} - \theta_\gamma) \,. \tag{3.3.12}$$

The factor $R_{\gamma{\rm b}}$ in front of the interaction term ensures momentum conservation in the scattering process and is a shorthand notation for

$$R_{\gamma{\rm b}} \equiv \frac{4\,\rho_\gamma}{3\,\rho_{\rm b}} \,. \tag{3.3.13}$$

The baryon sound speed, c_b, appears in Eq. (3.3.12), where it is multiplied with the baryon density contrast δ_b. To compute θ' at first order in perturbations, a zeroth-order expression of the baryon sound speed is required. The ideal gas law connects the baryon pressure to its energy density and temperature T_b, $P_\mathrm{b} = (\rho_\mathrm{b}/\bar{m}_\mathrm{b})\, k_\mathrm{B}\, T_\mathrm{b}$. The baryon molecular weight, $\bar{m}_\mathrm{b}$, includes free electrons and all ions and neutral atoms of hydrogen and helium, while k_B represents the Boltzmann constant. Using the conservation of the baryon energy density at zeroth order (1.1.8), $\bar{\rho}'_\mathrm{b} = -3\,\mathcal{H}\,\bar{\rho}_\mathrm{b}$, the baryon sound speed is

$$c_\mathrm{b}^2 = \frac{\bar{P}'_\mathrm{b}}{\bar{\rho}'_\mathrm{b}} = \bar{\rho}_\mathrm{b}^{-1}\,\frac{k_\mathrm{B}}{\bar{m}_\mathrm{b}}\,\left(\bar{\rho}'_\mathrm{b}\,T_\mathrm{b} + \bar{\rho}_\mathrm{b}\,T'_\mathrm{b}\right) = \frac{k_\mathrm{B}\,T_\mathrm{b}}{\bar{m}_\mathrm{b}}\left(1 - \frac{1}{3}\,\frac{\partial \ln T_\mathrm{b}}{\partial \ln a}\right) . \tag{3.3.14}$$

The derivation neglects variations in $\bar{m}_\mathrm{b}$, which are largest during recombination. At these times, the sound speed is dominated by the pressure support from photons in comparison to which the variations in the average molecular mass have a negligible effect [283]. Finally, to evaluate the baryon sound speed, we need to know the baryon temperature. It follows from the first law of thermodynamics, $dE = dW + dQ$, which implies that the heat supplied to a system is

$$dQ = m\,\left[\frac{3}{2}\,d\left(\frac{\bar{P}}{\bar{\rho}}\right) + \bar{P}\,d\left(\frac{1}{\rho}\right)\right] . \tag{3.3.15}$$

Equating the heat change with conformal time and the heating rate by the photons

$$Q' = k_\mathrm{B}\left(\frac{3}{2}\,T'_\mathrm{b} + 3\,\mathcal{H}\,T_\mathrm{b}\right) \stackrel{!}{=} \frac{4\rho_\gamma}{\rho_\mathrm{b}}\,k_\mathrm{B}\,\kappa'_{\gamma\mathrm{b}}\,(T_\gamma - T_\mathrm{b})\,, . \tag{3.3.16}$$

gives a differential equation for the evolution of the baryon temperature,

$$T'_\mathrm{b} = -2\mathcal{H}\,T_\mathrm{b} + \frac{8\rho_\gamma}{3\rho_\mathrm{b}}\,\kappa'_{\gamma\mathrm{b}}\,(T_\gamma - T_\mathrm{b}) . \tag{3.3.17}$$

which can be integrated numerically. While Thomson scattering is effective in heating the baryons, i.e. while $R_{\gamma\mathrm{b}}\,\kappa'_{\gamma\mathrm{b}} \gg \mathcal{H}$, the second term dominates the evolution of T_b, and the baryon temperature closely follows that of the photons. In contrast, for $R_{\gamma\mathrm{b}}\,\kappa'_{\gamma\mathrm{b}} \ll \mathcal{H}$, baryons are cooled by the cosmic expansion.

3.4 Evolution equations for relativistic species

Anisotropic stress and higher order multipoles of the phase space distribution are important for an accurate description of relativistic species. In this case, energy momentum conservation not suffices to describe the evolution of perturbations, instead the full Boltzmann equation needs to be considered. We derive its linearised form in the following, addressing the cases of photons and neutrinos.

3.4.1 Perturbed Boltzmann equations for massless species

The Boltzmann equation describes the time evolution of a specie's phase space distribution, including departures from the equilibrium configuration [29], and can be written as

$$\frac{D}{d\tau} f\left(x^i, P_j, \tau\right) = \left[\frac{\partial}{\partial\tau} f\left(x^i, P_j, \tau\right)\right]_{\mathrm{C}} . \tag{3.4.1}$$

The collision term on the right hand side accounts for interactions with other species, while the covariant derivative on the left side depends on the metric and thus describes how the phase space function reacts to changes in the geometry of the underlying space. In Eq. (3.4.1), we allow for an inhomogeneous phase space distribution, which depends on the spatial location x^i, on conformal time τ and on the conjugate momenta P^j. The latter are related to the proper momenta p_i by

$$P_i = a\ (1-\phi)\ p_i\,. \tag{3.4.2}$$

The dependence on metric perturbations can be migrated by defining the comoving three-momentum $\boldsymbol{q}$

$$\boldsymbol{q} \equiv a\,\boldsymbol{p} \equiv q\,\hat{\boldsymbol{n}}\,, \tag{3.4.3}$$

where $\hat{\boldsymbol{n}}$ is a unit vector in the direction of $\boldsymbol{q}$ and $q = |\boldsymbol{q}|$. With this definition, the phase space element becomes

$$\prod_{k=1}^{3} dP_k = (1-3\,\phi)\ q^2 dq\, d\Omega\,, \tag{3.4.4}$$

The time component of the conjugate momentum is related to the proper energy $\epsilon = \sqrt{q^2 + a^2\,m^2}$, measured by a comoving observer, as

$$P_0 = -\,(1+\phi)\ \epsilon\,. \tag{3.4.5}$$

We choose this set of coordinates to express the phase space distribution as a smooth, zeroth-order background distribution, f_0, plus a first order perturbation around f_0

$$f\left(x^i, q, \hat{n}_j, \tau\right) = f_0\left(q\right)\ \left[1 + \Psi\left(x^i, q, \hat{n}_j, \tau\right)\right] . \tag{3.4.6}$$

The background distribution is a Fermi-Dirac distribution in the case of neutrinos and a Bose-Einstein distribution for photons or. In the coordinates used here, Eq. (1.2.8) becomes

$$f_0 = g_a\ \left[e^{\epsilon/T_0} \pm 1\right]^{-1} . \tag{3.4.7}$$

The plus sign applies to fermions, the minus sign to bosons, $T_0 = a\,T(\tau)$ and g_a counts the internal degrees of freedom, which are $g_\gamma = 2$ and for photons and $g_\nu = 6$ for neutrinos.

The covariant derivative on the left hand side of the Boltzmann equation (3.4.1), evaluated in the just described coordinates, is

$$\frac{Df}{d\tau} = \frac{\partial f}{\partial\tau} + \frac{dx^i}{d\tau}\frac{\partial f}{\partial x^i} + \frac{dq}{d\tau}\frac{\partial f}{\partial q} + \frac{d\hat{n}^i}{d\tau}\frac{\partial f}{\partial \hat{n}^i}$$

$$= f_0 \frac{\partial \Psi}{\partial \tau} + \frac{q}{\epsilon} (\hat{n}_i \partial_i \Psi) + q \left(\phi' - \frac{\epsilon}{q} \hat{n}_i \partial_i \psi \right) \frac{\partial f_0}{\partial q} , \tag{3.4.8}$$

where, in the second line we only kept first order terms. Because f_0 is independent of $\hat{n}$, $\partial f / \partial \hat{n}_j$ is at least a first order term as well as the change of momentum direction with time, and the last term in the first line is dropped entirely. Further, in transforming the first two terms we used that, to first order in perturbations,

$$\frac{\partial q}{\partial \tau} = q \, \phi' - \epsilon_i \, \partial_i \phi , \quad \text{and} \quad \frac{d x_i}{d\tau} = \frac{q^i}{\epsilon} . \tag{3.4.9}$$

The zeroth order distribution obeys

$$\frac{q}{f_0} \frac{\partial f_0}{\partial q} = \frac{\partial \ln f_0}{\partial \ln q} , \tag{3.4.10}$$

which allows to simplify the equation in Fourier space as

$$\frac{\partial \Psi}{\partial \tau} + \frac{q}{\epsilon} i \, (\hat{\boldsymbol{n}} \cdot \boldsymbol{k}) \; \Psi + \frac{\partial \ln f_0}{\partial \ln q} \left(\phi' - i \, \frac{\epsilon}{q} \, \hat{\boldsymbol{n}} \cdot \boldsymbol{k} \, \psi \right) = \frac{1}{f_0} \left[\frac{\partial f_0}{\partial \tau} \right]_{\rm C} . \tag{3.4.11}$$

Expressing the stress-energy tensor in terms of the phase space distribution allows to make the connection between the evolution of metric perturbations and perturbations in the particle content,

$$T_{\mu\nu} = \int \left(\prod_{k=1}^{3} dP_k \right) (- |g_{\mu\nu}|)^{-1/2} \, \frac{P_\mu P_\nu}{P_0} \, f(x^i, P_j, \tau) . \tag{3.4.12}$$

Here, the determinant of the metric tensor evaluates to $(- |g_{\mu\nu}|)^{-1/2} = a^{-4} (1 - \psi + 3\phi)$, and the solid angle is associated with the momentum direction $\hat{n}_i$, such that $\int d\Omega \, \hat{n}_i \hat{n}_j = 4\pi \, \delta_{i,j}/3$ and $\int d\Omega \, \hat{n}_i = \int d\Omega \, \hat{n}_i \hat{n}_j \hat{n}_k = 0$. With the decomposition of the phase space distribution from Eq. (3.4.6), the energy momentum tensor reads

$$T^0{}_0 = a^{-4} \int d^2q \, d\Omega \, \sqrt{q^2 + m^2 a^2} \, f_0 \, (q) \; (1 + \Psi) , \tag{3.4.13a}$$

$$T^0{}_i = a^{-4} \int q^2 dq \, d\Omega \, q \, \hat{n}_i \, f_0 \, (q) \; \Psi , \tag{3.4.13b}$$

$$T^i{}_j = a^{-4} \int q^2 dq \, d\Omega \, \frac{q^2 \, \hat{n}^i \hat{n}_j}{\sqrt{q^2 + m^2 a^2}} \, f_0 \, (q) \, (1 + \Psi) . \tag{3.4.13c}$$

The equation of state for a fully relativistic species is $w = 1/3$ and therefore

$$\bar{\rho} = 3 \bar{P} = a^{-4} \int q^2 dq \, d\Omega \; q \, f_0 \, (q) . \tag{3.4.14}$$

Eliminating these zeroth order terms from Eq. (3.4.13), we obtain the first order perturbations of the stress-energy tensor,

$$\delta \rho = a^{-4} \int q^2 dq \, d\Omega \, q \, f_0 \, (q) \; \Psi , \tag{3.4.15a}$$

$$\delta T^0_i = a^{-4} \int q^2 dq \, d\Omega \, q \, \hat{n}_i \, f_0 \, (q) \; \Psi , \tag{3.4.15b}$$

$$\Pi^i{}_j = a^{-4} \int q^2 dq \, d\Omega \, q \left(\hat{n}^i \hat{n}_j - \frac{1}{3} \delta^i_j \right) f_0 \, (q) \; \Psi . \tag{3.4.15c}$$

3.4.2 Neutrino evolution

Unless interactions beyond the Standard Model are introduced, neutrinos decouple from the thermal bath at temperatures around 1 MeV. This is well before any scales probed by the CMB or the large-scale structure have entered the horizon. Therefore, in the context of the evolution of cosmological perturbations, neutrinos can be regarded as collisionless and the term in the right hand side of Eq. (3.4.11) vanishes. We further neglect the neutrino mass in this section, such that first order perturbations to the stress-energy tensor are given by Eq. (3.4.15). In addition, for a relativistic species, the dependence on the momentum q can be integrated from the Boltzmann equations. More precisely, integrating Eq. (3.4.11) over $\int d^3dq\, f_0\,(q)$ and finally dividing by the same integral yields

$$\left[\frac{\partial}{\partial\tau}\int dq\, q^3\, f_{\nu,0}\Psi_\nu + ik\mu\int dq\, q^3\, f_{\nu,0}\,\Psi_\nu \right. \\ \left. + \left(\phi' + i\,k\,\mu\,\psi\right)\int dq\, q^4\,\frac{\partial\, f_{\nu,0}}{\partial q}\right] \Big/ \left(\int dq\, q^3\, f_{\nu,0}(q)\right) = 0\,, \tag{3.4.16}$$

where we have introduced and additional subscript ν to denote neutrino quantities, and $\mu \equiv \hat{\boldsymbol{k}}\cdot\hat{\boldsymbol{n}}$ is the cosine of the angle between the Fourier mode and the momentum direction. An expansion in Legendre polynomials $P_l\,(\mu)$ absorbs the angular dependence

$$F_\nu(\boldsymbol{k},\hat{\boldsymbol{n}},\tau) \equiv \frac{\int q^3\, dq\, f_{\nu,0}\,(q)\;\Psi_\nu}{\int q^3\, dq\, f_{\nu,0}\,(q)} \equiv \sum_{l=0}^{\infty}(-i)^l\,(2l+1)\,F_{\nu l}\,(\boldsymbol{k},\tau)\;P_l\,(\mu)\;. \tag{3.4.17}$$

In terms of the normalised, momentum-integrated phase space perturbation F_ν the Boltzmann equation for neutrinos takes the simple form

$$\frac{\partial\, F_\nu}{\partial\tau} + i\,k\,\mu\,F_\nu = 4\left(\phi' - i\,k\,\mu\psi\right)\,. \tag{3.4.18}$$

Moreover, the lowest-order Legendre coefficients, $F_{\nu,l}$, of the expansion are directly related to perturbations in the stress-energy tensor. The lowest-order Legendre polynomials are given by,

$$P_0\,(\mu) = 1\,, \quad P_1\,(\mu) = \mu \quad \text{and} \quad P_2\,(\mu) = \frac{1}{2}\left(3\mu^2 - 1\right)\,, \tag{3.4.19}$$

and obey the orthogonality relation

$$\int d\Omega\, P_m(\mu)P_n(\mu) = 2\pi\int_{-1}^{1} dx\, P_m(x)P_n(x) = \frac{4\pi}{2n+1}\,\delta_{mn}\,. \tag{3.4.20}$$

Thus, the perturbations of the stress-energy tensor for a relativistic species (3.4.15) can be written in terms of Legendre coefficients as

$$\delta_\nu = \frac{1}{4\pi}\int d\Omega\,\left(\frac{\int dq\, q^3\, f_{\nu,0}\Psi_\nu}{\int dq\, q^3\, f_{\nu,0}}\right) = F_{\nu,0}\,, \tag{3.4.21a}$$

$$\theta_\nu = \frac{ik^j\int d\Omega\int dq\, q^3\, n_j\, f_{\nu,0}\,\Psi}{\frac{4}{3}\int dq\, q^3\, f_{\nu,0}\int d\Omega} = \frac{3k}{4}F_{\nu,1}\,, \tag{3.4.21b}$$

$$\sigma_\nu = \left[a^{-4}k^2 \int d\Omega \int dq\, q^3 \left(\mu^2 - \frac{1}{3}\right) f_{\nu,0}\, \Psi\right] / \left(\frac{4\,k^2}{3}\bar{\rho}_\nu\right) = \frac{1}{2}\, F_{\nu,2} \tag{3.4.21c}$$

To obtain evolution equations for the perturbed components of the stress energy tensor, we insert the multipole expansion (3.4.17) into the momentum-integrated Boltzmann equation (3.4.18) and use the recursion relation for Legendre polynomials,

$$(l+1)\, P_{l+1}(\mu) = (2l+1)\, \mu P_l(\mu) - l\, P_{l-1}(\mu)\ , \tag{3.4.22}$$

to obtain

$$\begin{aligned}\sum_{l=0}^{\infty} (-i)^l\, (2l+1)\, F'_{\nu,l}\, P_l(\mu) + ik\, P_1(\mu)\ F_{\nu,0} + \sum_{l=2}^{\infty} (i)^{l+2}\, k\, l\, F_{\nu,(l-1)}\, P_l(\mu) \\ + \sum_{l=0}^{\infty} (i)^{l+4}\, k\, l\, F_{\nu,(l+1)}\ (l+1)\, P_l(\mu) = 4\left(\phi' P_0(\mu) - i\, k\, P_1(\mu)\, \psi\right)\ .\end{aligned} \tag{3.4.23}$$

The evolution of the individual multipoles follows from integrating this equation against Legendre polynomials $\int_{-1}^{1} d\mu\, P_l(\mu)$:

$$\delta'_\nu = -\frac{4}{3}\theta_\nu + 4\phi'\,, \tag{3.4.24a}$$

$$\theta'_\nu = k^2\left(\frac{\delta_\nu}{4} - \sigma_\nu\right) + k^2\psi\,, \tag{3.4.24b}$$

$$F'_{\nu,l} = \frac{k}{2l+1}\left[l\, F_{\nu,(l-1)} - (l+1)\, F_{\nu,(l+1)}\right] \quad \text{for} \quad l \geq 3\,. \tag{3.4.24c}$$

Expressing the Boltzmann equation in terms of multipole moments of the momentum-integrated phase space distribution function leads to an infinite set of coupled differential equations. In this set, a particular multipole l only depends on the two neighbouring modes $l+1$ and $l-1$. To solve this so-called Boltzmann hierarchy numerically, requires its truncation at some high multipole $l_{\rm max}$. The naive method, setting $F_{\nu,l_{\rm max}} = 0$, creates propagation errors which proceed down to $l = 0$ where they are reflected and amplify. For a more robust truncation, the behaviour of $F_{\nu,l}$ is extrapolated to $l_{\rm max}+1$. We derive an analytical expression for the evolution of the neutrino multipoles in Sec. 7.3.4. The large multipoles exhibit damped oscillations, similar to spherical Bessel functions, with frequency $k\tau$, see Eq. (7.3.18). Using the recurrence relation for spherical Bessel functions, the evolution of $F_{\nu(l_{\rm max}+1)}$ is approximated by [283]

$$F_{\nu,(l_{\rm max}+1)} \simeq \frac{2l_{\rm max}+1}{k\tau} F_{\nu,l_{\rm max}} - F_{\nu,(l_{\rm max}-1)}\,, \tag{3.4.25}$$

and $F_{\nu,l_{\rm max}}$ accordingly evolves as

$$F'_{\nu,l_{\rm max}} = k\left(F_{\nu,(l_{\rm max}-1)} - \frac{l_{\rm max}+1}{k\,\tau} F_{\nu,l_{\rm max}}\right)\,. \tag{3.4.26}$$

3.4.3 Photon evolution

Considering the evolution of photon perturbations, the collision term in the right hand side of Eq. (3.4.12) can not be neglected, but describes Thomson scattering with electrons. As already elucidated in Sec. 2.3.2, these scatterings partly polarise the CMB and the phase space distribution functions of the polarisation states $\hat{\boldsymbol{\epsilon}}_1$ and $\hat{\boldsymbol{\epsilon}}_2$ differ

$$f\left(\boldsymbol{k}, q, \hat{\boldsymbol{n}}, \tau, \hat{\boldsymbol{\epsilon}}_{1/2}\right) = f_{\gamma,0}\left(q\right)\,\left[\Psi_{\gamma 1/\gamma 2}\left(\boldsymbol{k}, q, \hat{\boldsymbol{n}}, \tau\right)\right]\,. \tag{3.4.27}$$

The polarisation vectors are orthogonal to each other and orthogonal to the momentum direction, i.e. $\hat{\boldsymbol{n}} \cdot \hat{\boldsymbol{\epsilon}}_{1/2} = \hat{\boldsymbol{\epsilon}}_1 \cdot \hat{\boldsymbol{\epsilon}}_2 = 0$. The Boltzmann equation (3.4.1) applies to both phase space distributions individually, hence $\Psi_{\gamma 1}$ and $\Psi_{\gamma 2}$ both obey Eq. (3.4.18) and are coupled by the collision term. A practical choice is to track the sum and the difference of both polarisation states, which correspond to the intensity and the Stokes parameter Q, respectively. In analogy to the momentum-integrated neutrino phase space distribution (3.4.17), we define

$$F_\gamma = \frac{\int dq\, d^3\, f_{\gamma,0}\left(q\right)\left(\Psi_{\gamma 1} + \Psi_{\gamma 2}\right)}{\int dq\, q^3\, f_{\gamma,0}\left(q\right)}\,, \tag{3.4.28a}$$

$$G_\gamma = \frac{\int dq\, d^3\, f_{\gamma,0}\left(q\right)\left(\Psi_{\gamma 1} - \Psi_{\gamma 2}\right)}{\int dq\, q^3\, f_{\gamma,0}\left(q\right)}\,. \tag{3.4.28b}$$

The momentum-integrated Boltzmann equation for the Stokes parameters is

$$F_\gamma' + ik\,\mu\,F_\gamma - 4\left(\phi' - ik\,\mu\,\psi\right) = \left(\frac{\partial\, F_\gamma}{\partial \tau}\right)_{\mathrm{C}}\,, \tag{3.4.29a}$$

$$G_\gamma' + ik\,\mu\,G_\gamma = \left(\frac{\partial\, G_\gamma}{\partial \tau}\right)_{\mathrm{C}}\,. \tag{3.4.29b}$$

Again, it is useful to expand the momentum-integrated phase space distribution in multipoles,

$$F_\gamma\left(\boldsymbol{k}, \hat{\boldsymbol{n}}, \tau\right) = \sum_{l=0}^{\infty} \left(-i\right)^l\,\left(2l+1\right)\,F_{\gamma,l}\left(\boldsymbol{k}, \tau\right)\,P_l\left(\mu\right)\,, \tag{3.4.30a}$$

$$G_\gamma\left(\boldsymbol{k}, \hat{\boldsymbol{n}}, \tau\right) = \sum_{l=0}^{\infty} \left(-i\right)^l\,\left(2l+1\right)\,G_{\gamma,l}\left(\boldsymbol{k}, \tau\right)\,P_l\left(\mu\right)\,. \tag{3.4.30b}$$

The lowest-order intensity multipoles are closely related to the stress-energy tensor,

$$\delta_\gamma = F_{\gamma,0}\,, \quad \theta_\gamma = \frac{3k}{4}\,F_{\gamma,1}\,, \quad \text{and} \quad \sigma_\gamma = \frac{1}{2}\,F_{\gamma,2}\,. \tag{3.4.31}$$

And, given the intensity multipoles, the temperature autocorrelation spectrum is [283]

$$C_l^{\mathrm{TT}} = \frac{\pi}{4}\int d^3k\;\left|F_{\gamma,l}\left(\boldsymbol{k},\,\tau\right)\right|^2 \tag{3.4.32}$$

To evaluate the Boltzmann equation further, its scattering term needs to be specified. The

process of interest is Thomson scattering between photons and electrons, i.e.

$$\gamma\left(p_1\right)+\mathrm{e}^{-}\left(p_3\right) \quad \longleftrightarrow \quad \gamma\left(p_2\right)+\mathrm{e}^{-}\left(p_4\right) ,$$

for which the scattering term, to all orders in perturbations, is [21]

$$\begin{aligned}\left(\frac{\partial f_\gamma}{\partial \tau}\right)_{\mathrm{C}} = \frac{1}{E_1}\int\left(\prod_{i=2}^{4}\frac{d\,p_i}{(2\pi)^3\;2E_i}\right)\left|\mathcal{M}_{\mathrm{e}+\gamma\leftrightarrow\mathrm{e}+\gamma}\right|^2\;(2\pi)^4\;\delta^4\left(p_1+p_2-p_3-p_4\right)\\ \times\left\{f_{\mathrm{e}}\left(p_4\right)\;f_\gamma\left(p_2\right)-f_{\mathrm{e}}\left(p_3\right)\;f_\gamma\left(p_1\right)\right\} .\end{aligned} \tag{3.4.33}$$

Simulated emission and Pauli blocking have been neglected in the product of electron (f_{e}) and photon (f_γ) phase space distributions in the last parenthesis of this expression. The matrix element for electron-photon scattering $\mathcal{M}_{\mathrm{e}+\gamma\leftrightarrow\mathrm{e}+\gamma}$ can e.g. be found in Ref. [289]. Evaluating it in the low energy limit and expanding the scattering term to first order in perturbations yields [283, 289, 290]

$$\begin{aligned}\left(\frac{\partial F_\gamma}{\partial \tau}\right)_{\mathrm{C}} &= \kappa'_{\gamma\mathrm{b}}\left[-F_\gamma+F_{\gamma,0}+4\,\hat{\boldsymbol{n}}\cdot\boldsymbol{v}_{\mathrm{b}}-\frac{1}{2}\;\left(F_{\gamma,2}+G_{\gamma,0}+G_{\gamma,2}\right)P_2\left(\mu\right)\right]\\ &= \kappa'_{\gamma\mathrm{b}}\left[\frac{4i}{k}\;\left(\theta_\gamma-\theta_{\mathrm{b}}\right)\;P_1+\left(9\,\sigma_\gamma-\frac{1}{2}\,G_{\gamma,0}-\frac{1}{2}\,G_{\gamma,2}\right)P_2-\sum_{l=3}^{\infty}\left(-i\right)^l\left(2+l\right)\;F_{\gamma,l}\,P_l\right] ,\end{aligned} \tag{3.4.34a}$$

$$\begin{aligned}\left(\frac{\partial G_\gamma}{\partial \tau}\right)_{\mathrm{C}} &= \kappa'_{\gamma\mathrm{b}}\left[-G_\gamma+\frac{1}{2}\;\left(F_{\gamma,2}+G_{\gamma,0}+G_{\gamma,2}\right)\left(1-P_2\left(\mu\right)\right)\right]\\ &= \kappa'_{\gamma\mathrm{b}}\left[\frac{1}{2}\;\left(F_{\gamma,2}+G_{\gamma,0}+G_{\gamma,2}\right)\left(1-P_2\right)-\sum_{l=0}^{\infty}\left(-i\right)^l\left(2+l\right)\;G_{\gamma,l}\,P_l\right] .\end{aligned} \tag{3.4.34b}$$

The scalar product between the incident photon's momentum $\hat{\boldsymbol{n}}$ and the baryon velocity $\boldsymbol{v}_{\mathrm{b}}$ can be expressed as

$$\hat{\boldsymbol{n}}\cdot\boldsymbol{v}_{\mathrm{b}}=\left(\hat{\boldsymbol{n}}\cdot\hat{\boldsymbol{k}}\right)\left(\hat{\boldsymbol{k}}\cdot\boldsymbol{v}_{\mathrm{b}}\right)=-\frac{i\,\theta_{\mathrm{b}}}{k}\,\mu\,, \tag{3.4.35}$$

which was used to simplify the first line of the intensity scattering term.

With the in interaction terms in place, the evolution equations for the photon multipoles follow from integrating Eq. (3.4.29) against Legendre polynomials, $\int_{-1}^{1}d\mu\,P_l\left(\mu\right)$, just as in the neutrino case:

$$\delta'_\gamma=-\frac{4}{3}\,\theta_\gamma+4\,\phi'\,, \tag{3.4.36a}$$

$$\theta'_\gamma=k^2\,\left(\frac{1}{4}\,\delta_\gamma-\sigma_\gamma\right)+k^2\,\psi+\kappa'_{\gamma\mathrm{b}}\left(\theta_{\mathrm{b}}-\theta_\gamma\right) , \tag{3.4.36b}$$

$$\sigma'_\gamma=\frac{4}{15}\,\theta_\gamma-\frac{3}{10}\,k\,F_{\gamma,3}-\frac{9}{10}\,\kappa'_{\gamma\mathrm{b}}\sigma_\gamma+\frac{\kappa'_{\gamma\mathrm{b}}}{20}\;\left(G_{\gamma,0}+G_{\gamma,2}\right) , \tag{3.4.36c}$$

$$F'_{\gamma,l}=\frac{k}{2l+1}\;\left[l\,F_{\gamma,(l-1)}-\left(l+1\right)\;F_{\gamma,(l+1)}\right]-\kappa'_{\gamma\mathrm{b}}\,F_{\gamma,l}\quad l>3\,, \tag{3.4.36d}$$

$$G'_{\gamma,0}=-k\,G_{\gamma,1}-\frac{\kappa'_{\gamma\mathrm{b}}}{2}\;\left(G_{\gamma,0}-F_{\gamma,2}-G_{\gamma,2}\right) , \tag{3.4.36e}$$

$$G'_{\gamma,1}=\frac{k}{3}\;\left(G_{\gamma,0}-2G_{\gamma,2}\right)-\kappa'_{\gamma\mathrm{b}}\,G_{\gamma,1}\,, \tag{3.4.36f}$$

$$G'_{\Upsilon,2} = \frac{k}{5}\,(2\,G_{\Upsilon,1} - 3G_{\Upsilon,3}) + \frac{\kappa'_{\Upsilon\mathrm{b}}}{10}\,(F_{\Upsilon,2} + G_{\Upsilon,0} + G_{\Upsilon,2}) - \kappa'_{\Upsilon\mathrm{b}}\,G_{\Upsilon 2}\,, \tag{3.4.36g}$$

$$G'_{\Upsilon,l} = \frac{k}{2l+1}\,\Big(lG_{\Upsilon,(l-1)} - (l+1)\,G_{\Upsilon,(l+1)}\Big) - \kappa'_{\Upsilon\mathrm{b}}\,G_{\Upsilon,l} \quad l \geq 3\,. \tag{3.4.36h}$$

Obviously, Thomson scattering couples the lowest multipoles of the different polarisation states. For $l > 3$, however, we again obtain a hierarchy of equations in which each coefficient $F_{\Upsilon,l}$ and $G_{\Upsilon,l}$ only depends on its neighbouring higher and lower multipole. The same truncation scheme as for neutrinos (3.4.25) can be applied to this hierarchy, thus that the two highest-order equations are given by

$$F'_{\Upsilon,l_{\max}} = k\left(F_{\Upsilon,(l_{\max}-1)} - \frac{l_{\max}+1}{k\tau}\,F_{\Upsilon,l_{\max}}\right) - \kappa'_{\Upsilon\mathrm{b}}\,F_{\Upsilon,l_{\max}}\,, \tag{3.4.37a}$$

$$G'_{\Upsilon,l_{\max}} = k\left(G_{\Upsilon,(l_{\max}-1)} - \frac{l_{\max}+1}{k\tau}\,G_{\Upsilon,l_{\max}}\right) - \kappa'_{\Upsilon\mathrm{b}}\,G_{\Upsilon,l_{\max}}\,. \tag{3.4.37b}$$

3.5 Dark matter scattering with neutrinos

The preceding sections provide the equations required to predict the evolution of metric perturbations, dark matter, baryons, neutrinos and photons in the ΛCDM scenario. We now turn to one of the main objectives of this thesis, dark matter-neutrino scattering, and augment the respective Boltzmann equations by appropriate scattering terms.

A thermally produced dark matter particle must have a mass of at least 3.3 keV (1.2.34), and typical WIMP candidates are even heavier, in the GeV ballpark and above. In this case, the dark matter mass is much larger than the neutrino mass and the neutrino kinetic energy. We therefore consider elastic dark matter-neutrino scattering processes of the form [200, 281, 282, 291, 292]

$$\nu\,(p_1) + \nu\mathrm{dm}\,(p_3) \quad \longleftrightarrow \quad \nu\,(p_2) + \nu\mathrm{dm}\,(p_4)\,,$$

where νdm refers to a dark matter species which exhibits neutrino interactions. The case is similar to photon-baryon interactions, which likewise are treated in the low-energy Thomson limit.

Concerning the neutrino evolution, elastic scattering with electrons signifies that the interaction term on the right hand side of the Boltzmann equation (3.4.1) differs from zero and is given by an expression similar to Eq. (3.4.33)

$$\left(\frac{\partial\,f_\nu}{\partial\tau}\right)_{\mathrm{C}} = \frac{1}{E_1}\int\left(\prod_{i=2}^{4}\frac{d\,p_i}{(2\pi)^3\;2E_i}\right)\,|\mathcal{M}_{\nu\mathrm{dm}+\nu\leftrightarrow\nu\mathrm{dm}+\nu}|^2\;(2\pi)^4\;\delta^4\,(p_1+p_2-p_3-p_4)$$
$$\times\,\{f_{\nu\mathrm{dm}}\,(p_4)\;f_\nu\,(p_2) - f_{\nu\mathrm{dm}}\,(p_3)\;f_\nu\,(p_1)\}\;. \tag{3.5.1}$$

In principle, this implies that the Boltzmann equations depend on the precise particle-physics mechanism for the scattering through its matrix element. In practice, however, the model dependence can be absorbed in a few parameters, as shown in the following. Even

more important, of these parameters only one, the energy dependence of the scattering cross section, has a significant impact on the observables. Cosmological observations therefore allow to place constraints on the dark matter interaction strength with neutrinos which are largely independent of the underlying particle physics mechanism and apply to a wide range of models at the same time.

3.5.1 Interacting neutrino hierarchy

To include the dark matter-neutrino interaction term in the Boltzmann equations, we adopt the parameterisation of Ref. [293], defining the projection of the matrix element on the Legendre polynomials as

$$A_l\left(p\right) = \frac{1}{2}\int_{-1}^{1} d\mu\; P_l\left(\mu\right)\left(\frac{1}{g_{\nu\mathrm{dm}}\, g_\nu}\left|\mathcal{M}_{\nu\mathrm{dm}+\nu\leftrightarrow\nu\mathrm{dm}+\nu}\right|^2\right)\Big|_{\substack{t=2p^2(\mu-1)\\ s=m_{\nu\mathrm{dm}}^2+2\,m_{\nu\mathrm{dm}}\,p}}\,, \tag{3.5.2}$$

where g_ν and $g_{\nu\mathrm{dm}}$ are the internal degrees of freedom of the neutrinos and the dark matter particle, and $m_{\nu\mathrm{dm}}$ is the dark matter mass. In the low energy limit, the dark matter particle is at rest before and after the scattering and the neutrino changes its direction but not its energy. Then, the Mandelstam variables reduce to $t = 2p^2(\mu-1)$ and $s = m_{\nu\mathrm{dm}}^2 + 2\,m_{\nu\mathrm{dm}}\,p$, as indicated above, where $p = |\boldsymbol{p}_1| = |\boldsymbol{p}_2|$ and μ is the cosine between the ingoing and the outgoing neutrino direction. The neutrino scattering rate is related to the projection on the two lowest multipoles,

$$\kappa'_{\nu\mathrm{dm}} = \frac{a\, n_{\nu\mathrm{dm}}}{128\,\pi^3\, m_{\nu\mathrm{dm}}^2}\,\frac{g_\nu}{\rho_\nu}\int_0^\infty dp\left(\frac{\partial f_\nu}{\partial p}\right)p^4\left[A_0(p) - A_1(p)\right]\,. \tag{3.5.3}$$

Further, from the projected matrix element the angular coefficients α_l can be defined

$$\alpha_l \equiv \frac{\int dp\; p^4\left(\frac{\partial f_\nu}{\partial p}\right)\left[A_0(p) - A_l(p)\right]}{\int dp\; p^4\left(\frac{\partial f_\nu}{\partial p}\right)\left[A_0(p) - A_1(p)\right]}\,. \tag{3.5.4}$$

These coefficients absorb the model-dependent angular part of the scattering term in the Boltzmann equations, which become [282, 291, 293, 294]

$$\delta'_\nu = -\frac{4}{3}\,\theta_\nu + 4\phi'\,, \tag{3.5.5a}$$

$$\theta'_\nu = k^2\left(\frac{\delta_\nu}{4} - \sigma_\nu\right) + k^2\psi - \kappa'_{\nu\mathrm{dm}}\left(\theta_\nu - \theta_{\nu\mathrm{dm}}\right)\,, \tag{3.5.5b}$$

$$\sigma'_\nu = \frac{8}{30}\,\theta_\nu - \frac{3}{10}\,k\,F_{\nu,3} - \alpha_2\,\kappa'_{\nu\mathrm{dm}}\,\sigma_\nu\,, \tag{3.5.5c}$$

$$F'_{\nu,l} = \frac{k}{2l+1}\left[l\,F_{\nu,l-1} - (l+1)\,F_{\nu,l+1}\right] - \alpha_l\,\kappa'_{\nu\mathrm{dm}}F_{\nu,l}\,, \tag{3.5.5d}$$

$$F'_{\nu,l_{\max}} = k\left[F_{\nu,l_{\max}-1} - \frac{l_{\max}+1}{k\tau}F_{\nu,l_{\max}}\right] - \alpha_l\,\kappa'_{\nu\mathrm{dm}}F_{\nu,l_{\max}}\,. \tag{3.5.5e}$$

In Sec. 3.5.3 we investigate possible interaction scenarios and the scattering rates and angular coefficients they imply.

3.5.2 Modified dark matter evolution

Having derived the interacting neutrino hierarchy, the dark matter evolution has to be modified accordingly. The interactions do not affect the evolution of δ_ν, hence the conservation equation for δ (3.3.3) still applies to each species individually. In contrast, the coupling between the neutrino and the dark matter velocity divergence implies that we have to consider their combined momentum conservation, given by Eq. (3.3.7). Just as was the case for baryons, the scattering with neutrinos can transfer heat to the dark matter population and implies a non-zero sound speed

$$c^2_{\nu\mathrm{dm}} = \frac{k_\mathrm{B}\, T_{\nu\mathrm{dm}}}{m_{\nu\mathrm{dm}}} \left(1 - \frac{1}{3}\, \frac{\partial \ln T_{\nu\mathrm{dm}}}{\partial \ln a}\right) . \tag{3.5.6}$$

The magnitude of the sound speed, and correspondingly its influence on the evolution of dark matter perturbations, decreases with increasing dark matter mass, for large enough masses it becomes negligible. We investigate the effect of such a sound speed term for the case of dark matter-photon interactions. Concerning neutrino interactions, our main objective is to provide a physical understanding of the so-called mixed damping regime. In this context, we work in the most-baseline scenario, assume a sufficiently large value for $m_{\nu\mathrm{dm}}$ and neglect the sound speed term in the dark matter evolution equations, which become

$$\delta'_{\nu\mathrm{dm}} = -\theta_{\nu\mathrm{dm}} + 3\phi' \,, \tag{3.5.7a}$$

$$\theta'_{\nu\mathrm{dm}} = k^2\psi - \mathcal{H}\theta_{\nu\mathrm{dm}} - R_{\nu\mathrm{dm}}\kappa'_{\nu\mathrm{dm}}\left(\theta_{\nu\mathrm{dm}} - \theta_\nu\right) . \tag{3.5.7b}$$

Again, the factor $R_{\nu\mathrm{dm}}$ in front of the scattering term ensures momentum conservation and is defined as

$$R_{\nu\mathrm{dm}} = \frac{4\,\rho_\nu}{3\,\rho_{\nu\mathrm{dm}}} \,. \tag{3.5.8}$$

With the parameterisation of the scattering term chosen in Eq. (3.5.2) to (3.5.4), the two lowest neutrino multipoles are independent of the angular coefficients α_l, and neither do these enter the evolution of dark matter perturbations directly. Instead, the particle physics details of the interaction only manifest themselves in the evolution of the higher order neutrino multipoles.

3.5.3 Scattering terms

Previous works, which studied dark matter-neutrino scattering and its impact on the CMB and large-scale structure, have adopted differing values for the angular coefficients α_l, for instance, $\alpha_2 = 2$ and $\alpha_{l>2} = 1$ in Ref. [295] or $\alpha_2 = 9/5$ and $\alpha_{l>2} = 1$ in Ref. [277]. None of them refers to a particular model for the interaction to motivate these values. To gauge expectations on possible values of α_l and the energy dependence of $\kappa'_{\nu\mathrm{dm}}$, we consider the simplified-model classification of dark matter-neutrino interactions in [296]. This work lists all possible, renormalizable interactions between dark matter and active, left handed neutrinos, which arise if the Standard Model is extended by a dark matter

particle and a mediator. Those simplified scenarios violate gauge invariance and are only viable as part of a more complex UV-completion, see e.g. Ref [297]. Here, they serve us as a phenomenological benchmark to assess what structures are possible for the interaction term. The twelve possible simplified models found in Ref. [296] are summarised in Tab. 3.1, where we quote the full matrix element, and computed the respective low-energy limit, the scattering cross section and the angular coefficients.

The scattering rate $\kappa'_{\nu\mathrm{dm}}$ is always proportional to the dark matter number density $n_{\nu\mathrm{dm}}$, which prompts to rewrite the dark matter-neutrino scattering rate (3.5.3) in the same form as the rate for Thomson scattering (3.3.11)

$$\kappa'_{\nu\mathrm{dm}} = a\, n_{\nu\mathrm{dm}}\, \sigma_{\nu\mathrm{dm}}\,, \tag{3.5.9}$$

where all mode-dependence is contained in the elastic scattering cross section, $\sigma_{\nu\mathrm{dm}}$. Cosmological observations are neither sensitive to the precise value of the dark matter mass nor to the dark matter number density but can determine the energy density of dark matter to good precision. A practical way to parameterise the dark matter-neutrino scattering rate is by introducing a new, dimensionless parameter,

$$u_{\nu\mathrm{dm}} = \frac{\sigma_{\nu\mathrm{dm}}}{\sigma_{\mathrm{Th}}} \left(\frac{m_{\nu\mathrm{dm}}}{100\,\mathrm{GeV}}\right)^{-1}\,. \tag{3.5.10}$$

The temperature dependence of the scattering cross sections is given by a power law, and in Tab. 3.1 we encounter two different possibilities for its exponent, $n_{\nu\mathrm{dm}} = 2, 4$. The neutrino temperature obeys $T_\nu \propto a^{-1}$, hence we further account for the energy dependence of the scattering cross section by defining

$$u_{\nu\mathrm{dm}} \equiv u_{\nu\mathrm{dm},0}\, a^{-n_{\nu\mathrm{dm}}}\,. \tag{3.5.11}$$

The angular coefficients are always $\mathcal{O}(1)$ parameters and only couple to higher order neutrino multipoles. Their effect on cosmological observables is very minor. Thus, the twelve simplified models considered initially reduce to two scenarios, characterised by the temperature dependence of the cross sections. Each of these contains one additional parameter with respect to the baseline ΛCDM set, the normalised interaction strength $u_{\nu\mathrm{dm}}$. Comparison of the CMB spectra and the matter power spectrum predicted from these evolution equations with observations allows to put constraints on $u_{\nu\mathrm{dm}}$.

3.6 Dark matter-photon scattering

3.6.1 Modified Boltzmann hierarchy

The formalism to include elastic scattering between dark matter and photons into the Boltzmann equations is very similar to dark matter-neutrino interactions. Here, we consider the process

$$\gamma\,(p_1) + \gamma\mathrm{dm}\,(p_3) \quad \longleftrightarrow \quad \gamma\,(p_2) + \gamma\mathrm{dm}\,(p_4)\,, \tag{3.6.1}$$

scenario	$\left(\frac{1}{\eta_\nu\,\eta_{\nu\mathrm{dm}}}\sum_{\text{spins}}\lvert\mathcal{M}_{\nu+\nu\mathrm{dm}\leftrightarrow\nu+\nu\mathrm{dm}}\rvert^2\right)$	$s=m_{\nu\mathrm{dm}}^2+2m_{\nu\mathrm{dm}}p_1$ $t=2p_1^2(\mu-1)$ $p_1\ll m_M,\,m_{\nu\mathrm{dm}}$	scattering rate $\kappa'_{\nu\mathrm{dm}}$	higher order coefficients $\alpha_l\,, l\geq 2$
complex DM Dirac mediator N_R	$g^4\,\frac{m_{\nu\mathrm{dm}}^4-2sm_{\nu\mathrm{dm}}^2+s^2+ts}{(t+s-m_\mathrm{N})^2}$	$\frac{2g^4p_1^2m_{\nu\mathrm{dm}}^2(\mu+1)}{(m_\mathrm{N}^2-m_{\nu\mathrm{dm}}^2)^2}$	$\frac{155}{588}\,\frac{a\,n_{\nu\mathrm{dm}}\,\pi\,g^4}{(m_\mathrm{N}^2-m_{\nu\mathrm{dm}}^2)^2}\,T_\nu^2$	$\alpha_l=\frac{3}{2}$
real DM Dirac mediator N_R	$g^4\,\frac{\left(2s+t-2m_{\nu\mathrm{dm}}^2\right)^2\left[m_{\nu\mathrm{dm}}^4-2sm_{\nu\mathrm{dm}}+s(s+t)\right]}{\left(s-m_\mathrm{N}^2\right)^2\left(s+t+m_\mathrm{N}^2-2m_{\nu\mathrm{dm}}^2\right)^2}$	$\frac{32\,g^4\,m_{\nu\mathrm{dm}}^4\,p_1^4\,(1+\mu)}{\left(m_\mathrm{N}^2-m_{\nu\mathrm{dm}}^2\right)^4}$	$\frac{508}{21}\,\frac{g^4\pi^3m_{\nu\mathrm{dm}}^2\,a\,n_{\nu\mathrm{dm}}}{\left(m_\mathrm{N}^2-m_{\nu\mathrm{dm}}^2\right)^4}\,T_\nu^4$	$\alpha_l=\frac{3}{2}$
complex DM Majorana mediator N_L	$g^4\,\frac{m_{\nu\mathrm{dm}}^4-2sm_{\nu\mathrm{dm}}^2+s^2+ts}{(t+s-m_\mathrm{N})^2}$	$\frac{2g^4p_1^2m_{\nu\mathrm{dm}}^2(\mu+1)}{(m_\mathrm{N}^2-m_{\nu\mathrm{dm}}^2)^2}$	$\frac{155}{588}\,\frac{a\,n_{\nu\mathrm{dm}}\,\pi\,g^4}{(m_\mathrm{N}^2-m_{\nu\mathrm{dm}}^2)^2}\,T_\nu^2$	$\alpha_l=\frac{3}{2}$
real DM Majorana mediator N_L	$g^4\,\frac{\left(2s+t-2m_{\nu\mathrm{dm}}^2\right)^2\left[m_{\nu\mathrm{dm}}^4-2sm_{\nu\mathrm{dm}}+s(s+t)\right]}{\left(s-m_\mathrm{N}^2\right)^2\left(s+t+m_\mathrm{N}^2-2m_{\nu\mathrm{dm}}^2\right)^2}$	$\frac{32\,g^4\,m_{\nu\mathrm{dm}}^4\,p_1^4\,(1+\mu)}{\left(m_\mathrm{N}^2-m_{\nu\mathrm{dm}}^2\right)^4}$	$\frac{508}{21}\,\frac{g^4\pi^3m_{\nu\mathrm{dm}}^2\,a\,n_{\nu\mathrm{dm}}}{\left(m_\mathrm{N}^2-m_{\nu\mathrm{dm}}^2\right)^4}\,T_\nu^4$	$\alpha_l=\frac{3}{2}$
Dirac DM scalar mediator ϕ	$g^4\,\frac{\left(s+t-m_{\nu\mathrm{dm}}^2\right)^2}{2\left(s+t+m_\phi^2-2m_{\nu\mathrm{dm}}^2\right)}$	$\frac{2\,g^4m_{\nu\mathrm{dm}}^2\,p_1^2}{\left(m_{\nu\mathrm{dm}}^2-m_\phi^2\right)^2}$	$\frac{155}{392}\,\frac{\pi\,g^4\,a\,n_{\nu\mathrm{dm}}}{\left(m_\phi^2-m_{\nu\mathrm{dm}}^2\right)^2}\,T_\nu^2$	$\alpha_l=1$
Majorana DM scalar mediator ϕ	$\frac{g^4}{2}\left[\frac{\left(s-m_{\nu\mathrm{dm}}^2\right)^2}{\left(s-m_\phi^2\right)^2}+\frac{\left(s+t-m_{\nu\mathrm{dm}}^2\right)^2}{\left(s+t+m_\phi^2-2m_{\nu\mathrm{dm}}^2\right)^2}\right]$	$\frac{4\,g^4\,m_{\nu\mathrm{dm}}^2\,p_1^2}{\left(m_\phi^2-m_{\nu\mathrm{dm}}^2\right)^2}$	$\frac{155}{196}\,\frac{\pi\,g^4\,a\,n_{\nu\mathrm{dm}}}{\left(m_\phi^2-m_{\nu\mathrm{dm}}^2\right)^2}\,T_\nu^2$	$\alpha_l=1$
vector DM fermionic mediator N_L	- - -	$\frac{16\,g^4\,m_{\nu\mathrm{dm}}^2\,p_1^2\,(3-\mu)}{3\left(m_{\nu\mathrm{dm}}^2-m_\mathrm{N}^2\right)^2}$	$\frac{1240}{441}\,\frac{\pi\,g^4\,a\,n_{\nu\mathrm{dm}}}{\left(m_{\nu\mathrm{dm}}^2-m_\mathrm{N}^2\right)^2}\,T_\nu^2$	$\alpha_l=\frac{9}{10}$
scalar DM vector mediator Z_μ	$g^4\,\frac{4\left[m_{\nu\mathrm{dm}}^2-2m_{\nu\mathrm{dm}}^2s+s(s+t)\right]}{\left(m_\mathrm{Z}^2-t\right)^2}$	$\frac{8\,g^4\,m_{\nu\mathrm{dm}}\,p_1^2\,(\mu+1)}{m_\mathrm{Z}^4}$	$\frac{3}{2}\,\frac{310}{441}\,\frac{\pi g^4\,a\,n_{\nu\mathrm{dm}}}{m_\mathrm{Z}^4}\,T_\nu^2$	$\alpha_l=\frac{3}{2}$
Dirac DM vector mediator Z_μ	$g^4\,\frac{4\left(m_{\nu\mathrm{dm}}^2-s\right)^2+4st+2t^2}{\left(m_\mathrm{Z}^2-t\right)^2}$	$8g^4\,\frac{m_dm^2\,p_1^2\,(1+\mu)}{m_\mathrm{Z}^4}$	$\frac{155}{147}\,\frac{g^4\,\pi\,a\,n_{\nu\mathrm{dm}}}{m_\mathrm{Z}^4}\,T_\nu^2$	$\alpha_l=\frac{3}{2}$
Majorana DM vector mediator Z_μ	$g^4\,\frac{2m_{\nu\mathrm{dm}}^4+2s^2+2st+t^2-4m_{\nu\mathrm{dm}}^2(s+t)}{\left(t-m_z^2\right)^2}$	$2g^4\,\frac{m_dm^2\,p_1^2\,(3-\mu)}{m_\mathrm{Z}^4}$	$\frac{155}{441}\,\frac{\pi\,g^4\,a\,n_{\nu\mathrm{dm}}}{m_z^4}\,T_\nu^2$	$\alpha_l=\frac{9}{10}$
vector DM vector mediator Z_μ	- - -	$48\,g^4\,\frac{m_{\nu\mathrm{dm}}^2p_1^2(1+\mu)}{m_\mathrm{Z}^4}$	$\frac{310}{49}\,\frac{\pi\,g^4\,a\,n_{\nu\mathrm{dm}}}{m_\mathrm{Z}^4}\,T_\nu^2$	$\alpha_l=\frac{3}{2}$

Table 3.1: Scenarios for dark matter-neutrino interactions and the corresponding matrix elements, scattering cross sections and angular coefficients.

where γdm refers to a dark matter species with photon interactions. Following the same steps as in the previous section, that is projecting the squared matrix element for the scattering process in the low energy limit onto Legendre polynomials, we can again obtain a modified Boltzmann hierarchy for the evolution of photon perturbations. Instead of classifying all possible interaction scenarios, we here adopt a different approach and consider a single baseline scenario, where the matrix element for dark matter photon scattering exhibits the same angular and polarisation dependence as Thomson scattering. This structure arises, for example, in the case of millicharged dark matter [293]. Still, our results are not limited to a specific choice of model, and we expect that the angular coefficients do not affect limits on the scattering rate significantly. Of course, the explicit verification of this assumption would be desirable for future projects.

The modified Boltzmann equations for photons are now given by

$$\delta'_\gamma = -\frac{4}{3}\theta_\gamma + 4\phi' \,, \tag{3.6.2a}$$

$$\theta'_\gamma = k^2\left(\frac{1}{4}\delta_\gamma - \sigma_\gamma\right) + k^2\psi + \kappa'_{\gamma\mathrm{b}}\left(\theta_\mathrm{b} - \theta_\gamma\right) + \kappa'_{\gamma\mathrm{dm}}\left(\theta_{\gamma\mathrm{dm}} - \theta_\gamma\right) \,, \tag{3.6.2b}$$

$$\begin{aligned}\sigma'_\gamma = {}& \frac{4}{15}\theta_\gamma - \frac{3}{10}\,kF_{\gamma,3} - \frac{9}{10}\left(\kappa'_{\gamma\mathrm{b}} + \kappa'_{\gamma\mathrm{dm}}\right)\sigma_\gamma \\ & + \frac{1}{20}\left(\kappa'_{\gamma\mathrm{b}} + \kappa'_{\gamma\mathrm{dm}}\right)\left(G_{\gamma,0} + G_{\gamma,2}\right) \,,\end{aligned} \tag{3.6.2c}$$

$$F'_{\gamma,l} = \frac{k}{2l+1}\left[l\,F_{\gamma,(l-1)} - (l+1)\,F_{\gamma,(l+1)}\right] - \left(\kappa'_{\gamma\mathrm{b}} + \kappa'_{\gamma\mathrm{dm}}\right)F_{\gamma,l} \,, \quad l \geq 3 \tag{3.6.2d}$$

$$G'_{\gamma,0} = -k\,G_{\gamma,1} - \frac{1}{2}\left(\kappa'_{\gamma\mathrm{b}} + \kappa'_{\gamma\mathrm{dm}}\right)\left(G_{\gamma,0} - F'_{\gamma,2} - G_{\gamma,2}\right) \,, \tag{3.6.2e}$$

$$G'_{\gamma,1} = \frac{k}{3}\left(G_{\gamma,0} - 2G_{\gamma,2}\right) - \left(\kappa'_{\gamma\mathrm{b}} + \kappa'_{\gamma\mathrm{dm}}\right)G_{\gamma,1} \,, \tag{3.6.2f}$$

$$\begin{aligned}G'_{\gamma 2} = {}& \frac{k}{5}\left(2G_{\gamma,1} - 3G_{\gamma,3}\right) + \frac{\kappa'_{\gamma\mathrm{b}} + \kappa'_{\gamma\mathrm{dm}}}{10}\left(F_{\gamma,2} + G_{\gamma,0} + G_{\gamma,2}\right) \\ & - \left(\kappa'_{\gamma\mathrm{b}} + \kappa'_{\gamma\mathrm{dm}}\right)G_{\gamma,2} \,,\end{aligned} \tag{3.6.2g}$$

$$G'_{\gamma,l} = \frac{k}{2l+1}\left(lG_{\gamma,(l-1)} - (l+1)\,G_{\gamma,(l+1)}\right) - \left(\kappa'_{\gamma\mathrm{b}} + \kappa'_{\gamma\mathrm{dm}}\right)G_{\gamma,l} \,, \quad l \geq 3\,. \tag{3.6.2h}$$

Scatterings with two different species, the baryons and dark matter, now affect the evolution of photon perturbations. The latter occurs at a rate of $\kappa'_{\gamma\mathrm{dm}}$, which is given by

$$\kappa'_{\gamma\mathrm{dm}} = a\,n_{\gamma\mathrm{dm}}\,\sigma_{\gamma\mathrm{dm}}\,. \tag{3.6.3}$$

Two possibilities are commonly considered for the energy dependence of the dark matter scattering cross section [285], namely $\sigma_{\gamma\mathrm{dm}} = \text{const.}$ and $\sigma_{\gamma\mathrm{dm}} \propto T_\gamma^{-2}$. For the highest multipoles, l_max, the truncation equations (3.4.37) remain valid, given that $\kappa'_{\gamma\mathrm{b}}$ is replaced by $\kappa'_{\gamma\mathrm{b}} + \kappa'_{\gamma\mathrm{dm}}$.

To constraint the dark matter interactions from cosmological data, the introduction of a dimensionless parameter, which is proportional to the scattering rate, again is beneficial. We define

$$u_{\gamma\mathrm{dm}} = \frac{\sigma_{\gamma\mathrm{dm}}}{\sigma_\mathrm{Th}}\left(\frac{m_{\gamma\mathrm{dm}}}{100\,\mathrm{GeV}}\right)^{-1} \,, \tag{3.6.4}$$

where $m_{\gamma\mathrm{dm}}$ is the mass of the dark matter particle. In analogy to the neutrino case, we further account for an energy dependent cross section as

$$u_{\gamma\mathrm{dm}} \equiv u_{\gamma\mathrm{dm},0}\, a^{-n_{\gamma\mathrm{dm}}} \,. \tag{3.6.5}$$

3.6.2 Dark matter evolution and dark matter sound speed

Scattering between dark matter and photons affects the evolution of dark matter perturbations, and in particular the dark matter velocity divergence is modified. The photon density contrast, on the other hand, is unaffected by the scattering terms and likewise does $\delta'_{\gamma\mathrm{dm}}$ keep its original form. From Eq. (3.3.7) and the result obtained on θ'_γ in Eq. (3.6.2) it follows that the dark matter perturbations obey

$$\delta'_{\gamma\mathrm{dm}} = -\theta_{\gamma\mathrm{dm}} + 3\phi' \,, \tag{3.6.6a}$$

$$\theta'_{\gamma\mathrm{dm}} = k^2\psi - \mathcal{H}\theta_{\gamma\mathrm{dm}} + c^2_{\gamma\mathrm{dm}}\, k^2\, \delta_{\gamma\mathrm{dm}} - R_{\gamma\mathrm{dm}}\, \kappa'_{\gamma\mathrm{dm}}\, (\theta_{\gamma\mathrm{dm}} - \theta_\gamma) \,. \tag{3.6.6b}$$

The momentum conserving factor in front of the scattering term is defined as

$$R_{\gamma\mathrm{dm}} = \frac{4\,\rho_\gamma}{3\,\rho_{\gamma\mathrm{dm}}} \,. \tag{3.6.7}$$

For the case of dark matter-photon scattering we do not restrict the analysis to the limit of large dark matter masses but explicitly allow for a non-vanishing dark matter sound speed

$$c^2_{\gamma\mathrm{dm}} = \frac{k_\mathrm{B}\, T_{\gamma\mathrm{dm}}}{m_{\gamma\mathrm{dm}}} \left[1 - \frac{1}{3}\frac{\partial \ln T_{\gamma\mathrm{dm}}}{\partial \ln a}\right] \,. \tag{3.6.8}$$

The derivation of the dark matter temperature works completely analogous to the baryon temperature, presented in Eq. (3.3.15) to (3.3.17), and we obtain

$$T'_{\gamma\mathrm{dm}} = -2\mathcal{H}\, T_{\gamma\mathrm{dm}} + \frac{8\,\rho_\gamma}{3\,\rho_{\gamma\mathrm{dm}}}\, \kappa'_{\gamma\mathrm{dm}}\, (T_\gamma - T_{\gamma\mathrm{dm}}) \,. \tag{3.6.9}$$

An important difference to the baryon case is, however, that the dark matter mass $m_{\gamma\mathrm{dm}}$ is a priori unknown and can vary over several orders of magnitude. If the dark matter mass is large enough, the sound speed becomes negligible and the evolution of perturbations depends on seven free parameters, only: the six baseline ΛCDM parameters and $u_{\gamma\mathrm{dm}}$. Below this limit, the dark matter mass has to be considered as an additional free parameter. We discuss the effect of the dark matter sound speed on cosmological perturbations in Sec. 5.1.3.

Chapter 4

Numerical considerations and approximation schemes

The evolution of cosmological perturbations in the linear regime is determined by an extensive set of coupled differential equations, the linearised Boltzmann and Einstein equations. While there exist approximative analytic solutions [132, 298], only numerical results achieve the precision required by present-day cosmological observations. Specific Boltzmann codes exist for this purpose, the two most widespread being CAMB [299] and CLASS [288]. In this thesis we exclusively use the latter.

To constrain a cosmological model from observations, several thousands or millions of spectra often need to be computed, each for a different set of parameters. In this context, the speed of Boltzmann codes is essential and addressed by several approximation schemes. In some cases, these schemes also cure numerical instabilities and further improve the codes' accuracy. However, the introduction of additional scattering terms requires a careful review of the simplifying assumptions.

In particular the line of sight integration and the tight coupling approximation receive modifications from dark matter-photon interactions. In the case of dark matter-neutrino scattering, the conditions under which the ultra-relativistic fluid approximation is applicable have to be reviewed. The latter scenario also causes changes in the initial conditions. In this section, we derive the required modifications.

4.1 Line of sight integration

In principle, it is possible to evolve the differential equations for the metric, baryon and dark matter perturbations alongside with the multipole hierarchies for photons and neutrinos numerically and to predict the CMB spectrum from these results. In practice, such an approach requires to solve a system of thousands of coupled equations. Furthermore, the multipoles oscillate rapidly, which demands a dense sampling over wavenumbers.

It is also possible to express the CMB anisotropies as time integral over the past light cone, where the integrand is the product of a source and a geometrical term [300, 301].

The geometrical term is rapidly oscillating but independent of the cosmological model, while the source term varies only slowly as a function of the wavelength. In addition, the latter only depends on the lowest-order multipoles. This formulation greatly reduces computational efforts.

The line of sight integration approach is exact in the sense that it can achieve arbitrary precision within the limits of linear perturbation theory [301]. Because the generalisation to scenarios with dark matter-photon interactions is straightforward, we directly treat this extended case. From our results, the ΛCDM equations can be recovered easily, by imposing $\kappa'_{\gamma\mathrm{dm}} = 0$.

4.1.1 Modified equations for dark matter-photon scattering

To match the notation of the original derivation of the line of sight integration [301], we define a rescaled version of the momentum-integrated phase space perturbations, $\Delta^T \equiv F_\gamma/4$ and $\Delta^P \equiv G_\gamma/4$, as well as the short hand notation $\Gamma \equiv F_{\gamma,2} + G_{\gamma,0} + G_{\gamma,2}$. Starting point for our derivation are the momentum-integrated Boltzmann equations (3.4.29), expressed in terms of these new variables

$$\Delta^{T\prime} + ik\,\mu\Delta^T = (\phi' - ik\,\mu\,\psi) + \left(\kappa'_{\gamma\mathrm{b}} + \kappa'_{\gamma\mathrm{dm}}\right)\left[-\Delta^T + {\Delta^T}_0 - \frac{1}{8}\,\Gamma\,P_2\left(\mu\right)\right] + \kappa'_{\gamma\mathrm{b}}\,\mu\,v_\mathrm{b} + \kappa'_{\gamma\mathrm{dm}}\,\mu\,v_{\gamma\mathrm{dm}}\,, \tag{4.1.1a}$$

$$\Delta^{P\prime} + ik\,\mu\Delta^P = \left(\kappa'_{\gamma\mathrm{b}} + \kappa'_{\gamma\mathrm{dm}}\right)\left[-\Delta^P + \frac{1}{8}\,\left(1 - P_2\left(\mu\right)\right)\Gamma\right]\,. \tag{4.1.1b}$$

In analogy to the baryon velocity (3.4.35), we here express the dark matter velocity divergence in terms of μ, the cosine of the angle between $\boldsymbol{k}$ and the photon's momentum direction $\hat{\boldsymbol{n}}$, and the dark matter velocity

$$\hat{\boldsymbol{n}}\cdot\boldsymbol{v}_{\gamma\mathrm{dm}} = -\frac{i\,\theta_{\gamma\mathrm{dm}}}{k}\,\mu = \mu\,v_{\gamma\mathrm{dm}}\,. \tag{4.1.2}$$

Equally, we have for the modulus of the baryon velocity $\hat{\boldsymbol{n}}\cdot\boldsymbol{v}_\mathrm{e} = \mu\,v_\mathrm{e}$.

To simplify the notation in the following, we define integrals over the Thomson and the dark matter scattering rates

$$\kappa_{\gamma\mathrm{b}} \equiv -\int_{\tau_0}^{\tau} d\tau'\,\kappa'_{\gamma\mathrm{b}}\left(\tau'\right) \quad \text{and} \quad \kappa_{\gamma\mathrm{dm}} \equiv -\int_{\tau_0}^{\tau} d\tau'\,\kappa'_{\gamma\mathrm{dm}}\left(\tau'\right)\,, \tag{4.1.3}$$

where $\tau_0 \geq \tau$ is the current conformal time. For either of these integrals, i.e. for $i = \gamma\mathrm{b}\,,\ \gamma\mathrm{dm}$, the following relation holds

$$\frac{d}{d\tau}\,e^{-\kappa_i} = e^{-\kappa_i}\,\frac{d}{d\tau}\,\left(\int_{\tau_0}^{\tau} d\tau'\kappa'_i\left(\tau'\right)\right) = \kappa'_i\,e^{-\kappa_i}\,. \tag{4.1.4}$$

First, we focus on the polarisation term Δ^P. By multiplying Eq. (4.1.1b) with $\exp\left(ik\mu - \kappa_{\gamma\mathrm{b}} - \kappa_{\gamma\mathrm{dm}}\right)$ and using the just derived relation (4.1.4) we obtain

$$\frac{\partial}{\partial\tau}\left(\Delta^P e^{ik\mu-\kappa_{\gamma\mathrm{b}}-\kappa_{\gamma\mathrm{dm}}}\right) = \Delta^{P\prime}\,e^{ik\mu-\kappa_{\gamma\mathrm{b}}-\kappa_{\gamma\mathrm{dm}}} + \Delta^P\left(ik\mu - \kappa_{\gamma\mathrm{b}} - \kappa_{\gamma\mathrm{dm}}\right)e^{ik\mu-\kappa_{\gamma\mathrm{b}}-\kappa_{\gamma\mathrm{dm}}}$$

$$= \frac{1}{8}\, e^{ik\mu - \kappa_{\gamma\mathrm{b}} - \kappa_{\gamma\mathrm{dm}}} \left(\kappa'_{\gamma\mathrm{b}} + \kappa'_{\gamma\mathrm{dm}}\right) \left[1 - P_2\left(\mu\right)\right] \Gamma\,. \tag{4.1.5}$$

By definition we have $\kappa_{\gamma\mathrm{b}}\left(\tau_0\right) = \kappa_{\gamma\mathrm{dm}}\left(\tau_0\right) = 0$. On the other hand, the smaller τ, the denser is the universe and correspondingly the scattering rate increases, hence $\kappa_{\gamma\mathrm{b}}\,,\ \kappa_{\gamma\mathrm{dm}} \to \infty$ for $\tau \to 0$. With this, integrating both sides of Eq. (4.1.5) over the past light cone, we obtain

$$\Delta^P\left(\tau_0\right) = \frac{3}{16} \int_0^{\tau_0} d\tau\, e^{i\,k\,\mu\,(\tau - \tau_0)}\, g(\tau)\, \left(1 - \mu^2\right) \Gamma\,, \tag{4.1.6}$$

where we wrote the second Legendre polynomial in its explicit form (3.4.19) and defined the combined visibility function as

$$g\left(\tau\right) \equiv \left(\kappa'_{\gamma\mathrm{b}} + \kappa'_{\gamma\mathrm{dm}}\right)\, e^{-\kappa_{\gamma\mathrm{b}} - \kappa_{\gamma\mathrm{dm}}}\,. \tag{4.1.7}$$

Finally, to absorb the wavenumber dependence fully in the exponential function, we express μ as derivative of $e^{i\,k\,\mu\,\tau}$ with respect to τ and perform an integration by parts,

$$\Delta^P\left(\tau_0\right) = \frac{3}{16} \int_0^{\tau_0} d\tau\, e^{ik\mu(\tau - \tau_0)}\, \left[g\,\Gamma + \frac{1}{k^2}\frac{d^2}{d\tau^2}\left(g\,\Gamma\right)\right]\,. \tag{4.1.8}$$

In principle, this procedure produces two boundary terms, namely

$$\left[\frac{e^{i\,k\,\mu(\tau - \tau_0)}}{i\,k\,\mu}\,\mu^2 g\,\Gamma\right]_0^{\tau_0} \quad \text{and} \quad \left[-\frac{e^{i\,k\,\mu(\tau - \tau_0)}}{\left(ik\mu\right)^2}\frac{d}{d\tau}\,\left(\mu^2 g\,\Gamma\right)\right]_0^{\tau_0}\,. \tag{4.1.9}$$

However, at $\tau = 0$ the visibility function is zero and the corresponding boundary terms vanish, while the terms at τ_0 only affect the monopole and hence are not observable [301].

The intensity term Δ^T can be manipulated in a very similar manner. We first multiply Eq. (4.1.1a) with $\exp\left(ik\mu - \kappa_{\gamma\mathrm{b}} - \kappa_{\gamma\mathrm{dm}}\right)$ and take the derivative with respect to conformal time to obtain the relation

$$\begin{aligned}
&\frac{\partial}{\partial\tau}\left(e^{i\,k\,\mu\,\tau - \kappa_{\gamma\mathrm{b}} - \kappa_{\gamma\mathrm{dm}}}\Delta^T\right) = e^{i\,k\,\mu\,\tau - \kappa_{\gamma\mathrm{b}} - \kappa_{\gamma\mathrm{dm}}}\left[{\Delta^T}' + \left(ik\,\mu + \kappa'_{\gamma\mathrm{b}} + \kappa'_{\gamma\mathrm{dm}}\right)\Delta^T\right] \\
&= e^{ik\,\mu\,\tau - \kappa_{\gamma\mathrm{b}} - \kappa_{\gamma\mathrm{dm}}}\left[\phi' - ik\,\mu\,\psi + \left(\kappa'_{\gamma\mathrm{b}} + \kappa'_{\gamma\mathrm{dm}}\right)\left({\Delta^T}_0 - \frac{1}{8}\,P_2\left(\mu\right)\,\Gamma\right) + \kappa'_{\gamma\mathrm{b}}\,\mu\,v_{\mathrm{b}} + \kappa'_{\gamma\mathrm{dm}}\,\mu\,v_{\gamma\mathrm{dm}}\right]\,.
\end{aligned} \tag{4.1.10}$$

In case of the intensity distribution, the integration over the past light cone, followed by an integration by parts to completely absorb the μ-dependence in the exponential function, yields

$$\begin{aligned}
\Delta^T\left(\tau_0\right) &= \int_0^{\tau_0} d\tau\, e^{ik\,\mu(\tau - \tau_0)}\left[e^{-\kappa_{\gamma\mathrm{b}} - \kappa_{\gamma\mathrm{dm}}}\phi' - \mu\, e^{-\kappa_{\gamma\mathrm{b}} - \kappa_{\gamma\mathrm{dm}}}\left(i\,k\,\psi - \kappa'_{\gamma\mathrm{b}} v_{\mathrm{b}} - \kappa'_{\gamma\mathrm{dm}} v_{\gamma\mathrm{dm}}\right)\right. \\
&\qquad \left. - \frac{3}{16}\,g\,\mu^2\,\Gamma + g\,\left({\Delta^T}_0 + \frac{1}{16}\,\Gamma\right)\right] \\
&= \int_0^{\tau_0} d\tau\, e^{ik\mu(\tau - \tau_0)}\left\{e^{-\kappa_{\gamma\mathrm{b}} - \kappa_{\gamma\mathrm{dm}}}\,\phi' + \frac{g}{4}\,\left(\delta_\gamma + \frac{1}{4}\,\Gamma\right) + \frac{d}{d\tau}\,\left[e^{-\kappa_{\gamma\mathrm{b}} - \kappa_{\gamma\mathrm{dm}}}\,\psi\right]\right. \\
&\qquad - \frac{e^{-\kappa_{\gamma\mathrm{b}} - \kappa_{\gamma\mathrm{dm}}}}{ik}\left(\kappa''_{\gamma\mathrm{b}} v_{\mathrm{b}} + \kappa'_{\gamma\mathrm{b}}\left(\kappa'_{\gamma\mathrm{b}} + \kappa'_{\gamma\mathrm{dm}}\right) v_{\mathrm{b}} + \kappa'_{\gamma\mathrm{b}}\, v'_{\mathrm{b}} + \kappa''_{\gamma\mathrm{dm}} v_{\gamma\mathrm{dm}}\right. \\
&\qquad \left.\left. + \kappa'_{\gamma\mathrm{dm}}(\kappa'_{\gamma\mathrm{b}} + \kappa'_{\gamma\mathrm{dm}}) v_{\gamma\mathrm{dm}} + \kappa_{\gamma\mathrm{dm}} v'_{\gamma\mathrm{dm}}\right) + \frac{3}{16\,k^2}\,\frac{d}{d\tau}\,\left(g'\,\Gamma + g\,\Gamma'\right)\right\}\,.
\end{aligned} \tag{4.1.11}$$

As advanced in the introduction, with these manipulations we have expressed the temperature and the polarisation phase space distributions as integrals along the past light cone, and the integrand is the product of a geometrical term and a cosmological source term. To make the latter decomposition explicit, we write

$$\Delta^{T/P}(k,\mu,\tau_0) = \int_0^{\tau_0} d\tau e^{ik\,\mu\,(\tau-\tau_0)}\, S^{T/P}(k,\tau)\ . \tag{4.1.12}$$

By comparison with Eq. (4.1.8) and Eq. (4.1.11), the source functions are given by

$$S^T(k,\tau) = e^{-\kappa_{\gamma\mathrm{b}}-\kappa_{\gamma\mathrm{dm}}}\,\phi' + \frac{g}{4}\left(\delta_\gamma + \frac{1}{4}\,\Gamma\right) + \frac{e^{-\kappa_{\gamma\mathrm{b}}-\kappa_{\gamma\mathrm{dm}}}}{k^2}\left\{\left[\kappa''_{\gamma\mathrm{b}} + \kappa'_{\gamma\mathrm{b}}\left(\kappa'_{\gamma\mathrm{b}} + \kappa_{\gamma\mathrm{dm}}\right)\right]\theta_\mathrm{b} + \kappa'_{\gamma\mathrm{b}}\theta'_\mathrm{b}\right.$$
$$\left. + \left[\kappa''_{\gamma\mathrm{dm}} + \kappa'_{\gamma\mathrm{dm}}\left(\kappa'_{\gamma\mathrm{dm}} + \kappa'_{\gamma\mathrm{b}}\right)\right]\theta_{\gamma\mathrm{dm}} + \kappa'_{\gamma\mathrm{b}}\theta'_{\gamma\mathrm{dm}}\right\} + \frac{d}{d\tau}\left[e^{-\kappa_{\gamma\mathrm{b}}-\kappa_{\gamma\mathrm{dm}}}\psi + \frac{3}{16k^2}\left(g'\,\Gamma + g\,\Gamma'\right)\right]\ , \tag{4.1.13a}$$

$$S^P(k,\tau) = \frac{3}{16}\left[g\,\Gamma + \frac{1}{k^2}\,\frac{d^2}{d\tau^2}\left(g\,\Gamma\right)\right] \tag{4.1.13b}$$

As expected, if $\kappa'_{\gamma\mathrm{b}}$ is set to zero our results reduces to Eq. (12) of Ref. [301] and we have also verified that it agrees with the results from Ref. [6].

To obtain present-day multipole moment, we expand the plane wave in the integral of Eq. (4.1.12) in terms of its radial and angular eigenfunctions. These are spherical Bessel functions j_l and Legendre polynomials P_l, respectively,

$$e^{i\,k\,\mu} = \sum_{l=0}^{\infty}\,(2l+1)\;i^l\,j_l\,(k)\;P_l\,(\mu)\ . \tag{4.1.14}$$

Taking the ensemble average over the angular component μ, we obtain [301]

$$\Delta_l^{T,P}(k) = \int_0^{\tau_0} d\tau\, S^{T,P}(k,\tau)\;j_l\left[k\,(\tau_0-\tau)\right]\ . \tag{4.1.15}$$

Just as Δ^T and Δ^P are directly proportional to the momentum-integrated phase space distributions G_γ and G_γ, ${\Delta^T}_l$ and ${\Delta^P}_l$ are a rescaled version of the multipole expansions $F_{\gamma,l}$ and $G_{\gamma,l}$.

4.1.2 Numerical implementation

To obtain CMB spectra with the line of sight approach, one has to sample the source term over time and wavenumber and then numerically perform the integral over the past light cone (4.1.15). The original Boltzmann hierarchy (3.4.36) is well suited to obtain $S^{T,P}$ as a function of conformal time. However, because the source term only requires knowledge about the lowest-order multipoles, $l \leq 4$, the hierarchy can be truncated at much smaller l_{max}, than if the anisotropies were computed using brute force. Within the CLASS code [288], the temperature source function is split into three pieces, which are stored individually [302]. In the past, this split generated some confusion about the correct way to include the additional terms caused by dark matter-photon scattering. We therefore think it is useful to explicitly give the expressions we implemented.

In the absence of dark matter-photon scattering, the three source functions in CLASS are defined as

$$S_0^T\big|_{\kappa'_{\gamma\mathrm{dm}}=0} \equiv g\,\left(\frac{\delta_\gamma}{4}+\phi\right) 2e^{-\kappa_{\gamma\mathrm{b}}}\,\phi' + k^{-2}\,\left(g\,\theta'_\mathrm{b} + g'\,\theta_\mathrm{b}\right)\,, \tag{4.1.16a}$$

$$S_1^T\big|_{\kappa'_{\gamma\mathrm{dm}}=0} \equiv e^{-\kappa_{\gamma\mathrm{b}}}\,k\,\left(\psi-\phi\right)\,, \tag{4.1.16b}$$

$$S_2^T\big|_{\kappa'_{\gamma\mathrm{dm}}=0} \equiv g\,\Gamma/8\,. \tag{4.1.16c}$$

These source functions combine to the full expression according to

$$\begin{aligned} S_T\big|_{\kappa'_{\gamma\mathrm{dm}}=0} &= e^{-\kappa_{\gamma\mathrm{b}}} + \frac{g}{4}\,\left(\delta_\gamma+\frac{1}{4}\,\Gamma\right) + \frac{d}{d\tau}\,\left[e^{-\kappa_{\gamma\mathrm{b}}}\psi\right] + k^{-2}\,g\,\theta_\mathrm{b} + \frac{3}{16\,k^2}\,\frac{d^2}{d\tau^2}\,\left(g\,\Gamma\right) \\ &= S_T^0\big|_{\kappa'_{\gamma\mathrm{dm}}=0} + \frac{1}{k}\frac{d}{d\tau}\,S_T^1\big|_{\kappa'_{\gamma\mathrm{dm}}=0} + \frac{1}{2}\,\left(\frac{3}{k^2}\frac{d^2}{d\tau^2}\,S_T^2\big|_{\kappa'_{\gamma\mathrm{dm}}=0} + S_T^2\big|_{\kappa'_{\gamma\mathrm{dm}}=0}\right)\,. \end{aligned} \tag{4.1.17}$$

We require that the same combination of individual components should produce Eq. (4.1.13a), in the case where the dark matter-photon scattering term included, and obtain

$$\begin{aligned} S_0^T = {}& g\,\left(\frac{\delta_\gamma}{4}+\phi\right) + 2e^{-\kappa_{\gamma\mathrm{b}}-\kappa_{\gamma\mathrm{dm}}}\,\phi' + \frac{1}{k^2}\,\Big[g\,\left(\kappa'_{\gamma\mathrm{b}}\theta_\mathrm{b} + \kappa'_{\gamma\mathrm{dm}}\theta_{\gamma\mathrm{dm}}\right) \\ & + e^{-\kappa_{\gamma\mathrm{b}}-\kappa_{\gamma\mathrm{dm}}}\,\left(\kappa''_{\gamma\mathrm{b}}\theta_\mathrm{b} + \kappa''_{\gamma\mathrm{dm}}\theta_{\gamma\mathrm{dm}}\right) + e^{-\kappa_{\gamma\mathrm{b}}-\kappa_{\gamma\mathrm{dm}}}\,\left(\kappa'_{\gamma\mathrm{b}}\,\theta'_\mathrm{b} + \kappa'_{\gamma\mathrm{dm}}\theta'_{\gamma\mathrm{dm}}\right)\Big] \end{aligned} \tag{4.1.18a}$$

$$S_T^1 = e^{-\kappa_{\gamma\mathrm{b}}-\kappa_{\gamma\mathrm{dm}}}\,k\,\left(\psi-\phi\right)\,, \tag{4.1.18b}$$

$$S_T^2 = g\,\Gamma/8\,. \tag{4.1.18c}$$

For the polarisation multipoles the situation is simpler. Dark matter-photon scattering enters the polarisation source function (4.1.13b) only indirectly, through the definition of the visibility function, g. Hence, once these modifications are accounted for, no explicit changes to the computation of the source function are required.

4.2 Tight coupling approximation

At early times, baryon and possibly also dark matter scattering significantly affects the photon evolution. Well before recombination, the Thomson scattering rate (3.3.11) evolves as $\kappa'_{\gamma\mathrm{b}} \propto a^{-3}$ but drops rapidly when free electrons and protons combine to neutral hydrogen, see Fig. 4.1. On the other hand, the dark matter-photon scattering rate (3.6.3) evolves as a power law of temperature at all epochs, that is $\kappa'_{\gamma\mathrm{dm}} \propto a^{-n_{\gamma\mathrm{dm}}-3}$.

In particular at early times, the respective scattering rates are large and lead to a very stiff system of equations, which is difficult to integrate numerically. The rapid scattering also suppresses the higher order photon multipoles. In this regime, it is possible to remove the scattering terms from the evolution of the velocity divergence and to expand all higher order multipoles in inverse powers of the scatting rate [232]. This approach is called the tight coupling approximation and allows to significantly reduce computational efforts [288].

We restrict this discussion to the case where $\sigma_{\gamma\mathrm{dm}}$ is constant, i.e. $n_{\gamma\mathrm{dm}} = 0$. In this case,

for viable interaction cross section, the photon scattering rate with dark matter is much smaller than the Thomson scattering rate, $\kappa_{\gamma\mathrm{dm}} \ll \kappa'_{\gamma\mathrm{b}}$, and no specific dark matter tight coupling approximation needs to be devised. Still, the presence of dark matter-photon scattering affects the conventional tight coupling approximation in the photon-baryon sector and needs to be taken into account carefully.

The photon-baryon tight coupling approximation in the presence of dark matter-photon scattering was derived in Ref. [6] and e.g. employed in Refs. [201, 202, 285, 303]. Yet, our final result differs from this expression. We therefore proceed in two steps and first obtain the baryon-photon tight coupling approximation disregarding the dark matter-photon scattering terms. This derivation was presented in [288] for synchronous gauge. By reproducing the steps in Newtonian gauge and comparing our final expressions to those implemented in CLASS, we can affirm the correctness of our procedure. We then repeat the derivation but in the presence of the dark matter-photon scattering term.

4.2.1 Baryon-photon tight coupling approximation

The large magnitude of $\kappa'_{\gamma\mathrm{b}}$ at early times handicaps the numerical integration of the Boltzmann hierarchy, and the first step in the derivation of the tight coupling approximation is to obtain equations for the photon and baryon velocity divergence where this rate does not appear explicitly. To this end we combine Eq. (3.4.36b) and Eq. (3.3.12) to

$$\theta'_{\mathrm{b}} + R_{\gamma\mathrm{b}}\,\theta'_{\gamma} = (1+R)\;k^2\psi + R_{\gamma\mathrm{b}}\,k^2\left(\frac{\delta_{\gamma}}{4} - \sigma_{\gamma}\right) - \mathcal{H}\theta_{\mathrm{b}} + c_{\mathrm{b}}^2\,k^2\,\delta_{\mathrm{b}}\,. \tag{4.2.1}$$

The photon-baryon slip $\Theta'_{\gamma\mathrm{b}}$ is defined as the time derivative of the difference between the photon's and the baryon's velocity divergence, i.e.

$$\Theta_{\gamma\mathrm{b}} \equiv \theta_{\gamma} - \theta_{\mathrm{b}}\,. \tag{4.2.2}$$

Subtracting $R_{\gamma\mathrm{b}}\Theta_{\gamma\mathrm{b}}$ from the previous equation yields an expression for the baryon velocity divergence, from which indeed any explicit appearance of $\kappa'_{\gamma\mathrm{b}}$ has been removed. Further, inserting this new form for θ'_{b} back into Eq. (4.2.1) the same can be achieved for the photon velocity term. The new equations read

$$\theta'_{\mathrm{b}} = -\,(1+R_{\gamma\mathrm{b}})^{-1}\left[\mathcal{H}\theta_{\mathrm{b}} - c_{\mathrm{b}}^2\,k^2\,\delta_{\mathrm{b}} - k^2\,R_{\gamma\mathrm{b}}\left(\frac{\delta_{\gamma}}{4} - \sigma_{\gamma}\right) + R_{\gamma\mathrm{b}}\Theta_{\gamma\mathrm{b}}\right] + k^2\,\psi\,, \tag{4.2.3a}$$

$$\theta'_{\gamma} = -R_{\gamma\mathrm{b}}^{-1}\left[\theta'_{\mathrm{b}} + \mathcal{H}\,\theta_{\mathrm{b}} - c_{\mathrm{b}}^2\,k^2\,\delta_{\mathrm{b}}\right] + k^2\left(\frac{\delta_{\gamma}}{4} - \sigma_{\gamma}\right) + \frac{1+R_{\gamma\mathrm{b}}}{R_{\gamma\mathrm{b}}}\,k^2\,\psi\,. \tag{4.2.3b}$$

At first sight, rewriting the velocity divergences in the form of Eq. (4.2.3) just seems to shift the problem. However, when Thomson scattering occurs at a rapid rate, the photon-baryon slip and the photon shear are small and can be expanded in inverse powers of the Thomson scattering rate,

$$\kappa'^{-1}_{\gamma\mathrm{b}} \equiv \tau_{\mathrm{c}}\,. \tag{4.2.4}$$

In fact, the opacity due to Thomson scattering τ_c is a dimensional quantity. In treating it as a small parameter, we assume that the opacity is much smaller than all other time and length scales, which affect the evolution of photon perturbations, i.e.

$$\tau_c \mathcal{H} \gg 1 \quad \text{and} \quad \tau_c k \gg 1 . \tag{4.2.5}$$

We first focus on $\Theta_{\gamma b}$ for which we obtain from Eq. (3.4.36b) and Eq. (3.3.12)

$$\tau_c \left[\Theta'_{\gamma b} - \mathcal{H} \theta_b + k^2 \left(-\frac{\delta_\gamma}{4} + \sigma_\gamma + c_b^2 \delta_b \right) \right] + (1 + R_{\gamma b}) \Theta_{\gamma b} = 0 . \tag{4.2.6}$$

Schematically, we can write this equation as

$$\epsilon y' (\tau) + y (\tau) / f (\tau) + \epsilon g (\tau) = 0 , \tag{4.2.7}$$

where ϵ is a small parameter, and $f(\tau)$ and $g(\tau)$ are known functions that vary smoothly on scales of ϵ. We obtain a partial solution to Eq. (4.2.7) from a sum series ansatz,

$$y (\tau) = \sum_{n=1} \epsilon^n y_n (\tau) , \quad y_1 (\tau) = -f (\tau) \, g (\tau) , , \quad y_2 (\tau) = -y'_1 (\tau) \, f (\tau) . \tag{4.2.8}$$

The most general solution is given by the sum of the partial solution and $y_h(\tau)$, the solution to the homogeneous equation. For $g(\tau) = 0$ Eq. (4.2.7) is solved by

$$y_h (\tau) = C \, \exp \left(-\frac{1}{\epsilon} \int d\tau' f^{-1} (\tau') \right) . \tag{4.2.9}$$

In the physical scenario, $f(\tau)$ is always positive, see Eq. (4.2.12b), and the homogeneous solution gets exponentially suppressed. Thus, up to second order in the small parameter ϵ, Eq. (4.2.7) is solved by

$$y = -\epsilon \, f \, g + \epsilon^2 \, f \, \left(f' \, g + \, f \, g' \right) . \tag{4.2.10}$$

Before making the connection between $\Theta_{\gamma b}$ and the schematic equation (4.2.7), we have to recognise a subtlety. The expansion parameter ϵ is constant in time while $\tau'_c \neq 0$. To overcome this obstacle, we introduce $\bar{\tau}_c$, the opacity at some arbitrary time around which the expansion is performed. Multiplying Eq.(4.2.6) by $\bar{\tau}_c / \tau_c$ gives

$$\begin{aligned} 0 &= \bar{\tau}_c \Theta'_{\gamma b} + \bar{\tau}_c \left[-\mathcal{H} \theta_b + k^2 \left(c_b^2 \delta_b - \frac{\delta_\gamma}{4} + \sigma_\gamma \right) \right] + \frac{\bar{\tau}_c}{\tau_c} (1 + R_{\gamma b}) \Theta_{\gamma b} \\ &= \bar{\tau}_c \Theta'_{\gamma b} + \bar{\tau}_c g_\Theta (\tau) + \Theta_{\gamma b} / \bar{f}_\Theta (\tau) , \end{aligned} \tag{4.2.11}$$

from which we can identify the functions f and g in the schematic solution as

$$g_\Theta = -\mathcal{H} \theta_b + k^2 \left(c_b^2 \delta_b - \frac{\delta_\gamma}{4} + \sigma_\gamma \right) , \tag{4.2.12a}$$

$$\bar{f}_\Theta = \frac{\tau_c}{\bar{\tau}_c} \frac{1}{1 + R_{\gamma b}} = \frac{\tau_c}{\bar{\tau}_c} f_\Theta . \tag{4.2.12b}$$

Thus, the photon and the baryon velocity divergence differ by

$$\Theta_{\gamma\mathrm{b}} = -\tilde{f}_\Theta\, g_\Theta + \tilde{f}_\Theta \left(\tilde{f}'_\Theta\, g_\Theta + \tilde{f}_\Theta\, g_\Theta\right) + \mathcal{O}\left(\tau_\mathrm{c}^3\right) , \tag{4.2.13}$$

where we have defined

$$\tilde{f}_\Theta \equiv \frac{\tau_\mathrm{c}}{1 + R_{\gamma\mathrm{b}}} . \tag{4.2.14}$$

The evolution of the baryon and the photon velocity divergence (4.2.3) depends on the first derivative of $\Theta_{\gamma\mathrm{b}}$, which can be written as

$$\Theta'_{\gamma\mathrm{b}} = \left(\frac{\tilde{f}'_\Theta}{\tilde{f}_\Theta}\right) \Theta_{\gamma b} + \tilde{f}_\Theta \left(-g'_\Theta + \tilde{f}''_\Theta\, g_\Theta + 2\tilde{f}'_\Theta\, g'_\Theta + \tilde{f}_\Theta\, g''_\Theta\right) + \mathcal{O}\left(\tau_\mathrm{c}^3\right) .$$

The derivative of $\tilde{f}_\Theta$ with respect to conformal time is straightforward to compute and contains terms proportional to τ'_c and f'_Θ. In the implementation, the former is provided by the numerical modelling of recombination. The latter follows from the relations $R_{\gamma\mathrm{b}} \propto a^{-1}$ and $R'_{\gamma\mathrm{b}} = -\mathcal{H}\, R_{\gamma\mathrm{b}}$ and hence is

$$f'_\Theta = \frac{\mathcal{H}\, R_{\gamma\mathrm{b}}}{\left(1 + R_{\gamma\mathrm{b}}\right)^2} . \tag{4.2.15}$$

As in Ref. [288], we write the derivative of g_Θ as

$$\begin{aligned}
g'_\Theta &= -\mathcal{H}'\,\theta_\mathrm{b} - \mathcal{H}\,\theta'_\mathrm{b} + k^2 \left(\left(c_\mathrm{b}^2\right)'\delta_\mathrm{b} + c_\mathrm{b}^2\,\delta'_\mathrm{b} - \frac{\delta'_\gamma}{4} + \sigma'_\gamma\right) \\
&= 2\mathcal{H}\Theta'_{\gamma\mathrm{b}} - \frac{a''}{a}\theta_\mathrm{b} + k^2 \left[\bar{c_\mathrm{b}^2}\,\delta_\mathrm{b} + c_\mathrm{b}^2\delta'_\mathrm{b} - \frac{\delta'_\gamma}{4} + \sigma'_\gamma - \mathcal{H}\,\psi\right] + \mathcal{H}\,\theta'_\mathrm{b} + \mathcal{H}^2\,\theta_\mathrm{b} \\
&- k^2\,\mathcal{H} c_\mathrm{b}^2\,\delta_\mathrm{b} + k^2\,\mathcal{H}\,\psi - 2\mathcal{H}\,\theta'_\gamma \\
&= 2\mathcal{H}\Theta'_{\gamma\mathrm{b}} - \frac{a''}{a}\theta_\mathrm{b} + k^2 \left[\bar{c_\mathrm{b}^2}\,\delta_\mathrm{b} + c_\mathrm{b}^2\delta'_\mathrm{b} - \frac{\delta'_\gamma}{4} + \sigma'_\gamma - \mathcal{H}\,\psi - \frac{\mathcal{H}}{2}\,\delta_\gamma + 2\mathcal{H}\,\sigma_\gamma\right] \\
&+ \frac{\mathcal{H}\,\left(R_{\gamma\mathrm{b}} + 2\right)}{\tau_\mathrm{c}}\,\Theta_{\gamma\mathrm{b}} .
\end{aligned} \tag{4.2.16}$$

A number of relations are necessary to obtain this expression for g'_Θ. Firstly, we defined

$$\bar{c_\mathrm{b}^2} \equiv \left(\mathcal{H}\, c_\mathrm{b}^2 + \left(c_\mathrm{b}^2\right)'\right) . \tag{4.2.17}$$

This quantity is zero while $c_\mathrm{b}^2 \propto a^{-1}$, i.e. while Thomson scattering is rapid and the baryon temperature in Eq. (3.3.14) tracks the photon temperature closely. Further we used that $\mathcal{H}' + \mathcal{H}^2 = a''/a$ and that $-2\mathcal{H}\,\theta'_\mathrm{b} = 2\mathcal{H}\left(\Theta'_{\gamma\mathrm{b}} - \theta'_\gamma\right)$. Finally from Eq. (3.4.36b) and Eq. (3.3.12) obtain

$$\frac{R_{\gamma\mathrm{b}}}{\tau_\mathrm{c}}\,\Theta_{\gamma\mathrm{b}} = \theta'_\mathrm{b} + \mathcal{H}\,\theta_\mathrm{b} - k^2\psi - k^2\, c_\mathrm{b}^2\,\delta_\mathrm{b} , \tag{4.2.18}$$

$$\theta'_\gamma = k^2\,\psi + k^2 \left(\frac{\delta_\gamma}{4} - \sigma_\mathrm{b}\gamma\right) - \frac{\Theta_{\gamma\mathrm{b}}}{\tau_\mathrm{c}} . \tag{4.2.19}$$

Now, at first order in τ_c, the photon-baryon slip is

$$\begin{aligned}\Theta'_{\gamma\mathrm{b}} &= \left(\frac{\tau'_\mathrm{c}}{\tau_\mathrm{c}} + \frac{f'_\Theta}{f_\Theta}\right)\Theta_{\gamma\mathrm{b}} - \tau_\mathrm{c}\, f_\Theta\, g'_\Theta + \mathcal{O}(\tau^2) \\ &= \left(\frac{\tau'}{\tau_\mathrm{c}} - \frac{2\mathcal{H}}{1+R_{\gamma\mathrm{b}}}\right)\Theta_{\gamma\mathrm{b}} - \frac{\tau_\mathrm{c}}{1+R_{\gamma\mathrm{b}}}\left[-\frac{a''}{a}\theta_\mathrm{b}\right. \\ &\left. + k^2\left(-\mathcal{H}\psi - \frac{\mathcal{H}\,\delta_\gamma}{2} + \bar{c}_\mathrm{b}^2\delta_\mathrm{b} + c_\mathrm{b}^2\delta'_\mathrm{b} - \frac{\delta'_\gamma}{4}\right)\right] + \mathcal{O}\left(\tau_\mathrm{c}^2\right). \end{aligned} \tag{4.2.20}$$

In this result we neglected the $\Theta'_{\gamma\mathrm{b}}$ and the σ_γ term in g'_Θ. Both are first order in τ_c by themselves and multiplied by an additional factor of τ_c, therefore they do not contribute to the first order result.

While $\Theta_{\gamma\mathrm{b}} \sim \mathcal{O}(\tau_\mathrm{c})$ follows directly from the expansion in Eq. (4.2.13), $\sigma_\gamma \sim \mathcal{O}(\tau_\mathrm{c})$ is not as obvious. To see that the photon shear indeed contributes at first order in τ_c, we rewrite Eq. (3.4.36c) as

$$\sigma_\gamma - \frac{1}{18}\left(G_{\gamma,0} + G_{\gamma,2}\right) = \frac{\tau_\mathrm{c}}{9}\left[\frac{8}{3}\,\theta_\gamma + 3k^2\,F_{\gamma,3} - 10\sigma'_\gamma\right]. \tag{4.2.21}$$

In combination with the equations for the zeroth and the first polarisation multipole (Eq. (3.4.36e) and Eq. (3.4.36e)) this is consistent with $G_{\gamma,0} \sim G_{\gamma,2} \sim \sigma_\gamma$ at first order in τ_c. For the first polarisation multipole, Eq. (3.4.36f) gives

$$G_{\gamma,1} = \tau_\mathrm{c}\left[-G'_{\gamma,1} + \frac{k}{3}\left(G_{\gamma,0} - 2G_{\gamma,2}\right)\right], \tag{4.2.22}$$

from which we conclude that it only contributes at $G_{\gamma,1} \sim \mathcal{O}\left(\tau_\mathrm{c}^2\right)$. Finally, from Eq. (3.4.36d) and Eq. (3.4.36h), the leading order behaviour for multipoles at $l \geq 3$ is

$$F_{\gamma,l} = \frac{l\,k\,\tau_\mathrm{c}}{2l+1}\,F_{\gamma,(l-1)} \quad \text{and} \quad G_{\gamma,l} = \frac{l\,k\,\tau_\mathrm{c}}{2l+1}\,G_{\gamma,(l-1)}\,. \tag{4.2.23}$$

The $l = 3$ multipoles only contribute at $\mathcal{O}\left(\tau_\mathrm{c}^2\right)$, and with increasing multipole moment the terms become more and more suppressed.

For the second-order solution in the tightly coupled limit, we require a first order expression for σ_γ, in order to evaluate g'_Θ, as well as second order expressions to σ_γ, $G_{\gamma,0}$ and $G_{\gamma,2}$. The latter set the initial conditions for the integration of the Boltzmann hierarchy, when the tight coupling approximation is switched off. From Eq. (3.4.36e) and Eq. (3.4.36g) we obtain that

$$G_{\gamma,0} = -2\tau_\mathrm{c}\,G'_{\gamma,0} + 2\sigma_\gamma + G_{\gamma,2} + \mathcal{O}\left(\tau_\mathrm{c}^3\right), \tag{4.2.24a}$$

$$G_{\gamma,2} = \frac{10\,\tau_\mathrm{c}}{9}\left(\frac{2k}{5}G_{\gamma,1} - G'_{\gamma,2}\right) + \frac{2}{9}\,\sigma_\gamma + \frac{1}{9}\,G_{\gamma,0} + \mathcal{O}\left(\tau^3\right), \tag{4.2.24b}$$

Inserting the second into the first expression, we obtain $G_{\gamma,0}$, which we use in turn to determine $G_{\gamma,2}$

$$G_{\gamma,0} = \frac{5}{2}\,\sigma_\gamma - \frac{25}{4}\,\tau_\mathrm{c}\,\sigma'_\gamma + \mathcal{O}\left(\tau_\mathrm{c}^3\right), \tag{4.2.25a}$$

$$G_{\gamma,2} = \frac{1}{2}\,\sigma_\gamma - \frac{5}{3}\,\tau_\mathrm{c}\sigma'_\gamma + \mathcal{O}\left(\tau_\mathrm{c}^3\right) . \tag{4.2.25b}$$

With these results, Eq. (3.4.36c) for the evolution of the photon shear becomes

$$\sigma'_\gamma = \frac{16}{45}\left(\tau_\mathrm{c}\,\theta'_\gamma + \tau'_\mathrm{c}\,\theta_\gamma\right) , \tag{4.2.26}$$

and the final first and second order results for the photon shear are

$$\begin{aligned}\sigma_\gamma &= \frac{16}{45}\,\tau_\mathrm{c}\,\theta_\gamma + \mathcal{O}\left(\tau_\mathrm{c}^2\right) \\ &= \frac{8\,\tau_\mathrm{c}}{45}\left[2\,\theta_\gamma\left(1 - \frac{11}{6}\,\tau'_\mathrm{c}\right) - 2\,\theta'_\gamma\left(\frac{11}{6}\,\tau_\mathrm{c}\right)\right] + \mathcal{O}\left(\tau_\mathrm{c}^3\right) .\end{aligned} \tag{4.2.27}$$

Finally, all ingredients are in place to compute the second order results for the photon-baryon slip according to Eq. (4.2.15)

$$\begin{aligned}\Theta'_{\gamma\mathrm{b}} = \left(1 - 2\mathcal{H}\,\tilde{f}_\Theta\right)\left\{\left(\frac{\tau'_\mathrm{c}}{\tau_\mathrm{c}} - \frac{2\mathcal{H}}{1+R_{\gamma\mathrm{b}}}\right)\Theta_{\gamma\mathrm{b}} - \tilde{f}_\Theta\left[-\frac{a''}{a}\,\theta_\mathrm{b} + k^2\left(\bar{c_\mathrm{b}^2}\,\delta_\mathrm{b} c_\mathrm{b}^2\,\delta'_\mathrm{b} - \frac{\delta'_\gamma}{4} - \mathcal{H}\,\psi - \frac{\mathcal{H}\,\delta_\gamma}{2}\right)\right]\right\} \\ - k^2\,\tilde{f}_\Theta\left(\sigma'_\gamma + 2\mathcal{H}\,\sigma_\gamma\right) + \tilde{f}_\Theta\left(\tilde{f}''_\Theta\,g_\Theta + 2\tilde{f}'_\Theta\,g'_\Theta + \tilde{f}_\Theta\,g''_\Theta\right) + \mathcal{O}\left(\tau_\mathrm{c}^3\right) .\end{aligned} \tag{4.2.28}$$

To evaluate the last brackets requires expressions for g_Θ, g'_Θ and g''_Θ which are accurate to zeroth order in τ_c. Those follow directly from the definition of g_Θ in Eq. (4.2.12) and read

$$g_\Theta = -\mathcal{H}\,\theta_\mathrm{b} + k^2\left(c_\mathrm{b}^2\delta_\mathrm{b} - \frac{\delta_\gamma}{4}\right) + \mathcal{O}\left(\tau_\mathrm{c}\right) \tag{4.2.29a}$$

$$g'_\Theta = \mathcal{H}'\,\theta_\mathrm{b} - \mathcal{H}\,\theta'_\mathrm{b} + k^2\left[\left(c_\mathrm{b}^2\right)'\,\delta_\mathrm{b} + \left(c_\mathrm{b}^2 - \frac{1}{3}\right)\left(-\theta_\mathrm{b} + 3\psi'\right)\right] + \mathcal{O}\left(\tau_\mathrm{c}\right) \tag{4.2.29b}$$

$$\begin{aligned}g''_\Theta = &-\mathcal{H}\,\theta''_\mathrm{b} - 2\mathcal{H}'\,\theta'_\mathrm{b} - \mathcal{H}''\,\theta_\mathrm{b} + k^2\left[\left(c_s^2\right)''\,\delta_\mathrm{b} - 2\left(c_s^2\right)'\left(\theta_\mathrm{b} - 3\psi'\right)\right. \\ &\left. + \left(\frac{1}{3} - c_\mathrm{b}^2\right)\left(\theta'_\mathrm{b} - 3\phi'\right)\right] + \mathcal{O}\left(\tau_\mathrm{c}\right) .\end{aligned} \tag{4.2.29c}$$

Our result agrees with the expressions implemented in CLASS for Newtonian gauge.

4.2.2 Inclusion of dark matter-photon interactions in the tight coupling approximation

We now turn to the inclusion of dark matter-photon scattering into the tight coupling approximation. Starting from the evolution of the baryon and photon velocity divergences in Eq. (3.3.12) and Eq. (3.6.2b), respectively, we obtain a new set of evolution equations without any explicit occurrence of the Thomson scattering rate $\kappa'_{\gamma\mathrm{b}}$

$$\begin{aligned}\theta'_\mathrm{b} = &-\frac{1}{1+R_{\gamma\mathrm{b}}}\left[\mathcal{H}\,\theta_\mathrm{b} - c_\mathrm{b}^2\,k^2\,\delta_\mathrm{b} - k^2\,R_{\gamma\mathrm{b}}\left(\frac{\delta_\gamma}{4} - \sigma_\gamma\right) + R_{\gamma\mathrm{b}}\Theta'_{\gamma\mathrm{b}} + \kappa'_{\gamma\mathrm{dm}}R_{\gamma\mathrm{b}}\left(\theta_\gamma - \theta_{\gamma\mathrm{dm}}\right)\right] \\ &+ k^2\,\psi ,\end{aligned} \tag{4.2.30a}$$

$$\theta'_\gamma = -R_{\gamma\mathrm{b}}^{-1}\left[\mathcal{H}\,\theta_\mathrm{b} - c_\mathrm{b}^2\,k^2\,\delta_\mathrm{b} + \theta'_\mathrm{b}\right] + k^2\left(\frac{\delta_\gamma}{4} - \sigma_\gamma\right) + \frac{1+R_{\gamma\mathrm{b}}}{R_{\gamma\mathrm{b}}}\,k^2\,\psi - \kappa'_{\gamma\mathrm{dm}}\left(\theta_\gamma - \theta_{\gamma\mathrm{dm}}\right) . \tag{4.2.30b}$$

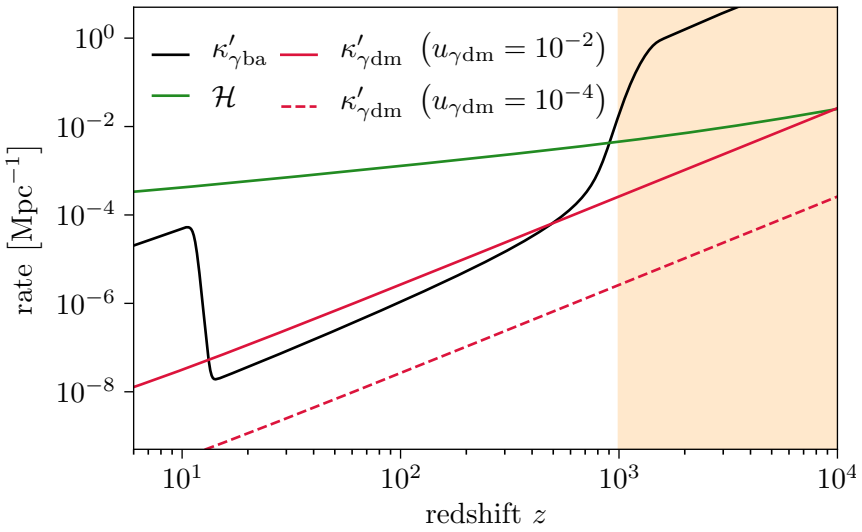

Figure 4.1: Comparison of the rates for photon scattering and the cosmological expansion, assuming a constant dark matter-photon interaction cross section. The orange shaded region roughly indicates when the tight coupling approximation is applied.

These equations still contain the rate for dark matter-photon scattering $\kappa'_{\gamma\mathrm{dm}}$, and in our derivation we assume it to be much smaller than the Thomson scattering rate. This means the tight coupling conditions (4.2.8), now generalise to

$$\tau_\mathrm{c}\,\mathcal{H} \gg 1\,, \quad \tau_\mathrm{c}\,k \gg 1\,, \quad \text{and} \quad \tau_\mathrm{c}\,\kappa'_{\gamma\mathrm{dm}} \gg 1\,. \tag{4.2.31}$$

If $\sigma_{\gamma\mathrm{dm}} = \text{const.}$, the condition on $\kappa'_{\gamma\mathrm{dm}}$ does not impose an actual new constraint on the applicability of the tight coupling approximation. This becomes very clear from Fig. 4.1, where we compare the dark matter-photon scattering rate to the Thomson scattering rate and the Hubble parameter. Well before recombination, the photon scattering rates with electrons and dark matter evolve parallel with their ratio set by $u_{\gamma\mathrm{dm}}$. Phenomenological viable models require $u_{\gamma\mathrm{dm}} \sim 10^{-4}$ or smaller (c.f. Sec. 5.3), for which $\kappa'_{\gamma\mathrm{dm}} \ll \kappa'_{\gamma\mathrm{b}}$ is safely guaranteed whenever $\kappa'_{\gamma\mathrm{b}} \gg \mathcal{H}$. More care is required when non-constant dark matter scattering cross sections are concerned. In those cases where $\sigma_{\gamma\mathrm{dm}}$ increases with temperature, $\kappa'_{\gamma\mathrm{dm}}$ might easily become larger than the Thomson scattering rate at early times. A tight coupling approximation then still is possible but requires an expansion in both inverse scattering rates.

Generalising the expression for the photon-baryon slip to include interactions between photons and dark matter, we obtain from Eq. (3.3.12) and Eq. (3.6.2b)

$$\tau_\mathrm{c}\left[\Theta'_{\gamma\mathrm{b}} - \mathcal{H}\,\theta_\mathrm{b} + k^2\left(c_\mathrm{b}^2\,\delta_\mathrm{b} - \frac{\delta_\gamma}{4} + \sigma_\gamma\right) + \kappa'_{\gamma\mathrm{dm}}\,(\theta_\gamma - \theta_{\gamma\mathrm{dm}})\right] + (1 + R_{\gamma\mathrm{b}})\,\Theta_{\gamma\mathrm{b}} = 0\,. \tag{4.2.32}$$

This equation has the same structure as the schematic equation (4.2.7), which we used to derive the expansion in the previous section. However, it differs from the precise expression in Eq. (4.2.6) by the appearance of an additional term proportional to $\kappa'_{\gamma\mathrm{dm}}$. Thus Eq. (4.2.15), which determines $\Theta'_{\gamma\mathrm{b}}$ up to second order in τ_c, remains valid given that

we redefine the function g_Θ accordingly,

$$g_\Theta = -\mathcal{H}\,\theta_\mathrm{b} + k^2\left(c_\mathrm{b}^2\,\delta_\mathrm{b} - \frac{\delta_\gamma}{4} + \sigma_\gamma\right) + \kappa'_{\gamma\mathrm{dm}}\,(\theta_\gamma - \theta_{\gamma\mathrm{dm}})\;. \tag{4.2.33}$$

Performing the same manipulations as in Eq. (4.2.16), the time derivative of g_Θ is

$$\begin{aligned}
g'_\Theta &= -\mathcal{H}'\,\theta_\mathrm{b} - \mathcal{H}\,\theta'_\mathrm{b} + k^2\left(c_\mathrm{b}^2\right)'\delta_\mathrm{b} + k^2\,c_\mathrm{b}^2\,\delta'_\mathrm{b} - \frac{k^2\,\delta'_\gamma}{4} + k^2\,\sigma'_\gamma \\
&\quad + \kappa''_{\gamma\mathrm{dm}}\,(\theta_\gamma - \theta_{\gamma\mathrm{dm}}) + \kappa'_{\gamma\mathrm{dm}}\left(\theta'_\gamma - \theta'_{\gamma\mathrm{dm}}\right) \\
&= 2\,\mathcal{H}\Theta'_{\gamma\mathrm{b}} - \frac{a''}{a}\,\theta_\mathrm{b} + k^2\left[\bar{c_\mathrm{b}^2}\,\delta_\mathrm{b} + c_\mathrm{b}^2\,\delta'_\mathrm{b} - \frac{\delta'_\gamma}{4} + \sigma'_\gamma - \mathcal{H}\psi\right] + \kappa''_{\gamma\mathrm{dm}}\,(\theta_\gamma - \theta_{\gamma\mathrm{dm}}) \\
&\quad + \kappa'_{\gamma\mathrm{dm}}\left(\theta'_\gamma - \theta'_{\gamma\mathrm{dm}}\right) + \mathcal{H}R_{\gamma\mathrm{b}}\kappa'_{\gamma\mathrm{b}}\Theta_{\gamma\mathrm{b}} + 2\,k^2\,\mathcal{H}\psi - 2\,k^2\,\mathcal{H}\,\psi \\
&\quad - \frac{1}{2}\mathcal{H}\,k^2\,\delta_\gamma + 2\mathcal{H}\,k^2\,\sigma_\gamma + 2\mathcal{H}\kappa'_{\gamma\mathrm{b}}\Theta_{\gamma\mathrm{b}} + 2\mathcal{H}\kappa'_{\gamma\mathrm{dm}}\,(\theta_\gamma - \theta_{\gamma\mathrm{dm}}) \\
&= 2\mathcal{H}\,\Theta'_{\gamma\mathrm{b}} - \frac{a''}{a}\,\theta_\mathrm{b} + k^2\left[\bar{c_\mathrm{b}^2}\,\delta_\mathrm{b} + c_\mathrm{b}^2\,\delta'_\mathrm{b} - \frac{\delta'_\gamma}{4} + \sigma'_\gamma - \mathcal{H}\,\psi - \frac{\mathcal{H}\,\delta_\gamma}{2} + 2\mathcal{H}\sigma_\gamma\right] \\
&\quad + \kappa'_{\gamma\mathrm{dm}}\left(\theta'_\gamma - \theta'_{\gamma\mathrm{dm}}\right) + \mathcal{H}\,\kappa'_{\gamma\mathrm{b}}\,(2 + R_{\gamma\mathrm{b}})\,\Theta_{\gamma\mathrm{b}}\,.
\end{aligned} \tag{4.2.34}$$

To arrive at the final expression we used that

$$\kappa'''_{\gamma\mathrm{dm}} = \frac{\sigma_{\gamma\mathrm{dm}}}{m_{\gamma\mathrm{dm}}}\left(a'\,\rho_{\gamma\mathrm{dm}} + a\,\rho'_{\gamma\mathrm{dm}}\right)\;. = -2\,\mathcal{H}\,\kappa'_{\gamma\mathrm{dm}} \tag{4.2.35}$$

The first order solution for the photon-baryon slip in the presence of dark matter-photon scattering is now given by

$$\begin{aligned}
\Theta'_{\gamma\mathrm{b}} &= \left(\frac{\tau'}{\tau_\mathrm{c}} - \frac{2\,\mathcal{H}}{1 + R_{\gamma\mathrm{b}}}\right)\Theta_{\gamma\mathrm{b}} - \frac{\tau_\mathrm{c}}{1 + R_{\gamma\mathrm{b}}}\left[-\frac{a''}{a}\theta_\mathrm{b} + k^2\left(\bar{c_\mathrm{b}^2}\,\delta_\mathrm{b} + c_\mathrm{b}^2\,\delta'_\mathrm{b} - \frac{\delta'_\gamma}{4} - \frac{\mathcal{H}\,\delta_\gamma}{2} - \mathcal{H}\,\psi\right)\right. \\
&\quad \left. + \kappa'_{\gamma\mathrm{dm}}\left(\theta'_\gamma - \theta'_{\gamma\mathrm{dm}}\right)\right] + \mathcal{O}\left(\tau_\mathrm{c}^2\right)\;.
\end{aligned} \tag{4.2.36}$$

At this point, we are not able to confirm the findings of Ref. [6] and in particular Eq. (3.2.19) therein. The term $\kappa'_{\gamma\mathrm{dm}}\left(\theta'_\gamma - \theta'_{\gamma\mathrm{dm}}\right)$ does not appear in our result but instead we obtain a term $\kappa''_{\gamma\mathrm{dm}}\,(\theta_\gamma - \theta_{\gamma\mathrm{dm}})$. Since the steps which led to the expression of Ref. [6] were not explicitly presented, we are unable to trace back at which point the discrepancy occurred.

In order to obtain expressions for the photon shear and the zeroth and the second polarisation multipole, we compare the governing equations with and without the dark matter-photon scatting term, that is Eq. (3.6.2) and Eq. (3.4.36). They take the exactly same form, except for the replacement $\kappa'_{\gamma\mathrm{b}} \to \kappa'_{\gamma\mathrm{b}} + \kappa'_{\gamma\mathrm{dm}}$. Because the dark matter scattering rate is much smaller than that for Thomson scattering, we have

$$\left(\kappa'_{\gamma\mathrm{b}} + \kappa'_{\gamma\mathrm{dm}}\right)^{-1} = \tau_{\mathrm{c},2} \sim \mathcal{O}\,(\tau_\mathrm{c})\;, \tag{4.2.37}$$

and we can repeat the exact same steps as in the previous section but using $\tau_{\mathrm{c},2}$ as expansion parameter. We then recover Eq. (4.2.25) as result for the polarisation multipoles and Eq. (4.2.27) for the photon shear but with τ_c replaced by $\tau_{\mathrm{c},2}$.

Finally, at second order in τ_c the photon-baryon slip is given by

$$\begin{aligned}\Theta'_{\gamma\mathrm{b}} = &\left(1 - 2\mathcal{H}\frac{\tau_\mathrm{c}}{1+R_{\gamma\mathrm{b}}}\right)\left\{\left(\frac{\tau'}{\tau_\mathrm{c}} - \frac{2\mathcal{H}}{1+R_{\gamma\mathrm{b}}}\right)\Theta_{\gamma\mathrm{b}}\right.\\ &\left.-\frac{\tau_\mathrm{c}}{1+R_{\gamma\mathrm{b}}}\left[-\frac{a''}{a}\theta_\mathrm{b} + k^2\left(\bar{c_\mathrm{b}^2}\delta_\mathrm{b} + c_\mathrm{b}^2\,\delta'_b - \frac{\delta'_\gamma}{4} - \frac{\mathcal{H}\,\delta_\gamma}{2} - \mathcal{H}\,\psi\right) + \kappa'_{\gamma\mathrm{dm}}\left(\theta'_\gamma - \theta'_{\gamma\mathrm{dm}}\right)\right]\right\}\\ &-\frac{\tau_\mathrm{c}\,k^2}{1+R_{\gamma\mathrm{b}}}\left(2\mathcal{H}\sigma_\gamma + \sigma'_\gamma\right) + \tilde{f}_\Theta\left(\tilde{f}'_\Theta\,g_\Theta + 2\tilde{f}'_\Theta\,g'_\Theta + \tilde{f}\,g''_\Theta\right) + \mathcal{O}\left(\tau_\mathrm{c}^3\right)\,, \end{aligned} \tag{4.2.38}$$

where the required first order expressions for g_Θ and its derivatives follow directly from Eq. (4.2.33)

$$g_\Theta = -\mathcal{H}\,\theta_\mathrm{b} + k^2\left(c_\mathrm{b}^2\delta_\mathrm{b} - \frac{\delta_\gamma}{4}\right) + \kappa'_{\gamma\mathrm{dm}}\left(\theta_\gamma - \theta_{\gamma\mathrm{dm}}\right) + \mathcal{O}\left(\tau_\mathrm{c}\right) \tag{4.2.39}$$

$$\begin{aligned}g'_\Theta = &-\mathcal{H}'\theta_\mathrm{b} - \mathcal{H}\theta'_\mathrm{b} + k^2\left[\left(c_\mathrm{b}^2\right)'\delta_\mathrm{b} + \left(\frac{1}{3} - c_\mathrm{b}^2\right)\left(\theta_\mathrm{b} - 3\phi'\right)\right] + \kappa''_{\gamma\mathrm{dm}}\left(\theta_\gamma - \theta_{\gamma\mathrm{dm}}\right)\\ &+\kappa'_{\gamma\mathrm{dm}}\left(\theta'_\gamma - \theta'_{\gamma\mathrm{dm}}\right) + \mathcal{O}\left(\tau_\mathrm{c}\right)\end{aligned} \tag{4.2.40}$$

$$\begin{aligned}g''_\Theta = &-\mathcal{H}''\theta_\mathrm{b} - 2\mathcal{H}'\,\theta'_\mathrm{b} - \mathcal{H}\,\theta''_\mathrm{b} + k^2\left[\left(c_\mathrm{b}^2\right)''\delta_\mathrm{b} - 2\left(c_s^2\right)'\left(\theta_\mathrm{b} - 3\phi'\right) + \left(\frac{1}{3} - c_\mathrm{b}^2\right)\left(\theta'_\mathrm{b} - 3\phi'\right)\right]\\ &+\kappa'''_{\gamma\mathrm{dm}}\left(\theta_\gamma - \theta_{\gamma\mathrm{dm}}\right) + 2\kappa''_{\gamma\mathrm{dm}}\left(\theta'_\gamma - \theta'_{\gamma\mathrm{dm}}\right) + \kappa'_{\gamma\mathrm{dm}}\left(\theta''_\gamma - \theta''_{\gamma\mathrm{dm}}\right) + \mathcal{O}\left(\tau_\mathrm{c}\right)\,.\end{aligned} \tag{4.2.41}$$

For the numerical implementation of this result we choose the accuracy level "class compromise". This is the CLASS default setting for the tight coupling approximation [288]. It considers the photon shear at second order but uses a reduced expression for the photon-baryon slip, which avoids some of the numerically most expensive terms.

4.3 Ultra-relativistic fluid approximation

Both approximation schemes discussed previously address perturbations in the photon fluid and are modified by photon couplings with dark matter. Dark matter-neutrino scattering, in contrast, affects neither the line of sight integration, nor the tight coupling approximation. However, it requires a careful re-examination of the conditions under which the ultra-relativistic fluid approximation can be applied.

In the ΛCDM scenario, where neutrinos interact only gravitationally, the lowest multipoles δ_ν, θ_ν and σ_ν suffice to account for the neutrino's impact on the Einstein equations and on the evolution of other species. Nevertheless, because higher and lower multipoles are coupled, the latter can not simply be neglected. The original truncation scheme for the Boltzmann hierarchy (3.4.25) is designed to avoid unphysical reflections but works imperfectly if $l_\mathrm{max} < k\tau$. However, once a neutrino perturbation is well inside the Hubble radius, multipoles in the range $2 < l \ll k\tau$ become suppressed, and the lowest moments decouple from the higher ones. This central observation permits the ultra-relativistic fluid approximation, a consistent truncation for free-streaming radiation on sub-horizon scales that only considers multipoles up to the shear. During the radiation-dominated era, $\tau = \mathcal{H}^{-1}$ holds, and imposing a lower threshold on $k\tau$, i.e. $k\tau \geq (k\tau)_\mathrm{ufa}$, is a good

criterion to evaluate whether a perturbation is well within the Hubble radius. In practice, the threshold $(k\tau)_{\mathrm{ufa}}$ typically ranges between 10 and 50 [288].

The advantages of such a truncation are twofold. First, it immediately reduces the number of equations which have to be integrated at late times to just three. Second, because the full Boltzmann hierarchy is only evolved until some early time $(k\tau)_{\mathrm{ufa}}/k$, a lower multipole moment can be chosen for the cut-off l_{max}. Accordingly, the ultra-relativistic fluid approximation also benefits the computational costs at early times.

4.3.1 Truncation scheme for collisionless neutrinos

Before we discuss how the ultra-relativistic fluid approximation can be applied in the case of dark matter-neutrino interactions, we briefly sketch the most important steps of its derivation in the ΛCDM scenario. Only synchronous gauge was discussed in Ref. [288], here we obtain the truncation equations in Newtonian gauge. Our result agrees with the expression implemented in CLASS.

The argumentation begins with the free streaming solution to the momentum-integrated Boltzmann equation, which we derive in Sec. 7.3.4. Here, we anticipate the result (7.3.18),

$$\begin{aligned} F_{\nu,l}\left(\boldsymbol{k},\mu,\tau\right) = \left[\delta_\nu\left(\boldsymbol{k}\right)+4\psi\right]_{\tau=0} j_l\left(k\tau\right) - \frac{4\,i\,\mu}{k}\left[\theta_\nu\left(\boldsymbol{k}\right)\right]_{\tau=0} j_l'\left(k\tau\right) \\ + 4\int_0^\tau d\tilde{\tau}\, j_l\left[k\left(\tau-\tilde{\tau}\right)\right]\left(\phi'+\psi'\right) . \end{aligned}$$

as starting point. The first line of this expression describes how initial conditions propagate to later times, the second line how perturbations adjust to power injection from metric perturbations. The spherical Bessel functions obey the identity

$$j_l''\left(k\,\tau\right) = j_l'\left(k\,\tau\right) - \frac{l+1}{k\,\tau}\, j'\left(k\,\tau\right) + \frac{l+1}{\left(k\,\tau\right)^2}\, j_l\left(k\,\tau\right) , \tag{4.3.1}$$

and vary over time scales $\sim k^{-1}$. Thus, in the limit $k\tau \gg 1$, that is when a perturbation is well inside the Hubble radius, the last term in Eq. (4.3.1) can be omitted. The free streaming solution becomes

$$F_l' - k\,F_{l-1} + \frac{l+1}{\tau}\,F_l = 4k\,\psi\,\delta_{(l-1),0} - 4\,\frac{l+1}{\tau}\int_0^\tau d\tilde{\tau}\,\left(\frac{\tilde{\tau}}{\tau-\tilde{\tau}}\right) j_l\left[k\left(\tau-\tilde{\tau}\right)\right]\left(\phi'+\psi'\right) \tag{4.3.2}$$

Crucially, the metric perturbations vary smoothly over the timescale of τ, while the Bessel function oscillates over k^{-1} and shows a peak around $l+\frac{1}{2}$. If the integral runs over a large enough interval, i.e. when $\tau \gg k/l$, the convolution only picks up a significant contribution near $\tilde{\tau} \sim \tau$. Hence, one can approximate it as

$$\int_0^\tau d\tilde{\tau}\,\left(\frac{\tilde{\tau}}{\tau-\tilde{\tau}}\right) j_l\left[k\left(\tau-\tilde{\tau}\right)\right]\left(\phi'+\psi'\right) \simeq \tau\left[\phi'\left(\tau\right)+\psi'\left(\tau\right)\right]\int_0^{\tilde{\tau}} d\tilde{\tau}\,\frac{j_l\left[k\left(\tau-\tilde{\tau}\right)\right]}{\tau-\tilde{\tau}} \tag{4.3.3}$$

For $l = 2$, the remaining integrand is of the form $j_2\left(x\right)/x$, and evaluates to $-1/3$. By

further assuming $\psi \simeq \phi$, which is justified for small anisotropic stress, we obtain

$$\sigma_\nu' = \frac{2}{3}\,\theta_\nu - \frac{3}{\tau}\,\sigma_\nu + 4\,\phi' \,. \tag{4.3.4}$$

This expression for the time derivative of the anisotropic stress only depends on neutrino multipoles of the same or lower order and on the metric perturbations, hence it cuts off the Boltzmann hierarchy. In contrast to the ordinary truncation scheme, which is based on the assumption $F_{\nu,l} \propto j_l\,(k\tau)$ and neglects the metric term in the free streaming solution, the ultra-relativistic fluid approximation accounts metric contributions at leading order [288].

4.3.2 Revised treatment for interacting neutrinos

Unfortunately, the ultra-relativistic fluid approximation does not readily generalise when interactions with dark matter affect the neutrino evolution. Starting point for the derivation was the free streaming solution to the collisionless Boltzmann equations (7.3.18), which is not valid for interacting neutrinos. In some numerical codes, used e.g. to study the impact of dark matter-neutrino scattering on the CMB spectra [277] or on the matter power spectrum [295], we encountered a modified version of the truncation equation (4.3.4),

$$\sigma_\nu' = \frac{2}{3}\,\theta_\nu - \frac{3}{\tau}\,\sigma_\nu + 4\,\phi' - \alpha_l\,\kappa_{\nu\mathrm{dm}}'\,\sigma_\nu \,, \tag{4.3.5}$$

where $\alpha_l = 9/10, 1$, respectively. However, we neither found a derivation of this expression, nor did we manage to calculate it from the steps outline in the previous section.

Instead of incorporating the scattering term in the truncation equation, we choose to delay the ultra-relativistic fluid approximation until neutrinos have decoupled from dark matter. The scale factor at neutrino decoupling $a_{\nu,\mathrm{dec}}$ can be estimated from the condition

$$\mathcal{H}\,(a_{\nu,\mathrm{dec}}) = \kappa_{\nu\mathrm{dm}}'\,(a_{\nu,\mathrm{dec}}) \,. \tag{4.3.6}$$

Assuming that the decoupling occurs in the radiation-dominated epoch, $a_{\nu,\mathrm{dec}}$ is given by

$$a_{\nu,\mathrm{dec}}^{n_{\nu\mathrm{dm}}+1} = \frac{3\,m_\mathrm{P}^2}{8\pi}\,H_0\,\frac{\Omega_{\nu\mathrm{dm}}h^2}{\sqrt{\Omega_\mathrm{r}h^2}}\,\frac{u_{\nu\mathrm{dm},0}\,\sigma_\mathrm{T}}{100\,\mathrm{GeV}} = 1.2\times10^{-2}\times u_{\nu\mathrm{dm},0}\,\left(\frac{\Omega_{\nu\mathrm{dm}}h^2}{0.1186}\right) . \tag{4.3.7}$$

Indeed, neutrino decoupling during matter domination is ruled out by CMB constraints for $n_{\nu\mathrm{dm}} = 0, 2$, and in the mixed damping study of Sec.7 we are exclusively concerned with decoupling before matter-radiation equality. The conformal time at $a_{\nu,\mathrm{dec}}$ is

$$\tau_{\nu,\mathrm{dec}} = \frac{a_{\nu,\mathrm{dec}}}{H_0\,\sqrt{\Omega_\mathrm{r}}} = \begin{cases} 5.53\times10^3\,\mathrm{Mpc}\times\left(\frac{u_{\nu\mathrm{dm}}}{\epsilon_\mathrm{ufa}}\right)\times\left(\frac{\Omega_\mathrm{dm}}{0.1186}\right) & \mathrm{if} n_{\nu\mathrm{dm}} = 0 \\ 10.6\times10^4\,\mathrm{Mpc}\times\left(\frac{u_{\nu\mathrm{dm}}}{\epsilon_\mathrm{ufa}}\right)^{\frac{1}{3}}\times\left(\frac{\Omega_\mathrm{dm}}{0.1186}\right)^{\frac{1}{3}} & \mathrm{if} n_{\nu\mathrm{dm}} = 2 \\ 19.2\times10^4\,\mathrm{Mpc}\times\left(\frac{u_{\nu\mathrm{dm}}}{\epsilon_\mathrm{ufa}}\right)^{\frac{1}{5}}\times\left(\frac{\Omega_\mathrm{dm}}{0.1186}\right)^{\frac{1}{5}} & \mathrm{if} n_{\nu\mathrm{dm}} = 4 \end{cases} . \tag{4.3.8}$$

To delay the ultra-relativistic fluid approximation beyond neutrino decoupling, we impose for the largest mode of interest k_max

$$\tau_{\nu,\mathrm{dec}}\,k_\mathrm{max} > (k\tau)_\mathrm{ufa} \,. \tag{4.3.9}$$

With the described approach we evolve the full, interacting Boltzmann hierarchy (3.5.5) up to a larger conformal time. Unphysical reflections affect the solution after $\tau = l_{\max}/k$, and we adapt $l_{\max}$ accordingly, to minimise their impact. As a benchmark point we use

$$l_{\max} \simeq (k\tau)_{\text{ufa}} \simeq k_{\max}\, \tau_{\nu,\text{dec}} \tag{4.3.10}$$

In Sec. 7.2.1 we assess the accuracy of our treatment and compare our results to those obtained by previous studies.

4.4 Initial conditions

Before the evolution equations for cosmological perturbations can be solved numerically, initial conditions need to be specified. In particular neutrino interactions with dark matter modify the initial conditions from the canonical ΛCDM expressions. The the traceless space-space component of the linearised Einstein equations (3.2.17d)

$$k^2\,(\phi - \psi) = \frac{12\pi}{m_{\text{P}}^2}\, a^2\, \left(\bar{\rho} + \bar{P}\right) \sigma\,,$$

illustrate the cause for the change. In general, the numerical evolution of perturbations commences well before recombination, in the radiation-dominated era. Then, Thomson scattering suppresses σ_γ, but in the ΛCDM scenario free streaming neutrinos contribute some anisotropic stress and causes a small difference between the metric potentials. If, in contrast, neutrinos are in kinetic equilibrium with dark matter, then σ_ν is small, and the two metric perturbations equal each other.

Initial conditions for the ΛCDM scenario have mostly been derived in synchronous gauge [283, 304]. From these expressions staring values in Newtonian gauge are obtained by a gauge transformation [283]. To be able to compare our results at an intermediate level and thereby verify our calculations, we follow the same approach here. That is, we derive the default initial conditions in synchronous gauge in Sec. 4.4.1 and for the interacting neutrino scenario in Sec. 4.4.2. We then perform a gauge transformation to obtain starting values for the numerical integration in Newtonian gauge in Sec. 4.4.3.

4.4.1 Default initial conditions in synchronous gauge

In synchronous gauge, scalar metric perturbations are described by two variables, h and η. To derive their initial conditions, we start from the time-time and the space-space component of the linearised Einstein equations [283]

$$k^2\,\eta - \frac{1}{2}\mathcal{H} h' = -\frac{4\pi\, a^2}{m_{\text{P}}^2} \sum_i \delta\rho_i^{\text{syn}}\,, \tag{4.4.1a}$$

$$h'' + 2\mathcal{H} h' - 2k^2\tau = -\frac{8\pi\, a^2}{m_{\text{P}}^2} \sum_i 3\,\delta P_i^{\text{syn}}\,, \tag{4.4.1b}$$

where we have introduced the superscript "syn" to explicitly denote perturbations in the synchronous gauge (perturbations in Newtonian gauge do not carry a superscript). During the radiation-dominated epoch, only photons and neutrinos, whose equation of state is $\delta P = \delta\rho/3$, contribute significantly in the sums on the right hand side, and the conformal Hubble rate is $\mathcal{H} = \tau^{-1}$. By adding Eq. (4.4.1a) and Eq. (4.4.1b) and using the Friedman equation (1.1.4), we obtain a second order equation for h

$$\tau^2\, h'' + \tau\, h' + 6\left[(1 - R_\nu)\,\delta_\gamma + R_\nu\,\delta_\nu\right] = 0\,. \tag{4.4.2}$$

For briefness, we denote the fractional energy density in neutrinos as $R_\nu \equiv \bar{\rho}_\nu / \left(\bar{\rho}_\nu + \bar{\rho}_\gamma\right)$.

While Eqs. (4.4.1a) and (4.4.2) describe the metric perturbations, we also require expressions for the matter fluctuations. The tight coupling between photons and baryons suppresses the photon multipoles for $l \geq 2$ and drives $\theta_\gamma - \theta_\mathrm{b}$ to zero, as discussed in Sec. 4.2.1. Similarly, the higher order neutrino multipoles are suppressed by successive powers of $k\tau$. Initial conditions have to be chosen when the mode of concern is larger than the Hubble radius, hence $k\tau \ll 1$, and we neglect all neutrino multipoles beyond the anisotropic shear. Under these assumptions, the evolution equations for matter perturbations in synchronous gauge simplify to [283]

$$\delta_\gamma'^{\mathrm{syn}} + \frac{4}{3}\,\theta_\gamma'^{\mathrm{syn}} + \frac{2}{3}\,h' = 0\,, \tag{4.4.3a}$$

$$\delta_\nu'^{\mathrm{syn}} + \frac{4}{3}\,\theta_\nu'^{\mathrm{syn}} + \frac{2}{3}\,h' = 0\,, \tag{4.4.3b}$$

$$\theta_\gamma'^{\mathrm{syn}} - \frac{1}{4}k^2\,\delta_\gamma^{\mathrm{syn}} = 0\,, \tag{4.4.3c}$$

$$\theta_\nu'^{\mathrm{syn}} - \frac{1}{k}k^2\left(\delta_\nu^{\mathrm{syn}} - 4\sigma_\nu^{\mathrm{syn}}\right) = 0\,, \tag{4.4.3d}$$

$$\sigma_\nu'^{\mathrm{syn}} - \frac{2}{15}\left(2\theta_\nu^{\mathrm{syn}} + h' + 6\eta'\right) = 0\,. \tag{4.4.3e}$$

The system of coupled differential equations, composed of Eq. (4.4.2), Eq. (4.4.2) and Eqs. (4.4.3), determines the initial conditions. To find a solution, we expand each perturbation variable as a power series in $k\tau$. Substituting the expansion and matching terms of like powers in $k\tau$ yields a set of linear equations, which we solve for the individual coefficients. For a high precision study of the tight coupling approximation, Ref. [304] follows a similar approach but also considers σ_ν and extends the expansion to inverse powers of the Thomson scattering rate. In CLASS the initial conditions are implemented to lowest order in $k\tau$ and zeroth order in $\kappa_{\gamma\mathrm{b}}'^{-1}$. As we discuss in Sec. 7.2.2, the lowest order expressions are also sufficient for our purpose.

To ease the comparison with Ref. [283], we denote the second order coefficient in the expansion of h as C_ini and reformulate all other variables in terms of it. With this, we obtain as initial conditions in the ΛCDM scenario

$$h_\mathrm{ini}\left(k\,,\tau\right) = C_\mathrm{ini}\;(k\tau)^2 - \frac{5 + 4R_\nu}{36\,(15 + 4R_\nu)}\,C_\mathrm{ini}\;(k\tau)^4 + \mathcal{O}\left((k\tau)^5\right)\,, \tag{4.4.4a}$$

$$\eta_{\mathrm{ini}}\left(k\,,\tau\right) = 2C_{\mathrm{ini}} - \frac{5+4R_\nu}{6\left(15+4R_\nu\right)}\,C_{\mathrm{ini}}\,\left(k\tau\right)^2 + \mathcal{O}\left(\left(k\tau\right)^3\right)\,, \tag{4.4.4b}$$

$$\delta^{\mathrm{syn}}_{\gamma,\,\mathrm{ini}}\left(k\,,\tau\right) = -\frac{2}{3}C_{\mathrm{ini}}\,\left(k\tau\right)^2 + \frac{10+4R_\nu}{27\left(15+4R_\nu\right)}\,C_{\mathrm{ini}}\,\left(k\tau\right)^4 + \mathcal{O}\left(\left(k\tau\right)^5\right)\,, \tag{4.4.4c}$$

$$\delta^{\mathrm{syn}}_{\nu,\,\mathrm{ini}}\left(k\,,\tau\right) = -\frac{2}{3}C_{\mathrm{ini}}\,\left(k\tau\right)^2 + \frac{2\left(7+2R_\nu\right)}{27\left(15+4R_\nu\right)}\,C_{\mathrm{ini}}\,\left(k\tau\right)^4 + \mathcal{O}\left(\left(k\tau\right)^5\right)\,, \tag{4.4.4d}$$

$$\theta^{\mathrm{syn}}_{\gamma,\,\mathrm{ini}}\left(k\,,\tau\right) = -\frac{C_{\mathrm{ini}}}{18}\,k^4\tau^3 + \mathcal{O}\left(\left(k\tau\right)^5\right)\,, \tag{4.4.4e}$$

$$\theta^{\mathrm{syn}}_{\nu,\,\mathrm{ini}}\left(k\,,\tau\right) = -\frac{2\left(23+4R_\nu\right)}{3\left(15+4R_\nu\right)}\,C_{\mathrm{ini}}\,k^4\tau^3 + \mathcal{O}\left(\left(k\tau\right)^4\right)\,, \tag{4.4.4f}$$

$$\sigma^{\mathrm{syn}}_{\nu,\,\mathrm{ini}}\left(k\,,\tau\right) = \frac{4\,C_{\mathrm{ini}}}{3\left(15+4R_\nu\right)}\,\left(k\tau\right)^2 + \mathcal{O}\left(\left(k\tau\right)^3\right)\,. \tag{4.4.4g}$$

Our results agree with those quoted in Ref. [283] and with the coefficients at corresponding power in Ref. [304]. Importantly, none of the arguments below Eq. (4.4.1), which we used to obtain the simplified evolution equations for the matter perturbations, looses its validity when dark matter-photon scattering is introduced. The additional scattering term in the photon evolution is driven to zero in the limit of tight coupling and suppressed by the smallness of the interaction rate in the decoupled limit. Thus, the default initial conditions (4.4.4) remain valid for dark matter-photon interactions.

For completeness, we also give the initial conditions for dark matter and baryons, which follow from the assumption of photon-baryon tight coupling and constant entropy per particle [283]

$$\delta^{\mathrm{syn}}_{\mathrm{dm},\,\mathrm{ini}} = \delta^{\mathrm{syn}}_{\mathrm{b},\,\mathrm{ini}} = \frac{3}{4}\,\delta^{\mathrm{syn}}_{\gamma,\,\mathrm{ini}}\,, \tag{4.4.5a}$$

$$\theta^{\mathrm{syn}}_{\mathrm{b},\,\mathrm{ini}} = \theta^{\mathrm{syn}}_{\gamma,\,\mathrm{ini}}\,, \tag{4.4.5b}$$

$$\theta_{\mathrm{dm},\,\mathrm{ini}} = 0\,. \tag{4.4.5c}$$

The last relation corresponds to the synchronous gauge condition. At first sight, this term seems not to generalise to dark matter-photon interactions, which drive $\theta_{\mathrm{dm}} \simeq \theta_\gamma$. Leading order contributions in Newtonian gauge, however, arise from gauge transformation terms and restore the equality, as shown in Sec. 4.4.3.

4.4.2 Interacting neutrinos in synchronous gauge

Tight coupling between dark matter and neutrinos suppresses the neutrino anisotropic stress, analogous to the suppression of σ_γ by Thomson scattering. Setting σ_ν to zero in Eq. (4.4.3d) allows to discard Eq. (4.4.3e) and the solution in powers of $k\tau$ simplifies to

$$h_{\mathrm{ini}}\left(k\,,\tau\right) = C_{\mathrm{ini}}\,\left(k\tau\right)^2 - \frac{C_{\mathrm{ini}}}{108}\,\left(k\tau\right)^4 + \mathcal{O}\left(\left(k\tau\right)^5\right)\,, \tag{4.4.6a}$$

$$\eta_{\mathrm{ini}}\left(k\,,\tau\right) = 2C_{\mathrm{ini}} - \frac{C_{\mathrm{ini}}}{18}\,\left(k\tau\right)^2 + \mathcal{O}\left(\left(k\tau\right)^3\right)\,, \tag{4.4.6b}$$

$$\delta^{\mathrm{syn}}_{\gamma,\,\mathrm{ini}}\left(k\,,\tau\right) = \delta^{\mathrm{syn}}_{\nu,\,\mathrm{ini}}\left(k\,,\tau\right) = -\frac{2}{3}C_{\mathrm{ini}}\,\left(k\tau\right)^2 + \frac{2}{81}C_{\mathrm{ini}}\,\left(k\tau\right)^4 + \mathcal{O}\left(\left(k\tau\right)^5\right)\,, \tag{4.4.6c}$$

$$\theta^{\mathrm{syn}}_{\gamma,\,\mathrm{ini}}\left(k\,,\tau\right) = \theta^{\mathrm{syn}}_{\nu,\,\mathrm{ini}} = -\frac{C_{\mathrm{ini}}}{18}\,k^4\tau^3 + \mathcal{O}\left(\left(k\tau\right)^5\right)\,. \tag{4.4.6d}$$

The initial conditions for the density perturbations of non-relativistic matter and for the baryon velocity remain unchanged from their original expressions (4.4.5a) and (4.4.5b). For the dark matter velocity we now impose

$$\theta^{\mathrm{syn}}_{\nu\mathrm{dm},\,\mathrm{ini}} = \theta^{\mathrm{syn}}_{\nu,\,\mathrm{ini}}\,. \tag{4.4.7}$$

As the succeeding section shows, the latter requirement does not impact the initial conditions in Newtonian gauge to lowest order.

The initial conditions derived in this section assume tight coupling between dark matter and neutrinos and between photons and baryons. CLASS ensures that the latter condition is met and starts the integration of a given mode when it is well outside the Hubble radius ($k\tau \ll 1$) and in the tight-coupling regime ($\kappa_{\gamma\mathrm{b}} \gg \mathcal{H}$). Dark matter-neutrino interactions demand a more complicated treatment. Depending on the coupling strength parameter $u_{\nu\mathrm{dm}}$, a mode can enter the Hubble radius in the decoupled regime ($\kappa_{\nu\mathrm{dm}} \ll \mathcal{H}$), where Eqs. (4.4.4) apply, in the tightly coupled limit, where Eqs. (4.4.6) are valid, or at an intermediate time. To decide between the limiting cases, we evaluate the ratio between the scattering and the Hubble rate for each mode at its default initial time. If it falls below a threshold, $\kappa_{\nu\mathrm{dm}}/\mathcal{H} \ll 1$, indicating that neutrinos have decoupled from dark matter, we proceed with default initial conditions. Otherwise, we ensure to advance the initial time sufficiently so that the condition of tight coupling is satisfied and use Eqs. (4.4.6) to set the initial conditions.

4.4.3 Gauge transformation

The metric perturbations in synchronous and Newtonian gauge are related by [283]

$$\psi\left(k\,,\tau\right) = \frac{1}{2k^2}\left\{h''\left(k\,,\tau\right) + 6\eta''\left(k\,,\tau\right) + \mathcal{H}\left[h'\left(k\,,\tau\right) + 6\eta'\left(k\,,\tau\right)\right]\right\}\,, \tag{4.4.8a}$$

$$\phi\left(k\,,\tau\right) = \eta\left(k\,,\tau\right) - \frac{\mathcal{H}}{2k^2}\left[h'\left(k\,,\tau\right) + 6\eta'\left(k\,,\tau\right)\right]\,, \tag{4.4.8b}$$

and the stress-energy tensor transforms as

$$(T^{\mathrm{syn}})^{\mu}_{\ \nu} = \frac{\partial\,\hat{x}^{\mu}}{\partial x^{\sigma}}\,\frac{\partial\,x^{\rho}}{\partial\hat{x}^{\nu}}\,T^{\sigma}_{\rho}\,, \tag{4.4.9}$$

where $\hat{x}^{\mu}$ denotes coordinates in synchronous and x^{μ} in Newtonian gauge. Expanding the derivatives and the stress-energy tensor to first order in perturbations yields transformation equations for the lowest multipoles [283]

$$\delta^{\mathrm{syn}}_{a} = \delta_a - \alpha\frac{\bar{\rho}'}{\bar{\rho}}\,, \tag{4.4.10a}$$

$$\theta^{\mathrm{syn}}_{a} = \theta_a - \alpha k^2\,, \tag{4.4.10b}$$

$$\sigma^{\mathrm{syn}}_{a} = \sigma_a\,. \tag{4.4.10c}$$

Here, the subscript a applies to all species which contribute to the stress-energy tensor, and the coefficient appearing in the density and velocity perturbation is

$$\alpha = \frac{1}{2k^2}\left(h' + 6\eta'\right) \,. \tag{4.4.11}$$

From the preceding relations it is straightforward to obtain the initial conditions in Newtonian gauge. During radiation domination $\bar{\rho}'/\bar{\rho} = -4\tau^{-1}$, and for the ΛCDM initial conditions the α-factor evaluates to

$$\alpha = -\frac{40\, C_{\mathrm{ini}}}{15 + 4R_\nu} \quad (\Lambda\mathrm{CDM}) \,. \tag{4.4.12}$$

To lowest order in $k\tau$ we obtain for the ΛCDM and the dark matter-photon interacting scenario

$$\psi_{\mathrm{ini}} = \frac{20}{15 + 4R_\nu}\, C_{\mathrm{ini}} \qquad (\Lambda\mathrm{CDM}/\gamma\mathrm{dm}) \,, \tag{4.4.13a}$$

$$\phi_{\mathrm{ini}} = \frac{20 + 8R_\nu}{15 + 4R_\nu}\, C_{\mathrm{ini}} \qquad (\Lambda\mathrm{CDM}/\gamma\mathrm{dm}) \,, \tag{4.4.13b}$$

$$\frac{4}{3}\,\delta_{\mathrm{b,\,ini}} = \frac{4}{3}\,\delta_{\mathrm{dm,\,ini}} = \delta_{\gamma,\,\mathrm{ini}} = \delta_{\nu,\,\mathrm{ini}} = -\frac{40}{15 + 4R_\nu}\, C_{\mathrm{ini}} \qquad (\Lambda\mathrm{CDM}/\gamma\mathrm{dm}) \,, \tag{4.4.13c}$$

$$\theta_{\mathrm{b,\,ini}} = \theta_{\mathrm{dm,\,ini}} = \theta_{\nu,\,\mathrm{ini}} = \theta_{\gamma,\,\mathrm{ini}} = \frac{10}{15 + 4R_\nu}\, C_{\mathrm{ini}}\, k^2\tau \qquad (\Lambda\mathrm{CDM}/\gamma\mathrm{dm}) \,, \tag{4.4.13d}$$

$$\sigma_{\nu,\,\mathrm{ini}} = \frac{4}{3\,(15 + 4R_\nu)}\, C_{\mathrm{ini}} \qquad (\Lambda\mathrm{CDM}/\gamma\mathrm{dm}) \,. \tag{4.4.13e}$$

The contribution from the gauge transformation determines the velocities at leading order, such that $\theta_{\mathrm{dm}} = \theta_\gamma$ is automatically guaranteed.

Evaluate in the limit of tight coupling between dark matter and neutrinos we obtain

$$\alpha = \frac{2}{3}\, C_{\mathrm{ini}}\tau \quad (\nu\mathrm{dm}) \,, \tag{4.4.14}$$

and the initial conditions become

$$\psi_{\mathrm{ini}} = \phi_{\mathrm{ini}} = \frac{4}{3}\, C_{\mathrm{ini}} \qquad (\nu\mathrm{dm}) \,, \tag{4.4.15a}$$

$$\frac{4}{3}\,\delta_{\mathrm{b,\,ini}} = \frac{4}{3}\,\delta_{\nu\mathrm{dm,\,ini}} = \delta_{\nu,\,\mathrm{ini}} = \delta_{\gamma,\,\mathrm{ini}} = -\frac{8}{3}\, C_{\mathrm{ini}} \qquad (\nu\mathrm{dm}) \,, \tag{4.4.15b}$$

$$\theta_{\mathrm{b,\,ini}} = \theta_{\nu\mathrm{dm,\,ini}} = \theta_{\nu,\,\mathrm{ini}} = \theta_{\gamma,\,\mathrm{ini}} = \frac{2}{3}\, C_{\mathrm{ini}}\, k^2\tau \qquad (\nu\mathrm{dm}) \,. \tag{4.4.15c}$$

As required by the absence of anisotropic stress, the two metric perturbations in Newtonian gauge equal each other in this case.

Chapter 5

Updated constraints on dark matter-photon scattering

The preceding section reveals difference with earlier studies of dark matter-photon interactions, concerning the tight coupling approximation. Further, in Sec. 3.6.2 we explicitly allow for a dark matter sound speed term, which has been neglected so far. Finally, since previous studies constrained the parameter space of the γdm-scenario from CMB observations, the Planck collaboration has released new data. In this section we aim to address all aforementioned points.

To this end, we implement the extended Boltzmann equations (3.6.2) in the cosmology code CLASS v2.6[1] [288]. The implementation also accounts for the modified dark matter evolution (3.6.6) and computes the dark matter sound speed according to Eq. (3.6.8). For the source functions in the line of sight integration and for the tight coupling approximation we use the modified expressions of Eq. (4.1.18) and Eq. (4.2.38), respectively.

We focus on a constant cross section for dark matter-photon scattering, and, in the first section of this chapter, investigate its effect on cosmological observables. There, we also study the impact of our revised expressions for the tight coupling approximation and the consequences of the dark matter sound speed. The Planck CMB observations and our inference strategy are detailed in Sec. 5.2, while we present our results in Sec. 5.3 and put them into context with other studies in Sec. 5.4.

5.1 Phenomenology of dark matter-photon scattering

5.1.1 CMB anisotropies and large-scale structure

The photon scattering rate with dark matter (3.6.3) is proportional to the dark matter number density times the scale factor and, if $n_{\gamma\mathrm{dm}} \geq -2$, decreases as the universe expands. Eventually, the scattering rate drops below the expansion rate, and photons kinetically decouple from the dark matter. Only if photon decoupling from dark matter occurs before recombination, the anisotropy spectrum observed in the CMB is not altered completely.

[1] Our modified code is publicly available from https://github.com/bufeo/class_v2.6_gcdm.git.

A rough estimate for the scale factor at which photons decouple from dark matter, $a_{\gamma,\mathrm{dec}}$, is provided by the condition

$$\mathcal{H}\left(a_{\gamma,\mathrm{dec}}\right) = \kappa'_{\gamma\mathrm{dm}}\left(a_{\gamma,\mathrm{dec}}\right) . \tag{5.1.1}$$

This does not coincide with the scale factor $a_{\gamma\mathrm{dm},\mathrm{dec}}$ at which dark matter kinetically decouples from photons. Rather, because of the momentum conserving factor $R_{\gamma\mathrm{dm}}$ in the evolution of the dark matter perturbations (3.6.6), the latter is determined by the condition

$$\mathcal{H}\left(a_{\gamma\mathrm{dm},\mathrm{dec}}\right) = R_{\gamma\mathrm{dm}}\,\kappa'_{\gamma\mathrm{dm}}\left(a_{\gamma\mathrm{dm},\mathrm{dec}}\right) . \tag{5.1.2}$$

Assuming that either species decouples during the radiation-dominated epoch, as is indeed the case for all phenomenological viable scenarios, the respective scale factors are

$$a_{\gamma,\mathrm{dec}} = 0.016 \times u_{\gamma\mathrm{dm}} , \tag{5.1.3a}$$

$$a_{\gamma\mathrm{dm},\mathrm{dec}} = 0.002 \times \sqrt{u_{\gamma\mathrm{dm}}} . \tag{5.1.3b}$$

Interactions with dark matter leave a distinct imprint on the CMB angular spectra. Some examples, namely two interacting and the ΛCDM scenario, are compared in Fig. 5.1 to the Planck 2015 results. For all spectra we set the six ΛCDM parameters to their Planck 2015 best-fit value (see Tab. 2.1) and vary $u_{\gamma\mathrm{dm}}$ as indicated. Unrealistically large scattering cross sections make the effect of dark matter-photon scattering visible by eye, indeed both values chosen in Fig. 5.1 exceed the upper bound found in Sec. 5.3. For now, we neglect the dark matter sound speed, but return to its impact in Sec. 5.1.3. Essentially, the scattering of photons with dark matter leads to [282, 294]

- a shift of the acoustic peaks to higher multipoles,
- an increase of the first acoustic peak, and
- the damping of fluctuations on small scales.

In the following, we discuss the physical mechanisms which cause each of the changes.

The peak-trough structure of the CMB arises from acoustic oscillations in the tightly coupled baryon-photon plasma prior to recombination, and the location of the peak is determined by the plasma's sound speed, c_{pl}. In the ΛCDM scenario, c_{pl} is given by Eq. (2.2.2), but additional interactions with dark matter modify its value to

$$c_{\mathrm{pl}}^2 = \frac{1}{3}\left[1 + \frac{3\,\rho_{\mathrm{b}}}{4\,\rho_\gamma} + \frac{3\,\rho_{\gamma\mathrm{dm}}}{4\,\rho_\gamma}\right]^{-1} . \tag{5.1.4}$$

This expression is valid while photons are in equilibrium with dark matter, but the decoupling is not an instantaneous process, and residual effects increase the sound speed with respect to its ΛCDM value even beyond $a_{\gamma,\mathrm{dec}}$. Correspondingly, perturbations in the

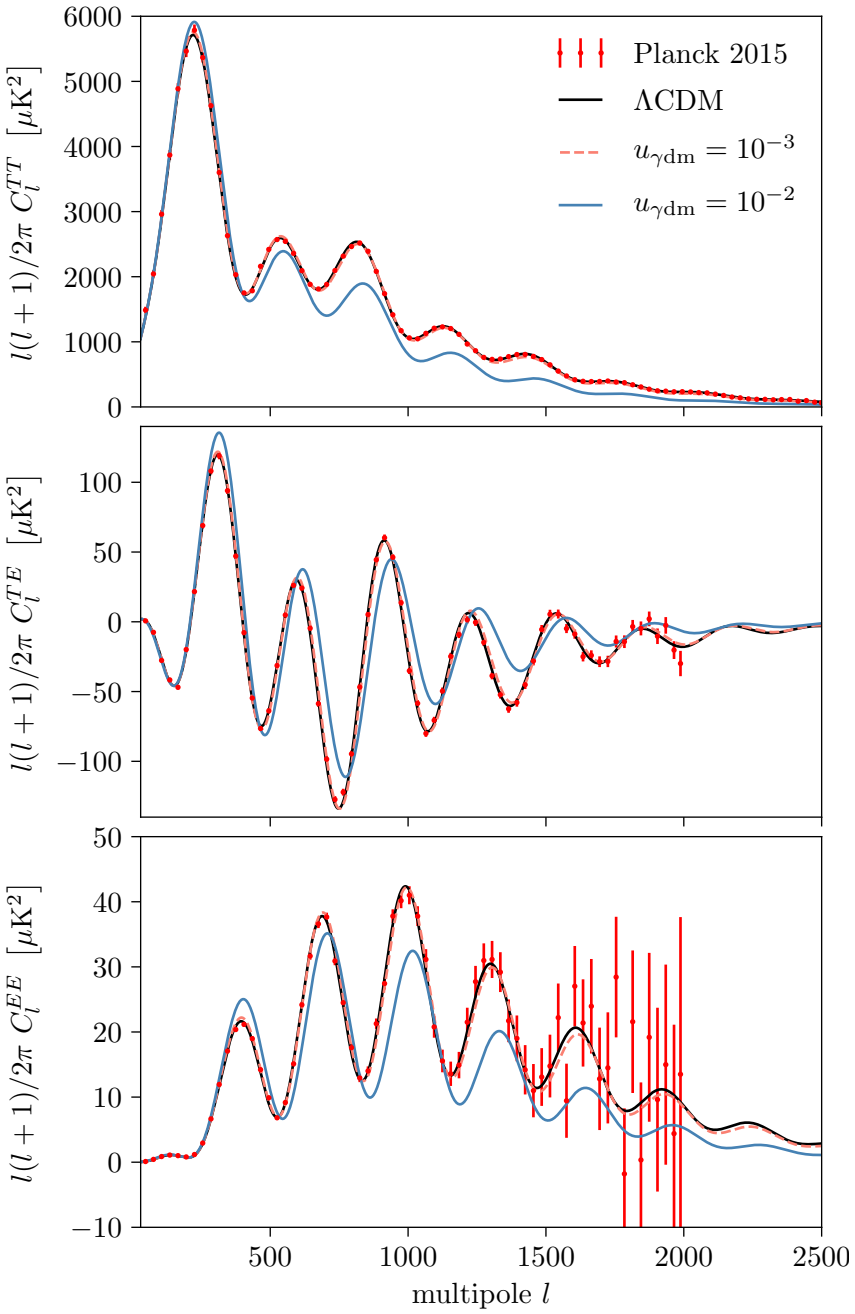

Figure 5.1: CMB angular power spectra measurements from the Planck satellite [5] in comparison to the corresponding best-fit ΛCDM predictions and two different realisations of the dark matter-photon interacting scenario.

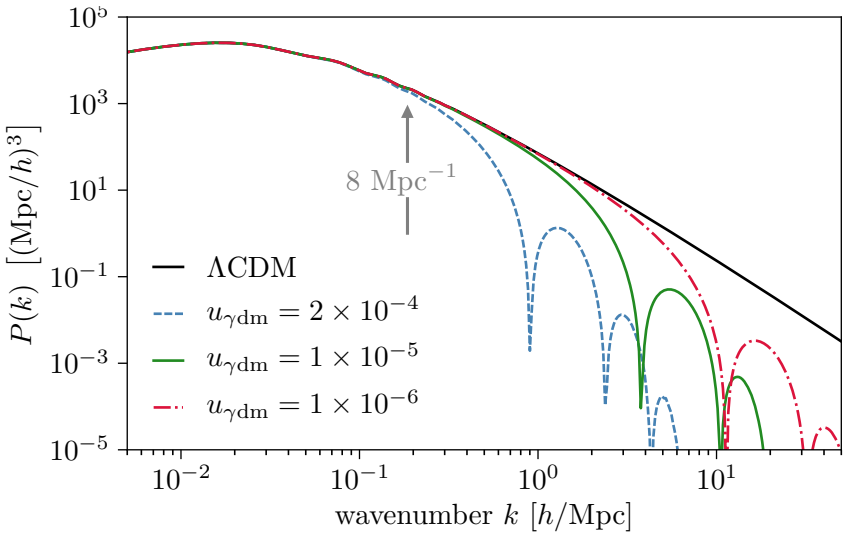

Figure 5.2: The linear matter power spectrum for a ΛCDM cosmology and several scenarios in which dark matter interacts with photons.

baryon-photon plasma oscillate at a lower frequency and the acoustic peaks are shifted to higher multipoles.

Second, the interactions with the dark matter component decrease the photon diffusion length, which in turn causes the increase of the first acoustic peak. The increase is noticeable for both interacting scenarios in Fig. 5.1. Still, for a lower normalised scattering rate of $u_{\gamma\mathrm{dm}} = 10^{-4}$, it amounts to a $\sim 0.1\%$ effect in the temperature and a $\sim 0.3\%$ effect in the E-mode polarisation autocorrelation spectrum [294].

The decreased amplitude of fluctuations on small scales, finally, results from diffusion damping at the photons' last scattering surface with dark matter. The effect is very apparent for the model with $u_{\gamma\mathrm{dm}} = 10^{-2}$. For such a large interaction parameter, photons decouple from dark matter at $a_{\gamma,\mathrm{dec}} = 1.2 \times 10^{-4}$, where we accounted for the effect of matter and radiation on the expansion rate. Indeed, this is only briefly before recombination at $a_* \simeq 9.2 \times 10^{-4}$. The damping is still recognisable in Fig. 5.1 for $u_{\gamma\mathrm{dm}} = 10^{-3}$ in the temperature and the polarisation spectrum, but as the interaction strength parameter decreases, it becomes less distinct and affects only larger multipoles.

The distribution of dark matter, and in particular inhomogeneities on small scales, are also affected by dark matter-photon scattering. In Fig. 5.2 we illustrates the impact in terms of the linear matter power spectrum at $z = 0$. In general, interactions with a relativistic species suppress the growth of perturbations in the dark matter sector. Large modes, however, enter the Hubble radius after dark matter has kinetically decoupled. Their evolution is not affected by the scattering, and on the corresponding scales the matter power spectrum remains unaltered. According to Eq. (5.1.3), dark matter decouples from photons the earlier, the smaller the parameter $u_{\gamma\mathrm{dm}}$. Hence, for smaller values of $u_{\gamma\mathrm{dm}}$ the suppression of power sets in at smaller scales.

To further illustrate how photon scattering affects dark matter perturbations, we show the evolution of a single mode in Fig. 5.3 and compare it to the ΛCDM scenario. In

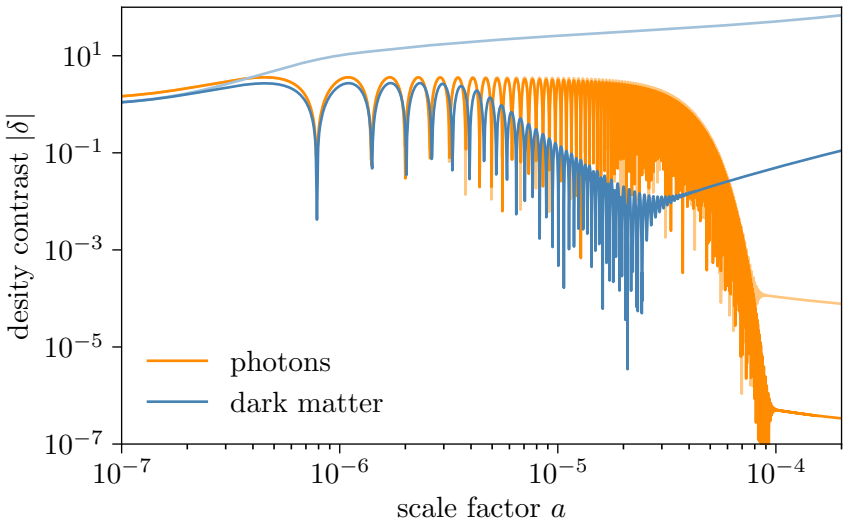

Figure 5.3: Time evolution of a mode with wavenumber $k = 2.0\,\mathrm{Mpc}^{-1}$ in an interacting scenario with $u_{\gamma\mathrm{dm}} = 10^{-4}$ (dark colours) and for the ΛCDM case (pale colours).

the latter case, perturbations start to increase upon Hubble crossing. The interacting mode, in contrast, enters the horizon while dark matter and photons are coupled, and participates in the acoustic oscillations of the baryon-photon plasma. For the parameters chosen, dark matter decouples from photons around $a_{\gamma\mathrm{dm,dec}} \simeq 2.0 \times 10^{-5}$ and photons from dark matter at $a_{\gamma,\mathrm{dec}} = 1.6 \times 10^{-6}$. By the time photons stop feeling the impact of dark matter, neither the baryons nor dark matter contribute significantly to the plasma's sound speed (5.1.4). Hence, the oscillation frequency of the baryon-photon plasma is largely the same in either scenario. The situation would be different for larger interaction strengths, as the previous discussion of CMB anisotropies showed. Diffusion damping prior to the time of dark matter decoupling is clearly noticeable from Fig. 5.3 and further decreases the perturbation's amplitude. Eventually, the combination of impeded growth at early times and damping around decoupling causes the suppression observed in the matter power spectrum. Upon dark matter decoupling, the phase of the acoustic oscillations in the baryon-photon-dark matter plasma is imprinted on the dark matter mode. Analogous to baryon acoustic oscillations, this causes the oscillatory feature apparent on small scales in Fig. 5.2.

5.1.2 Impact of the tight coupling approximation

The tight coupling approximation address the evolution of photon and baryon perturbations at early times, when the large Thomson scattering rate leads to a stiff system of equations. We have generalised the formulae to account for dark matter-photon scattering under the condition that $\kappa'_{\gamma\mathrm{dm}} \ll \kappa'_{\gamma\mathrm{b}}$ in Sec. 4.2.2, but could not reproduce the result quoted in earlier studies [6].

To evaluate how discrepancies in the tight coupling approximation affect the theory predictions, we obtain the numerical code used in Refs. [6,294], which is based on the CLASS version 1.6. With this and or own implementation, we predict $l\,(l+1)\,/\,(2\pi)\,C_l$ for the

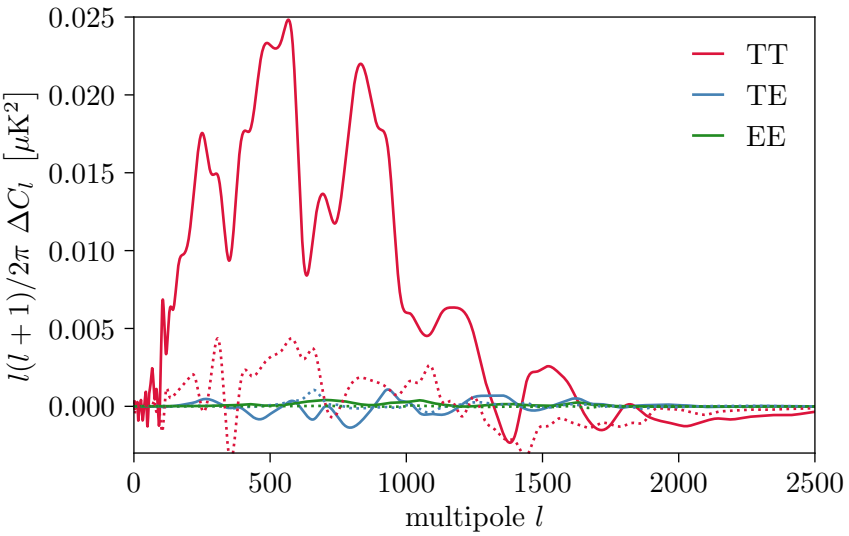

Figure 5.4: The difference between lensed CMB spectra obtained either with Eq. (4.2.36) for the tight coupling approximation or the expressions quoted in Ref. [6], where the plot shows the former minus the latter result. The normalised scattering rate is $u_{\gamma\mathrm{dm}} = 10^{-3}$ for solid and $u_{\gamma\mathrm{dm}} = 10^{-4}$ for dashed lines.

temperature and E-mode autocorrelation and the cross-correlation spectrum on multipoles up to $l = 2500$. Considering $u_{\gamma\mathrm{dm}} = 10^{-4}$ and the Planck 2015 best-fit ΛCDM parameters from Tab. 2.1, the largest differences occur in case of the temperature autocorrelation spectrum and can reach up to $\sim 10\,\mu\mathrm{K}$. CLASS itself, however, has undergone major changes from the 1.6 to the 2.6 version [302], and many precision and cosmological parameters, concerning e.g. reionisation or the primordial helium abundance during BBN, are altered.

To isolate the effect of the differing tight coupling approximation, we transfer the respective expressions of Ref. [6] to a later version CLASS. More precisely, we use CLASS v2.5 with all modifications required by dark matter-photon interactions implemented and allow two options for the tight coupling formulae. An additional input parameter decides between them. The differences between CMB spectra predicted with either version of the tight coupling approximation are shown in Fig. 5.4. We have updated our earlier results [1], to also show a larger normalised interaction rate of $u_{\gamma\mathrm{dm}} = 10^{-3}$. Notably, the precise shape of the curves depends on some precision parameters which are not directly related to the tight coupling approximation. This causes the differences between Fig. 5.4 here and results in Fig. 4 of Ref. [1]. In the present case, we leave all precision parameters to their default settings. Because the default precision parameters are also used to obtain fits for observational data, we believe this gives the most meaningful comparison.

Our main conclusion [1] remains unaltered. The inconsistencies in the tight coupling approximation impact theory predictions for the CMB angular spectra at a level far below the experimental sensitivity. We further assess the effect on the matter power spectra and find it equally negligible. Even though we think it is important to have the formalism on a solid footing, the discrepancies should not modify constraints obtained in previous studies of dark matter-photon scattering [6, 294].

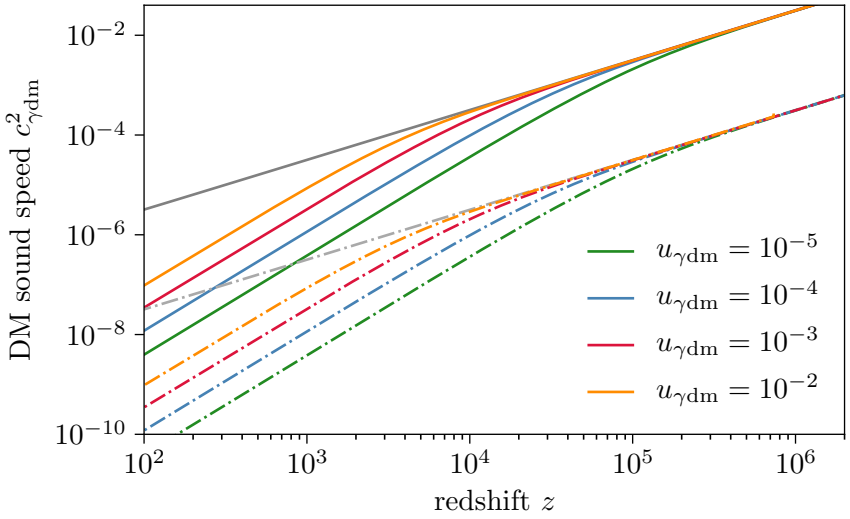

Figure 5.5: The dark matter sound speed for $m_{\gamma\mathrm{dm}} = 10\,\mathrm{keV}$ (solid lines) and $m_{\gamma\mathrm{dm}} = 1\,\mathrm{MeV}$ (dashed lines) as a function of redshift. Gray curves extrapolate the evolution, assuming that dark matter remains in kinetic equilibrium with photons at all times.

5.1.3 The dark matter sound speed

The dark matter sound speed was neglected in the preceding discussion. Because its magnitude is inversely proportional to the dark matter mass (3.6.8), discarding the sound speed is equivalent to considering the limit of large dark matter masses. Here, we quantify the threshold above which this large mass limit applies and investigate how the sound speed affects observational signatures.

We show the redshift dependence of the dark matter sound speed in Fig. 5.5, considering a lighter and a heavier dark matter particle and several possibilities for $u_{\gamma\mathrm{dm}}$. The effect of the dark matter mass on the magnitude of the sound speed is very apparent, it directly determines the overall scaling of the curves. Furthermore, from Fig. 5.5 two distinct phases in the evolution are noticeable. At early times, when dark matter is in kinetic equilibrium with photons, the coupling term in Eq. (3.6.9) determines the dark matter temperature and $T_{\gamma\mathrm{dm}} \simeq T_\gamma \propto a^{-1}$. In contrast, after dark matter has decoupled, its temperature redshifts as $T_{\gamma\mathrm{dm}} \propto a^{-2}$. The transition between both regimes is set by the normalised rate for dark matter-photon scattering and occurs later for larger values of $u_{\gamma\mathrm{dm}}$.

To estimate at which level the sound speed impacts CMB anisotropies, we consider several benchmark scenarios. In a first set, we fix the six ΛCDM parameters to their Planck best-fit values (see Tab. 2.1) and vary the dark matter mass and interaction strength. A second set considers the same ΛCDM parameters and interaction strengths but explicitly imposes $c^2_{\gamma\mathrm{dm}} = 0$. We then compare the values predicted for $l\,(l+1)\,/\,(2\pi)\,C_l$ by the corresponding scenarios, considering the TT-, TE- and EE-spectrum at multipoles up to $l = 2500$. This is about the range over which the Planck satellite has measured the CMB, and noticeable differences would affect the constraints presented in Sec. 5.3.

In Tab. 5.1, we give some examples for differences between our benchmark scenarios, obtained for $u_{\gamma\mathrm{dm}} = 0.01$. As expected, the observed differences only mildly depend on $u_{\gamma\mathrm{dm}}$

$m_{\gamma\mathrm{dm}}$	$l\,(l+1)\,/\,(2\pi)\;\Delta C_l^{\mathrm{TT}}$	$l\,(l+1)\,/\,(2\pi)\;\Delta C_l^{\mathrm{TE}}$	$l\,(l+1)\,/\,(2\pi)\;\Delta C_l^{\mathrm{EE}}$
10 keV	$13.4\,\mu\mathrm{K}^2$	$0.74\,\mu\mathrm{K}^2$	$0.08\,\mu\mathrm{K}^2$
1 MeV	$0.14\,\mu\mathrm{K}^2$	$0.007\,\mu\mathrm{K}^2$	$8\times10^{-4}\,\mu\mathrm{K}^2$
1 GeV	$0.003\,\mu\mathrm{K}^2$	$3\times10^{-4}\,\mu\mathrm{K}^2$	$4\times10^{-5}\,\mu\mathrm{K}^2$

Table 5.1: Maximal differences in the CMB spectra, generated by the dark matter sound speed, over the multipole range $2 \leq l \leq 2500$.

and decrease for smaller interaction parameters. In contrast, the differences vary strongly with the dark matter mass, and become largest for light dark matter candidates. For either spectrum, we observe that the inclusion of the dark matter sound speed affects our computations below the percent level, given that $m_{\gamma\mathrm{dm}} \gtrsim 10\,\mathrm{keV}$. In this case, the impact on the temperature autocorrelation is at most 0.3% and on the E-mode autocorrelation at most 0.8%. For dark matter even lighter than $\sim 10\,\mathrm{keV}$, the sound speed approaches unity when small modes of interest cross inside the Hubble radius. This would necessitate more profound modifications to the dark matter evolution, which are beyond the scope of this work. Therefore, we neglect the sound speed term when fitting the Planck data. As an advantage, this removes the dark matter mass as free parameter, which otherwise would be very weakly constrained by the data.

The CMB probes large cosmological scales. Those cross inside the Hubble radius late, when the sound speed is already small and only has a minor impact. In contrast, small scales in the matter power spectrum can indeed be sensitive to the dark matter sound speed. Today, these scales are in the non-linear regime, where n-body simulations are required to predict observable signatures [201,202,295,303]. Still, these simulations depend on the linear matter power spectrum to determine the initial conditions.

We present some examples for the matter power spectrum in presence of a sound speed term in Fig. 5.6. Clearly, the sound speed causes a decrease of small scale power. Thereby, the onset of the suppression is largely determined by the dark matter mass, which sets the overall scaling of $c^2_{\gamma\mathrm{dm}}$ as discussed previously. On the other hand, the suppression of structure caused by scattering terms in the Boltzmann equations is only sensitive to the normalised interaction rate, $u_{\gamma\mathrm{dm}}$. Whether the suppression due to the sound speed or due to the scattering terms dominates, depends on the precise combination of interaction strength and dark matter mass considered. When the dark matter sound speed gives the dominant contribution, the matter power spectrum is significantly altered with respect to the high mass limit but rather insensitive to changes in the dark matter interaction strength. The two scenarios with $m_{\gamma\mathrm{dm}} = 10\,\mathrm{keV}$ from Fig. 5.6 serve as an example for this case. Even though $u_{\gamma\mathrm{dm}}$ varies by two orders of magnitude, the scale at which the suppression sets in and the shape of $P(k)$ are only mildly affected. Transition to the latter limiting case, where the suppression is entirely caused by scattering terms, occurs earlier for larger $u_{\gamma\mathrm{dm}}$. Correspondingly, the zero sound speed limit is applicable for smaller dark matter masses if $u_{\gamma\mathrm{dm}}$ is larger. In any case, for a normalised scattering rate of $u_{\gamma\mathrm{dm}} \geq 10^{-9}$, we find that already a reasonably small dark matter mass of $m_{\gamma\mathrm{dm}} \simeq 1\,\mathrm{GeV}$ can be treated in the zero sound speed limit.

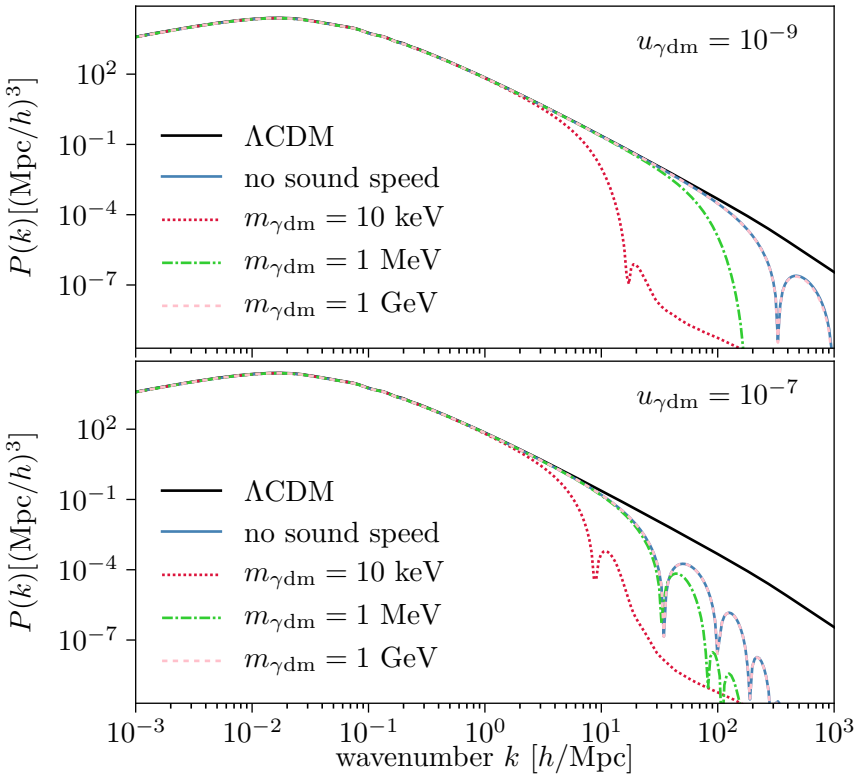

Figure 5.6: Impact of the dark matter sound speed on the linear matter power spectrum.

5.2 Data and methodology

5.2.1 The Planck likelihoods

At present, the best measurement of the CMB anisotropy spectrum on large scales, which are the most relevant for cosmology, is provided by the Planck satellite [15]. It operated from August 2009 to October 2013, scanned the intensity and the linear polarisation of the full microwave sky, and produced maps for nine frequencies between 25 GHz and 1000 GHz. Cosmological results were released in three major steps. The 2013 results [305] comprised mainly temperature data obtained over the first 14 month of the mission. In the 2015 release [5], full-mission results were published, while the final 2018 data [15] saw several updates to the analysis pipeline, in particular for the polarisation data. In this study, we exclusively consider data from the 2015 release.

The Planck maps are contaminated by instrumental noise, instrumental systematics and astrophysical foregrounds, all to be addressed before a meaningful comparison between the data and any theoretical model is possible. Cosmological models only predict the correlation of fluctuations, not the precise location of over- or underdensities. Accordingly, the Planck collaboration released their data in form of a likelihood code [231] which estimates, given a theoretical prediction for the CMB spectrum, the probability that it leads to the observed data. In this computation a hybrid approach is adopted, splitting the CMB spectra into a low multipole ($l \leq 29$) and a high multipole part.

For low multipoles, $l \leq 29$, the number of pixels is small, and the direct computation of

the likelihood in pixel space is feasible. The most important foregrounds at large scales are synchrotron emission by electrons in the galaxy's magnetic field, thermal bremsstrahlung from electrons in ionised hydrogen clouds (free-free emission), spinning dust emission caused by the dipole moment of dust grains in the interstellar medium [306] and thermal emission from galactic dust. These foregrounds are removed from the data by template fits [307], and, based on the χ^2 of the fit, low confidence regions are masked. The remaining polarisation map at 70 GHz covers 46% of the sky, and 7% of the sky are disguised from the CMB temperature maps. The power spectra are obtained from the cleaned, masked maps. Eventually, this results in the lowTEB likelihood for the C_l^{TT}, C_l^{TE}, C_l^{EE} and C_l^{BB} coefficients. A lowP likelihood, which excludes the temperature autocorrelation spectrum, would in principle also be available, but for the analysis in Sec. 5.3 we always consider the full lowTEB likelihood.

At high multipoles, $l \geq 30$, the strategy for obtaining likelihoods is based on a pseudo-C_l approach. To the debiased, deconvolved maps a numerical spherical harmonic transformation is applied, and a Gaussian approximation estimates the distribution of cross power spectra. The CMB is brightest between 70 GHz and 217 GHz. Three frequency channels fall in this range, at 100 GHz, 143 GHz and 217 GHz, which are considered for the maps. Foreground emission, especially that by galactic dust and radio point sources, is a significant contribution to the data and can exceed the CMB. The most contaminated regions are therefore excised from the maps, but still foregrounds contribute to the power spectra at high multipoles. Apart from the aforementioned galactic dust and radio point sources, there are contributions from the cosmic infrared background (CIB) and the Sunyaev–Zeldovich effect [308]. The former component, the CIB, is radiated by thermal dust in early galaxies. These are too distant to be spatially resolved, and their emission blurs into a smooth background. The latter, the Sunyaev–Zeldovich effect, arises when CMB photons Compton scatter with high energy electrons in galaxy clusters along the line of sight and, on average, receive an energy boost. It can be further classified into the thermal Sunyaev–Zeldovich (tSZ) effect, where the electron energy is due to high thermal velocities and the kinetic Sunyaev–Zeldovich (kSZ) effect, a much smaller contribution due to the bulk motion of the gas in the galaxy cluster. While the Sunyaev–Zeldovich effect is interesting on its own for the detection and study of galaxy clusters [309, 310], it has to be taken into account as a foreground in the analysis of CMB data. Fifteen nuisance parameters describe how calibration uncertainties and foregrounds contribute to the temperature autocorrelation spectrum. The nuisance parameters are inferred simultaneously with the cosmological parameters when computing fits for a model. Six additional parameters each characterise foregrounds in the E-mode autocorrelation spectrum and in the cross-correlation between temperature and E-mode polarisation. Extensive tests by the Planck collaboration [231] showed that, for the ΛCDM model, degeneracies between foreground and calibration parameters do not affect the determination of cosmological parameters in general. However, cosmological parameters are mildly correlated with the amplitudes of the point source contribution and of the Sunyaev–Zeldovich effect. In particular the latter is only weakly constrained by the Planck data. To keep the tSZ and

Name	Multipoles	Description	Nuisance parameters
lowTEB	$2 \leq l \leq 29$	temperature and polarisation, C_l^{TT}, C_l^{TE}, C_l^{EE}, C_l^{BB}	1 (redundant)
highTT	$30 \leq l \leq 2508$	temperature autocorrelation, C_l^{TT}.	15
highTTTEEE	$30 \leq l \leq 1996$ (polarisation)	temperature and polarisation, C_l^{TT}, C_l^{TE}, C_l^{EE}	27
lensing	$40 \leq l \leq 400$	CMB lensing, $C_l^{\varphi\varphi}$	1 (redundant)

Table 5.2: Overview of the Planck likelihoods considered in Sec. 5.3.

kSZ nuisance parameters from wandering into unphysical regions, which have already been excluded by ACT and SPT observations on small scales [311], the Planck collaboration imposes a Gaussian prior on their combined amplitude

$$l\,(l+1)\left[C_l^{\mathrm{kSZ}} + 1.6\,C_l^{\mathrm{tSZ}}\right] = (9.5 \pm 3)\ \mu\mathrm{K}\,. \tag{5.2.1}$$

In the following analysis, we consider either the temperature-only highTT likelihood or the full highTTTEEE likelihood for the C_l^{TT}, C_l^{TE} and C_l^{EE} coefficients. This split is necessary, because of residual systematics in the E-mode polarisation measurements at the $\mu\mathrm{K}^2$ level. Due to these systematics, results obtained with the highTTTEEE likelihood have to be interpreted with caution and are considered preliminary. The temperature likelihood at high multipoles, on the other hand, can be considered very robust [231], and its uncertainty is dominated by cosmic variance up to $l \lesssim 1586$.

Lensing potentials along the line of sight, finally, can be estimated from non-Gaussianities in the CMB fluctuations. There autocorrelation spectrum, $C_l^{\varphi\varphi}$, is included in the 2015 data release in form of a lensing likelihood [312], and we consider it for some of our fits. An overview of the previously discussed likelihoods is provided in Tab. 5.2.

5.2.2 Inference strategy

Eventually, the goal of our analysis is to determine what values the parameters of the interacting dark matter model can take, given the CMB spectra observed by Planck. Correlations between the dark matter-photon scattering parameter, $u_{\gamma\mathrm{dm}}$, the six ΛCDM parameters (1.3.2) and the likelihoods' nuisance parameters can not be excluded a priori, hence all have to be inferred simultaneously. The parameters' probability distribution, given the experimental results, is connected to the previously discussed likelihood, $\mathcal{P}\left(\boldsymbol{d}\,|\,\boldsymbol{\vartheta}, \mathcal{M}\right)$, by Bayes theorem

$$\mathcal{P}\left(\boldsymbol{\vartheta}\,|\,\boldsymbol{d}, \mathcal{M}\right) = \frac{\mathcal{P}\left(\boldsymbol{d}\,|\,\boldsymbol{\vartheta}, \mathcal{M}\right)\,\mathcal{P}\left(\boldsymbol{\vartheta}\,|\,\mathcal{M}\right)}{\mathcal{P}\left(\boldsymbol{d}\,|\,\mathcal{M}\right)}\,. \tag{5.2.2}$$

In this formulation, the vector $\boldsymbol{\vartheta}$ contains nuisance and cosmological parameters, $\boldsymbol{d}$ is the data vector and $\mathcal{M}$ denotes the model. Assumptions underlying the likelihood construction are equally addressed by $\mathcal{M}$ as the cosmological scenario. The Planck likelihoods evaluate the probability of the observed data given the coefficients C_l, rather than for a set of cosmological parameters. However, because the anisotropy spectrum is uniquely predicted by the cosmological parameters, this subtlety does not affect the following discussion. In the context of parameter inference, the evidence $\mathcal{P}(\boldsymbol{d} \,|\, \mathcal{M})$ is simply a normalisation constant and usually ignored [313].

Finally, the parameters' probability previous to the experimental results is reflected by the prior, $\mathcal{P}(\boldsymbol{\vartheta} \,|\, \mathcal{M})$. Common choices include Gaussian, uniformly flat or logarithmically flat priors, the latter being particularly popular for quantities that are unconstrained over several orders of magnitude. Priors are not invariant under a reparameterization, thus a flat prior, chosen to be possibly uninformative, can be strongly informative on a non-linear function of the original parameter [313]. In the context of one-sided parameter constraints, logarithmically flat priors pose the threat of assigning a large prior weight to regions where the data is uninformative. A further issue is the choice of prior boundaries. So would $u_{\gamma\mathrm{dm}} = 0$ be a natural lower bound in the dark matter-photon interacting scenario, but, considering logarithmic intervals, some negative number has to serve as proxy. Indeed, constraints derived on dark matter-photon interactions from logarithmic priors show considerable sensitivity to the interval range and can become unrealistically tight [314]. For this inference, we generally adopt uniformly flat priors apart from some rare, specially emphasised cases with Gaussian priors.

Given the full posterior, $\mathcal{P}(\boldsymbol{\vartheta} \,|\, \boldsymbol{d}, \mathcal{M})$, the probability of a single parameter ϑ_i is obtained from marginalisation over all other parameters [313]

$$\mathcal{P}(\vartheta_i \,|\, \boldsymbol{d}, \mathcal{M}) = \int \left(\prod_{j \neq i} d\vartheta_j \right) \mathcal{P}(\boldsymbol{\vartheta} \,|\, \boldsymbol{d}, \mathcal{M}) \ . \tag{5.2.3}$$

Only few cases exist where the posterior is analytically accessible, but the Planck CMB data is certainly not amongst them. To evaluate the likelihood at some point in parameter space, the angular power spectrum, C_l, is first computed with a Boltzmann code and then passed to the numerical Planck tools. The straightforward option, to explore the posterior numerically on a rectangular grid, is only feasible for a very small number of free parameters. Indeed, the required number of grid points scales exponentially with the dimensionality of the parameter space. Even for the simplest case studied here, with seven cosmological and 15 nuisance parameters, a different approach is required.

Sampling techniques allow to map the posterior distribution of high dimensional parameter spaces [315]. The approach is based on a set of independent samples, obtained by a procedure which ensures that the probability of taking taking a sample at a particular position is proportional to the posterior at that location. The number density of samples in parameter space then is proportional to the posterior. To find the expectation value of

a quantity of interest, $f(\boldsymbol{\vartheta})$, one can consider the estimator

$$E_f \equiv \frac{1}{N} \sum_{i=1}^{N} f(\vartheta_i) \; . \tag{5.2.4}$$

The central limit theorem states that, for a large enough number of samples, N, the probability of E_f tends towards a Gaussian, which is centred at $\langle f(\boldsymbol{\vartheta}) \rangle$ and has the variance $\sigma_E^2 = \sigma_f^2/N$, where σ_f^2 is the true variance for $f(\boldsymbol{\vartheta})$. The statement does not depend on whether $f(\boldsymbol{\vartheta})$ follows a Gaussian itself, so reliable estimates can be obtained for general distributions [315].

The most common method to generate appropriate samples are Monte Carlo Markov chains. Its name derives from the Markov property, meaning that the rule to obtain a sample at position $\boldsymbol{\vartheta}^{(i+1)}$ only depends on the previous point $\boldsymbol{\vartheta}^{(i)}$ but not on any earlier samples. The number density of samples is proportional to the posterior density if the transition probability, $\mathcal{T}\left(\boldsymbol{\vartheta}^{(i)}, \boldsymbol{\vartheta}^{(i+1)}\right)$, meets the condition of detailed balance [315]

$$\mathcal{P}\left(\boldsymbol{\vartheta}^{(i+1)} \,|\, \boldsymbol{d}, \mathcal{M}\right) \mathcal{T}\left(\boldsymbol{\vartheta}^{(i+1)}, \boldsymbol{\vartheta}^{(i)}\right) = \mathcal{P}\left(\boldsymbol{\vartheta}^{(i)} \,|\, \boldsymbol{d}, \mathcal{M}\right) \mathcal{T}\left(\boldsymbol{\vartheta}^{(i)}, \boldsymbol{\vartheta}^{(i+1)}\right) \; . \tag{5.2.5}$$

That is, if the probability of being at position $\boldsymbol{\vartheta}^{(i)}$ and going to $\boldsymbol{\vartheta}^{(i+1)}$ is the same a for being at $\boldsymbol{\vartheta}^{(i+1)}$ and going to $\boldsymbol{\vartheta}^{(i)}$. There is a number of possible definitions for the transition probability, and the efficiency of the sampling depends on this choice. Amongst the most common is the Metropolis-Hastings algorithm. Starting from the current position, $\boldsymbol{\vartheta}^{(i)}$, a new point is proposed from some arbitrary proposal density $\mathcal{Q}\left(\boldsymbol{\vartheta}^{(i)}, \boldsymbol{\vartheta}^{(i+1)}\right)$. This new point is accepted with probability

$$\mathcal{A}\left(\boldsymbol{\vartheta}^{(i)}, \boldsymbol{\vartheta}^{(i)}\right) = \min\left\{1\,, \; \frac{\mathcal{P}\left(\boldsymbol{\vartheta}^{(i+1)} \,|\, \boldsymbol{d}, \mathcal{M}\right) \mathcal{Q}\left(\boldsymbol{\vartheta}^{(i+1)}, \boldsymbol{\vartheta}^{(i)}\right)}{\mathcal{P}\left(\boldsymbol{\vartheta}^{(i)} \,|\, \boldsymbol{d}, \mathcal{M}\right) \mathcal{Q}\left(\boldsymbol{\vartheta}^{(i)}, \boldsymbol{\vartheta}^{(i+1)}\right)}\right\} \; , \tag{5.2.6}$$

such that the overall transition probability is [315]

$$\mathcal{T}\left(\boldsymbol{\vartheta}^{(i)}, \boldsymbol{\vartheta}^{(i+1)}\right) = \mathcal{A}\left(\boldsymbol{\vartheta}^{(i)}, \boldsymbol{\vartheta}^{(i+1)}\right) \mathcal{Q}\left(\boldsymbol{\vartheta}^{(i)}, \boldsymbol{\vartheta}^{(i+1)}\right) \; . \tag{5.2.7}$$

Otherwise, if the proposal is rejected, there are two samples at the exact same location. For a symmetric proposal probability, $\mathcal{Q}\left(\boldsymbol{\vartheta}^{(i)}, \boldsymbol{\vartheta}^{(i+1)}\right) = \mathcal{Q}\left(\boldsymbol{\vartheta}^{(i+1)}, \boldsymbol{\vartheta}^{(i)}\right)$, a new point is always accepted if it has a higher posterior than the current, and otherwise it is accepted with a probability that equals the ratio of posterior probabilities at the new and the current position.

For the application of the Metropolis-Hastings algorithm in practice, it is important to choose a proposal density which can be sampled easily. This choice will, however, affect the performance of the algorithm and how efficiently it explores the parameter space. An acceptance rate of order unity should be aspired for the method to perform well, realistic cases often achieve 0.2 to 0.3. Strong degeneracies between the model parameters confine the posterior to thin sheets in the high-dimensional parameter space and usually reduce the acceptance rate drastically. If known beforehand, such a situation is best avoided by adopting a suitable parameterisation of the problem with parameters as independent as

possible [315]. The choice of ΛCDM parameters stated in Eq. (1.3.2) is primarily motivated by this concern. Once the samples have been obtained, expectation values and confidence intervals can be derived according to Eq. (5.2.4).

A common choice for the proposal density is a Gaussian distribution whose covariance, if unknown, can be obtained from some short, preliminary chains. However, for the Planck data there already exist covariance matrices for the analysis of the ΛCDM scenario. Since the model we aim to study only contains one parameter more than ΛCDM, we find it practical to fall back to these covariance matrices. We augment them by an additional line and column for $u_{\gamma\mathrm{dm}}$, these contain an initial guess on the variance as diagonal entry and zeros otherwise. We then experiment with two different approaches. Either we compute a new covariance matrix from some initial chains and obtain our final results from it. Or we remain with the initial matrix throughout the analysis, and compensate for the reduced acceptance rate by requiring more samples in our chains. In either way, we obtain good convergence. Although the choice of a Gaussian proposal density is very practical and appropriate for many cases, it leads to poor acceptance rates if the posterior distribution significantly departs from a Gaussian, like, for example, in the case of "banana shaped" posteriors [315].

The estimate of parameters and confidence regions from Monte Carlo Markov chains is based on the assumption that each position is an independent sample of the underlying posterior. This, however, is only accurate asymptotically. At the beginning of the sampling process, the chains successively proceed to larger likelihoods, and in the case of multi-modal posteriors, a chain is likely to explore only one of the posterior maxima. An adequate way to determine whether the chain is sampling the underlying distribution correctly is to compare the results of multiple realisations of the sampling process. For an estimate to be reliable, the root mean square difference between individual chains' results should be much smaller than the posterior uncertainty. Following this logic, a possible measure for the convergence of chains is the Gelman-Rubin ratio [315]

$$R = \frac{\text{variance between chains}}{\text{mean variance within chain}}\,. \tag{5.2.8}$$

For reliable estimates, this ratio should tend to $R-1 \sim 0$. Practically, we aim for $R < 0.05$ at least [316].

We use the MontePython v2.2.2 [316] implementation of the Metropolis-Hastings algorithms to sample our model's posterior distribution. Monte Python is interfaced with our modified CLASS [288] version for the computation of CMB angular spectra. Finally, the likelihood is provided by the Planck software plc-2.0.

5.3 Planck constraints

5.3.1 Parameters and data sets

Our baseline cosmological model has seven free parameters, six of which are the same as in ΛCDM (1.3.2) and the additional dark matter-photon scattering parameter $u_{\gamma\mathrm{dm}}$. For all we assume flat priors. As in the original Planck analyses, we consider two massless and one massive neutrino species, for the latter we choose $m_\nu = 0.06\,\mathrm{eV}$. The effective number of neutrinos (1.2.17) is fixed to the Standard Model expectation $N_{\mathrm{eff}} = 3.046$. In what follows we refer to this set of parameters as "γdm". We also test scenarios in which the effective neutrino number is free to vary, again assuming flat priors on all parameters and fixing the neutrino mass. This set we denote as "$\gamma\mathrm{dm} + N_{\mathrm{eff}}$". Finally, we obtain results for the canonical ΛCDM case, setting $u_{\gamma\mathrm{dm}} = 0$ (denoted as "ΛCDM"). By comparing our ΛCDM results to those published by the Planck collaboration we can cross-check that our analysis pipeline is performing correctly.

As baseline parameter set we consider the low-multipole temperature and polarisation likelihood (lowTEB) and the temperature cross-correlations spectrum at high multipoles (highTT). In addition, we also obtain results from the full temperature and polarisation likelihood at high multipoles (highTTTEEE). Further, we extend either of these inferences by including the lensing likelihood (lensing). The respective likelihoods and the naming convention we use for them are also summarised in Tab. 5.2.

For some scenarios we find that inferred value of H_0 is in less than 2σ tensions with local Cepheids measurement of Ref. [114]. Those scenarios are reanalysed, replacing $100\,\theta_*$ by H_0 as a free parameter and assuming a Gaussian prior for it, namely $H_0 = 73.24 \pm 1.75$ km(s Mpc)$^{-1}$. The corresponding results are denoted by the extension "+ R16".

5.3.2 ΛCDM cross-checks

We infer the cosmological parameters for the ΛCDM scenario using the lowTEB + highTT and the lowTEB + highTTTEEE data sets. Comparing our results with those published by the Planck collaboration[2], we observe that some of the nuisance parameters differ by as much as 1σ. Those parameters affected worst describe the amplitude of the thermal Sunyaev–Zeldovich effect at 143 GHz (A^{tSZ}_{143}), the amplitude of the kinetic Sunyaev–Zeldovich effect (A^{kSZ}) and the contributions of point sources to the power spectrum at 100 GHz and at 143 GHz (A^{PS}_{100} and A^{PS}_{143}). While our results overestimate contributions from the Sunyaev–Zeldovich effect, they underestimate the amplitudes related to point sources.

We believe that this discrepancy originates from the additional prior, which the Planck collaboration applies to the combined amplitudes of the thermal and the kinetic Sunyaev–Zeldovich effect [7], see Eq. (5.2.1). While the Planck collaboration uses the Cos-

[2] http://wiki.cosmos.esa.int/planckpla2015/images/f/f7/Baseline_params_table_2015_limit68.pdf

data set	lowTEB + highTT		lowTEB + highTT + lensing	
scenario	γdm	γdm + $N_{\rm eff}$	γdm	γdm + $N_{\rm eff}$
$\Omega_{\rm b}\,h^2$	$0.02231^{+0.00022}_{-0.00025}$	$0.02238^{+0.00036}_{-0.00039}$	$0.0223^{+0.00023}_{-0.00024}$	$0.0224^{+0.00034}_{-0.00039}$
$\Omega_{\gamma{\rm dm}}\,h^2$	0.1198 ± 0.0023	$0.1208^{+0.0039}_{-0.0043}$	0.119 ± 0.002	0.1203 ± 0.004
$100\,\theta_*$	$1.042324^{+0.00048}_{-0.00064}$	$1.042443^{+0.00076}_{-0.00056}$	$1.042350^{+0.0005}_{-0.00054}$	$1.042182^{+0.00069}_{-0.00079}$
$\ln(10^{10}A_{\rm s})$	$3.094^{+0.033}_{-0.038}$	$3.1^{+0.043}_{-0.050}$	$3.072^{+0.028}_{-0.030}$	$3.082^{+0.033}_{-0.045}$
$n_{\rm s}$	$0.9661^{+0.0061}_{-0.0064}$	$0.9696^{+0.014}_{-0.017}$	$0.9672^{+0.0055}_{-0.0063}$	$0.9721^{+0.015}_{-0.016}$
$\tau_{\rm re}$	$0.08005^{+0.018}_{-0.019}$	$0.08205^{+0.018}_{-0.025}$	$0.07022^{+0.016}_{-0.017}$	$0.07405^{+0.015}_{-0.022}$
$10^{+4}\ u_{\gamma{\rm dm}}$	< 2.254	< 2.142	< 1.805	< 1.818
$N_{\rm eff}$	3.046	$3.137^{+0.29}_{-0.35}$	3.046	$3.161^{+0.30}_{-0.33}$
H_0 [3]	$67.56^{+0.94}_{-1.00}$	$68.27^{+2.6}_{-2.9}$	$67.83^{+0.91}_{-0.93}$	$68.78^{+2.5}_{-3.0}$
σ_8	$0.8003^{+0.029}_{-0.02}$	$0.8057^{+0.032}_{-0.028}$	$0.7942^{+0.024}_{-0.014}$	$0.7999^{+0.028}_{-0.023}$

Table 5.3: Cosmological parameters obtained from the baseline data set in the dark matter-photon interacting scenario. Upper and lower bounds correspond to the 68 C.L. interval, while upper limits are quoted at 95% C.L..

moMC package [299,317] to sample the parameter space, the MontePython implementation only accounts for priors on individual parameters but not for cross-correlations.

Ultimately, we are only interested in the correct determination of the model parameters. The central values obtained for them vary by at most 0.4σ with respect to Planck results. In particular, the parameter for which discrepancies are the largest is the optical depth to reionisation. Comparable shifts have been obtained by the Planck collaboration, comparing results obtained with the codes CAMB and PICO [231]. To further verify the validity of our results, we use the "lite" likelihood, which has been marginalised over nuisance parameters and thus is unaffected by the issue described above. We find a very good agreement between the confidence intervals for cosmological parameters extracted from the "lite" and the full likelihood. Therefore we believe the intervals found for our model parameters are accurate.

5.3.3 Results based on the high-multipole temperature spectrum

Using our baseline data set (lowTEB + highTT), we can constrain all seven parameters of the γdm model as well as the eight parameters in the γdm + $N_{\rm eff}$ case. These results are summarised in Tab. 5.3. We also present the constraints obtained when extending the baseline data by the lensing likelihood. From the lowTEB + highTT data set, we find a 95 % C.L. upper limit on the dark matter-photon scattering cross section of $\sigma_{\gamma{\rm dm}} \leq 2.25\times10^{-6}\ \sigma_{\rm T}\ (m_{\gamma{\rm dm}}/{\rm GeV})$. This limit is about 20% stronger than those derived previously [285] from the 2013 Planck data release. The constraint tightens up by another 20% when the lensing data is included in the analysis.

[3] H_0 is given in units of km/(Mpc s)

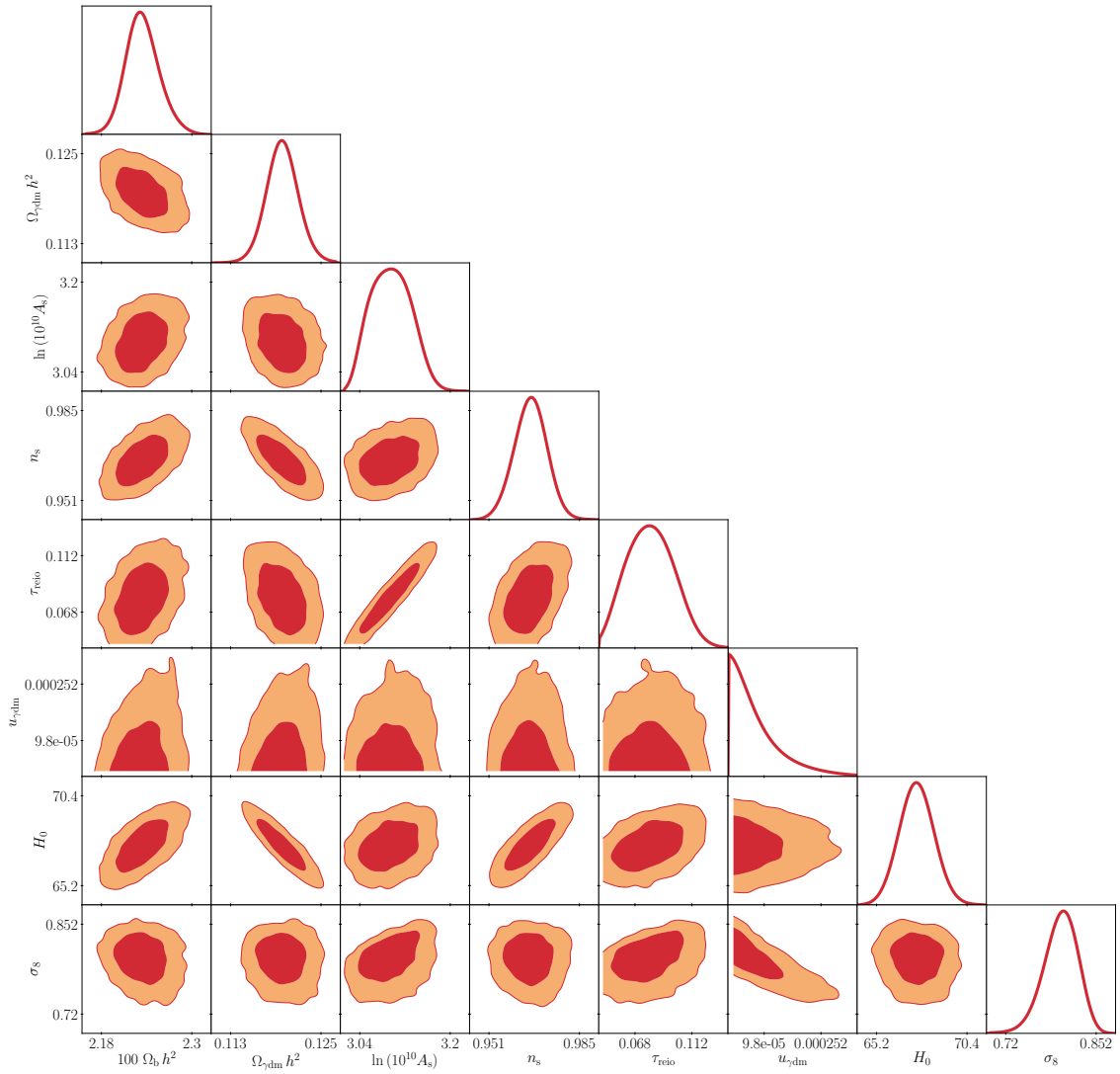

Figure 5.7: One and two dimensional posterior distributions for selected cosmological parameters obtained from the lowTEB + highTT baseline parameter set for the γdm scenario, assuming flat priors. The two dimensional contours depict 68% (red) and 95% (orange) confidence levels respectively.

Treating the effective number of neutrinos as a free parameter only marginally affects the limits on $u_{\gamma dm}$. While the central values of $N_{\rm eff}$ lie somewhat above the Standard Model prediction, $N_{\rm eff} = 3.046$, the difference remains well below 1σ for all scenarios. However, for the scenarios where $N_{\rm eff}$ is free to vary, we observe a slight increase of H_0. Two different causes are possible. First, interactions between dark matter and photons increase the magnitude of the first acoustic CMB peaks and shift them to larger multipoles, a larger Hubble constant counteracts those effects. Second, already in the ΛCDM scenario there is a degeneracy between H_0 and $N_{\rm eff}$, that effects a rise of the Hubble constant when the effective number of neutrinos is free to vary. The Planck collaboration reported $H_0 = 68.0^{+2.6}_{-3.0}$ km/(s Mpc) for the ΛCDM scenario when analysing the lowTEB + highTT data sets for variable $N_{\rm eff}$ and $H_0 = 68.5^{+2.5}_{-3.0}$ km/(s Mpc) by adding the lensing data. The similarity with our constraints from Tab. 5.3 indicates that H_0 is well constrained

from the CMB data and cannot be significantly altered by the inclusion of dark matter-photon scattering. The robustness of H_0 constraints with respect to dark matter-photon interactions is further supported from the two dimensional posterior distributions. One example, considering the baseline lowTEB + highTT data set and the γdm scenario, is shown in Fig. 5.7. Dark matter-photon scattering leads to a decreased amplitude for small-scale anisotropies, and if this effect is leading the constraint indeed no degeneracy with H_0 would be expected. Nevertheless, because the tension with local H_0 measurements [114] is below 2σ, we study the combined analysis of the γdm + $N_{\rm eff}$ scenario from the lowTEB + highTT and the R16 data sets and present the corresponding results in Sec. 5.3.5.

Finally, we note that all the data sets reported in this section prefer a smaller central value and larger confidence limits for σ_8 than in the ΛCDM scenario. The Planck collaboration reported $\sigma_8 = 0.829 \pm 0.014$ for the lowTEB + highTT analysis and $\sigma_8 = 0.8149 \pm 0.0093$ with the addition of lensing data. Allowing $N_{\rm eff}$ to vary these intervals become $\sigma_8 = 0.834^{+0.022}_{-0.025}$ and $\sigma_8 = 0.820^{+0.018}_{-0.021}$ respectively. In comparison, our value of σ_8 decreases by roughly 3% (see Tab. 5.3) while the size of the lower confidence interval increases by about 50% when $N_{\rm eff}$ is kept fixed and 10% if it is free to vary. These combined effects reduce the tensions with the KiDS-450 measurement $\sigma_8\sqrt{\Omega_m/0.3} = 0.745 \pm 0.039$. [104] below 1σ. The reason for the change becomes apparent in Fig. 5.2, where we show the linear matter power spectrum for various interaction strengths. Dark matter-photon interactions lead to a suppression of power on small scales. The largest value of the elastic scattering cross section to mass ratio, that is allowed by CMB observations, leads to a visible suppression of the linear matter power spectrum at 8 Mpc, precisely. Correspondingly, we note a degeneracy between $u_{\gamma\rm dm}$ and σ_8 in the two dimensional posterior shown in Fig. 5.7, where a larger dark matter-photon scattering parameter prefers a smaller value for σ_8.

5.3.4 Parameter constraints considering high-multipole polarisation

Our results obtained under the inclusion of high-multipole polarisation data are summarised in Tab. 5.4. The additional information from polarisation at small scales further tightens the constrain $u_{\gamma\rm dm}$. Including data from temperature and polarisation at low and high multipoles as well as lensing potentials, the limit at 95% C.L. becomes as small as $\sigma_{\gamma\rm dm} \leq 1.49 \times 10^{-6}\ \sigma_{\rm T}\ (m_{\gamma\rm dm}/\rm GeV)$. This makes the constraint 35% stronger than that derived in Ref. [285].

The addition of small-scale polarisation data partially breaks the degeneracy between H_0 and $N_{\rm eff}$. Now, the data requires values of H_0, which are too low to reduce tensions with local measurements below 2σ, even if $N_{\rm eff}$ is free to vary. All our results on $N_{\rm eff}$ are perfectly compatible with the Standard Model expectation.

As in the previous section, we find lower values for σ_8 than in the ΛCDM scenario. Namely the Planck collaboration reports $\sigma_8 = 0.831 \pm 0.013$ for the lowTEB + highTTTEEE data set and $\sigma_8 = 0.8150 \pm 0.0087$ if lensing data is included. Allowing $N_{\rm eff}$ to vary, this

[4] H_0 is given in units of km/(Mpc s)

data set	lowTEB + highTTTEEE		lowTEB + highTTTEEE + lensing	
scenario	γdm	γdm + $N_{\rm eff}$	γdm	γdm + $N_{\rm eff}$
$\Omega_{\rm b}\,h^2$	0.02228 ± 0.00016	$0.02221^{+0.00022}_{-0.00026}$	$0.02228^{+0.00015}_{-0.00017}$	$0.02218^{+0.00022}_{-0.00024}$
$\Omega_{\gamma{\rm dm}}\,h^2$	$0.1201^{+0.0014}_{-0.0016}$	$0.1192^{+0.0030}_{-0.0032}$	$0.1197^{+0.0015}_{-0.0014}$	$0.1182^{+0.0031}_{-0.0028}$
$100\,\theta_*$	$1.042057^{+0.00034}_{-0.00039}$	$1.042218^{+0.00059}_{-0.00061}$	$1.042119^{+0.00037}_{-0.00038}$	$1.042306^{+0.00054}_{-0.00056}$
$\ln(10^{10}A_s)$	$3.097^{+0.038}_{-0.028}$	$3.087^{+0.035}_{-0.039}$	$3.069^{+0.021}_{-0.028}$	$3.06^{+0.026}_{-0.028}$
$n_{\rm s}$	$0.964^{+0.0046}_{-0.0048}$	$0.961^{+0.0096}_{-0.0095}$	$0.9646^{+0.0051}_{-0.0047}$	$0.9604^{+0.0091}_{-0.0095}$
$\tau_{\rm re}$	$0.08107^{+0.019}_{-0.016}$	$0.07734^{+0.016}_{-0.018}$	$0.06755^{+0.012}_{-0.014}$	$0.06557^{+0.012}_{-0.014}$
$10^{+4}\ u_{\gamma{\rm dm}}$	< 1.579	< 1.623	< 1.490	< 1.359
$N_{\rm eff}$	3.046	$2.974^{+0.20}_{-0.21}$	3.046	$2.943^{+0.19}_{-0.20}$
H_0 [4]	$67.33^{+0.67}_{-0.66}$	66.8 ± 1.6	$67.52^{+0.66}_{-0.60}$	$66.78^{+1.5}_{-1.6}$
σ_8	$0.8103^{+0.024}_{-0.018}$	$0.8036^{+0.027}_{-0.021}$	$0.7982^{+0.022}_{-0.012}$	$0.7946^{+0.021}_{-0.016}$

Table 5.4: Cosmological parameters for dark matter-photon interacting scenarios from data sets including high-multipole polarisation. Upper and lower bounds correspond to 68% C.L. intervals, while upper limits are given at 95% C.L..

confidence limits become $\sigma_8 = 0.828 \pm 0.018$ and $\sigma_8 = 0.809 \pm 0.013$. Even for the tighter constraints on $u_{\gamma{\rm dm}}$, provided by high-multipole polarisation, damping in the matter power spectrum sets in close enough to 8 Mpc to cause the decrease. Consequently, all data sets presented here are in less than 1σ tension with the KiDS-450 measurement of σ_8.

5.3.5 Combination with local measurements of H_0

For those scenarios where $N_{\rm eff}$ is free to vary and high-multipole polarisation data is excluded, the tension between the value inferred for H_0 and local measurements [114] is less than 2σ. However, applying an Gaussian prior on the Hubble constant that reflects the R16 results, we notice that larger values of H_0 and $N_{\rm eff}$ are not supported by CMB data. That is true even when dark matter-photon scattering is allowed, and the corresponding results are summarised in Tab. 5.5. In both cases studied, H_0 only shifts very slightly and tensions remain at 1.9σ and 1.7σ respectively. Likewise, $N_{\rm eff}$ experiences only a small shift towards larger values, remaining compatible with the Standard Model expectation at the 1σ level.

5.4 Discussion

In the standard ΛCDM model, dark matter is completely collisionless. Yet, the late kinetic decoupling between dark matter and photons leads to observational signatures not only in the CMB temperature and polarisation spectra, but also affect the matter power spectrum.

[5] H_0 is given in units of km/(Mpc s)

data set	lowTEB + highTT	lowTEB + highTT + lensing
scenario	γdm + $N_{\rm eff}$	
$\Omega_{\rm b}\,h^2$	$0.02241^{+0.00036}_{-0.00039}$	$0.02246^{+0.0031}_{-0.0046}$
$\Omega_{\gamma{\rm dm}}\,h^2$	$0.1212^{+0.0034}_{-0.0044}$	0.1208 ± 0.0039
H_0 [5]	$68.36^{+2.6}_{-3.0}$	$69.27^{+2.3}_{-3.5}$
$\ln(10^{10} A_s)$	$3.104^{+0.04}_{-0.05}$	$3.089^{+0.037}_{-0.047}$
$n_{\rm s}$	$0.9704^{+0.014}_{-0.017}$	$0.9746^{+0.012}_{-0.02}$
$\tau_{\rm re}$	$0.08369^{+0.018}_{-0.025}$	$0.07686^{+0.017}_{-0.021}$
$10^{+4}\ u_{\gamma{\rm dm}}$	< 2.488	< 1.724
$N_{\rm eff}$	$3.154^{+0.27}_{-0.35}$	$3.215^{+0.25}_{-0.39}$
σ_8	$0.805^{+0.035}_{-0.025}$	$0.8048^{+0.027}_{-0.025}$

Table 5.5: Cosmological parameters in dark matter-photon interacting scenarios considering a R16 inspired prior. Upper and lower bounds correspond to the 68% C.L. interval, while upper limits are given at 95% C.L..

In light of the null-results obtained at colliders and direct detection experiments these imprints provide an alternative, highly complementary opportunity to investigate the particle physics nature of dark matter.

To ensure the robustness of theory predictions in the linear regime, we review the governing formalism, explicitly deriving the modified Boltzmann equations (Sec. 3.6), the source functions for the line of sight integration (Sec. 4.1), and modifications to the tight coupling approximation (Sec. 4.2). Various expressions have been used in the past for the tight coupling approximation. We show that these discrepancies only affect the computed CMB spectra at the $0.01\mu{\rm K}^2$ level, well below the experimental sensitivity. However, we think it self-sufficient to have the formalism standing on a solid footing. Dark matter-photon interactions lead to non-zero dark matter sound speed. The inclusion of such a term affects the CMB predictions at a sub-percent level and hence can be neglected in this context. Its effect on the matter power spectrum can, however, be sizeable and has the potential to strengthen constraints, especially for light dark matter candidates.

We perform a similar analysis to Ref. [277,285] and include the full 2015 Planck temperature, polarisation, and lensing data. Already from the high multipole temperature data, i.e. the lowTEB + highTT data set, we obtain a 20% tighter constraint than those based on the 2013 data release [285], giving $\sigma_{\gamma{\rm dm}} \leq 2.25 \times 10^{-6}\,\sigma_{\rm T}\,(m_{\gamma{\rm dm}}/{\rm GeV})$ at 95% confidence level. Further improvement are achieved by considering lensing and high-multipole polarisation data, leading to an overall decrease by 35% with respect to the results of Ref. [285]. However, our tightest constraint, $\sigma_{\gamma{\rm dm}} \leq 1.49 \times 10^{-6}\,\sigma_{\rm T}\,(m_{\gamma{\rm dm}}/{\rm GeV})$ (at 95% confidence level), based on the lowTEB + highTTTEEE + lensing data set, has to be taken with a grain of salt. The Planck collaboration considers the high-multipole polarisation data as preliminary due to unresolved systematics of $\mathcal{O}(\mu{\rm K}^2)$. The Planck 2018 data release [15] provides more accurate polarisation data and can further improve constraints on $u_{\gamma{\rm dm}}$.

The prior dependence of interacting dark matter scenarios is explicitly addressed by Ref. [314]. While the linear flat and Jeffrey's prior produce mutually consistent results within 20%, bounds from logarithmically flat priors are sensitive to the precise values adopted for the boundaries and can bear artificially tight constraints. The conservative result from Ref. [314], $\sigma_{\gamma\mathrm{dm}} \leq 1.72 \times 10^{-6}\,\sigma_\mathrm{T}\,(m_{\gamma\mathrm{dm}}/\mathrm{GeV})$, derived from the lowTEB + highTTTEEE + lensing data set under the assumption of a Jeffrey's prior agrees with our limits.

The energy transfer between dark matter and photons due to the intrinsically different scaling relations of their respective temperatures was neglected in our study. Depending on the dark matter mass and the scattering cross section, the photons' energy loss changes the effective number of radiative degrees of freedom [318]. The difference amounts to $|\Delta N_\mathrm{eff}| \sim \mathcal{O}\left(10^{-3}\right)$ for most of the parameter space and hence does not affect our results. However, the thermal coupling between non-relativistic dark matter and photons also effects spectral distortions, i.e. departures from a perfect black body spectrum, in the CMB. Constraints on the magnitude of spectral distortions from COBE/FIRAS [87] place limits on the dark matter-photon scattering rate, in particular for light dark matter candidates, and impose $\sigma_{\gamma\mathrm{dm}} \leq 1.5 \times 10^{-9}\,\sigma_\mathrm{T}\,(m_{\gamma\mathrm{dm}}/\mathrm{GeV})$ for $m_{\gamma\mathrm{dm}} \lesssim 0.1\,\mathrm{MeV}$. A future experiment like PIXIE could extend this limit to $m_{\gamma\mathrm{dm}} \sim 1\,\mathrm{GeV}$ [319]. Also cosmological perturbations impact spectral distortions, on an level to which future experiments, like PRISM [320], are sensitive. The prospective constraint extends to heavier dark matter masses and becomes competitive with current CMB limits, namely $\sigma_{\gamma\mathrm{dm}} \leq 1.65 \times 10^{-6}\,\sigma_\mathrm{T}\,(m_{\gamma\mathrm{dm}}/\mathrm{GeV})$ [321].

The scale at which departures between the ΛCDM and the interacting scenario emerge decreases with the scattering parameter $u_{\gamma\mathrm{dm}}$. Despite its robustness, the CMB has only limited sensitivity to small scales. Studies of the abundance of dwarf galaxies can improve constrains by several orders of magnitude but are subject to larger theory uncertainties from the correct modelling of baryonic effects. Dark matter-only n-body simulations of Milky Way like halos obtained $\sigma_{\gamma\mathrm{dm}} \leq 5.5{\times}10^{-9}\,\sigma_\mathrm{T}\,(m_{\gamma\mathrm{dm}}/\mathrm{GeV})$ [303]. Subsequent studies of halo properties, in particular spin and concentration, found that the missing satellite and the too-big-to-fail problem (c.f. Sec. 2.2.5) are alleviated for $\sigma_{\gamma\mathrm{dm}} \sim 10^{-9}\,\sigma_\mathrm{T}\,(m_{\gamma\mathrm{dm}}/\mathrm{GeV})$. The latter value, however, is in mild tension with the latest constraints on dark matter-photon scattering, obtained from the measurements of the reionisation history and counts of Milky Way satellites analysed with a semi-analytical approach, $\sigma_{\gamma\mathrm{dm}} \leq 8{\times}10^{-10}\,\sigma_\mathrm{T}\,(m_{\gamma\mathrm{dm}}/\mathrm{GeV})$.

Currently, Milky Way satellite counts reach the best sensitivity to dark matter-photon interactions, but results from the CMB anisotropy spectrum are far more robust. Probing the matter power spectrum between these two extremes and searching for the imprint of dark matter particle properties is one of the science goals of the Euclid mission [322]. Euclid can constrain dark matter-photon scattering through its impact on the linear matter power spectrum at considerably smaller scales than the CMB. Such an analysis requires precise theory predictions and up-to-date constraints on the possible interaction strength [323]. In this regard, the presented assessment of systematic errors in the theory predictions and the updated Planck constraints make an important contribution.

Chapter 6

On the effect of multi-component dark matter

The existence of multiple dark matter components, which differ in their particle physics properties, is a natural extension to the canonical scenario of a single, pressureless fluid. Hidden sectors have been studied extensively. However, the simplest examples contain the dark matter particle itself and a mediator, whose abundance becomes suppressed in the late universe [324]. Small scale problems, amongst others, motivate us to consider admixtures of cold and warm or hot dark matter, recent limits on such scenarios are e.g. given in Ref. [325]. Multi component dark matter in the sense that species differ in their kinetic decoupling, on the other hand, have not received much attention. Some exceptions are the case of dark matter interactions with dark radiation. A small fraction of such an interacting dark matter has the potential to alleviate tensions between independent measurements of H_0 and σ_8 [326]. Dissipative interactions between two dark matter components can affect non-linear cosmological structure formation [327] and are interesting in the context of small scale problems. Finally, for an example where dark matter interacts with the Standard Model, a decaying component which features interactions with photons affects weak lensing signals [328]. This model, however, constitutes a special case, where the dark matter decoupling time is fixed at recombination.

Here, we take a first step towards a more general understanding of mixed dark matter models featuring interactions with the Standard Model. Concretely, we study two-component dark matter, of which one component is collisionless and the other scatters elastically with photons. The damping of small scale perturbations in this scenario has a rich and interesting phenomenology. Especially the impact of a small fraction of interacting dark matter on the matter power spectrum is very similar to that of massive neutrinos. This begs the risk of confusing the two scenarios when searching for a signal of non-zero neutrino masses in future large-scale structure surveys.

We start our discussion by establishing the mixed damping scenario and the governing equations in Sec. 6.1, and discuss the relevant physical effects in Sec. 6.2. Finally, we confront our predictions with existing CMB measurements by Planck and perform a Fisher forecast to assess the ability of future large-scale structure survey to discriminate between massive neutrinos and interacting dark matter in Sec. 6.4.

6.1 The mixed dark matter scenario

There are two distinct dark matter components in the scenario considered. The former, denoted as "CDM", is truly collisionless at all times and on all scales relevant to the CMB and large-scale structure. The latter "γdm" component, alike the dark matter model discussed in Sec. 5, features elastic interactions with photons, which fall out of equilibrium some time prior to recombination. We assume a constant cross section, $\sigma_{\gamma\mathrm{dm}}$, for the scattering process and express its impact in terms of the normalised scattering parameter $u_{\gamma\mathrm{dm}}$, defined in Eq. (3.6.4) as

$$u_{\gamma\mathrm{dm}} = \frac{\sigma_{\gamma\mathrm{dm}}}{\sigma_{\mathrm{T}}} \left(\frac{m_{\gamma\mathrm{dm}}}{100\,\mathrm{GeV}}\right)^{-1} .$$

Further, the total dark matter abundance is the sum of the individual components, i.e. $\Omega_{\mathrm{dm}} = \Omega_{\mathrm{cdm}} + \Omega_{\gamma\mathrm{dm}}$, and we define the interacting dark matter fraction as

$$f_{\gamma\mathrm{dm}} \equiv \frac{\Omega_{\gamma\mathrm{dm}}}{\Omega_{\mathrm{dm}}} . \tag{6.1.1}$$

To embed this phenomenological description in a full particle physics model of dark matter would require the specification of a production mechanisms for either component. Before the respective comoving densities settle to the relic abundance, the interacting dark matter fraction is time dependent. Because the main objective of our study is to investigate the general impact of multi-component dark matter, we avoid these additional complications and presume that dark matter production completed before any modes of interest crossed into the Hubble radius.

The evolution equations for collisionless dark matter are given in Eqs. (3.3.8) and those for the collisional component in Eqs. (3.6.6). The sound speed of the collisional component in principle introduces and additional parametric dependence on the dark matter mass. However, for $m_{\gamma\mathrm{dm}} \gtrsim \mathcal{O}(\mathrm{GeV})$ its effect is negligible. In the following we focus on the heavy dark matter limit. Conveniently, this implies that the assumption of a constant $f_{\gamma\mathrm{dm}}$ is automatically satisfied for dark matter produced from freeze out.

The photon evolution is affected by the cold dark matter component only indirectly, through its contribution to the gravitational potentials. The collisional component, on the other hand, directly enters the term for the photon velocity, see Eqs. (3.6.2) for the full, coupled photon hierarchy. Alongside with the modified Boltzmann hierarchy, we also consider the modifications to the line of sight integration (4.1.18) and the tight coupling approximation (4.2.38), required by the presence of dark matter-photon scattering. All modifications to the photon evolution caused by dark matter interactions depend on the scattering rate $\kappa'_{\gamma\mathrm{dm}} = a\, n_{\gamma\mathrm{dm}}\, \sigma_{\gamma\mathrm{dm}}$. The fact that interacting dark matter contributes only a fraction to the total dark matter abundance is reflected in a reduction of the number density, $n_{\gamma\mathrm{dm}}$, with respect to the fully interacting scenario.

Baryon and neutrino perturbations, finally, are affected by the mixed dark matter scenario only indirectly, through the gravitational potentials. Their evolution equations maintain their canonical form given in Eq. (3.3.9), Eq. (3.3.12) and in Eqs. (3.4.24), respectively.

To evolve the coupled Boltzmann and Einstein equations numerically, we modified the Boltzmann code CLASS v2.6[1] [288]. The changes demanded by mixed dark matter are more comprehensive than in the purely interacting scenario. Rather than modifying the dark matter and photon equations, we now introduce an additional dark matter species and account for its effect on the background evolution and on the metric potentials. In an extensive set of cross-checks we firstly impose $u_{\gamma\mathrm{dm}} = 0$ and compare the results for various fractions of interacting dark matter to ΛCDM predictions. Second, we set $f_{\gamma\mathrm{dm}} = 1$, vary $u_{\gamma\mathrm{dm}}$, and consider the implementation of purely interacting dark matter from the previous section as reference. In all cases we find that the CMB spectra and the matter power spectrum agree to the level of the numerical accuracy.

6.2 Phenomenological implications of mixed dark matter

Our numerical implementation of the mixed dark matter scenario in CLASS enables us to precisely predict the CMB angular spectra and the matter power spectrum in the linear regime. In this section we discuss how these observables are affected by the presence of an interacting component supplemental to the canonical collisionless dark matter.

6.2.1 CMB temperature and polarisation spectra

The phenomenological implications of purely interacting dark matter are discussed in the previous chapter, Sec. 5.1, where we identify three major effects on the CMB angular spectra. These are an increase of the first acoustic peak, a shift of the peaks towards larger multipoles and the damping of power on small scales.

The same features are present in the mixed dark matter case, as Fig. 6.1 reveals. There, we have chosen a large interaction strength parameter of $u_{\gamma\mathrm{dm}} = 0.01$ to make all effects visible by eye. Modifications to the ΛCDM predictions become less pronounced as the fraction of interacting dark matter decreases, and the mixed dark matter spectra are intermediate between the purely collisional and the ΛCDM case. The fraction of interacting dark matter, $f_{\gamma\mathrm{dm}}$ controls the interpolation between the two limiting cases.

6.2.2 Matter power spectrum

While the CMB spectra of purely interacting and of mixed dark matter are closely related, this is not the case for the matter power spectrum, where the impact of mixed dark matter can considerably differ from the purely interacting scenario. In the pure-γdm scenario, the matter power spectrum exhibits a characteristic cut-off scale and, proceeding from the cut-off to larger wavenumbers, a series of damped oscillations. As one example, we show the matter power spectrum for $u_{\gamma\mathrm{dm}} = 10^{-5}$ in Fig. 6.2 in comparison to several mixed dark matter realisations of equal interaction strengths. Several features are common to all mixed dark matter scenarios:

[1] Our modified code is publicly available from https://github.com/bufeo/class_v2.6_mixedDM.git.

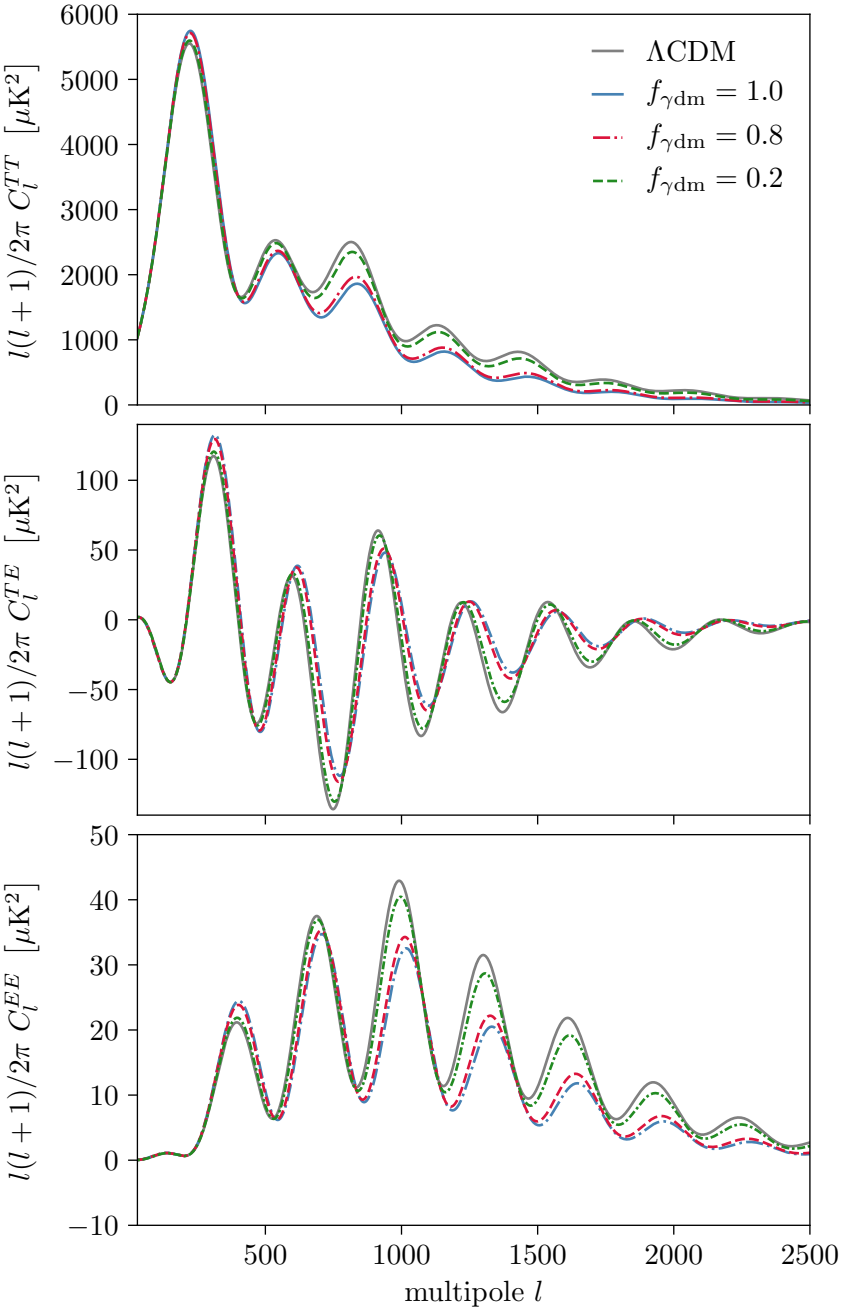

Figure 6.1: CMB angular spectra predicted in the mixed dark matter scenario for an interaction strength parameter of $u_{\gamma\mathrm{dm}} = 0.01$ and varying fractions of interacting dark matter.

a) On large scales there is no difference between ΛCDM, pure-γdm and mixed DM.

b) On intermediate scales, those following the cut-off scale for pure-γdm, there is a suppression of power. The decrease is more pronounced for larger fractions of interacting dark matter. In particular can a large fraction of interacting dark matter produce less power in this regime than pure-γdm.

c) On small scales, the mixed-DM power spectrum evolves parallel to the ΛCDM one but with reduced magnitude. The reduction is controlled by the fraction of interacting dark matter and less pronounced if $f_{\gamma\mathrm{dm}}$ is smaller.

The classification applies regardless of the precise value of $u_{\gamma\mathrm{dm}}$, but the cross section to mass ratio controls the wavenumber where the transition between individual regimes occurs.

The ΛCDM-like behaviour on the large scales of region (a) is understood easily. These modes enter the Hubble radius after dark matter has kinetically decoupled from photons, and therefore are not affected by the scattering processes. The time of dark matter decoupling, $a_{\gamma\mathrm{dm,dec}}$, is determined by the condition

$$\mathcal{H}\left(a_{\gamma\mathrm{dm,dec}}\right) = \kappa'_{\gamma\mathrm{dm}}\left(a_{\gamma\mathrm{dm,dec}}\right) = \left.\frac{4\,\rho_\gamma}{3\,\rho_{\gamma\mathrm{dm}}}\,a\,n_{\gamma\mathrm{dm}}\,\sigma_{\gamma\mathrm{dm}}\right|_{a_{\gamma\mathrm{dm,dec}}} . \tag{6.2.1}$$

Because the energy density of non-relativistic matter is proportional to its number density, both quantities cancel in the second equality. The time of dark matter kinetic decoupling is therefore independent of $f_{\gamma\mathrm{dm}}$ and given by Eq. (5.1.3a). In contrast, the scale factor at which photons decouple from dark matter is proportional to the dark matter number density. Its value in the purely interacting scenario (5.1.3b) is reduced by a factor $f_{\gamma\mathrm{dm}}$ for the mixed dark matter case.

A striking feature of mixed dark matter is the reduction of power at intermediate scales even in comparison to the purely interacting scenario. To illustrate its cause, we show the evolution of a single mode with wavelength $k = 5\,h/\mathrm{Mpc}$, interaction strength $u_{\gamma\mathrm{dm}} = 10^{-5}$ and varying dark matter fractions in the top panel of Fig. 6.3. In the matter power spectrum of Fig. 5.2, this mode precisely lies at the dip. The matter power spectrum (1.2.3) measures the magnitude of the density contrast in Fourier space, but is insensitive to the phase. Perturbations in the collisionless component start to grow upon entering the Hubble radius and their growth always proceeds in the negative direction. The collisional component, in contrast, participates in the oscillation of the photon baryon plasma, which modifies the mode's phase. Upon decoupling, the perturbation in the collisional component starts to grow in the positive direction.

Both modes depicted in Fig. 6.3 enter the Hubble radius before matter-radiation equality ($a_{\mathrm{eq}} \simeq 3.0 \times 10^{-4}$), and the growth of matter perturbations accelerates once the universe has transitioned to the matter-dominated epoch. In this era, the gravitational potentials are dominated by matter perturbations and both components, the collisional and the

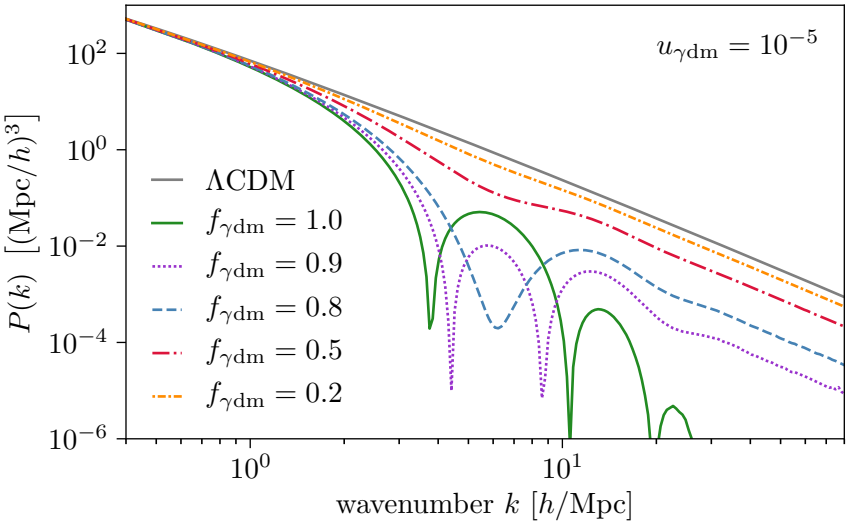

Figure 6.2: The linear matter power spectrum predicted for several scenarios of mixed dark matter with an interacting strength of $u_{\gamma\mathrm{dm}} = 10^{-5}$. Only the smallest scales, where a departure from the ΛCDM predictions becomes evident, are shown.

collisionless one, act as sources. For example, the source term of the time-time component of the Einstein equations (3.2.17) becomes

$$\delta\rho \simeq \rho_{\mathrm{dm}} \left[(1 - f_{\gamma\mathrm{dm}})\, \delta_{\mathrm{cdm}} + f_{\gamma\mathrm{dm}}\, \delta_{\gamma\mathrm{dm}}\right] + \rho_{\mathrm{b}}\, \delta_{\mathrm{b}}\,. \tag{6.2.2}$$

Two factors are decisive for the late time evolution of perturbations: the time passed between Hubble crossing and kinetic decoupling of the γdm perturbation, and the fraction of interacting dark matter. If the γdm component spends only a short time in the coupled regime and simultaneously there is a significant fraction of interacting dark matter, the γdm component dominates the potentials and eventually determines the evolution of the dark matter perturbations as a whole. This is the case for $f_{\gamma\mathrm{dm}} = 0.9$ in the top panel of Fig. 6.3, where the collisional component overturns the collisionless one. For all other mixed dark matter scenarios in Fig. 6.3, the fraction of interacting dark matter is too small for the γdm-component to dominate. Because cold dark matter perturbations start growing upon horizon entry and the γdm component experiences collisional damping, perturbations in the collisionless component dominate even for a comparably large fraction of interacting dark matter. In these cases, the collisional component experiences the turn around after matter-radiation equality. The larger the fraction of collisionless dark matter, the earlier the turn around occurs. Regardless of which species comes to dominate the evolution, the growth of perturbations is hampered while the collisional and the collisionless component compete.

For an intuitive understanding of how the competition between dark matter components hinders the growth of perturbations, it is useful to consider the configuration in position space. There, the phase shifts between CDM and γdm perturbations correspond to a configuration in which overdensities in the collisional component predominantly coincide with underdense regions in the collisionless component and vice versa. Hence, perturbations

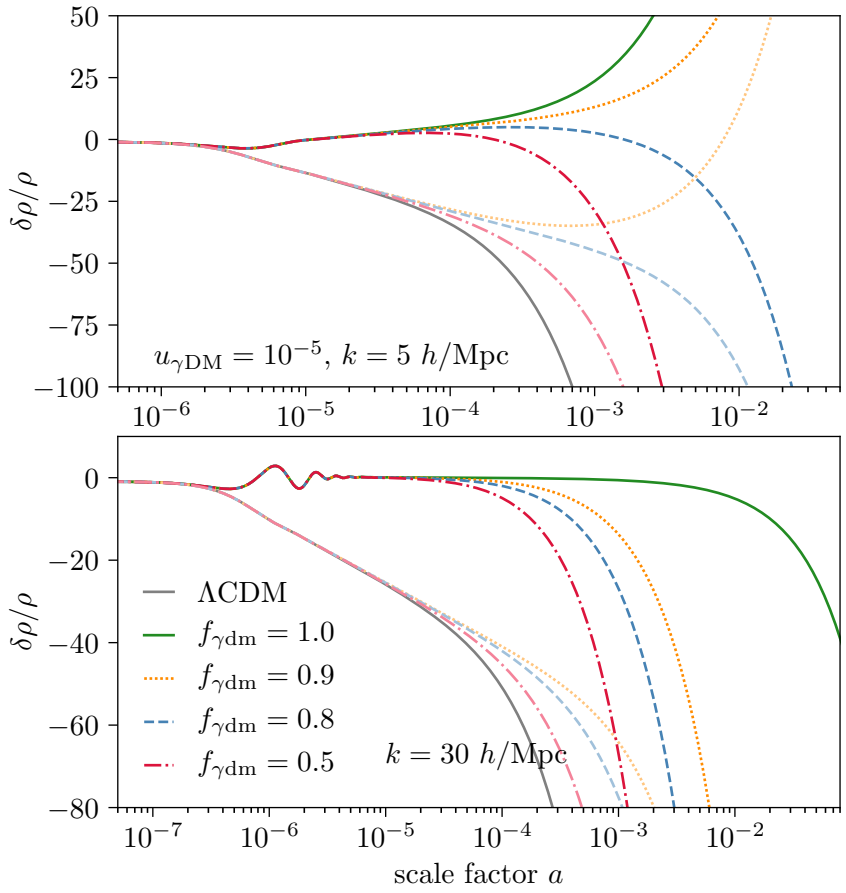

Figure 6.3: Time evolution of the density contrast in the γdm (bold colours) and the CDM (pastel colours) component. The remaining model parameters are chosen to match those of the matter power spectrum in Fig. 6.2.

in the individual dark matter species partially chancel each other, and the potential wells are less deep than they would be for single component dark matter of either kind.

The cancellation between individual dark matter components is less severe if perturbations in the γdm component are sufficiently suppressed. This is the case for modes in region (c), which cross the Hubble radius earlier. By the time the pressure from photon interaction ceases, perturbations in the CDM component are already well developed, and the γdm component falls in their potential wells. Some examples are shown in the bottom panel of Fig. 6.3, where the γdm component follows the collisionless evolution regardless of the fraction of interacting dark matter. Still, because the potential wells are less deep initially, there is a suppression in the matter power spectrum on the scales in region (c). This suppression is the more severe the larger $f_{\gamma\mathrm{dm}}$.

6.2.3 Comparison with the case of heavy neutrinos

In many respects, the mixed dark matter scenario is similar to a ΛCDM cosmology with heavy neutrinos. After weak decoupling when $T_\gamma \sim 1\,\mathrm{MeV}$, neutrinos behave as hot dark matter, that is as a relativistic, collisionless fluid. Flavour oscillations indicate that at least

two neutrino states are massive, but provide only lower bounds on their masses (1.2.19). Given these constraints [43], at least two states have transitioned to the non-relativistic regime before the present epoch, at a scale factor of

$$a_{\nu,\mathrm{nr}} = \frac{\left(\frac{4}{11}\right)^{1/3} T_{\gamma,0}}{m_\nu} \simeq 2.80 \times 10^{-3} \times \left(\frac{m_\nu}{0.06\,\mathrm{eV}}\right)^{-1} . \tag{6.2.3}$$

In either scenario, mixed dark matter and ΛCDM with heavy neutrinos, a fraction of the late-time dark matter abundance arises from a component which does not evolve as a cold, collisionless fluid at early times. In the former case, interacting dark matter transitions from the collisional to the collisionless regime, in the latter, neutrinos develop from hot into cold dark matter.

At the present epoch, the contribution from heavy neutrinos to the critical density is

$$\Omega_\nu h^2 = \frac{3\,g_\nu}{4} \frac{\xi\,(3)}{\pi^2} \frac{4}{11} T_\gamma^3 \times \left(\sum m_\nu\right) \simeq 6.39 \times 10^{-4} \left(\frac{\sum m_\nu}{0.06\,\mathrm{eV}}\right) , \tag{6.2.4}$$

where $g_\nu = 2$ counts the internal degrees of freedom of a single mass state. The fractional contribution of neutrinos to the present matter density is denoted as

$$f_\nu \equiv \frac{\Omega_\nu}{\Omega_\mathrm{m}} . \tag{6.2.5}$$

There is a subtle difference between this definition and the interacting dark matter fraction (6.1.1). While the former is normalised with respect to the total dark matter abundance, i.e. $\Omega_\mathrm{dm} = \Omega_\mathrm{cdm} + \Omega_{\gamma\mathrm{dm}}$, also baryons and neutrinos contribute to Ω_m in Eq. (6.2.5). In contrast to mixed dark matter, where a priori $f_{\gamma\mathrm{dm}}$ can take any value between zero and one, observational bounds on the neutrino mass imply a neutrino fraction much smaller than unity. More precisely, within the ΛCDM model Eq. (1.2.19) and Eq. (2.3.20) imply $0.005 \lesssim f_\nu \lesssim 0.01$.

Neutrinos behave identicaly to cold dark matter on large scales which enter the Hubble radius after $a_{\nu,\mathrm{nr}}$, and the transition is characterised by the comoving wave number

$$k_{\nu,\mathrm{nr}} = (a\,H)|_{a=a_{\nu,\mathrm{nr}}} = 0.0024\,\mathrm{Mpc}^{-1} \left(\frac{0.06\,\mathrm{eV}}{m_\nu}\right)^{-1/2} \left(\frac{0.142}{\Omega_\mathrm{m} h^2}\right)^{-1/2} . \tag{6.2.6}$$

On smaller scales, free streaming prevents the neutrinos from clustering and initially suppresses their perturbations. Only when neutrinos have become non-relativistic, they fall into the dark matter potential wells. In this epoch, the neutrino density contrast grows faster than the characteristic $\propto a$ evolution during matter domination to catch up with δ_dm. However, due to the strong initial suppression, only modes very close to $k_{\nu,\mathrm{nr}}$ reach the asymptote, on smaller scales $\delta_\nu \ll \delta_\mathrm{dm}$ persists up to the present epoch [88]. The lack of small scale structure in the neutrino sector displays in the matter power spectrum as a suppression on scales below $k_{\nu,\mathrm{nr}}$. Back reaction of the neutrino perturbations on the metric perturbations further amplifies the suppression. Perturbations grow by gravitational instability and are diluted by the universe's expansion, in a matter-dominated universe both effects cancel at the level of metric perturbations, which remain constant. Below

$k_{\nu,\mathrm{nr}}$ neutrinos contribute to the expansion but not to the density contrast. The unbalance causes the slow decay of the metric perturbations and impedes the growth of dark matter perturbations [88]. Eventually, the cumulative effect of massive neutrinos is to suppress the matter power spectrum below the free streaming scale by a factor $\sim 8f_\nu$ with respect to a scenario characterised by identical Ω_m but massless neutrinos [329].

Galaxy surveys are sensitive to the power suppression induced by heavy neutrinos [330], and thus to the neutrino mass scale. The effect, however, strongly resembles the impact of mixed dark matter with a small fraction of interacting dark matter, see Fig. 2.1 for an example. In the following we explore the vulnerability of cosmological neutrino mass bounds to the presence of mixed dark matter further. In particular, we obtain limits on the mixed dark matter scenario from Planck CMB data and perform a Fisher forecast for the Dark Energy Spectroscopic Instrument (DESI) [331] survey.

6.3 Data and methodology

6.3.1 Neutrino mass measurements from galaxy surveys

Neutrino oscillations established that neutrinos have non-zero masses [40–42], and probe the mass difference between states [43]. Cosmology, in contrast, is primarily sensitive to the sum of neutrino masses. The neutrino mass scale can also be probed in the laboratory, by the kinematics of β-decay and, if neutrinos are Majorana particles, by searches for neutrinoless double-β ($0\nu2\beta$) decay [332]. The strongest laboratory limits at present, $m_{\nu_\mathrm{e}} \leq 2\,\mathrm{eV}$ from tritium decay [19], are surpassed by cosmological constraints $\sum m_\nu \leq 0.12\,\mathrm{eV}$ [4]. In the future, β-decay measurements, such as the ongoing KATRIN experiment [333] and Project8 [334], can improve the laboratory limit by an order of magnitude, and $0\nu2\beta$ searches have the potential to discover a mass around 0.020 eV at 3σ significance [335]. In comparison, redshift surveys in combination with Planck data and possibly lensing surveys, are expected to measure the sum of neutrino masses to $\sim (0.01 - 0.02)$ eV in the next decade [264]. The disadvantage of these cosmological limits is their dependence on the assumed cosmology, and bounds can weaken significantly when more complex models with additional free parameters are considered [265]. In this regard, a detection of the neutrino mass scale with cosmology is also a crucial test for the consistency with laboratory probes [264].

Here, we focus on prospective neutrino mass constraints from the Dark Energy Spectroscopic Instrument (DESI) [331]. In combination with Planck data, DESI is expected to measure the neutrino mass sum to at least 0.02 eV at 68% C.L. for the minimal allowed value of 0.06 eV [9]. DESI is a ground based experiment at the Mayall telescope in Kitt Peak, Arizona. The instrument is devised to track the redshift evolution of the matter power spectrum, which is sensitive to the dark energy equation of state and modifications of general relativity. Over a duration of five years, DESI will cover a survey area of 14,000 square degrees at wavelength $360\,\mathrm{nm} \leq \lambda \leq 980\,\mathrm{nm}$. First light is planned for January

2020 and the first data assembly for a cosmology analysis for April 2022. The survey considers three types of tracers of the matter power spectrum: luminous red galaxies (LRGs), emission line galaxies (ELGs) and quasars (QSOs). Luminous red galaxies are massive galaxies with no recent star formation, DESI expects to observe 4×10^6 of them over a redshift range $0.4 \lesssim z \lesssim 1.0$. Emission line galaxies, which have a high star formation rate and exhibit strong emission line features in their spectra, are more abundant in the survey with 1.71×10^7 observations expected for $0.6 \lesssim z \lesssim 1.7$. Ly-α absorption lines in quasar spectra offer sensitivity to hydrogen clouds along the line of sight, and, in addition, quasars directly serve as tracers. The observation of 1.7×10^6 quasars at redshifts $0.9 \lesssim z \lesssim 2.1$ is expected in the former mode and, continuing to higher redshifts $2.1 \lesssim z \lesssim 3.5$, about 7×10^5 Ly-α spectra [336].

6.3.2 Fisher forecast

To investigate DESI's sensitivity to mixed dark matter and to the neutrino mass in the presence of mixed dark matter, we perform a Fisher forecast. This standard tool is often used to predict how well future experiments can determine cosmological parameters. It is based on the Fisher information matrix, defined as the second derivative of the log-likelihood $\mathcal{L}$ with respect to the parameters of interest ϑ_i [337, 338]

$$F_{ij} = -\left\langle \frac{\partial^2 \ln \mathcal{L}}{\partial \vartheta_i \, \partial \vartheta_j} \right\rangle . \tag{6.3.1}$$

The angle brackets indicate an ensemble average over the experimental data expected for a fiducial model with parameters $\vartheta_i^{\mathrm{fid}}$. Further, the likelihood in the Fisher matrix formalism is identical to the definition used earlier in Eq. (5.2.2), i.e. $\mathcal{L} = \mathcal{P}\left(\boldsymbol{d} \,|\, \boldsymbol{\vartheta}, \mathcal{M}\right)$. An estimation of the fiducial parameter's prospective error follows from the Cramér-Rao bound

$$\sigma_{ij}^2 \geq \left(F^{-1}\right)_{ij} , \tag{6.3.2}$$

which states that that no unbiased estimator can perform better than the Fisher matrix error. Thus, after marginalisation over all other parameters, a single parameter ϑ_i can at best be measured with accuracy $\left(F^{-1}\right)_{ii}$. The equality applies for Gaussian likelihoods, in more general cases the Fisher matrix formalism can only provide an optimistic estimate.

The combined likelihood of several, independent experiments is given by the product of their individual likelihoods. Accordingly, Eq. (6.3.1) implies that the Fisher matrices of several observations can be added to estimate their combined error [338]. This is particularly useful to judge the complementarity of experiments. Following the same line

C.L.	68.3%	95.5%	99.7%
$\Delta\chi^2$	2.30	6.18	11.8

Table 6.1: The value of $\Delta\chi^2$ for two dimensional confidence contours at the level of 1σ, 2σ and 3σ, respectively [8].

of thought, a Fisher matrix with the respective 1σ intervals on its diagonal can account for (Gaussian) prior information, for example from a previous experiment [339].

Two dimensional confidence regions are useful, for example to search for parameter degeneracies. They can be estimated from the inverse Fisher matrix by taking the rows and columns of interest and inverting this sub-matrix back. The resulting 2×2 matrix, denoted as D, describes a two dimensional Gaussian likelihood surface [338]

$$\chi^2 = \sum_{i,j} \left(\vartheta_i - \vartheta_i^{\mathrm{fid}}\right) D_{ij} \left(\vartheta_j - \vartheta_j^{\mathrm{fid}}\right) , \tag{6.3.3}$$

where χ^2 refers to the chi-square distribution. Surfaces of constant $\chi^2 = \Delta\chi^2$ define the boundaries of confidence intervals, and Tab. 6.1 quotes the correspondence between the value of $\Delta\chi^2$ and some most common choices for the confidence level in two dimensions [8]. The two dimensional confidence regions of a Gaussian probability distributions are always ellipses, whose semi-major axis a and, the semi-minor axis b and the rotation angle α are given by

$$a = \sqrt{\Delta\chi^2} \left(\frac{D_{ii} + D_{jj}}{2} + \sqrt{\frac{\left(D_{ii} - D_{jj}\right)^2}{4} + D_{ij}^2} \right)^{-1/2} , \tag{6.3.4a}$$

$$b = \sqrt{\Delta\chi^2} \left(\frac{D_{ii} + D_{jj}}{2} - \sqrt{\frac{\left(D_{ii} - D_{jj}\right)^2}{4} + D_{ij}^2} \right)^{-1/2} , \tag{6.3.4b}$$

$$\tan\left(2\alpha\right) = \frac{2D_{ij}}{D_{ii} - D_{jj}} . \tag{6.3.4c}$$

For poorly constrained parameters or in cases where the likelihood is very non-Gaussian, results obtained by a Fisher forecast have to be interpreted with caution. In particular should the obtained error estimates not be taken too literally, but regarded as optimistic estimates. The comparison with Monte Carlo Markov chain likelihood sampling showed, for example, that the Fisher matrix can not reproduce the highly non-elliptical shapes when the dark energy equation of state is determined from purely geometrical probes, such as supernovae and baryon acoustic oscillations. The consequence is an underestimation of the error on w_0 and w_a by $30\% - 70\%$ [340]. In the context of cluster surveys, the Fisher forecast performs well for minimal cosmological models, but, concerning modifications to the equation of state, the results vary by $30\% - 100\%$ in comparison with MCMC sampling [341]. Still, even in these weakly constrained cases, the sense that a constraint is poor is generally preserved by the Fisher forecast [9].

To estimate the Fisher matrix of galaxy surveys, one can consider the tracer two-point correlation $P_{\mathrm{tt}}\left(k\right)$ as observable. That is the n-th entry to the data vector $\boldsymbol{d}$ is the average power spectrum measured in a thin shell of radius k_n in Fourier space [342]. Tracers are biased with respect to the underlying matter distribution $P\left(k\right)$, c.f. Sec. 2.2.2. Restricting the analysis to large scales, we assume a linear bias b_{t} such that

$$P_{\mathrm{tt}}\left(k, \mu\right) = \left(b_{\mathrm{t}} + \beta\mu^2\right)^2 P\left(k\right) . \tag{6.3.5}$$

The second contribution in the parenthesis is proportional to the cosine, μ, between a mode's wavevector $\boldsymbol{k}$ and the line of sight, and to the growth rate $\beta \equiv d\ln\left(\sqrt{P\left(k,a\right)}\right)/d\ln a$ [148]. This term accounts for redshift space distortions, i.e. the fact that galaxies are observed in redshift space rather than real space, and corrects the redshift space power spectrum for the effect of peculiar motions [343].

Under the assumption that the likelihood is a multivariant, n-dimensional Gaussian with covariance C and mean $\boldsymbol{m}$,

$$\mathcal{L} = \frac{1}{\sqrt{(2\pi)^n\ |C|}}\ \exp\left[-\frac{1}{2}\left(\boldsymbol{x}-\boldsymbol{m}\right)\ C^{-1}\ \left(\boldsymbol{x}-\boldsymbol{m}\right)^{\dagger}\right]\,, \tag{6.3.6}$$

the Fisher matrix (6.3.1) becomes

$$F_{ij} = \frac{1}{2}\mathrm{tr}\left(C^{-1}\,\frac{\partial\, C}{\partial\vartheta_i}\,C^{-1}\,\frac{\partial\, C}{\partial\vartheta_j}\right) + \frac{\partial\,\boldsymbol{m}^{\dagger}}{\partial\vartheta_i}\,C^{-1}\,\frac{\partial\,\boldsymbol{m}}{\partial\vartheta_j}\,. \tag{6.3.7}$$

Two main sources of statistical uncertainty contribute to the covariance of $P_{\mathrm{tt}}\left(k,\mu\right)$, cosmic variance, due to the finite survey volume, and Poissonian shot noise in the counting of galaxies. Their combined variance is

$$\frac{\sigma_{\mathrm{P}}\left(k\right)}{P_{\mathrm{tt}}\left(k\right)} = \frac{P_{\mathrm{tt}}\left(k\right)+n_{\mathrm{t}}^{-1}}{P_{\mathrm{tt}}\left(k\right)}\,, \tag{6.3.8}$$

where n_{t} refers to the number density of the tracer population, averaged over redshifts. Nearby modes in a survey with finite volume are highly correlated over a cell size of $(2\pi)^3/V_{\mathrm{survey}}$. If all available modes are to be considered for Eq. (6.3.7) nevertheless, their individual contribution needs to be weighted down by a factor $2\pi\sqrt{2/\left(K^2\,\delta k\,\delta\mu\,V_{\mathrm{survey}}\right)}$, where δk and $\delta\mu$ define the bin size [338]. If the shell size δk is small compared to the survey volume, the first term in Eq. (6.3.7) dominates [342] the variance. Promoting the sum over k_n, which is implicit in the trace, into a continuous integral, the Fisher matrix is [338, 342]

$$F_{ij} = \int_{-1}^{1}\int_{k_{\mathrm{min}}}^{k_{\mathrm{max}}} \frac{k^2\,dk d\mu}{2\,(2\pi)^3}\ \frac{\partial\,\ln P_{\mathrm{tt}}\left(k\,,\mu\right)}{\partial\vartheta_i}\frac{\partial\,\ln P_{\mathrm{tt}}\left(k\,,\mu\right)}{\partial\vartheta_j}\,V_{\mathrm{eff}}\left(k\,,\mu\right)\,, \tag{6.3.9}$$

where the effective volume is

$$V_{\mathrm{eff}} = \left(\frac{n\,P\left(k\,,\mu\right)}{1+n\,P\left(k\,,\mu\right)}\right)^2\,V_{\mathrm{survey}}\,. \tag{6.3.10}$$

The lower integration limit in Eq. (6.3.9) is set by the survey design, only modes with $k_{\mathrm{min}} \geq 2\pi/\sqrt[3]{V_{\mathrm{survey}}}$ fit into its volume. For the upper limit we choose $k_{\mathrm{max}} = 0.2\,h/\mathrm{Mpc}$ to exclude highly non-linear scales.

In surveys with multiple tracers, the relative clustering between different types of tracers improves constraints beyond the limit expect from cosmic variance arguments [344]. Considering the effective power of a tracer $P_{\alpha}^{\mathrm{eff}} = n_{\alpha}\,P_{\alpha}$ as parameter of interest, which should

be inferred from the data, the multi-tracer Fisher matrix is [344, 345]

$$F_{\alpha\beta} = \frac{1}{4}\left[\frac{P_\alpha^{\rm eff}\,P_{\rm tot}^{\rm eff}}{1+P_{\rm tot}^{\rm eff}}\,\delta_{\alpha\beta} + \frac{P_\alpha^{\rm eff}P_\beta^{\rm eff}\left(1-P_{\rm tot}^{\rm eff}\right)}{\left(1+P_{\rm tot}^{\rm eff}\right)^2}\right] . \tag{6.3.11}$$

Here, $P_{\rm tot}^{\rm eff} = \sum_\alpha P_\alpha^{\rm eff}$ is the total effective power. A parameter transformation generalises the result to an alternative set of free parameters ϑ_i

$$F_{ij} = \sum_{\alpha,\beta}\int \frac{d^3k\,d^3x}{(2\pi)^3}\frac{d\,\log P_\alpha^{\rm eff}}{d\vartheta_i}F_{\alpha\beta}\frac{d\,\log P_\beta^{\rm eff}}{d\vartheta_j} . \tag{6.3.12}$$

6.4 Observational impact of mixed dark matter

6.4.1 Parameter space allowed by the CMB

To constrain the mixed damping parameter space from CMB measurements, we use the approach of Sec. 5.2.2 and interface our modified CLASS version with the MCMC sampling code MontePython version 3.0.1 [316, 346]. As data set we consider the lowTEB + highTT + lensing combination of likelihoods from the Planck 2015 data release [231], see Tab. 5.2.

Our results show that the posterior is very non-Gaussian shaped in the $(u_{\gamma{\rm dm}}, f_{\gamma{\rm dm}})$ plane. Although MCMC sampling still provides valid results, the use of a Gaussian proposal density decreases the acceptance rate and slows down the chain's convergence. The situation can be somewhat improved by sampling over two auxiliary parameters, $u_{\gamma{\rm dm}}^{\pm}$ and $f_{\gamma{\rm dm}}^{\pm}$, which can take positive and negative values. They are related to the physical parameters as

$$u_{\gamma{\rm dm}} = \left|u_{\gamma{\rm dm}}^{\pm}\right| , \quad f_{\gamma{\rm dm}} = \left|f_{\gamma{\rm dm}}^{\pm}\right| . \tag{6.4.1}$$

Given the samples of the auxiliary parameters, the physical parameters' expectation values follow directly from Eq. (5.2.4). For all cosmological and nuisance parameters we adopt flat priors, and the ranges for the auxiliary parameters are $u_{\gamma{\rm dm}}^{\pm} \in [-10^{-3}, 10^{-3}]$ and $f_{\gamma{\rm dm}}^{\pm} \in [-1, 1]$.

The parameter space allowed by Planck data for the mixed damping scenario is shown in Fig. 6.4. If the fraction of interacting dark matter is large, the interaction strength parameter $u_{\gamma{\rm dm}}$ can be fairly well constrained. The limits, however, weaken considerably as $f_{\gamma{\rm dm}}$ decreases, and for less than 10% interacting dark matter there no longer are restrictions on $u_{\gamma{\rm dm}}$. A large scattering rate can be compensated by a small fraction of interacting dark matter, and, vice versa, a large γdm abundance is allowed if the cross section to mass ratio is small.

Further, we probe explicitly what cross sections to mass ratios are allowed if the fraction of interacting dark matter is fixed to 50% and to 10%. For these inferences we extend the prior range for $u_{\gamma{\rm dm}}$ to $u_{\gamma{\rm dm}}^{\pm} \in [-10^{-2}, 10^{-2}]$, and obtain $u_{\gamma{\rm dm}}^{(50\%)} < 5.36\times10^{-4}$ and $u_{\gamma{\rm dm}}^{(10\%)} < 3.18\times10^{-2}$ at 95% C.L.. In comparison to the purely interacting scenario, where $u_{\gamma{\rm dm}} < 1.81\times10^{-4}$ (c.f. Tab 5.3), the bound relaxes just mildly when only half of the dark

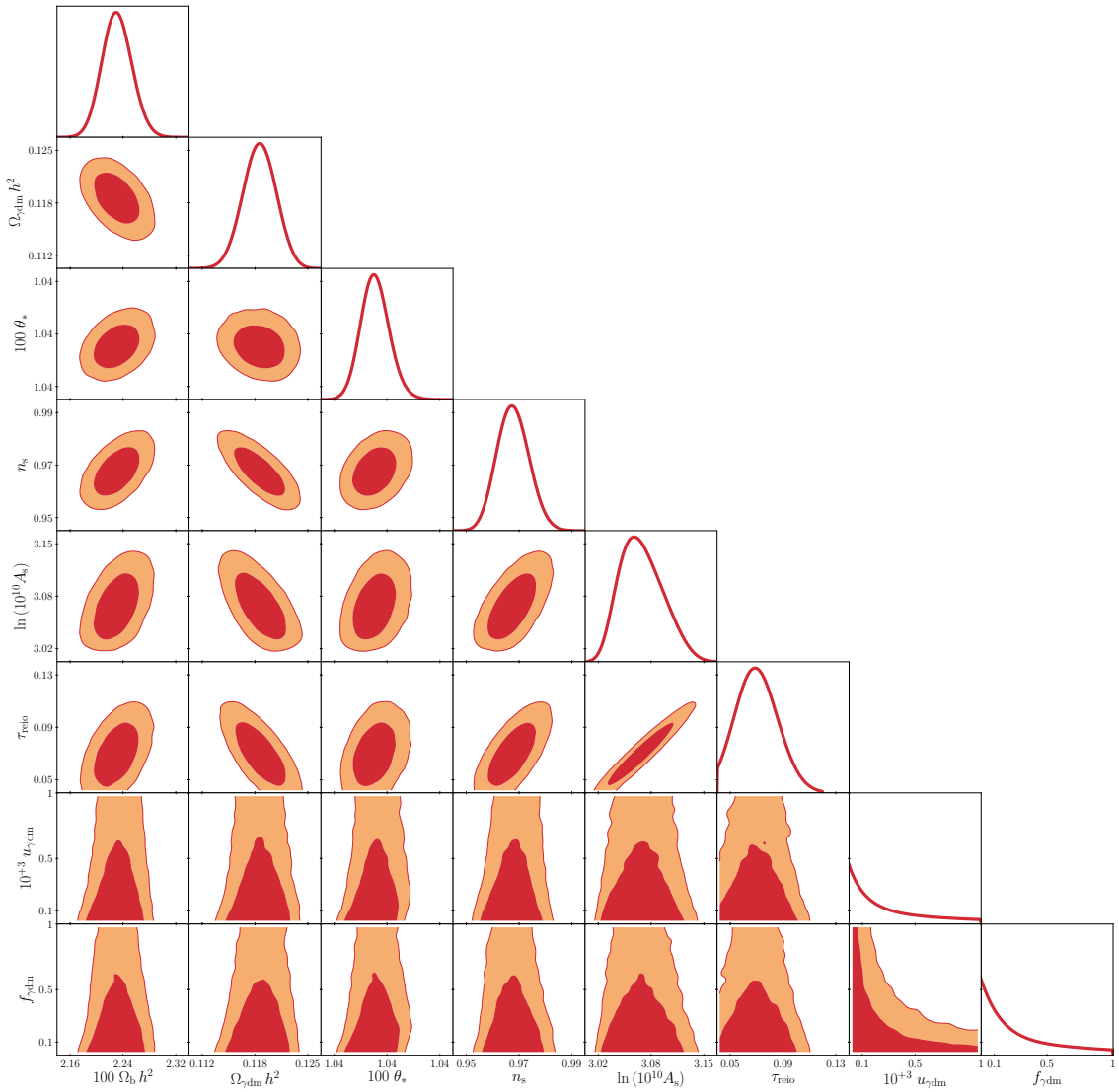

Figure 6.4: One and two dimensional posterior contours for cosmological parameters in the mixed dark matter model, inferred from the Planck 2015 "lowTEB + highTT + lensing" likelihoods, assuming flat priors. The two dimensional contours depict 68% (red) and 95% (orange) confidence levels, respectively.

matter participates in the photon interactions. However, for an interacting dark matter fraction of 10% the allowed cross section to mass ratio is almost two orders of magnitude larger as in the purely interacting case.

6.4.2 Fisher forecast for future observations of the large-scale structure

Considering future DESI observations, our main questions are whether DESI can lift the degeneracy between $u_{\gamma dm}$ and $f_{\gamma dm}$ in the mixed dark matter scenario, and how well the data can discriminate the effect of massive neutrinos from mixed dark matter. For comparison, we also present results on DESI's sensitivity to purely interacting dark matter.

The Fisher matrix formalism is outlined in Sec. 6.3.2. In addition to the interaction strength parameter, the interacting dark matter fraction and the neutrino mass scale

tracer	bias
emission line galaxies (ELG)	$b_{\mathrm{ELG}}(z) \times D(z) = 0.84$
luminous red galaxies (LRG)	$b_{\mathrm{LRG}}(z) \times D(z) = 1.7$
high redshift quasars (QSO)	$b_{\mathrm{QSO}}(z) \times D(z) = 1.2$

Table 6.2: Linear bias parameters for the DESI tracers taken from Ref. [9]. The growth factor is normalised at the present epoch, i.e. $D(1) = 1$.

our scenarios contain five cosmological baseline parameters, namely $\Omega_{\mathrm{b}}h^2$, $\Omega_{\mathrm{dm}}h^2$, $100\,\theta_*$, n_{s} and A_{s}. As their fiducial values we assume the Planck 2018 best-fit results [4], see Tab. 2.1. Galaxy surveys can not constrain the six free parameters of the ΛCDM model by themselves, let alone the up to eight free parameters in the extended models considered here. To break degeneracies, large-scale structure data is usually analysed in conjunction with CMB observations. We include Planck information on the five baseline parameters in form of a diagonal Fisher matrix, which contains the individual squared inverse one sigma intervals for each parameter as quoted in Tab. 2.1. This conservative approach neglects any information CMB data might provide on the neutrino mass or mixed dark matter parameters as well as on possible correlations between parameters.

In additional to the five baseline parameters, we fix the optical depth to reionisation, $\tau_{\mathrm{re}} = 0.0543$, and the effective number of neutrinos, $N_{\mathrm{eff}} = 3.046$. In the pure-γdm and mixed dark matter scenarios we describe the neutrino sector by two massless and a massive state with $m_\nu = 0.06\,\mathrm{eV}$. Where the neutrino mass is considered a free parameter, we correct the dark matter density for its variations according to Eq. (6.2.4). This approach is equivalent to considering the total non-relativistic matter density at the present epoch as free parameter rather than the dark matter density. Its advantage is, that the effect of the increased matter density and of the power suppression on small scales, both caused by heavy neutrinos, are separated. Concerning the bias, we adopt the customary assumption that its redshift dependence is cancelled by the linear growth factor $D(z)$, and thus that $b(z)\,D(z)$ is constant [338]. All tracers considered in our analysis, namely emission line galaxies, luminous red galaxies and the clustering of quasars, experiences a different bias for which we adopt the same values as in Ref. [9]. These are summarised in Tab. 6.2.

We first consider purely interacting dark matter and fix $f_{\gamma\mathrm{dm}} = 1$. For a fiducial interaction strength of $u_{\gamma\mathrm{dm}} = 2.0 \times 10^{-4}$, we obtain as estimate for the 1σ error bound $\delta u_{\gamma\mathrm{dm}} = 8.5 \times 10^{-6}$. Lowering the cross section to mass ratio further to 2.0×10^{-5} gives $\delta u_{\gamma\mathrm{dm}} = 7.1 \times 10^{-6}$. Thus, DESI could robustly detect interacting dark matter whose interaction strength saturates the CMB bounds and improve CMB constraints by close to an order of magnitude.

However, the sensitivity reduces seriously if the fraction of interacting dark matter is added as free parameter. This becomes very evident from the summary of forecasted error bounds in Tab. 6.3. For a fiducial cross section to mass ratio of 2×10^{-4} the error on the fraction of interacting dark matter is so large that mixed dark matter can not be discriminated from the canonical ΛCDM case. Simultaneously, the bound on $u_{\gamma\mathrm{dm}}$

$u_{\gamma\mathrm{dm}}^{\mathrm{fid}}$	$f_{\gamma\mathrm{dm}}^{\mathrm{fid}}$	$\delta u_{\gamma\mathrm{dm}}$	$\delta f_{\gamma\mathrm{dm}}$
2×10^{-4}	0.1	2.0×10^{-4}	1.8
	0.3	8.6×10^{-4}	2.3
	0.5	5.9×10^{-4}	2.6
	0.7	4.9×10^{-4}	3.0
	0.9	2.7×10^{-4}	2.1
2×10^{-3}	0.1	1.3×10^{-2}	0.76
	0.3	5.1×10^{-4}	9.5×10^{-2}
	0.5	3.2×10^{-4}	9.9×10^{-2}
	0.7	2.4×10^{-4}	0.10
	0.9	1.9×10^{-4}	0.11

Table 6.3: 1-σ marginalised errors estimated for DESI in combination with Planck 2018 CMB priors, assuming a mixed dark matter scenario and a fixed neutrino mass of $m_\nu = 0.06$ eV.

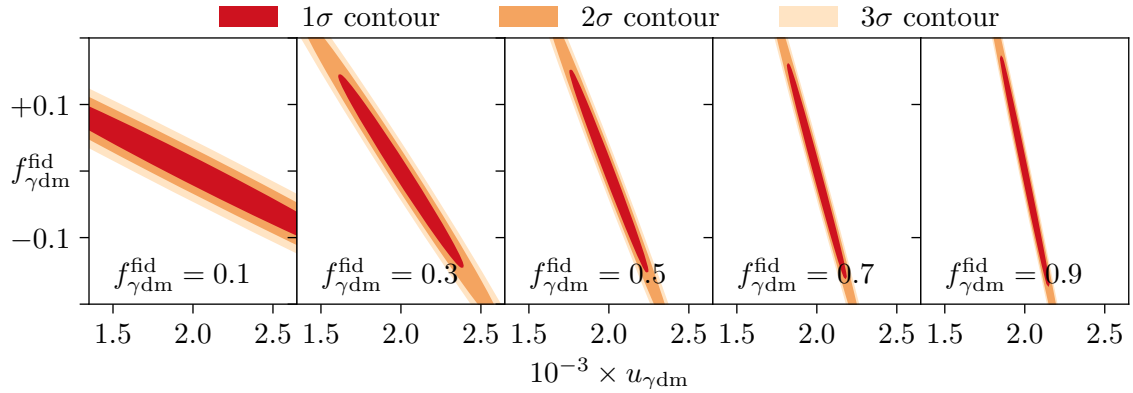

Figure 6.5: Confidence contours predicted for a DESI analysis of the mixed dark matter scenario. All illustrated scenarios assume $u_{\gamma\mathrm{dm}}^{\mathrm{fid}} = 2 \times 10^{-3}$.

increases, indicating a degeneracy between the two mixed dark matter parameters. Alike, if the fiducial interaction strength increases, the sensitivity on $f_{\gamma\mathrm{dm}}$ also improves. For $u_{\gamma\mathrm{dm}}^{\mathrm{fid}} = 2 \times 10^{-3}$ it is possible to discriminate mixed dark matter from ΛCDM if the fraction of interacting dark matter is at least 30%. The degeneracy between the interaction strength and the fraction of interacting dark matter is also apparent from Fig. 6.5, where we show the corresponding two dimensional confidence regions for $u_{\gamma\mathrm{dm}}^{\mathrm{fid}} = 2 \times 10^{-3}$ and several choices of $f_{\gamma\mathrm{dm}}^{\mathrm{fid}}$. Interestingly, it becomes less severe as the fraction of interacting dark matter increases, allowing for a more accurate determination of the interaction strength parameter.

Finally, we investigate how well mixed dark matter and neutrino masses can be determined simultaneously from future DESI data. In these scenarios, we always assume a fiducial neutrino mass of $m_\nu^{\mathrm{fid}} = 0.06\,\mathrm{eV}$ and test several assumptions on the mixed dark matter parameters. For comparison, we also estimate the neutrino mass error in the absence of any interacting dark matter and obtain $\delta m_\nu = 9.1 \times 10^{-3}$. This limit is stronger than that of Ref. [9], presumably because it does not account for uncertainties in τ_{re}. Despite being optimistic, the bound provides a reference to which the mixed dark matter forecasts

$u_{\gamma\mathrm{dm}}^{\mathrm{fid}}$	$f_{\gamma\mathrm{dm}}^{\mathrm{fid}}$	$\delta\, u_{\gamma\mathrm{dm}}$	$\delta\, f_{\gamma\mathrm{dm}}$	$\delta\, m_\nu$
1.0×10^{-3}	0.5	4.13×10^{-4}	0.30	2.08×10^{-2}
1.0×10^{-3}	0.3	6.79×10^{-4}	0.30	2.03×10^{-2}
1.0×10^{-3}	0.1	1.96×10^{-3}	0.28	1.97×10^{-2}
4.0×10^{-4}	0.5	5.55×10^{-4}	1.15	2.05×10^{-2}

Table 6.4: 1-σ marginalised errors estimated for DESI in combination with Planck 2018 CMB priors, assuming a mixed dark matter scenario with unknown neutrino mass. The fiducial value for the neutrino mass is always $m_\nu = 0.06$ eV.

can be compared. In all tested fiducial scenarios, we observe that the error bound on the neutrino mass increases by about a factor of two, see Tab. 6.4. The reduced sensitivity is explainable from the two dimensional confidence regions of which Fig. 6.6 depicts one example considering a fiducial model with $u_{\gamma\mathrm{dm}}^{\mathrm{fid}} = 1.0{\times}10^{-3}$, $f_{\gamma\mathrm{dm}}^{\mathrm{fid}} = 0.5$ and $m_\nu^{\mathrm{fid}} = 0.06\,\mathrm{eV}$. As already suspected from the discussion of the matter power spectrum, the neutrino mass estimate is degenerate with both parameters of the mixed dark matter model, $f_{\gamma\mathrm{dm}}$ and $u_{\gamma\mathrm{dm}}$. The example in Fig. 6.6 affirms that a large neutrino mass can be compensated by a decrease in $u_{\gamma\mathrm{dm}}$, and, in addition, the strong degeneracy between $u_{\gamma\mathrm{dm}}$ and $f_{\gamma\mathrm{dm}}$ is inherited in the $(m_\nu\,, f_{\gamma\mathrm{dm}})$ plane.

6.5 Summary

We consider a scenario with two dark matter components, one of which is cold and collisionless at all scales and times of interest and thus behaves like canonical cold dark matter. The second component scatters elastically with photons. The CMB angular spectra for such a mixed dark matter model are intermediate between the ΛCDM and the fully interacting case, with the interpolation between both limits controlled by the fraction of interacting dark matter, $f_{\gamma\mathrm{dm}}$. In contrast, the matter power spectrum receives an additional suppression at intermediate scales from the cancellation of perturbations in both components. This effect is the more pronounced for a larger value of $f_{\gamma\mathrm{dm}}$, and, in some cases, can generate less power on intermediate scales than a purely interacting scenario. A small abundance of interacting dark matter, on the other hand, has a very similar impact on the matter power spectrum as massive neutrinos.

Limits on the mixed dark matter parameter space from CMB observations, using the Planck 2015 data, leave the cross section to mass ratio $u_{\gamma\mathrm{dm}}$ unconstrained if less than 10% of dark matter participates in the photon scattering. To assess the sensitivity of future large-scale structure observations to the mixed dark matter scenario, we perform a Fisher forecast for the upcoming DESI survey. It reveals a strong degeneracy between the two parameters characterising the mixed dark matter scenario, $u_{\gamma\mathrm{dm}}$ and $f_{\gamma\mathrm{dm}}$. Consequently, the sensitivity to the interaction strength $u_{\gamma\mathrm{dm}}$ is considerably reduced for mixed dark matter models in the comparison with a purely interacting scenario. Similarly, we diagnose a degeneracy between the neutrino mass and both parameters of the mixed dark matter

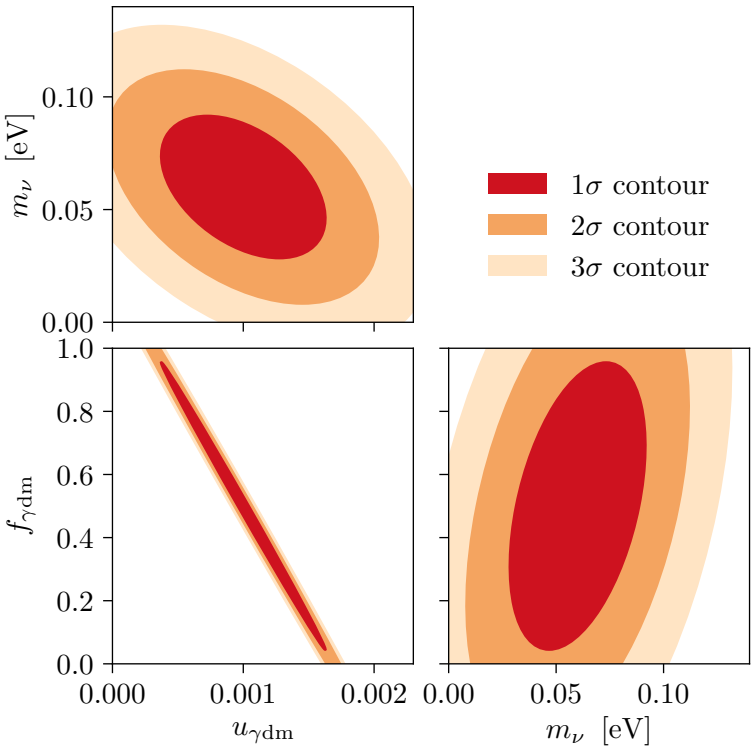

Figure 6.6: Two dimensional confidence contours in a scenario where mixed dark matter and neutrino masses are to be determined simultaneously from DESI data. The fiducial model is determined by $u_{\gamma\mathrm{dm}}^{\mathrm{fid}} = 1.0 \times 10^{-3}$, $f_{\gamma\mathrm{dm}}^{\mathrm{fid}} = 0.5$ and $m_\nu^{\mathrm{fid}} = 0.06\,\mathrm{eV}$.

model. Thus, the mixed dark matter scenario could mislead the interpretation of large-scale structure data and the reconstruction of neutrino masses from the matter power spectrum. Upper limits on the neutrino mass scale, in particular, might overestimate its impact on the matter power spectrum.

Chapter 7

Mixed damping in dark matter-neutrino interactions

The preceding two chapters concerned various aspects of dark matter-photon scattering in the early universe. Another intriguing possibility for dark matter interactions with Standard Model radiation is to postulate a coupling to neutrinos. Within the Standard Model, neutrinos are the least understood particles, and laboratory tests of such interactions with dark matter are currently not feasible. In contrast, the high abundances of neutrinos and dark matter in the early universe allows to assess a possible link between them from cosmological observations [323].

For consistency with observations of the CMB and the universe's large-scale structure, dark matter has to decouple from neutrinos well before these become non-relativistic. Still, there is a fundamental difference to dark matter-photon interactions, which always suppresses dark matter perturbations by collisional damping. For dark matter-neutrino scatterings there is an alternative damping mechanism, characterised by a period where

$$\Gamma_{\nu\mathrm{dm}-\nu} > H > \Gamma_{\nu} \tag{7.0.1}$$

holds true. That is, dark matter, denoted here as νdm, is coupled to neutrinos while the latter free stream. Besides dark matter scattering, Standard Model interactions with electrons contribute to the neutrino interaction rate, i.e. $\Gamma_{\nu} = \Gamma_{\nu-\mathrm{e}} + \Gamma_{\nu-\nu\mathrm{dm}}$. For the dark matter component we assume that it only interacts with neutrinos. The rate for dark matter scattering off neutrinos and for the reverse process are not identical due to the presence of the momentum conserving prefactor $R_{\nu\mathrm{dm}}$ in the dark matter equations (3.5.7). Rather, the respective rates read

$$\Gamma_{\nu-\nu\mathrm{dm}} = n_{\nu\mathrm{dm}}\,\sigma_{\nu\mathrm{dm}}\,, \tag{7.0.2a}$$

$$\Gamma_{\nu\mathrm{dm}-\nu} = \frac{4\,\rho_{\nu}}{3\,\rho_{\nu\mathrm{dm}}}\,\Gamma_{\nu-\nu\mathrm{dm}}\,. \tag{7.0.2b}$$

In this alternative scenario, called mixed damping, dark matter is dragged along by the relativistic, free streaming neutrinos, which thereby erase perturbations in the dark matter component [292]. While, in the context of dark matter interactions with Standard Model radiation, neutrinos are particularly relevant for mixed damping, it can also arise for dark

matter-dark radiation interactions [347]. A similar effect, Silk damping [91], exists in the evolution of the baryon-photon plasma, where photons decouple briefly before the end of the baryon drag epoch [132, 298]. However, there are fundamental differences in the decoupling histories of the baryon-photon plasma and of the coupled dark matter-neutrino sector. As a consequence, mixed damping can last longer and affect a larger range of modes than Silk damping. We discuss the differences in detail in Sec. 7.3.1.

Current constraints on dark matter-neutrino interactions touch on the region of parameter space where mixed damping is important for the suppression of structure. Thus, a profound physical understanding of the mechanism is desirable. The Boltzmann hierarchy of interacting neutrinos (3.5.5) in combination with the interacting dark matter equations (3.5.7) automatically accounts for the mixed damping mechanism, but does not provide an intuitive insight into the underlying physics. Also, in Sec. 4 we showed that Boltzmann codes require modifications beyond the level of the multipole hierarchy in order to obtain accurate results. In this chapter we focus on either aspect, the understanding the physical mechanism for mixed damping and accurately describing it numerically.

We start by examining the parameter space over which mixed damping is relevant in Sec. 7.1 and assess the accuracy of our numerical results, more precisely the impact of the ultra-relativistic fluid approximation and the choice of initial conditions, in Sec. 7.2. Section 7.3 is devoted to the derivation of an analytical approximation to the evolution of dark matter perturbations in the mixed damping regime. Finally, in Sec. 7.4 we use this analytical solution discuss the physical mechanism of mixed damping.

7.1 The parameter space for mixed damping

The rate for neutrino scatting with dark matter (7.0.2a) and hence the neutrino decoupling time depend on the dark matter number density. In general, a further to be specified dark matter production mechanism fixes the comoving dark matter number density, and at late times $n_{\rm dm} \propto a^{-3}$. At early times, however, the dark matter density can be a more complex function of the scale factor. So causes dark matter annihilation in the freeze out scenario an exponential decrease of the dark matter density prior to chemical decoupling. Here, for simplicity, we assume that the comoving dark matter density was fixed before neutrino weak decoupling. As a result, the bounds quoted in the following have to be interpreted with precaution for a thermal dark matter candidate with mass $\lesssim \mathcal{O}\,(\mathrm{MeV})$.

7.1.1 Minimum mixed damping scale

Only if dark matter stays coupled to neutrinos beyond neutrino-electron weak decoupling at $T_\gamma \sim 1\,\mathrm{MeV}$, a period where Eq. (7.0.1) is satisfied can exist and mixed damping is possible. The requirement that dark matter does not decouple before $a_{\rm min} = a\,(1\,\mathrm{MeV}) \simeq 2.35\times10^{-10}$ immediate puts a lower bound to the dark matter-neutrino scattering cross section. With

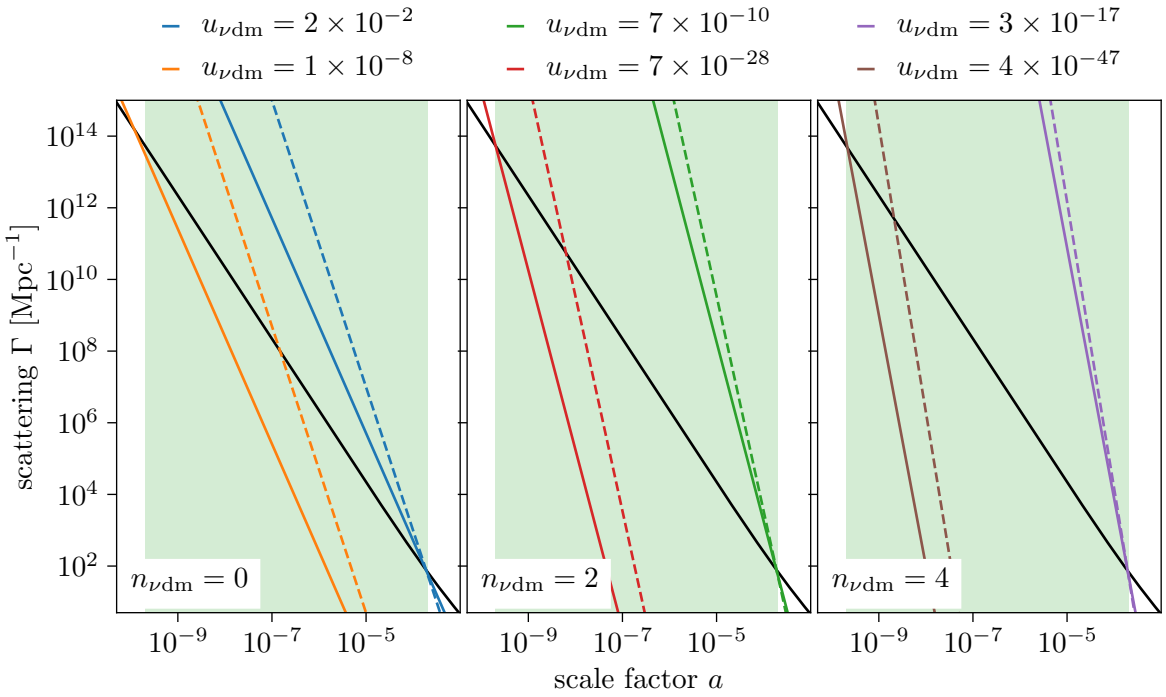

Figure 7.1: The evolution of the neutrino-dark matter scattering rate $\Gamma_{\nu-\nu\mathrm{dm}}$ (solid lines) and the dark matter-neutrino scattering rate $\Gamma_{\nu\mathrm{dm}-\nu}$ (dashed lines) in comparison to the Hubble rate (black line). The green shaded region indicates the range of dark matter decoupling for which mixed damping can occur.

the parameterisation of Eq. (3.5.10) and Eq. (3.5.11) the constraint is

$$u_{\nu\mathrm{dm},0}^{\mathrm{min}} = 2\pi \frac{\sqrt{\Omega_\mathrm{r} h^2}}{\Omega_\nu h^2} \left(100 \frac{\mathrm{km}}{\mathrm{Mpc\,s}}\right)^{-1} \frac{100\,\mathrm{GeV}}{\sigma_\mathrm{T}\, m_\mathrm{P}^2}\, a_{\mathrm{min}}^{n_{\nu\mathrm{dm}}+2} = \begin{cases} 2.4 \times 10^{-14} & \text{if } n_{\nu\mathrm{dm}} = 0 \\ 1.4 \times 10^{-33} & \text{if } n_{\nu\mathrm{dm}} = 2 \\ 7.4 \times 10^{-53} & \text{if } n_{\nu\mathrm{dm}} = 4 \end{cases}, \tag{7.1.1}$$

where $\Omega_\mathrm{r} = \Omega_\gamma + \Omega_\nu$. In Fig. 7.1 the left edge of the green shaded region indicates the minimum scale factor for dark matter decoupling. Corresponding to this limit, only scales above a minimum mass and length scale can be subject to mixed damping, namely

$$r_{\mathrm{min}} = 0.11\,\mathrm{kpc} \tag{7.1.2a}$$

$$M_{\mathrm{min}} = 0.2\,M_\odot\,. \tag{7.1.2b}$$

Smaller scales still experience a suppression of perturbations, but these cross the Hubble radius at a time when neutrinos interact with electrons and then are subject to collisional damping. In any case, the smallest, ultra faint dwarf galaxies discovered in the Milky Way and Andromeda have stellar masses of at least $10^2\,M_\odot$ [178, 189]. Scales as small as r_{min} are far below the experimental reach.

The requirement that dark matter decouples from neutrinos when these are collisionless also puts an upper limit on the scales affected by mixed damping and provides a maximal allowed value of the cross section to mass ratio $u_{\nu\mathrm{dm}}$. This bound depends on the decoupling

history, and in particular on whether neutrinos decouple from electrons or from dark matter first. We explore both possibilities in the following.

7.1.2 Maximum scale set by neutrino weak decoupling

Mixed damping is the sole process responsible for the suppression of dark matter perturbations on scales larger than $r_{\rm min}$ if Standard Model interactions determine the time of neutrino decoupling. In this case, the mixed damping condition (7.0.1) becomes

$$\Gamma_{\nu-\nu\rm dm} < \Gamma_{\nu-\rm e} < H < \Gamma_{\nu\rm dm-\nu}\,. \tag{7.1.3}$$

The size of the Hubble radius at the time of dark matter decoupling sets the scale up to which mixed damping can affect dark matter perturbations. It is the larger, the larger the cross section to mass ratio parameter is. Still, requiring that neutrino decoupling is set by weak interactions also restricts the time of dark matter decoupling. Momentum conservation relates the respective interaction rates (7.0.2b), and for the largest allowed dark matter interaction rate the dark matter decoupling condition ($\Gamma_{\nu\rm dm-\nu} \simeq H$) can be recast as

$$\frac{4\,\rho_\nu}{3\,\rho_{\rm dm}}\,\Gamma_{\nu-\rm e} \simeq H\,. \tag{7.1.4}$$

Combined with the previous section's discussion, there only exists a period over which Eq. (7.1.3) can be satisfied if $u^{\rm min}_{\nu\rm dm,0} < u_{\nu\rm dm,0} < u^{\rm wdec}_{\nu\rm dm,0}$, and

$$u^{\rm wdec}_{\nu\rm dm,0} = 1.34\times10^{-8}\times a^{\nu\rm dm}_{\rm min}\left(\frac{h}{0.678}\right)\left(\frac{\Omega_{\nu\rm dm}}{0.1186}\right)^{-1} = \begin{cases} 1.3\times10^{-8} & \text{if } n_{\nu\rm dm}=0 \\ 7.4\times10^{-28} & \text{if } n_{\nu\rm dm}=2 \\ 4.1\times10^{-47} & \text{if } n_{\nu\rm dm}=4 \end{cases}. \tag{7.1.5}$$

Then, the maximal length and mass scales which can be affected by mixed damping are

$$r_{\rm wdec} = \begin{cases} 79\,\rm kpc & \text{if } n_{\nu\rm dm}=0 \\ 2.6\,\rm kpc & \text{if } n_{\nu\rm dm}=2 \\ 0.8\,\rm kpc & \text{if } n_{\nu\rm dm}=4 \end{cases}, \qquad M_{\rm wdec} = \begin{cases} 8\times10^{7}\,M_\odot & \text{if } n_{\nu\rm dm}=0 \\ 3\times10^{3}\,M_\odot & \text{if } n_{\nu\rm dm}=2 \\ 1\times10^{2}\,M_\odot & \text{if } n_{\nu\rm dm}=4 \end{cases}. \tag{7.1.6}$$

In Fig. 7.1 we illustrate the time evolution of scattering rates for $u_{\nu\rm dm} = u^{\rm wdec}_{\nu\rm dm}$. Neutrino kinetic decoupling occurs at the left boundary of the green region, when $T_\gamma \simeq 1\,\rm MeV$. In contrast, the dark matter scattering rate crosses the Hubble rate at a later time. On scales which enter the Hubble radius between both events dark matter perturbations get suppressed by mixed damping.

7.1.3 Maximum scale set by neutrino-dark matter decoupling

Mixed damping also plays an important role if the neutrino kinetic decoupling is determined by the neutrino-dark matter interactions. This scenario applies to larger scales, which

are more accessible by observations. To illustrate the situation, first consider a small mode, which enters the Hubble radius while $\Gamma_{\nu\mathrm{dm}-\nu}, \Gamma_{\nu-\nu\mathrm{dm}} > H > \Gamma_{\nu-\mathrm{e}}$. Initially, this mode experiences collisional damping but transitions to the mixed damping regime upon neutrino decoupling. A larger mode, in contrast, enters the Hubble radius later, possibly when neutrinos are free streaming. It then is subject to mixed damping only. However, the transition from the collisional to the mixed damping regime can only occur if the ratio of densities in Eq. (7.0.2b) is larger than unity by the time dark matter decouples from the neutrino fluid. This condition, $4\rho_\nu\left(a_{\mathrm{md-max}}\right) = 3\rho_{\nu\mathrm{dm}}\left(a_{\mathrm{md-max}}\right)$, puts an upper limit on the dark matter decoupling time

$$a_{\mathrm{md-max}} = 1.9 \times 10^{-4} \left(\frac{\Omega_{\nu\mathrm{dm}} h^2}{0.1186}\right) . \tag{7.1.7}$$

The largest scale which can in principle be affected by mixed damping enters the Hubble radius at $a_{\mathrm{md-max}}$ and is given by

$$r_{\mathrm{md-max}} = 71.0\,\mathrm{Mpc}\,\frac{\left(\frac{0.1186}{\Omega_{\nu\mathrm{dm}}h^2}\right)}{\sqrt{1 + 0.068\left(\frac{\Omega_\mathrm{b}h^2}{0.0223}\right)\left(\frac{0.1186}{\Omega_{\nu\mathrm{dm}}h^2}\right)}} . \tag{7.1.8}$$

It corresponds to a mass scale of roughly $M_{\mathrm{md-max}} = 6 \times 10^{16}\, M_\odot$. Finally, the criterion of dark matter decoupling before $a_{\mathrm{md-max}}$ translates into an upper bound on the $u_{\nu\mathrm{dm}}$,

$$\begin{aligned} u_{\nu\mathrm{dm}}^{\mathrm{md-max}} &= 1.97 \times 10^{-2} a_{\mathrm{md-max}}^{n_{\nu\mathrm{dm}}} \left(\frac{0.1186}{\Omega_{\nu\mathrm{dm}}h^2}\right)^2 \sqrt{1 + 0.066\left(\frac{\Omega_\mathrm{b}h^2}{0.0223}\right)\left(\frac{0.1186}{\Omega_{\nu\mathrm{dm}}h^2}\right)} \\ &\simeq \begin{cases} 1.98 \times 10^{-2} & \text{if } n_{\nu\mathrm{dm}} = 0 \\ 7.12 \times 10^{-10} & \text{if } n_{\nu\mathrm{dm}} = 2 \\ 2.56 \times 10^{-17} & \text{if } n_{\nu\mathrm{dm}} = 4 \end{cases} \end{aligned} \tag{7.1.9}$$

If the interaction strength parameter exceeds $u_{\nu\mathrm{dm}}^{\mathrm{md-max}}$, dark matter always decouples from neutrinos first, and the damping of fluctuations is purely collisional. The right boundary of the green shaded region in Fig. 7.1 marks $a_{\mathrm{md-max}}$. Also shown is the time evolution of scattering rates for $u_{\nu\mathrm{dm}} = u_{\nu\mathrm{dm}}^{\mathrm{md-max}}$. In this limiting configuration, neutrinos and dark matter decouple simultaneously, at $a_{\mathrm{md-max}}$ precisely.

7.1.4 Comparison with observational constraints

Numerous cosmological observations are sensitive to the effects of dark matter-neutrino scattering, amongst them the CMB temperature, polarisation and lensing spectra, the Ly-α forest, galaxy surveys and CMB spectral distortions. We summarise the corresponding limits and forecasts in Tab. 7.1. A recent study emphasised the difficulties of one-sided constraints, obtained with a logarithmically flat prior, in the context of CMB limits on dark matter-radiation interactions [314]. Those studies are inclined to produce artificially tight bounds, and we therefore quote the prior adopted for $u_{\nu\mathrm{dm}}$ explicitly.

Planck 2013 temperature, WMAP low-multipole polarisation, 68% C.L. [294]	$u_{\nu\mathrm{dm}} \leq 3.99 \times 10^{-2}$, $n_{\nu\mathrm{dm}} = 0$ $u_{\nu\mathrm{dm},0} \leq 0.54 \times 10^{-13}$, $n_{\nu\mathrm{dm}} = 2$
Planck 2013 temperature, WMAP low-multipole polarisation, Lyman-α (HIRES & MIKE), 68% C.L. [294]	$u_{\nu\mathrm{dm}} \leq 1.5 \times 10^{-7}$, $n_{\nu\mathrm{dm}} = 0$ $u_{\nu\mathrm{dm},0} \leq 1.5 \times 10^{-19}$, $n_{\nu\mathrm{dm}} = 2$
Planck 2013 temperature, WMAP low-multipole polarisation, logarithmic flat prior, 95% C.L. [295]	$u_{\nu\mathrm{dm}} \leq 9.0 \times 10^{-5}$, $n_{\nu\mathrm{dm}} = 0$ $u_{\nu\mathrm{dm},0} \leq 3.0 \times 10^{-14}$, $n_{\nu\mathrm{dm}} = 2$
Planck 2013 temperature, WMAP low-multipole polarisation, logarithmic flat prior, WiggleZ up to $k = 0.2\,h/\mathrm{Mpc}$, 95% C.L. [295]	$u_{\nu\mathrm{dm}} \leq 3 \times 10^{-5}$, $n_{\nu\mathrm{dm}} = 0$ $u_{\nu\mathrm{dm}} \leq 1 \times 10^{-14}$, $n_{\nu\mathrm{dm}} = 2$
Planck 2015 lowTEB highTT, logarithmic flat prior, 95% C.L. [277]	$u_{\nu\mathrm{dm}} = 4.5 \times 10^{-5}$, $n_{\nu\mathrm{dm}} = 0$
Planck 2015 lowTEB highTTTEEE lensing, logarithmic flat prior, 95% C.L. [277]	$u_{\nu\mathrm{dm}} = 9.0 \times 10^{-5}$, $n_{\nu\mathrm{dm}} = 0$
Planck 2015 lowP highTTTEEE lensing, Jeffrey's prior, 95% C.L. [314]	$u_{\nu\mathrm{dm}} \leq 2.14 \times 10^{-4}$, $n_{\nu\mathrm{dm}} = 0$ $u_{\nu\mathrm{dm}} \leq 2.46 \times 10^{-13}$, $n_{\nu\mathrm{dm}} = 2$
CMB (COrE+) forecast, 95% C.L. limits [295]	$u_{\nu\mathrm{dm}} \leq 4.5 \times 10^{-5}$, $n_{\nu\mathrm{dm}} = 0$ $u_{\nu\mathrm{dm},0} \leq 3.0 \times 10^{-15}$, $n_{\nu\mathrm{dm}} = 2$
Large-scale structure (DESI) forecast, 2.5σ detection [295]	$u_{\nu\mathrm{dm}} = 10^{-5}$, $n_{\nu\mathrm{dm}} = 0$ $u_{\nu\mathrm{dm},0} = 10^{-14}$, $n_{\nu\mathrm{dm}} = 2$
Spectral distortions (PRISM) forecast, 2σ detection [321]	$u_{\nu\mathrm{dm}} = 7.2 \times 10^{-6}$, $n_{\nu\mathrm{dm}} = 0$ $u_{\nu\mathrm{dm},0} = 3.8 \times 10^{-21}$, $n_{\nu\mathrm{dm}} = 2$

Table 7.1: Overview over existing (top) and forecasted (bottom) constraints on the dark matter-neutrino scattering strength $u_{\nu\mathrm{dm}}$. The quoted prior models apply to $u_{\nu\mathrm{dm}}$.

A general trend of Tab. 7.1 is that constraints become tighter as observations concern smaller scales. Indeed, because small modes gain causal contact earlier, they are sensitive to smaller dark matter decoupling and smaller interaction rates. When judging the derived limits, one further has to keep in mind that the ΛCDM parameters (1.3.2) can shift in analyses of alternative cosmologies. However, in the case of dark matter-neutrino interactions the impact is not large enough to alter the parameter ranges from the previous section significantly. Importantly, already the bounds derived from large-scale CMB observations, like the conservative bound using Planck 2015 data and a Jeffrey's prior [314], undercut the minimum required cross section for mixed damping, $u_{\nu\mathrm{dm}}^{\mathrm{md-max}}$. Evidently, cosmological constraints on dark matter-photon interactions derive from scales and epochs where mixed damping matters to the suppression of perturbations. In this context, a correct numerical modelling and a thorough physical understanding of the mechanism are vital.

7.2 Numerical accuracy in cosmologies with dark matter-neutrino interactions

To predict the evolution of cosmological perturbations in the presence of dark matter-neutrino interactions accurately, we modified the CLASS code, version 2.7[1]. Our changes include the interacting neutrino hierarchy (3.5.5), the modified dark matter evolution equations (3.5.7) and the revised treatment of the initial conditions discussed in Sec. 4.4. Further, the code not only accepts the interaction strength $u_{\gamma\mathrm{dm}}$ as additional input parameter, but also the exponent of the cross-section's temperature dependence, $n_{\nu\mathrm{dm}}$, and the angular coefficients α_l. Dark matter scattering terms are implemented for ultra-relativistic neutrinos only, and in this chapter we consider three massless neutrino species, which uniformly participate in the interactions. While this treatment is adequate to study the physical processes behind mixed damping, it should be revised when parameter constraints from observations are at concern.

Beyond the aforementioned modifications, dark matter-neutrino interactions also require to reassess the applicability of the ultra-relativistic fluid approximation (UFA). Because previous studies of the νdm scenario neither considered the initial conditions nor the UFA treatment, we examine in this section how those changes impact theory predictions for the CMB angular spectra and the matter power spectrum.

7.2.1 Ultra-relativistic fluid approximation

The late time evolution of neutrino perturbations in CLASS is addressed by the ultra-relativistic fluid approximations [288], which explicitly assumes free streaming neutrinos. This assumption can break down if neutrinos are coupled to dark matter. We therefore advocate in Sec. 4.3 to delay the onset of the ultra-relativistic fluid approximation sufficiently to ensure neutrino decoupling. Here we assess the effect of such a delay on the numerical results. Even though our primary concern is the mixed damping regime, where neutrinos indeed are free streaming, this control is important. The preceding section showed that there is a smooth transition from the mixed to the collisional damping regime, hence we need to at least establish the scales up to which our results are reliable. Second, previous constraints have been obtained either with a modified UFA truncation scheme (4.3.5) or neglecting the effect of neutrino interactions on the ultra-relativistic fluid approximation altogether, and we aim to estimate the impact this has on the results.

We consider two benchmark scenarios to investigate the effect of the UFA approach on CMB constraints. These scenarios are loosely motivated by the limits quoted in Ref. [314]. Explicitly, we assume $u_{\nu\mathrm{dm}} = 5.0 \times 10^{-4}$ for $n_{\nu\mathrm{dm}} = 0$ and $u_{\nu\mathrm{dm},0} = 5 \times 10^{-13}$ for $n_{\nu\mathrm{dm}} = 2$. Further, the angular coefficients are set to $\alpha_l = 3/2$ for $l \geq 2$, and we fix the remaining cosmological to their Planck best-fit value from the 2018 data release, given in Tab. 2.1. For either benchmark case, we increase the trigger value of $(k\tau)_{\mathrm{ufa}}$ simultaneously with l_{max}

[1] Our modified code is publicly available from https://github.com/bufeo/class_v2.7_nuDM.git.

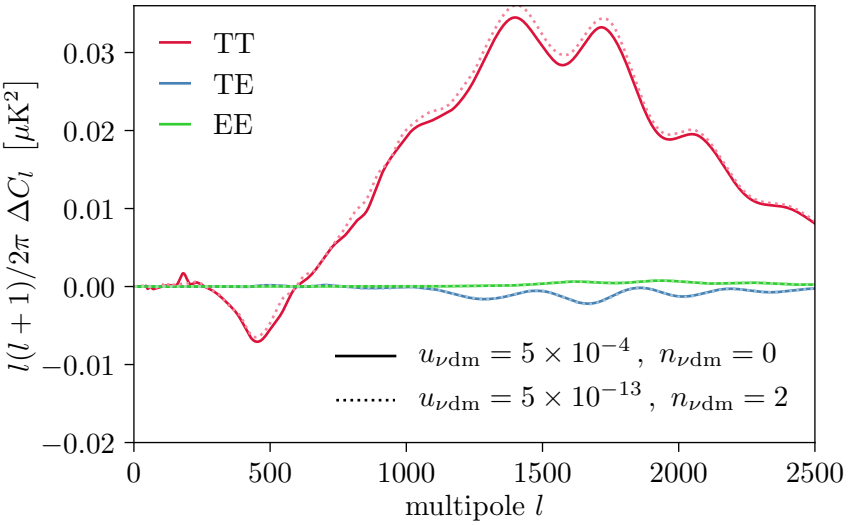

Figure 7.2: Differences between the lensed CMB spectra obtained for default UFA settings and a delayed UFA approach with $(k\tau)_{\mathrm{ufa}} = l_{\mathrm{max}} = 400$.

and ensure that the resulting CMB spectra converge. In the following we always present results obtained with $(k\tau)_{\mathrm{ufa}} = l_{\mathrm{max}} = 400$, in comparison the CLASS v2.7 default setting $(k\tau)_{\mathrm{ufa}} = 30$ and $l_{\mathrm{max}} = 17$. Our results, the difference between the lensed CMB spectra obtained with the default and the delayed UFA procedure, are shown in Fig. 7.2 for both benchmark models. Considering $l\,(l+1)\,/\,(2\pi)\,C_l$ up to $l = 2500$ for the temperature and the E-mode autocorrelation and their cross-correlation spectra, we find small differences of at most 0.03 µK, which clearly are below the experimental sensitivity. Hence we conclude that the CMB constraints quoted in Tab. 7.1 are robust with respect to the treatment of the ultra-relativistic fluid approximation.

The large scales probed by the CMB enter the horizon comparably late, when the impact of dark matter scattering on the neutrino evolution is small. The situation is different in case of the matter power spectrum, as the comparison of results with default and delayed UFA settings in Fig. 7.3 reveals. There, we vary $u_{\nu\mathrm{dm}}$ as indicated, choose $n_{\nu\mathrm{dm}} = 0$ and set the remaining cosmological parameters to the Planck 2018 best-fit values. The morphology of the matter power spectrum in cosmologies with dark matter-neutrino interactions is similar to that of the dark matter-photon interacting scenario, discussed in Sec. 5.1.1. In either case, there is no difference to the ΛCDM predictions on the largest scales, and a cut-off occurs towards smaller scales, whose precise location is governed by the cross section to mass ratio. Instead of the damped oscillations, succeeding the cut-off in the γdm-scenario, the νdm power spectrum only oscillates once and after that decreases monotonically. The default and delayed UFA results typically agree up to this bump, but on smaller scales differences are evident. We also test the generalised UFA truncation equation (4.3.5), employed by previous works, and find that it neither reproduces the delayed not the default results of the standard truncation (4.3.5), if the respective trigger values are left to their default values. Typically, the deviations emerge at the same wavenumbers and are at the same level as those between the default and delayed UFA results of Fig. 7.3. For a delayed UFA, on the other hand, the standard and the generalised truncation scheme

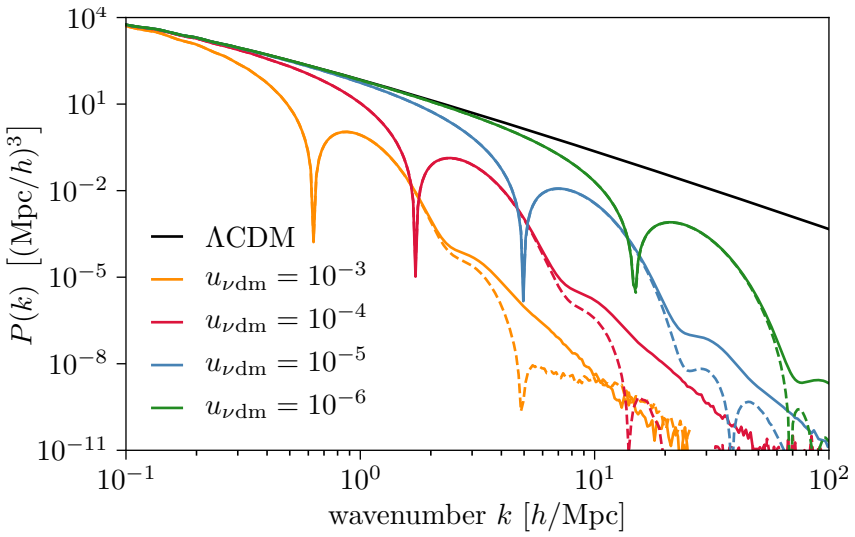

Figure 7.3: The matter power spectrum for several dark matter-neutrino interacting scenarios with $n_{\nu\mathrm{dm}} = 0$. Dashed curves show results obtained for default UFA settings, solid lines those from the delayed UFA approach with $(k\tau)_{\mathrm{ufa}} = l_{\mathrm{max}} = 400$.

converge to the same result. This is not surprising as the respective expressions only differ by a term proportional to the neutrino scattering rate $\kappa'_{\nu\mathrm{dm}}$, which becomes negligible at sufficiently late times. From these test we conclude that, to obtain precise predictions for the matter power spectrum on small scales, it is indeed necessary to delay the onset of the UFA regime. The more economical approach of including the interaction term to the truncation equation (4.3.5) fails to reproduce the correct small scale behaviour.

Even though discrepancies appear at small scales in the matter power spectrum when the UFA is not delayed, we do not expect these to affect constraints derived from large-scale structure observations. For viable scattering rates, the default and delayed UFA results do not diverge from each other until fluctuations in the interacting scenario are reduced by several orders of magnitude with respect to the ΛCDM prediction. In this case, details of the matter power spectrum's exact shape typically get erased by non-linear structure formation. Further, in predicting the abundance of dwarf galaxies, systematic uncertainties from non-linear effects and baryonic processes most likely overpower the linear small-scale differences.

To further illustrate the situation, we estimate the number of Milky Way satellites for several interacting scenarios, in which the differences between default and delayed UFA results appear on the dwarf galaxy scale. Our analysis, following closely Ref. [348], utilises a modified Press-Schechter approach based on a sharp k-filter [349, 350]. It is based on the conditional halo mass function, which predicts the number subhalos N_{sh} per logarithmic mass interval M_{sh} as

$$\frac{d\,N_{\mathrm{sh}}}{d\ln M_{\mathrm{sh}}} = \frac{1}{C_{\mathrm{sim}}}\frac{1}{6\pi^2}\left(\frac{M_{\mathrm{hh}}}{M_{\mathrm{sh}}}\right)\frac{P\left(R_{\mathrm{sh}}^{-1}\right)}{R_{\mathrm{sh}}^3\sqrt{2\pi\,(S_{\mathrm{sh}}-S_{\mathrm{hh}})}}\,. \tag{7.2.1}$$

The subscript "hh" refers to properties of the host halo, and the coefficient $C_{\mathrm{sim}} = 45$

$u_{\nu\mathrm{dm}}$	default UFA	delayed UFA
0	160	160
5.0×10^{-7}	8.5	8.5
1.0×10^{-6}	5.8	5.9
5.0×10^{-6}	0.72	0.74
1.0×10^{-5}	0.28	0.30
5.0×10^{-5}	0.055	0.058

Table 7.2: The number of Milky Way satellites, estimated from the linear matter power spectrum with default and delayed UFA settings, for several scenarios with dark matter-neutrino interactions, assuming $n_{\nu\mathrm{dm}} = 0$.

calibrates the expression to the results of n-body simulations. Further, $P(k)$ denotes the matter power spectrum, where a halo on the scale R_i is associated with the wavenumber $k_i = 1/R_i$ for $i = \mathrm{sh}, \mathrm{hh}$. Further, the relation between a halo's scale and mass is calibrated to simulations by the coefficient $c_{\mathrm{sim}} = 2.5$ and given by

$$M_i = \frac{4\pi}{3}\,\Omega_{\mathrm{m}}\rho_{\mathrm{crit}}\,\left(c_{\mathrm{sim}}R_i\right)^3\,. \tag{7.2.2}$$

Its variance is

$$S_i = \frac{1}{2\pi}\int_0^{k_i} dk\,k^2\,P(k)\,W^2(k\,,M_i)\,, \tag{7.2.3}$$

where $W(k\,,M)$ denotes the sharp k-filter, i.e.

$$W(k\,,M_i) = \begin{cases} 1 & \text{if } k < k_i\,(M_i) \\ 0 & \text{if } k > k_i\,(M_i) \end{cases} \tag{7.2.4}$$

Integrating the conditional halo mass function over the relevant mass range, we obtain an estimate for the number of satellites in the Milky Way

$$N_{\mathrm{sh}} = \int_{M_{\mathrm{min}}}^{M_{\mathrm{hh}}} \frac{d\,N_{\mathrm{sh}}}{d\ln M_{\mathrm{sh}}}\,(d\ln M_{\mathrm{sh}})\,. \tag{7.2.5}$$

Constraints derived from the observed number of Milky Way satellites suffer substantial theory uncertainties, which are associated with the upper and the lower bound of this integration. The mass of dwarf satellites has to be inferred from stellar kinematics and is difficult to determine, simultaneously the mass of the Milky Way is not known very precisely either [349]. In the present context, however, we aim to compare predictions based on matter power spectra from a default and a delayed UFA approach, and do not consider experimental results. Hence, the precise values adopted as integration limits are not so crucial, and we use $M_{\mathrm{sh}} \geq 10^8\,M_\odot/h$ and $M_{\mathrm{hh}} = 1.77 \times 10^{12}\,M_\odot/h$ from Ref. [348].

The predicted number of Milky Way satellites is summarised in Tab. 7.2. Evidently, the small-scale differences in the linear matter power spectrum caused by the UFA procedure only have a minor effect. Most importantly, the differences are well below the Poisson scatter those observations are subject to. Thus, constraints derived from observations of large-scale structure indeed remain valid, even when the linear matter power spectrum was obtained by the default UFA procedure.

7.2.2 Initial conditions for interacting neutrinos

If neutrinos interact with dark matter, the initial conditions for the integration of perturbation have to me modified from the standard ΛCDM expressions (4.4.13). A characteristic feature of the revised equations (4.4.15) is the equality of the metric perturbations, ϕ and ψ, due to the absence of neutrino anisotropic stress. Because previous studies of dark matter-neutrino interactions did not implement these changes, we here evaluate to what extent they affect the CMB spectra and the matter power spectrum. To this end we consider several benchmark scenarios with $n_{\nu\mathrm{dm}} = 0$ and varying interaction strength $u_{\nu\mathrm{dm}}$. The angular coefficients are set to $\alpha_l = 3/2$ for $l \geq 2$ and we fix the remaining cosmological parameters to their Planck 2018 best-fit values, see Tab. 2.1.

The correct choice of initial conditions in the dark matter-neutrino interacting scenario is mode dependent. Large modes, entering the Hubble radius after neutrino decoupling, are to be evolved from default initial conditions. Small modes, in contrast, require the expressions derived under the assumption of neutrino tight coupling. Therefore, our implementation of the νdm-scenario introduces two new trigger parameters. If $\kappa'_{\nu\mathrm{dm}}/\mathcal{H} < (\kappa'_{\nu\mathrm{dm}}/\mathcal{H})_{\nu-\mathrm{ini}}$ initially, default initial conditions are applied. Otherwise, the code imposes interacting initial conditions and adjusts the initial time to an epoch where $\mathcal{H}/\kappa'_{\nu\mathrm{dm}} > (\mathcal{H}/\kappa'_{\nu\mathrm{dm}})_{\nu-\mathrm{ini}}$ holds.

For the trigger values we adopt $(\mathcal{H}/\kappa'_{\nu\mathrm{dm}})_{\nu-\mathrm{ini}} = (\kappa'_{\nu\mathrm{dm}}/\mathcal{H})_{\nu-\mathrm{ini}} = 0.01$. To justify this choice, we further test the stability of our results with respect variations in the triggers. Dividing either of them by two, the CMB spectra remain stable on the sub-percent level for $u_{\nu\mathrm{dm}} = 10^{-4}$ and for $u_{\nu\mathrm{dm}} = 10^{-5}$. Differences in the matter power spectrum are negligible if $u_{\nu\mathrm{dm}} = 10^{-4}$, and for $u_{\nu\mathrm{dm}} = 10^{-5}$ they stay below the 10% level on scales larger than $50\,h/\mathrm{Mpc}$. In general, decreasing $(\kappa'_{\nu\mathrm{dm}}/\mathcal{H})_{\nu-\mathrm{ini}}$ affects the results more severely for smaller $u_{\nu\mathrm{dm}}$. To fulfil the tight coupling trigger condition for small interactions strengths, the integration has to start very early, and other numerical effects, indifferent to the initial conditions, affect the result as well.

The comparison of CMB spectra, obtained for default and revised initial condition, reveals differences in $l\,(l+1)\,/(2\pi)\,C_l$ below the $\mu\mathrm{K}^2$ level for multipoles up to 2500, $u_{\nu\mathrm{dm}} = 10^{-4}$ and $u_{\nu\mathrm{dm}} = 10^{-5}$. These differences are safely below the experimental sensitivity. Regarding the matter power spectrum, we show several examples of the relative difference between default and revised initial conditions in Fig. 7.4. These also illustrate some general features of our procedure. Large scales enter the horizon when the trigger condition for decoupled neutrinos is fulfilled, and discrepancies with the default approach are marginal. The switch to tightly coupled initial conditions, marked by a sudden increase in the relative difference, occurs at a larger wavenumber if the interaction strength parameter is small. In the ensuing intermediate regime, the initial conditions are modified, but also the earlier integration time affects the numerical stability. The latter effect seems to dominate, and the relative difference plateaus. Because the integration starts earlier for smaller interaction rates, the height of the plateau increases for smaller values of $u_{\nu\mathrm{dm}}$ but always remains below the percent level for the studied scenarios. Our procedure

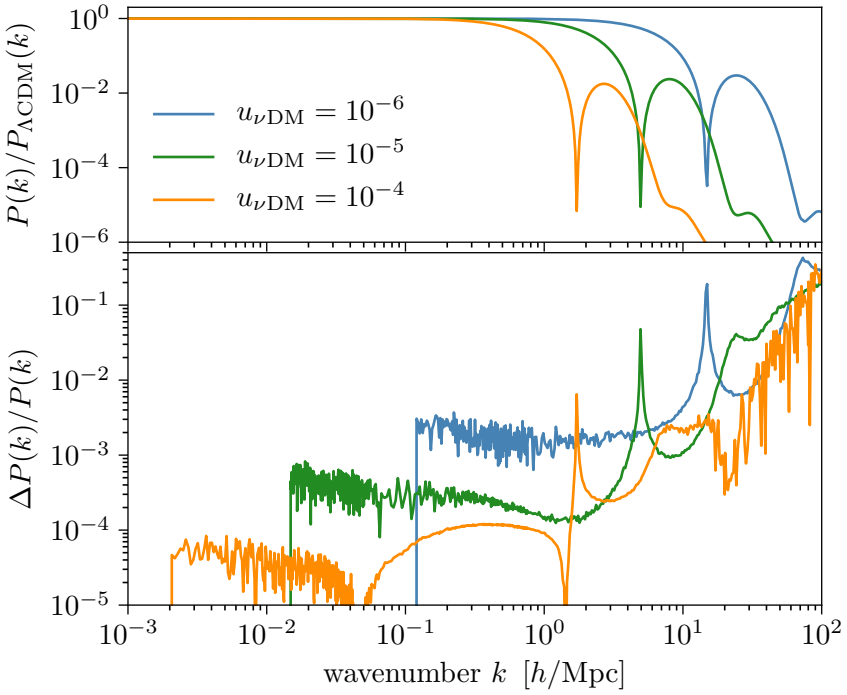

Figure 7.4: Comparison of the matter power spectra obtained with default initial conditions and with the revised approach, which accounts for neutrino interactions. For reference the upper panel shows the power spectra with revised initial conditions divided by the ΛCDM prediction.

modifies the location of the bump in the matter power spectrum very slightly. In relative differences this effect amplifies greatly and produces a spike. As one example, we show the metric perturbations of a mode towards the end of the intermediate regime in Fig. 7.5. When the default integration commences, the mode is neither in the decoupled nor in the tightly coupled limit, a steep increase in ψ indicates the misalignment of the default initial conditions. The integration starts much earlier for the revised treatment, however, in the intermediate regime both solutions rapidly converge to a common evolution. Only the smallest scales enter the Hubble radius when neutrinos are tightly coupled to dark matter. These constitute the third regime in Fig. 7.4, where the differences increase. For the large wavenumbers concerned, however, the matter power spectrum is already suppressed by many orders of magnitude with respect to the ΛCDM prediction. Recalling the discussion from Sec. 7.2.1, we do not expect that such differences in the linear matter power spectrum affect cosmological observables.

7.3 Analytical mixed damping solution

In the mixed damping regime, free streaming neutrinos drag along dark matter and thereby erase perturbations in the latter component. To get a more comprehensive understanding of this mechanism, we turn now to the evolution of individual modes. Our discussion starts with a brief summary of the ΛCDM evolution of neutrino and dark matter perturbations and with a comparison between the decoupling histories of the baryon-photon plasma and

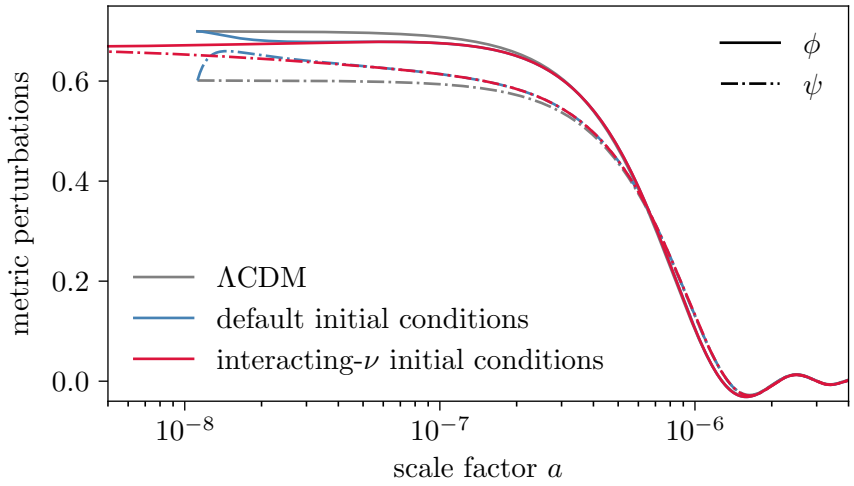

Figure 7.5: Comparison of the evolution of metric perturbations starting from default and revised initial condition. The considered mode has $k = 20\,h/\mathrm{Mpc}$, and the dark matter-neutrino interactions are characterised by $u_{\nu\mathrm{dm}} = 10^{-5}$ and $n_{\nu\mathrm{dm}} = 0$.

the dark matter-neutrino sector. The differences noted are important for the derivation of an analytical approximation to the evolution of dark matter perturbations, presented in the following.

The scale factors of dark matter and neutrino decoupling relate as

$$a_{\nu,\mathrm{dec}} = \left(\frac{a_{\mathrm{dm,dec}}}{a_{\mathrm{md-max}}}\right)^{\frac{1}{n_{\nu\mathrm{dm}}+1}} a_{\nu\mathrm{dm,dec}}\,. \tag{7.3.1}$$

Mixed damping requires $a_{\nu\mathrm{dm,dec}} < a_{\mathrm{md-max}}$, and for a fixed dark matter decoupling time, neutrinos decouple earlier if $n_{\nu\mathrm{dm}}$ is small. Correspondingly, the mixed damping regime lasts longer, see also Fig. 7.1, and a larger range of modes is subject to mixed damping only. Further, the numerical solution is more stable for small values of $n_{\nu\mathrm{dm}}$, because, for a given decoupling time, the initial dark matter and the neutrino scattering rate are smaller, and hence the system of differential equations is less stiff. We therefore concentrate on $n_{\nu\mathrm{dm}} = 0$ for the present discussion, but the generalisation of our arguments to other temperature dependencies of the cross section is straight forward.

7.3.1 Comparison with the ΛCDM evolution

The qualitative evolution of dark matter perturbations in the ΛCDM scenario is rather straightforward. They are constant while outside causal contact and receive a boost upon Hubble crossing, which sets them in a growing mode. The growth is proportional to $\log a$ in the radiation-dominated epoch proceeds as $\delta_{\mathrm{dm}} \propto a$ during matter domination [132, 298]. As an example, the evolution of four modes is shown in Fig. 7.6, where dashed pink lines indicate dark matter in the collisionless ΛCDM scenario. Matter-radiation equality occurs when $\tau_{\mathrm{eq}} \sim 115\,\mathrm{Mpc}$, outside the illustrated range, such that only the logarithmic behaviour can be observed. Neutrino perturbations receive the same initial boost from gravitational infall as dark matter. Being relativistic, they then diffuse out of overdense

regions, and the competition between gravitational forces and the neutrino pressure leads to damped oscillations in δ_ν, which can be clearly noticed in Fig. 7.6.

While the introduction of neutrino-dark matter interactions could render the dynamics of this coupled sector very similar to that of the baryon-photon plasma, an important difference arises due to the very different decoupling histories. The formation of neutral hydrogen at the epoch of recombination implies a steep decrease in the free electron fraction and hence in the photon-baryon scattering rate. Still, decoupling of baryons and photons does not occur simultaneously but very closely. The Planck collaboration obtained $z_* = 1090 \pm 0.41$ for the redshift of photon decoupling and $z_{\rm drag} = 1059.39 \pm 0.46$ for the end of the baryon drag epoch [15]. The damping of baryon perturbations by photon free streaming between those limits is very similar to the mixed damping mechanism. However, the dark matter and the neutrino scattering rate evolve as power laws of the scale factor for the entire relevant cosmological history. The difference between their respective decoupling times can be considerably larger as for the baryon-photon plasma and amount to several orders of magnitude. Correspondingly, mixed damping lasts longer than the Silk damping of baryon fluctuations, affects a larger range of wavelengths, and, depending on a mode's size, is not preceded by acoustic oscillations of the combined plasma.

7.3.2 Dark matter evolution in the mixed damping regime

The basic premises of mixed damping allow for some simplifying assumptions, which we use here to derive an analytical approximation for the evolution of dark matter perturbations. Firstly, as discussed in Sec. Sec. 7.1.3, mixed damping can only occur if dark matter decouples from neutrinos before matter-radiation equality. At these times, the metric potentials are dominated by radiation perturbations and insensitive to alterations in the dark matter evolution to good approximation. Secondly, neutrinos free stream and are coupled to all other species only by gravitational interactions. Hence, in the mixed damping regime neutrino perturbations are not affected by the modified dynamics of the dark matter sector. With these two assumptions, the dark matter evolution (3.5.7) only depends on an external source function, $S\left(k\,,\tau\right)$, and becomes

$$\delta''_{\nu\rm dm} + \left(\frac{1}{\tau} + \frac{C_\kappa}{\tau^3}\right)\delta'_{\nu\rm dm} = S\left(k\,,\tau\right)\,. \tag{7.3.2}$$

During radiation domination, the reduced Hubble rate is $\mathcal{H} = \tau^{-1}$ and for $n_{\nu\rm dm} = 0$ we decompose the scattering rate as $R_{\nu\rm dm}\,\kappa'_{\nu\rm dm} = C_\kappa\,\tau^{-3}$, where C_κ is a constant. The source function,

$$S\left(k\,,\tau\right) = 3\phi'' + \frac{3}{\tau}\,\phi' - k^2\psi + \frac{C_\kappa}{\tau^3}\left(3\phi' - \theta_\nu\right)\,, \tag{7.3.3}$$

depends on the metric potentials and on the neutrino velocity divergence. We derive an analytical expression for either of these quantities in the two ensuing subsections and here simply anticipate the result. Neglecting the neutrino anisotropic stress implies $\phi = \psi$, and

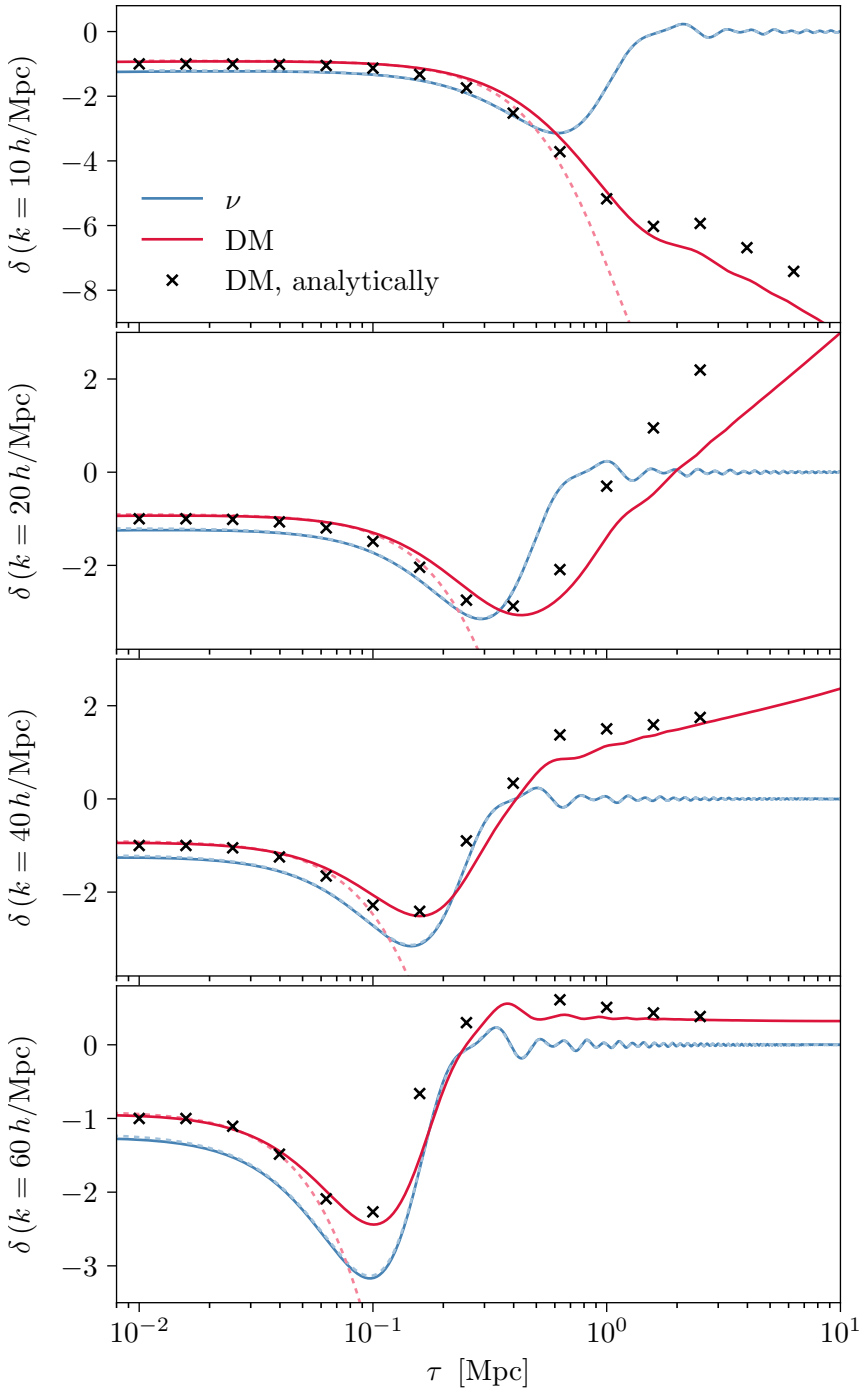

Figure 7.6: Evolution of density perturbations in the ΛCDM scenario (dashed, pastel lines) and for dark matter-neutrino interactions characterised by $u_{\nu\mathrm{dm}} = 10^{-6}$ and $n_{\nu\mathrm{dm}} = 0$ (dark, solid lines). Analytic predictions for the mixed damping evolution of dark matter, obtained from the integration of Eq. (7.3.8), are indicated by black crosses.

the metric perturbations deep in the radiation-dominated epoch are approximated by [21]

$$\phi\left(k\,,\tau\right)=3\,\phi_{\rm p}\left(k\right)\left(\frac{\sin\left(k\tau/\sqrt{3}\right)-\left(k\tau/\sqrt{3}\right)\cos\left(k\tau/\sqrt{3}\right)}{\left(k\tau/\sqrt{3}\right)^{3}}\right)\,, \tag{7.3.4}$$

where $\phi_{\rm p}$ is the primordial magnitude of the fluctuation, i.e. $\phi\left(k,\tau\to 0\right)=\phi_{\rm p}\left(k\right)$. For the neutrino free streaming evolution we take [288]

$$\theta_{\nu}\left(k\,,\tau\right)=\frac{3k}{4}\left(\delta_{\nu,{\rm ini}}+4\psi_{\rm ini}\right)\,j_{1}\left(k\tau\right)+6k\int_{0}^{\tau}d\tau'\,\dot{\phi}\,j_{1}\left[k\left(\tau-\tau'\right)\right]\,. \tag{7.3.5}$$

The two homogeneous solutions to Eq. (7.3.2) are $h_1\left(\tau\right)=$ const. $=C_1$ and $h_2\left(\tau\right)=C_2\,{\rm Ei}\left[C_{\kappa}/\left(2\tau^2\right)\right]$, where ${\rm Ei}\left(x\right)$ represents the exponential integral function

$${\rm Ei}\left(\tau\right)=\int_{-x}^{\infty}dt\,\exp\left(t\right)/t\,. \tag{7.3.6}$$

In general, the solution to a second order differential equation is given by a linear combination of the two homogeneous solutions, and a particular solution. The latter, constructed with Green's method, is given by the an integral over the source term weighted by Green's function

$$g\left(\tau\,,\eta\right)=\frac{h_1\left(\eta\right)\,h_2\left(\tau\right)-h_1\left(\eta\right)\,h_2\left(\tau\right)}{h_1'\left(\eta\right)h_2\left(\eta\right)-h_1\left(\eta\right)h_2'\left(\eta\right)}\,. \tag{7.3.7}$$

Thus, the full solution for the evolution of the dark matter density contrast (7.3.2) is

$$\delta_{\nu{\rm dm}}\left(k\,,\tau\right)=C_1+C_2\,{\rm Ei}\left(\frac{C_{\kappa}}{2\tau^2}\right)+\int_{0}^{\tau}d\eta\,S\left(k\,,\eta\right)\,\frac{\eta}{2}\,{\rm e}^{-\frac{C_{\kappa}}{2\eta^2}}\left[{\rm Ei}\left(\frac{C_{\kappa}}{2\eta^2}\right)-{\rm Ei}\left(\frac{C_{\kappa}}{2\tau^2}\right)\right]\,. \tag{7.3.8}$$

For small values of τ, when the mode is well outside the Hubble radius, $\delta_{\nu{\rm dm}}$ is constant. Hence the initial conditions dictate $C_2=0$ and $C_1=\delta_{\nu{\rm dm}}\left(k\,,0\right)$. We evaluate the integral numerically for several modes at consecutive conformal times. The results are indicated as black crosses in Fig. 7.6. Notice that our analytical results capture the qualitative features of the numerical solution rather well, even though our approximations are not perfect. While the analytic form for the metric evolution follows the numerical results rather well, its first and second derivatives are less accurate. We also find that our expression for the neutrino velocity gets damped slightly slower than the numerical results suggest. Because our main intention in deriving the analytical solution is to shed light on the underlying physics, we keep the simple analytic forms given above and not attempt to improve the accuracy using e.g. fitting formulae [132, 298].

7.3.3 Metric perturbations in the radiation-dominated era

The source function (7.3.3), driving the evolution of dark matter perturbations in the mixed damping regime, depends on the metric perturbations and their first and second time derivatives. In our derivation of an analytical expression for space component of the metric potentials, ϕ, we closely follow the arguments of Ref [21] but adapt the notation to our conventions.

Combining the time-time (3.2.17a) and the time-space (3.2.17b) component of the linearised Einstein equations yields a geometric equation for ϕ

$$k^2\,\phi = -\frac{4\pi\,a^2}{m_{\mathrm{P}}^2}\left[(\delta\rho)_{\mathrm{m}} + (\delta\rho)_{\mathrm{r}} + \frac{3\mathcal{H}}{k^2}\left((\theta\rho)_{\mathrm{m}} + \frac{4}{3}\,(\theta\rho)_{\mathrm{r}}\right)\right]. \tag{7.3.9}$$

The subscript "r" refers to radiation perturbations, to which neutrinos and photons contribute according to their energy density, i.e. $(\delta\rho)_{\mathrm{r}} = \delta_\gamma\rho_\gamma + \delta_\nu\rho_\nu$ and $(\theta\rho)_{\mathrm{r}} = \theta_\gamma\rho_\gamma + \theta_\nu\rho_\nu$. Baryon and dark matter add in the same fashion to form the combined matter perturbations, indicated by the subscript "m". However, presuming the universe is dominated by radiation, we neglect the latter in the following.

Early in the radiation-dominated epoch, the large Thomson scattering rate suppresses all photon multipoles beyond velocity divergence and drives the photon-baryon slip to zero (c.f. Sec. 4.2.1). Neutrino free streaming, in contrast, implies a non-zero neutrino anisotropic stress. However, its effect on the metric perturbations is not too large and can be treated perturbatively [298]. In this sense, our result, which neglects the impact of σ_ν, represents the zeroth-order solution. Then, the traceless component of the Einstein equations (3.2.17d) implies $\psi = \phi$ and the evolution of radiation perturbations approximately is

$$\delta_{\mathrm{r}}' = -\frac{2}{3}\,\theta_{\mathrm{r}} + 4\phi'\,, \tag{7.3.10a}$$

$$\theta_{\mathrm{r}}' = \frac{k^2}{4}\delta_{\mathrm{r}} + k^2\phi\,. \tag{7.3.10b}$$

The geometric metric equation (7.3.9) allows to eliminate the radiation density contrast from either equation

$$-\frac{4}{k^2\tau}\theta_{\mathrm{r}}' + \left[\frac{4}{(k\tau)^2} + \frac{4}{3}\right]\theta_{\mathrm{r}} = \left[4 + \frac{2}{3}\,(k\tau)^2\right]\phi' + \frac{4}{3}k^2\tau\phi\,, \tag{7.3.11a}$$

$$\theta_{\mathrm{r}}' = -\frac{1}{6}k^4\tau^2\phi = \frac{1}{\tau}\theta_{\mathrm{r}} + k^2\phi\,. \tag{7.3.11b}$$

Further, θ_{r}' can be removed from the first expression above by using the second one,

$$\phi' + \frac{1}{\tau}\phi = \frac{2}{(k\tau)^2}\theta_{\mathrm{r}}\,. \tag{7.3.12}$$

Taking the derivative with respect to conformal time and removing the resulting occurrences of photon perturbations with Eq. (7.3.11b) and Eq. (7.3.12) transforms this expression into a second order differential equation for the metric potential

$$\phi'' + \frac{4}{\tau}\phi' + \frac{k^2}{3}\phi = 0\,. \tag{7.3.13}$$

The analytical solution for ϕ is recognised more easily after the replacement $u = \phi\tau$, which yields

$$u'' + \frac{2}{\tau}u' + \left(\frac{k^2}{3} - \frac{2}{\tau^2}\right)u = 0\,. \tag{7.3.14}$$

This is the spherical Bessel equation of order one in the variable $k\tau/\sqrt{3}$. Of its two solutions, the spherical Bessel function and the spherical Neumann function, only the

former is finite at the origin. Thus, the evolution of the metric perturbations, in the limit of radiation domination and vanishing anisotropic stress, is given by Eq. (7.3.4).

7.3.4 Neutrino free streaming solution

The second ingredient to evaluate the source function (7.3.3) in the mixed damping evolution of dark matter perturbations is an expression for the velocity divergence of free streaming neutrinos. Such an expression was obtained for the synchronous gauge in Ref. [288]. Here, we translate the derivation to our choice of conformal Newtonian gauge.

The momentum-integrated Boltzmann equation of free streaming neutrinos (3.4.18) can be recast as

$$\frac{d}{d\eta}\left[F_\nu\left(k,\,\mu,\,\tau\right)\,\mathrm{e}^{-ik\mu(\tau-\eta)}\right] = 4\mathrm{e}^{-ik\mu(\tau-\eta)}\,\left(\phi' - ik\mu\psi\right)\,. \tag{7.3.15}$$

Integrating both sides from $\eta = 0$ until the conformal time τ gives

$$\begin{aligned} F_\nu\left(k,\,\mu,\,\tau\right) &= F_{\nu,\mathrm{ini}}\left(k,\,\mu\right)\mathrm{e}^{-ik\mu\tau} + 4\int_0^\tau d\eta\,\mathrm{e}^{-ik\mu(\tau-\eta)}\,\left(\phi' - ik\mu\psi\right) \\ &= \left(F_{\nu,\mathrm{ini}} + 4\psi_{\mathrm{ini}}\right)\mathrm{e}^{-ik\mu\tau} - 4\psi\left(\tau\right) + 4\int_0^\tau d\eta\,\mathrm{e}^{-ik\mu(\tau-\eta)}\,\left(\psi' + \phi'\right)\,, \end{aligned} \tag{7.3.16}$$

where the second line was obtained from integration by parts. Neglecting again terms beyond the dipole (3.4.17), we write the initial conditions as

$$F_{\nu,\mathrm{ini}} = F_{\nu,\mathrm{ini},0} - 3i\mu\,F_{\nu,\mathrm{ini},1} = \delta_{\nu,\mathrm{ini}} - \frac{4i\mu}{k}\theta_{\nu,\mathrm{ini}}\,, \tag{7.3.17}$$

where the second equality follows from Eq. (3.4.21). To obtain equations for the individual neutrino multipole moments, we expand the plane wave function in terms of spherical Bessel functions j_l and Legendre polynomials P_l according to Eq. (4.1.14). Following the same steps which allowed to expand the neutrino evolution equations in terms of individual multipoles in Sec. 3.4.2, we multiply Eq. (7.3.15) by the Legendre polynomial P_l and integrate over the full solid angle, using the orthogonality relation (3.4.20). The angular dependence in the initial conditions can be rewritten as a time derivative of $\exp\left(-ik\mu\tau\right)$ and is removed by integrating by parts. Eventually, we obtain

$$F_{\nu,l}\left(k,\,\tau\right) = \left[\delta_{\nu,\mathrm{ini}} + 4\psi_{\mathrm{ini}}\right]j_l\left(k\tau\right) + \frac{4}{k}\theta_{\nu,\mathrm{ini}}\,j_l'\left(k\tau\right) + 4\int_0^\tau d\eta\,j_l\left[k\left(\tau-\eta\right)\right]\left(\psi' + \phi'\right)\,. \tag{7.3.18}$$

The initial neutrino velocity divergence (4.4.13d) evaluated at $\tau = 0$ is zero, and in the limit of zero anisotropic stress the time and space component of the metric perturbations equal each other. Finally, this gives Eq. (7.3.5).

7.4 Mixed damping in terms of the matter power spectrum

The matter power spectrum for several neutrino-dark matter interacting scenarios is shown in Fig. 7.7. For the largest values of $u_{\nu\mathrm{dm}}$, perturbations on small scales are subject to a mixture of collisional and mixed damping, but for larger wavenumbers or smaller scattering

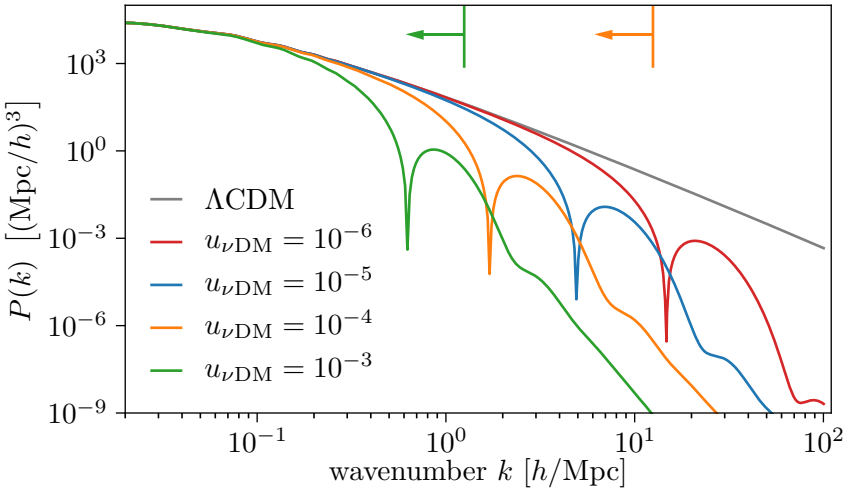

Figure 7.7: The matter power spectrum in presence of dark matter-neutrino interactions. Depending on the size of a mode and the particular value of $u_{\nu\mathrm{dm}}$, the suppression with respect to ΛCDM is caused by mixed damping only or a by combination of collisional and mixed damping. Arrows in the same colours as the graphs indicate the former regime. For the smallest scattering rates shown here these bounds lie outside the plotted range.

rates, all power suppression with respect to ΛCDM is caused by mixed damping. For each scenario in Fig. 7.7, we indicate the transition between the two regimes regimes by coloured arrows. In general, the matter power spectra show a common set of features, namely:

- At the largest scales, there is no difference with the ΛCDM prediction.
- Continuing to smaller wavenumbers, a steep decrease in power is followed by a bump after which the matter power spectrum continues to decrease again.
- A small plateau is encountered in the subsequent damping tail, after it the perturbations reduce further.

The ΛCDM-like behaviour on large scales arises because these enter the Hubble radius after dark matter has decoupled and hence are not affected by neutrino interactions. An estimate of the scale which enters the Hubble radius when $\Gamma_{\mathrm{dm}-\nu} = H$ yields

$$k_{\mathrm{dm,dec}} = 2\pi\, H_0\, \sqrt{\Omega_{\mathrm{r}}} \simeq \frac{6.67 \times 10^3}{\sqrt{u_{\nu\mathrm{dm}}}}\, h/\mathrm{Mpc}\,, \tag{7.4.1}$$

for $n_{\nu\mathrm{dm}} = 0$, reproducing the onset of the damping rather well. The evolution of dark matter perturbations in the ΛCDM scenario is approximated by [21]

$$\delta_{\mathrm{cdm}}\,(k,\,\tau) = C_1 - \int_0^{\tau} d\eta\; \eta\,[\ln\,(k\eta) - \ln\,(k\tau)]\;\; S\,(k,\,\eta)|_{\kappa'_{\nu\mathrm{dm}}=0}\,. \tag{7.4.2}$$

It is reassuring to note that the analytic solution (7.3.8) recovers the ΛCDM behaviour for $C_\kappa \ll \tau^2$. In this limit, the exponential integral can be expanded as

$$\mathrm{Ei}\left(\frac{C_\kappa}{2\tau^2}\right) = \gamma_{\mathrm{E}} + \ln\,(C_\kappa/2) - 2\ln\,(\tau) + \mathcal{O}\left(\frac{C_\kappa}{2\tau^2}\right)\,, \tag{7.4.3}$$

where γ_{E} is the Euler–Mascheroni constant, and the source function reduces to the ΛCDM expression when the last term of Eq. (7.3.3) is neglected.

We show the time evolution of neutrino and dark matter perturbations for several modes below the cut-off scale in Fig. 7.6, where we compare an interacting scenario with $u_{\nu\mathrm{dm}} = 10^{-6}$ to the ΛCDM evolution. Note that indeed no differences between the neutrino evolution in either case are noticeable. After horizon crossing in the radiation-dominated era, the gravitational potentials decay, and damped oscillations decrease the magnitude of θ_ν. Hence the source function (7.3.3) becomes zero at late times, and the dark matter evolution at $\tau > \tau_{\mathrm{late}}$ can be further approximated by

$$\delta_{\nu\mathrm{dm}}\left(k\,,\tau\right) = \delta_{\nu\mathrm{dm}}(k,\tau_{\mathrm{late}}) + 2\left(\int_0^{\tau_{\mathrm{late}}} d\tau'\, S(k\,,\tau')\,\frac{\tau'}{2}\,\mathrm{e}^{-\frac{C_{\mathrm{K}}}{2\tau'^2}}\right)\ln\left(\tau\right)\,, \tag{7.4.4}$$

where we used the decoupled limit of the exponential integral (7.4.3). The result indicates that, after dark matter decoupling in the radiation-dominated era, the perturbation still grows $\propto \ln a$. This is clearly noticeable for the largest mode in the top panel of Fig. 7.6, which lies in a regime where the matter power spectrum is already suppressed but before the bump. However, the presence of the neutrino velocity in the source function modifies the proportionality constant in front of the logarithm as well as the value of $\delta_{\nu\mathrm{dm}}(k,\tau_{\mathrm{late}})$ in comparison to the ΛCDM result.

In the ΛCDM case, $\delta_{\mathrm{cdm}}(k,\tau_{\mathrm{late}})$ and the integral in front of the logarithmic term in Eq. (7.4.4) always evaluate to negative values. Consequently, the dark matter density contrast evolves in the negative direction, as evident for all modes in Fig. 7.6. The contribution of the neutrino velocity divergence to the source function can alter this behaviour in interacting scenarios. As the analytical solution (7.3.5) implies, θ_ν is larger for larger k, and correspondingly its impact on the source function increases. This relation is evident from Fig. 7.8, which compares the ΛCDM and the νdm source functions for the three largest modes shown in Fig. 7.6. Figure 7.8 also reveals a sharp decrease at early times in the interacting source functions. However, in the full expression for the density contrast (7.3.8), this decrease is suppressed by the smallness of the exponential function in the integral. Instead, the relevant feature of the interacting source functions is the development of a positive peak, which grows with k. Eventually, it can turn the value of $\delta_{\nu\mathrm{dm}}\left(k,\,\tau_{\mathrm{late}}\right)$ and the proportionality constant in front of the logarithm positive. The second mode of Fig. 7.6 already lies in this latter regime. In terms of the matter power spectrum, the transition is marked by a sharp dip.

As the wavenumber increases further, oscillations in the neutrino velocity become stronger imprinted on the source functions, and, comparing the two larger modes in Fig. 7.8, lead to the development of a second zero crossing. While its contribution to the integral of Eq. (7.4.4) is not sufficient to turn the density contrast in the negative direction again, it still causes a partial cancellation. The reduction of the coefficient for the logarithmic growth is evident comparing the two centre panels of Fig. 7.6. Both modes grow logarithmically, though the larger $k = 40\,h/\mathrm{Mpc}$ mode increases at an slower rate than that with $k = 20\,h/\mathrm{Mpc}$. This cancellation is even more extreme in case of the largest mode in Fig. 7.6,

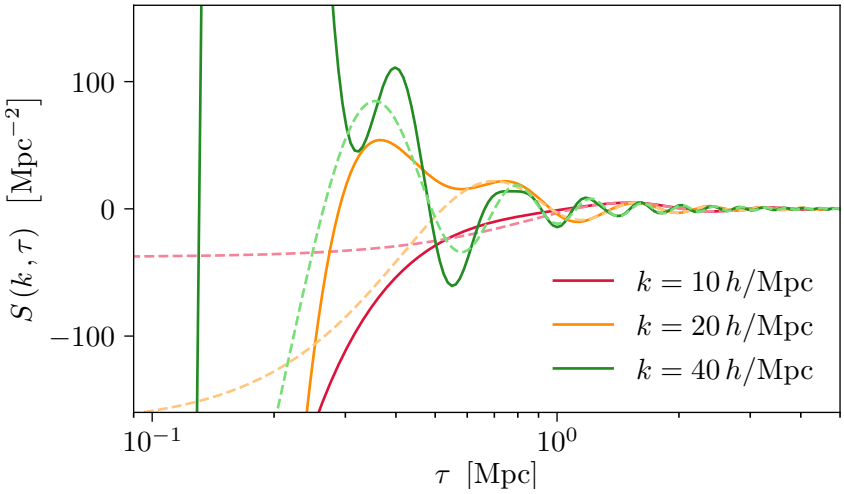

Figure 7.8: External source function driving the evolution of dark matter perturbations at early times according to Eqs. (7.3.2) and (7.3.3). The two cases illustrated are ΛCDM (pastel, dashed lines) and an interacting scenario with $u_{\mathrm{vdm}} = 10^{-6}$ (dark, solid lines).

whose late time evolution is almost flat. It is only upon matter-radiation equality at $\tau_{\mathrm{eq}} \sim 140\,\mathrm{Mpc}$, i.e. beyond the depicted range, that this mode starts growing significantly.

7.5 Summary

Mixed damping suppresses cosmological perturbations when a heavy species is coupled to a relativistic fluid which itself is free streaming. The effect is particularly relevant for interactions between dark matter and neutrinos but might also arise in scenarios with dark radiative degrees of freedom. In the latter case, limits on the effective neutrino number impose additional constraints on the mixed damping parameter space. Our study, however, focuses on scattering between dark matter and neutrinos.

The parameter space for mixed damping is bound from above and below in terms of the dark matter decoupling time, the interaction strength $u_{\gamma\mathrm{dm}}$ and the scales affected. The lower limit on u_{vdm} derives from the requirement that dark matter interactions remain in equilibrium beyond electroweak decoupling and is observationally out of reach. The upper bound originates because dark matter has to decouple before its energy density roughly equals that of neutrinos, later, only the canonical collisional damping can occur. Already to date, the sensitivity of CMB and large-scale structure observations exceeds the lower bound. Mixed damping is particularly relevant at larger scales, where a suppression of power with respect to the ΛCDM can be most robustly established. If future data reveals a departure from ΛCDM expectations due to dark matter-neutrino interactions, the discrepancy will be caused by mixed damping. Hence, precise numerical predictions and a profound physical understanding of the effect are desirable.

The Boltzmann hierarchy of interacting neutrinos and the interacting dark matter evolution equations automatically account for the mixed damping effect. However, several subtleties have to be considered for their numerical solution. These are not limited to

the mixed damping regime, but relevant in any case where additional couplings to otherwise free streaming radiation are postulated. More precisely, the ultra-relativistic fluid approximation has to be delayed sufficiently long for the radiative component to become collisionless, and the initial conditions require modifications in the presence of additional interactions. In the case of dark matter-neutrino interactions, we have verified that neither of these modifications affects theory predictions at a level relevant to the observational sensitivity. Thus, existing constraints on the dark matter-neutrino scattering, which did not consider the alterations, remain robust.

To illuminate the physical process of mixed damping, we derive an analytical approximation to the evolution of dark matter perturbations in this regime. The evolution of the dark matter density contrast is driven by an external source function, which receives non-standard contributions from the neutrino velocity divergence. The larger the scattering rate and a mode's wavenumber, the more distinctly reflect oscillations in θ_ν in the source function. The resulting cancellation in the time integration of the source function suppresses the growth of $\delta_{\nu\mathrm{dm}}$ in the radiation-dominated era. Eventually, this causes a decrease in the matter power spectrum on all scales which enter the Hubble radius before dark matter kinetically decouples from neutrinos.

Chapter 8

Conclusions

This thesis investigates the linear evolution of cosmological perturbations in extended cosmologies where dark matter is not entirely collisionless. In particular, we study late kinetic decoupling between dark matter and photons or neutrinos. One central aspect is the accuracy of theory predictions and in particular the impact of dark matter interactions on numerical approximation schemes. Further, we confront the scenarios with present and future observations to assess their viability.

Dark matter-photon interactions necessitate modifications to the line of sight integration and the tight coupling approximations. In particular for the latter we derive expressions which differ from those employed in previous works [285]. Still, our study confirms the robustness of these limits, as the discrepancies affect the CMB and the matter power spectrum only below the experimental sensitivity. We further consider the sound speed term, which arises for interacting dark matter, explicitly. Its impact on the CMB angular spectra over the multipole range probed by Planck is negligible, given the dark matter mass exceeds 10 keV, but the term can tighten large-scale structure limits for light dark matter candidates below 1 GeV. To obtain updated limits on the parameter space of dark matter-photon interactions, we consider the Planck 2015 data release [5] and perform a Monte Carlo Markov chain analysis. Our constraint tightens by 20% with respect to those based on the 2013 data [285] for the most conservative lowTEB + highTT baseline data set and read $\sigma_{\gamma\mathrm{dm}} \leq 2.25 \times 10^{-6}\,\sigma_{\mathrm{T}}\ (m_{\gamma\mathrm{dm}}/\mathrm{GeV})$ at 95% confidence level. If further the preliminary polarisation data and the lensing likelihoods are included, the limit tightens to $\sigma_{\gamma\mathrm{dm}} \leq 1.49 \times 10^{-6}\,\sigma_{\mathrm{T}}\ (m_{\gamma\mathrm{dm}}/\mathrm{GeV})$. We find that dark matter interactions with photons can alleviate a possible σ_8 tension but do not help in resolving the H_0 discrepancy.

We further extend dark matter-photon interactions to a mixed dark matter scenario in which a collisional and a collisionless dark matter component contribute to the relic abundance. If the fraction of interacting dark matter, $f_{\gamma\mathrm{dm}}$, is large, perturbations in the two component cancel each other effectively, and the matter power spectrum on intermediate scales gets suppressed even below the level expected in the purely interacting scenario. Even more importantly, a small abundance of interacting dark matter has a very similar impact on the matter power spectrum as massive neutrinos. Confronting the mixed dark matter scenario with Planck 2015 data, we find that the interaction strength

parameter, $u_{\gamma\mathrm{dm}}$, is almost unconstrained if less than 10% of dark matter resides in the interacting component. We further perform a Fisher forecast for the DESI survey, which reveals a strong degeneracy between $u_{\gamma\mathrm{dm}}$ and $f_{\gamma\mathrm{dm}}$. As a result, the expected sensitivity to the mixed dark matter scenario is significantly lower than in the case of a single, interacting dark matter component. The possible existence of mixed dark matter also complicates the determination of the neutrino mass scale, as both parameters of the model, $u_{\gamma\mathrm{dm}}$ and $f_{\gamma\mathrm{dm}}$, show a degeneracy with $\sum m_\nu$.

In the context of dark matter-neutrino interactions, we highlight the need to delay the ultra-relativistic fluid approximation sufficiently, until neutrinos have kinetically decoupled. The neutrino scattering also modifies the initial conditions, and we explicitly derive and implement the revised expressions. For either of those modifications, we find that their impact on the CMB spectra is negligible. Differences in the matter perturbations are confined to wavenumbers where the matter power spectrum is suppressed by several orders of magnitude with respect to the ΛCDM case. Thus, neither discrepancy with previous works affects observational limits from the CMB or large-scale structure observations.

In scenarios with dark matter-neutrino interactions, an alternative to the canonical collisional damping mechanism exists, called mixed damping [292]. In this regime, neutrinos are free streaming, but dark matter still feels their drag force, which prevents it from clustering. Mixed damping is automatically accounted for by the coupled neutrino Boltzmann hierarchy and the dark matter evolution equations, but these do not provide immediate insight into the underlying physical mechanism. Yet, our exploration of the parameter space shows that existing constraints already are sensitive to the mixed damping regime, future surveys will explore it further. We derive an analytical approximation to the evolution of dark matter perturbations in the mixed damping regime, which accomplishes to reproduce all qualitative features of the numerical result. An external source function drives the evolution of the dark matter density contrast and receives additional contributions from the neutrino velocity divergence. Oscillations in the latter become imprinted upon the source function more strongly as the interaction rate or the mode's wavenumber increase and lead to a partial cancellation that suppresses the growth of structure.

Already to date, cosmological observations allow for robust tests of the conditions in the early universe. Various ambitious efforts are planned and proposed for the future, such that the available data can be expected to improve even further. Amongst these are large-scale structure surveys, such as DESI [331] or EUCLID [322], as well as CMB experiments, like LiteBIRD [351] or CMB-S4 [352]. In context of the unknown nature of dark matter, cosmological constraints are highly complementary to other experimental efforts, like collider searches and direct detection. To fully exploit the experimental data, accurate theory predictions, which carefully assess uncertainties and precisely state the underlying assumptions, are vital. Up to date constraints, a profound understanding of the physical mechanism and the awareness of possible degeneracies between scenarios help to plan and analyse future observations. The thesis presented aims to contribute to those theoretical challenges.

Bibliography

[1] J. Stadler and C. Bœhm, *Constraints on γ-CDM interactions matching the Planck data precision*, *JCAP* **1810** (2018) 009, [1802.06589].

[2] J. Stadler, C. Bœhm and O. Mena, *Comprehensive Study of Neutrino-Dark Matter Mixed Damping*, *JCAP* **2019** (2020) 014, [1903.00540].

[3] J. Stadler, C. Bœhm and O. Mena, *Is it Mixed dark matter or neutrino masses?*, [1807.10034]. submitted to JCAP.

[4] Planck collaboration, N. Aghanim et al., *Planck 2018 results. VI. Cosmological parameters*, [1807.06209].

[5] Planck collaboration, R. Adam et al., *Planck 2015 results. I. Overview of products and scientific results*, *Astron. Astrophys.* **594** (2016) A1, [1502.01582].

[6] R. Wilkinson, *Deciphering Dark Matter with Cosmological Observations*, Ph.D. thesis, Durham U., IPPP, 2016-06-24.

[7] Planck collaboration, P. A. R. Ade et al., *Planck 2015 results. XIII. Cosmological parameters*, *Astron. Astrophys.* **594** (2016) A13, [1502.01589].

[8] W. H. Press, S. A. Teukolsky, W. T. Vetterling and B. P. Flannery, *Numerical recipes: the art of scientific computing*. Cambridge University Press, New York, 3rd ed. ed., 2007.

[9] A. Font-Ribera, P. McDonald, N. Mostek, B. A. Reid, H.-J. Seo and A. Slosar, *DESI and other dark energy experiments in the era of neutrino mass measurements*, *JCAP* **1405** (2014) 023, [1308.4164].

[10] A. Einstein, *The Foundation of the General Theory of Relativity*, *Annalen Phys.* **49** (1916) 769–822. [Annalen Phys.354,no.7,769(1916)].

[11] A. Friedmann, *On the Curvature of space*, *Z. Phys.* **10** (1922) 377–386. [Gen. Rel. Grav.31,1991(1999)].

[12] A. Friedmann, *On the Possibility of a world with constant negative curvature of space*, *Z. Phys.* **21** (1924) 326–332. [Gen. Rel. Grav.31,2001(1999)].

[13] G. Lemaitre, *A Homogeneous Universe of Constant Mass and Growing Radius Accounting for the Radial Velocity of Extragalactic Nebulae*, *Annales Soc. Sci. Bruxelles A* **47** (1927) 49–59. [Gen. Rel. Grav.45,no.8,1635(2013)].

[14] H. P. Robertson, *Kinematics and World-Structure*, *Astrophys. J.* **82** (1935) 284–301.

[15] Planck collaboration, Y. Akrami et al., *Planck 2018 results. I. Overview and the cosmological legacy of Planck*, [1807.06205].

[16] E. Hubble, *A relation between distance and radial velocity among extra-galactic nebulae*, *Proc. Nat. Acad. Sci.* **15** (1929) 168–173.

[17] A. Sandage, *A New Determination of the Hubble Constant from Globular Clusters in M87*, *Astrophys. J.* **152** (June, 1968) L149.

[18] LIGO Scientific, Virgo, 1M2H, Dark Energy Camera GW-E, DES, DLT40, Las Cumbres Observatory, VINROUGE, MASTER collaboration, B. P. Abbott et al., *A gravitational-wave standard siren measurement of the Hubble constant*, *Nature* **551** (2017) 85–88, [1710.05835].

[19] Particle Data Group collaboration, M. Tanabashi et al., *Review of Particle Physics*, *Phys. Rev.* **D98** (2018) 030001.

[20] COBE collaboration, G. F. Smoot et al., *Structure in the COBE differential microwave radiometer first year maps*, *Astrophys. J.* **396** (1992) L1–L5.

[21] S. Dodelson, *Modern Cosmology*. Academic Press, Amsterdam, 2003.

[22] A. H. Guth, *The Inflationary Universe: A Possible Solution to the Horizon and Flatness Problems*, *Phys. Rev.* **D23** (1981) 347–356. [Adv. Ser. Astrophys. Cosmol.3,139(1987)].

[23] A. D. Linde, *A New Inflationary Universe Scenario: A Possible Solution of the Horizon, Flatness, Homogeneity, Isotropy and Primordial Monopole Problems*, *Phys. Lett.* **108B** (1982) 389–393. [Adv. Ser. Astrophys. Cosmol.3,149(1987)].

[24] A. Albrecht and P. J. Steinhardt, *Cosmology for Grand Unified Theories with Radiatively Induced Symmetry Breaking*, *Phys. Rev. Lett.* **48** (1982) 1220–1223. [Adv. Ser. Astrophys. Cosmol.3,158(1987)].

[25] A. D. Linde, *Hybrid inflation*, *Phys. Rev.* **D49** (1994) 748–754, [astro-ph/9307002].

[26] L. Kofman, A. D. Linde and A. A. Starobinsky, *Towards the theory of reheating after inflation*, *Phys. Rev.* **D56** (1997) 3258–3295, [hep-ph/9704452].

[27] B. A. Bassett, S. Tsujikawa and D. Wands, *Inflation dynamics and reheating*, *Rev. Mod. Phys.* **78** (2006) 537–589, [astro-ph/0507632].

[28] S. Hannestad, *What is the lowest possible reheating temperature?*, *Phys. Rev.* **D70** (2004) 043506, [astro-ph/0403291].

[29] E. W. Kolb and M. S. Turner, *The Early Universe*, *Front. Phys.* **69** (1990) 1–547.

[30] V. F. Mukhanov, H. A. Feldman and R. H. Brandenberger, *Theory of cosmological perturbations. Part 1. Classical perturbations. Part 2. Quantum theory of perturbations. Part 3. Extensions*, *Phys. Rept.* **215** (1992) 203–333.

[31] H. Kodama and M. Sasaki, *Cosmological Perturbation Theory*, *Prog. Theor. Phys. Suppl.* **78** (1984) 1–166.

[32] A. A. Starobinsky, *Spectrum of relict gravitational radiation and the early state of the universe*, *JETP Lett.* **30** (1979) 682–685.

[33] V. A. Rubakov, M. V. Sazhin and A. V. Veryaskin, *Graviton Creation in the Inflationary Universe and the Grand Unification Scale*, *Phys. Lett.* **115B** (1982) 189–192.

[34] R. Fabbri and M. D. Pollock, *The effect of primordially produced gravitons upon the anisotropy of the cosmological microwave background radiation*, *Physics Letters B* **125** (June, 1983) 445–448.

[35] L. F. Abbott and M. B. Wise, *Constraints on Generalized Inflationary Cosmologies*, *Nucl. Phys.* **B244** (1984) 541–548.

[36] BICEP2, Planck collaboration, P. A. R. Ade et al., *Joint Analysis of BICEP2/KeckArray and Planck Data*, *Phys. Rev. Lett.* **114** (2015) 101301, [1502.00612].

[37] G. Mangano, G. Miele, S. Pastor, T. Pinto, O. Pisanti and P. D. Serpico, *Relic neutrino decoupling including flavor oscillations*, *Nucl. Phys.* **B729** (2005) 221–234, [hep-ph/0506164].

[38] P. F. de Salas and S. Pastor, *Relic neutrino decoupling with flavour oscillations revisited*, *JCAP* **1607** (2016) 051, [1606.06986].

[39] P. F. de Salas, S. Gariazzo, J. Lesgourgues and S. Pastor, *Calculation of the local density of relic neutrinos*, *JCAP* **1709** (2017) 034, [1706.09850].

[40] Super-Kamiokande collaboration, Y. Fukuda et al., *Evidence for oscillation of atmospheric neutrinos*, *Phys. Rev. Lett.* **81** (1998) 1562–1567, [hep-ex/9807003].

[41] SNO collaboration, Q. R. Ahmad et al., *Measurement of the rate of $\nu_e + d \to p + p + e^-$ interactions produced by ^8B solar neutrinos at the Sudbury Neutrino Observatory*, *Phys. Rev. Lett.* **87** (2001) 071301, [nucl-ex/0106015].

[42] SNO collaboration, Q. R. Ahmad et al., *Direct evidence for neutrino flavor transformation from neutral current interactions in the Sudbury Neutrino Observatory*, *Phys. Rev. Lett.* **89** (2002) 011301, [nucl-ex/0204008].

[43] I. Esteban, M. C. Gonzalez-Garcia, A. Hernandez-Cabezudo, M. Maltoni and T. Schwetz, *Global analysis of three-flavour neutrino oscillations: synergies and tensions in the determination of $\theta_2 3, \delta_C P$, and the mass ordering*, *JHEP* **01** (2019) 106, [1811.05487].

[44] A. D. Sakharov, *Violation of CP Invariance, C asymmetry, and baryon asymmetry of the universe*, *Pisma Zh. Eksp. Teor. Fiz.* **5** (1967) 32–35. [Usp. Fiz. Nauk161,no.5,61(1991)].

[45] D. E. Morrissey and M. J. Ramsey-Musolf, *Electroweak baryogenesis*, *New J. Phys.* **14** (2012) 125003, [1206.2942].

[46] C. S. Fong, E. Nardi and A. Riotto, *Leptogenesis in the Universe*, *Adv. High Energy Phys.* **2012** (2012) 158303, [1301.3062].

[47] F. Hoyle and R. J. Tayler, *The Mystery of the Cosmic Helium Abundance*, *Nature* **203** (1964) 1108.

[48] G. Gamow, *The Origin of Elements and the Separation of Galaxies*, *Physical Review* **74** (Aug., 1948) 505–506.

[49] R. A. Alpher, H. Bethe and G. Gamow, *The origin of chemical elements*, *Phys. Rev.* **73** (1948) 803–804.

[50] R. A. Alpher and R. Herman, *Evolution of the Universe*, *Nature* **162** (Nov., 1948) 774–775.

[51] R. A. Alpher and R. C. Herman, *Remarks on the evolution of the expanding universe*, *Phys. Rev.* **75** (Apr, 1949) 1089–1095.

[52] R. H. Cyburt, B. D. Fields and K. A. Olive, *Primordial nucleosynthesis in light of WMAP*, *Phys. Lett.* **B567** (2003) 227–234, [astro-ph/0302431].

[53] S. D. M. White, J. F. Navarro, A. E. Evrard and C. S. Frenk, *The Baryon content of galaxy clusters: A Challenge to cosmological orthodoxy*, *Nature* **366** (1993) 429–433.

[54] S. W. Allen, R. W. Schmidt and A. C. Fabian, *Cosmological constraints from the x-ray gas mass fraction in relaxed lensing clusters observed with Chandra*, *Mon. Not. Roy. Astron. Soc.* **334** (2002) L11, [astro-ph/0205007].

[55] N. Bernal, M. Heikinheimo, T. Tenkanen, K. Tuominen and V. Vaskonen, *The Dawn of FIMP Dark Matter: A Review of Models and Constraints*, *Int. J. Mod. Phys.* **A32** (2017) 1730023, [1706.07442].

[56] Ya. B. Zeldovic, L. B. Okun and S. B. Pikelner, *Quarks, astrophysical and physico-chemical aspects*, *Phys. Lett.* **17** (1965) 164–166.

[57] B. W. Lee and S. Weinberg, *Cosmological Lower Bound on Heavy Neutrino Masses*, *Phys. Rev. Lett.* **39** (1977) 165–168.

[58] P. Gondolo and G. Gelmini, *Cosmic abundances of stable particles: Improved analysis*, *Nucl. Phys.* **B360** (1991) 145–179.

[59] G. Arcadi, M. Dutra, P. Ghosh, M. Lindner, Y. Mambrini, M. Pierre et al., *The waning of the WIMP? A review of models, searches, and constraints*, *Eur. Phys. J.* **C78** (2018) 203, [1703.07364].

[60] M. Viel, G. D. Becker, J. S. Bolton and M. G. Haehnelt, *Warm dark matter as a solution to the small scale crisis: New constraints from high redshift Lyman-α forest data*, *Phys. Rev.* **D88** (2013) 043502, [1306.2314].

[61] L. J. Hall, K. Jedamzik, J. March-Russell and S. M. West, *Freeze-In Production of FIMP Dark Matter*, *JHEP* **03** (2010) 080, [0911.1120].

[62] J. Preskill, M. B. Wise and F. Wilczek, *Cosmology of the Invisible Axion*, *Phys. Lett.* **B120** (1983) 127–132.

[63] L. F. Abbott and P. Sikivie, *A Cosmological Bound on the Invisible Axion*, *Phys. Lett.* **B120** (1983) 133–136.

[64] M. Dine and W. Fischler, *The Not So Harmless Axion*, *Phys. Lett.* **B120** (1983) 137–141.

[65] P. Sikivie, *Axion Cosmology*, *Lect. Notes Phys.* **741** (2008) 19–50, [astro-ph/0610440].

[66] D. J. E. Marsh, *Axion Cosmology*, *Phys. Rept.* **643** (2016) 1–79, [1510.07633].

[67] R. D. Peccei and H. R. Quinn, *CP Conservation in the Presence of Instantons*, *Phys. Rev. Lett.* **38** (1977) 1440–1443.

[68] S. Weinberg, *A New Light Boson?*, *Phys. Rev. Lett.* **40** (1978) 223–226.

[69] F. Wilczek, *Problem of Strong P and T Invariance in the Presence of Instantons*, *Phys. Rev. Lett.* **40** (1978) 279–282.

[70] L. Hui, J. P. Ostriker, S. Tremaine and E. Witten, *Ultralight scalars as cosmological dark matter*, *Phys. Rev.* **D95** (2017) 043541, [1610.08297].

[71] D. J. E. Marsh and J. C. Niemeyer, *Strong Constraints on Fuzzy Dark Matter from Ultrafaint Dwarf Galaxy Eridanus II*, [1810.08543].

[72] E. D. Carlson, M. E. Machacek and L. J. Hall, *Self-interacting dark matter*, *Astrophys. J.* **398** (1992) 43–52.

[73] Y. Hochberg, E. Kuflik, T. Volansky and J. G. Wacker, *Mechanism for Thermal Relic Dark Matter of Strongly Interacting Massive Particles*, *Phys. Rev. Lett.* **113** (2014) 171301, [1402.5143].

[74] D. Pappadopulo, J. T. Ruderman and G. Trevisan, *Dark matter freeze-out in a nonrelativistic sector*, *Phys. Rev.* **D94** (2016) 035005, [1602.04219].

[75] X. Chu, T. Hambye and M. H. G. Tytgat, *The Four Basic Ways of Creating Dark Matter Through a Portal*, *JCAP* **1205** (2012) 034, [1112.0493].

[76] N. Bernal, X. Chu, C. Garcia-Cely, T. Hambye and B. Zaldivar, *Production Regimes for Self-Interacting Dark Matter*, *JCAP* **1603** (2016) 018, [1510.08063].

[77] K. Petraki and R. R. Volkas, *Review of asymmetric dark matter*, *Int. J. Mod. Phys.* **A28** (2013) 1330028, [1305.4939].

[78] K. M. Zurek, *Asymmetric Dark Matter: Theories, Signatures, and Constraints*, *Phys. Rept.* **537** (2014) 91–121, [1308.0338].

[79] A. Boyarsky, M. Drewes, T. Lasserre, S. Mertens and O. Ruchayskiy, *Sterile Neutrino Dark Matter*, *Prog. Part. Nucl. Phys.* **104** (2019) 1–45, [1807.07938].

[80] T. Tenkanen and V. Vaskonen, *Reheating the Standard Model from a hidden sector*, *Phys. Rev.* **D94** (2016) 083516, [1606.00192].

[81] S. Seager, D. D. Sasselov and D. Scott, *How exactly did the universe become neutral?*, *Astrophys. J. Suppl.* **128** (2000) 407–430, [astro-ph/9912182].

[82] S. Seager, D. D. Sasselov and D. Scott, *A new calculation of the recombination epoch*, *Astrophys. J.* **523** (1999) L1–L5, [astro-ph/9909275].

[83] D. Scott and A. Moss, *Matter temperature during cosmological recombination*, *Mon. Not. Roy. Astron. Soc.* **397** (Jul, 2009) 445–446, [0902.3438].

[84] A. G. Doroshkevich and I. D. Novikov, *Mean Density of Radiation in the Metagalaxy and Certain Problems in Relativistic Cosmology*, *Soviet Physics Doklady* **9** (Aug., 1964) 111.

[85] R. H. Dicke, P. J. E. Peebles, P. G. Roll and D. T. Wilkinson, *Cosmic Black-Body Radiation.*, *Astrophys. J.* **142** (July, 1965) 414–419.

[86] A. A. Penzias and R. W. Wilson, *A Measurement of Excess Antenna Temperature at 4080 Mc/s.*, *Astrophys. J.* **142** (July, 1965) 419–421.

[87] J. C. Mather, D. J. Fixsen, R. A. Shafer, C. Mosier and D. T. Wilkinson, *Calibrator design for theCOBEFar-infrared absolute spectrophotometer (FIRAS)*, *The Astrophysical Journal* **512** (feb, 1999) 511–520.

[88] J. Lesgourgues and S. Pastor, *Massive neutrinos and cosmology*, *Phys. Rept.* **429** (2006) 307–379, [astro-ph/0603494].

[89] P. Meszaros, *The behaviour of point masses in an expanding cosmological substratum*, *Astron. Astrophys.* **37** (1974) 225–228.

[90] J. Zavala and C. S. Frenk, *Dark matter haloes and subhaloes*, [1907.11775].

[91] J. Silk, *Cosmic black body radiation and galaxy formation*, *Astrophys. J.* **151** (1968) 459–471.

[92] S. Naoz, S. Noter and R. Barkana, *The first stars in the universe*, *Mon. Not. Roy. Astron. Soc.* **373** (2006) L98, [astro-ph/0604050].

[93] M. Tegmark, J. Silk, M. J. Rees, A. Blanchard, T. Abel and F. Palla, *How small were the first cosmological objects?*, *Astrophys. J.* **474** (1997) 1–12, [astro-ph/9603007].

[94] T. Abel, G. L. Bryan and M. L. Norman, *The formation of the first star in the Universe*, *Science* **295** (2002) 93, [astro-ph/0112088].

[95] T. H. Greif, V. Springel, S. D. M. White, S. C. O. Glover, P. C. Clark, R. J. Smith et al., *Simulations on a Moving Mesh: The Clustered Formation of Population III Protostars*, *Astrophys. J.* **737** (Aug., 2011) 75, [1101.5491].

[96] R. Barkana and A. Loeb, *In the beginning: The First sources of light and the reionization of the Universe*, *Phys. Rept.* **349** (2001) 125–238, [astro-ph/0010468].

[97] V. Bromm and N. Yoshida, *The First Galaxies*, *Ann. Rev. Astron. Astrophys.* **49** (2011) 373–407, [1102.4638].

[98] M. McQuinn, *The Evolution of the Intergalactic Medium*, *Ann. Rev. Astron. Astrophys.* **54** (2016) 313–362, [1512.00086].

[99] Supernova Search Team collaboration, A. G. Riess et al., *Observational evidence from supernovae for an accelerating universe and a cosmological constant*, *Astron. J.* **116** (1998) 1009–1038, [astro-ph/9805201].

[100] Supernova Search Team collaboration, P. M. Garnavich et al., *Supernova limits on the cosmic equation of state*, *Astrophys. J.* **509** (1998) 74–79, [astro-ph/9806396].

[101] Supernova Cosmology Project collaboration, S. Perlmutter et al., *Measurements of Omega and Lambda from 42 high redshift supernovae*, *Astrophys. J.* **517** (1999) 565–586, [astro-ph/9812133].

[102] Boomerang collaboration, P. de Bernardis et al., *A Flat universe from high resolution maps of the cosmic microwave background radiation*, *Nature* **404** (2000) 955–959, [astro-ph/0004404].

[103] S. Hanany et al., *MAXIMA-1: A Measurement of the cosmic microwave background anisotropy on angular scales of 10 arcminutes to 5 degrees*, *Astrophys. J.* **545** (2000) L5, [astro-ph/0005123].

[104] H. Hildebrandt et al., *KiDS-450: Cosmological parameter constraints from tomographic weak gravitational lensing*, *Mon. Not. Roy. Astron. Soc.* **465** (2017) 1454, [1606.05338].

[105] S. Weinberg, *The Cosmological Constant Problem*, *Rev. Mod. Phys.* **61** (1989) 1–23.

[106] B. Jain and J. Khoury, *Cosmological Tests of Gravity*, *Annals Phys.* **325** (2010) 1479–1516, [1004.3294].

[107] J. Lesgourgues, S. Pastor and L. Perotto, *Probing neutrino masses with future galaxy redshift surveys*, *Phys. Rev.* **D70** (2004) 045016, [hep-ph/0403296].

[108] A. Slosar, *Detecting neutrino mass difference with cosmology*, *Phys. Rev.* **D73** (2006) 123501, [astro-ph/0602133].

[109] Planck collaboration, P. A. R. Ade et al., *Planck 2013 results. XVI. Cosmological parameters*, *Astron. Astrophys.* **571** (2014) A16, [1303.5076].

[110] HST collaboration, W. L. Freedman et al., *Final results from the Hubble Space Telescope key project to measure the Hubble constant*, *Astrophys. J.* **553** (2001) 47–72, [astro-ph/0012376].

[111] H. S. Leavitt and E. C. Pickering, *Periods of 25 Variable Stars in the Small Magellanic Cloud.*, *Harvard College Observatory Circular* **173** (Mar., 1912) 1–3.

[112] A. G. Riess, S. Casertano, W. Yuan, L. M. Macri and D. Scolnic, *Large Magellanic Cloud Cepheid Standards Provide a 1% Foundation for the Determination of the Hubble Constant and Stronger Evidence for Physics Beyond LambdaCDM*, [1903.07603].

[113] G. Pietrzyński, D. Graczyk, A. Gallenne, W. Gieren, I. B. Thompson, B. Pilecki et al., *A distance to the Large Magellanic Cloud that is precise to one per cent*, *Nature* **567** (Mar, 2019) 200–203, [1903.08096].

[114] A. G. Riess et al., *A 2.4% Determination of the Local Value of the Hubble Constant*, *Astrophys. J.* **826** (2016) 56, [1604.01424].

[115] S. Refsdal, *On the possibility of determining Hubble's parameter and the masses of galaxies from the gravitational lens effect*, *Mon. Not. Roy. Astron. Soc.* **128** (1964) 307.

[116] S. H. Suyu, T.-C. Chang, F. Courbin and T. Okumura, *Cosmological distance indicators*, *Space Sci. Rev.* **214** (2018) 91, [1801.07262].

[117] T. Treu and P. J. Marshall, *Time Delay Cosmography*, *Astron. Astrophys. Rev.* **24** (2016) 11, [1605.05333].

[118] K. C. Wong et al., *H0LiCOW XIII. A 2.4% measurement of H_0 from lensed quasars: 5.3σ tension between early and late-Universe probes*, [1907.04869].

[119] A. Eigenbrod, F. Courbin, C. Vuissoz, G. Meylan, P. Saha and S. Dye, *COSMOGRAIL: The Cosmological MOnitoring of GRavItational Lenses. 1. How to sample the light curves of gravitationally lensed quasars to measure accurate time delays*, *Astron. Astrophys.* **436** (2005) 25, [astro-ph/0503019].

[120] LIGO Scientific collaboration, J. Aasi et al., *Advanced LIGO*, *Class. Quant. Grav.* **32** (2015) 074001, [1411.4547].

[121] VIRGO collaboration, F. Acernese et al., *Advanced Virgo: a second-generation interferometric gravitational wave detector*, *Class. Quant. Grav.* **32** (2015) 024001, [1408.3978].

[122] B. F. Schutz, *Determining the Hubble Constant from Gravitational Wave Observations*, *Nature* **323** (1986) 310–311.

[123] D. E. Holz and S. A. Hughes, *Using gravitational-wave standard sirens*, *Astrophys. J.* **629** (2005) 15–22, [astro-ph/0504616].

[124] N. Dalal, D. E. Holz, S. A. Hughes and B. Jain, *Short grb and binary black hole standard sirens as a probe of dark energy*, *Phys. Rev.* **D74** (2006) 063006, [astro-ph/0601275].

[125] S. Nissanke, D. E. Holz, S. A. Hughes, N. Dalal and J. L. Sievers, *Exploring short gamma-ray bursts as gravitational-wave standard sirens*, *Astrophys. J.* **725** (2010) 496–514, [0904.1017].

[126] S. Nissanke, D. E. Holz, N. Dalal, S. A. Hughes, J. L. Sievers and C. M. Hirata, *Determining the Hubble constant from gravitational wave observations of merging compact binaries*, [1307.2638].

[127] LIGO Scientific, Virgo, Fermi GBM, INTEGRAL, IceCube, AstroSat Cadmium Zinc Telluride Imager Team, IPN, Insight-Hxmt, ANTARES, Swift, AGILE Team, 1M2H Team, Dark Energy Camera GW-EM, DES, DLT40, GRAWITA, Fermi-LAT, ATCA, ASKAP, Las Cumbres Observatory Group, OzGrav, DWF (Deeper Wider Faster Program), AST3, CAASTRO, VINROUGE, MASTER, J-GEM, GROWTH, JAGWAR, CaltechNRAO, TTU-NRAO, NuSTAR, Pan-STARRS, MAXI Team, TZAC Consortium, KU, Nordic Optical Telescope, ePESSTO, GROND, Texas Tech University, SALT Group, TOROS, BOOTES, MWA, CALET, IKI-GW Follow-up, H.E.S.S., LOFAR, LWA, HAWC, Pierre Auger, ALMA, Euro VLBI Team, Pi of Sky, Chandra Team at McGill University, DFN, ATLAS Telescopes, High Time Resolution Universe Survey, RIMAS, RATIR, SKA South Africa/MeerKAT collaboration, B. P. Abbott et al., *Multi-messenger Observations of a Binary Neutron Star Merger*, *Astrophys. J.* **848** (2017) L12, [1710.05833].

[128] W. Del Pozzo, *Inference of the cosmological parameters from gravitational waves: application to second generation interferometers*, *Phys. Rev.* **D86** (2012) 043011, [1108.1317].

[129] LIGO Scientific, Virgo collaboration, B. P. Abbott et al., *A gravitational-wave measurement of the Hubble constant following the second observing run of Advanced LIGO and Virgo*, [1908.06060].

[130] M. Tegmark and M. Zaldarriaga, *Separating the early universe from the late universe: Cosmological parameter estimation beyond the black box*, *Phys. Rev.* **D66** (2002) 103508, [astro-ph/0207047].

[131] W. Hu, N. Sugiyama and J. Silk, *The Physics of microwave background anisotropies*, *Nature* **386** (1997) 37–43, [astro-ph/9604166].

[132] W. Hu and N. Sugiyama, *Small scale cosmological perturbations: An Analytic approach*, *Astrophys. J.* **471** (1996) 542–570, [astro-ph/9510117].

[133] SDSS collaboration, D. J. Eisenstein et al., *Detection of the Baryon Acoustic Peak in the Large-Scale Correlation Function of SDSS Luminous Red Galaxies*, *Astrophys. J.* **633** (2005) 560–574, [astro-ph/0501171].

[134] 2dFGRS collaboration, S. Cole et al., *The 2dF Galaxy Redshift Survey: Power-spectrum analysis of the final dataset and cosmological implications*, *Mon. Not. Roy. Astron. Soc.* **362** (2005) 505–534, [astro-ph/0501174].

[135] D. J. Eisenstein, W. Hu and M. Tegmark, *Cosmic complementarity: H(0) and Omega(m) from combining CMB experiments and redshift surveys*, *Astrophys. J.* **504** (1998) L57–L61, [astro-ph/9805239].

[136] D. J. Eisenstein, H.-j. Seo and M. J. White, *On the Robustness of the Acoustic Scale in the Low-Redshift Clustering of Matter*, *Astrophys. J.* **664** (2007) 660–674, [astro-ph/0604361].

[137] D. H. Weinberg, M. J. Mortonson, D. J. Eisenstein, C. Hirata, A. G. Riess and E. Rozo, *Observational probes of cosmic acceleration*, *Physics Reports* **530** (2013) 87 – 255.

[138] D. et. al., *THE BARYON OSCILLATION SPECTROSCOPIC SURVEY OF SDSS-III*, *The Astronomical Journal* **145** (dec, 2012) 10.

[139] P. Bode, J. P. Ostriker and N. Turok, *Halo formation in warm dark matter models*, *Astrophys. J.* **556** (2001) 93–107, [astro-ph/0010389].

[140] M. Viel, J. Lesgourgues, M. G. Haehnelt, S. Matarrese and A. Riotto, *Constraining warm dark matter candidates including sterile neutrinos and light gravitinos with WMAP and the Lyman-alpha forest*, *Phys. Rev.* **D71** (2005) 063534, [astro-ph/0501562].

[141] S. Hofmann, D. J. Schwarz and H. Stoecker, *Damping scales of neutralino cold dark matter*, *Phys. Rev.* **D64** (2001) 083507, [astro-ph/0104173].

[142] T. Bringmann, *Particle Models and the Small-Scale Structure of Dark Matter*, *New J. Phys.* **11** (2009) 105027, [0903.0189].

[143] C. J. Hogan and M. J. Rees, *AXION MINICLUSTERS*, *Phys. Lett.* **B205** (1988) 228–230.

[144] E. W. Kolb and I. I. Tkachev, *Axion miniclusters and Bose stars*, *Phys. Rev. Lett.* **71** (1993) 3051–3054, [hep-ph/9303313].

[145] E. W. Kolb and I. I. Tkachev, *Femtolensing and picolensing by axion miniclusters*, *Astrophys. J.* **460** (1996) L25–L28, [astro-ph/9510043].

[146] A. Vaquero, J. Redondo and J. Stadler, *Early seeds of axion miniclusters*, [1809.09241]. [JCAP1904,no.04,012(2019)].

[147] N. Kaiser, *On the Spatial correlations of Abell clusters*, *Astrophys. J.* **284** (1984) L9–L12.

[148] V. Desjacques, D. Jeong and F. Schmidt, *Large-Scale Galaxy Bias*, *Phys. Rept.* **733** (2018) 1–193, [1611.09787].

[149] A. Dekel and O. Lahav, *Stochastic nonlinear galaxy biasing*, *Astrophys. J.* **520** (1999) 24–34, [astro-ph/9806193].

[150] J. B. Muñoz and C. Dvorkin, *Efficient Computation of Galaxy Bias with Neutrinos and Other Relics*, *Phys. Rev.* **D98** (2018) 043503, [1805.11623].

[151] A. Raccanelli, L. Verde and F. Villaescusa-Navarro, *Biases from neutrino bias: to worry or not to worry?*, *Mon. Not. Roy. Astron. Soc.* **483** (2019) 734–743, [1704.07837].

[152] C. Carbone, L. Verde, Y. Wang and A. Cimatti, *Neutrino constraints from future nearly all-sky spectroscopic galaxy surveys*, *JCAP* **1103** (2011) 030, [1012.2868].

[153] J. Hamann, S. Hannestad and Y. Y. Y. Wong, *Measuring neutrino masses with a future galaxy survey*, *JCAP* **1211** (2012) 052, [1209.1043].

[154] B. Audren, J. Lesgourgues, S. Bird, M. G. Haehnelt and M. Viel, *Neutrino masses and cosmological parameters from a Euclid-like survey: Markov Chain Monte Carlo forecasts including theoretical errors*, *JCAP* **1301** (2013) 026, [1210.2194].

[155] M. Davis, G. Efstathiou, C. S. Frenk and S. D. M. White, *The Evolution of Large Scale Structure in a Universe Dominated by Cold Dark Matter*, *Astrophys. J.* **292** (1985) 371–394.

[156] V. Springel et al., *First results from the IllustrisTNG simulations: matter and galaxy clustering*, *Mon. Not. Roy. Astron. Soc.* **475** (2018) 676, [1707.03397].

[157] R. Scoccimarro, H. A. Feldman, J. N. Fry and J. A. Frieman, *The Bispectrum of IRAS redshift catalogs*, *Astrophys. J.* **546** (2001) 652, [astro-ph/0004087].

[158] L. Verde et al., *The 2dF Galaxy Redshift Survey: The Bias of galaxies and the density of the Universe*, *Mon. Not. Roy. Astron. Soc.* **335** (2002) 432, [astro-ph/0112161].

[159] T. Nishimichi, I. Kayo, C. Hikage, K. Yahata, A. Taruya, Y. P. Jing et al., *Bispectrum and Nonlinear Biasing of Galaxies: Perturbation Analysis, Numerical Simulation and SDSS Galaxy Clustering*, *Publ. Astron. Soc. Jap.* **59** (2007) 93, [astro-ph/0609740].

[160] Z. Slepian et al., *The large-scale three-point correlation function of the SDSS BOSS DR12 CMASS galaxies*, *Mon. Not. Roy. Astron. Soc.* **468** (2017) 1070–1083, [1512.02231].

[161] DES collaboration, E. Krause et al., *Dark Energy Survey Year 1 Results: Multi-Probe Methodology and Simulated Likelihood Analyses*, *Submitted to: Phys. Rev. D* (2017) , [1706.09359].

[162] A. Meiksin and M. J. White, *Particle-mesh simulations of the Lyman-alpha forest*, *Mon. Not. Roy. Astron. Soc.* **324** (2001) 141, [astro-ph/0008214].

[163] M. G. Haehnelt and M. Viel, *Cosmological and astrophysical parameters from the Sloan Digital Sky Survey flux power spectrum and hydrodynamical simulations of the Lyman α forest*, *Monthly Notices of the Royal Astronomical Society* **365** (01, 2006) 231–244, [http://oup.prod.sis.lan/mnras/article-pdf/365/1/231/5539814/365-1-231.pdf].

[164] V. de Sainte Agathe et al., *Baryon acoustic oscillations at $z = 2.34$ from the correlations of Lyα absorption in eBOSS DR14*, [1904.03400].

[165] R. D. Blandford, A. B. Saust, T. G. Brainerd and J. V. Villumsen, *The distortion of distant galaxy images by large-scale structure*, *Mon. Not. Roy. Astron. Soc.* **251** (1991) 600–627.

[166] M. Kilbinger, *Cosmology with cosmic shear observations: a review*, *Rept. Prog. Phys.* **78** (2015) 086901, [1411.0115].

[167] C. M. Hirata and U. Seljak, *Intrinsic alignment-lensing interference as a contaminant of cosmic shear*, *Phys. Rev.* **D70** (2004) 063526, [astro-ph/0406275]. [Erratum: Phys. Rev.D82,049901(2010)].

[168] DES collaboration, M. A. Troxel et al., *Survey geometry and the internal consistency of recent cosmic shear measurements*, *Mon. Not. Roy. Astron. Soc.* **479** (2018) 4998–5004, [1804.10663].

[169] R. Massey et al., *Weak lensing from space. 2. Dark matter mapping*, *Astron. J.* **127** (2004) 3089, [astro-ph/0304418].

[170] C. R. Contaldi, H. Hoekstra and A. Lewis, *Joint CMB and weak lensing analysis: physically motivated constraints on cosmological parameters*, *Phys. Rev. Lett.* **90** (2003) 221303, [astro-ph/0302435].

[171] W. Hu, *Power spectrum tomography with weak lensing*, *Astrophys. J.* **522** (1999) L21–L24, [astro-ph/9904153].

[172] A. Leauthaud et al., *Weak Gravitational Lensing with COSMOS: Galaxy Selection and Shape Measurements*, *Astrophys. J. Suppl.* **172** (2007) 219, [astro-ph/0702359].

[173] J. Shen, T. Abel, H. Mo and R. K. Sheth, *An excursion set model of the cosmic web: the abundance of sheets, filaments and halos*, *Astrophys. J.* **645** (2006) 783–791, [astro-ph/0511365].

[174] R. Massey et al., *Dark matter maps reveal cosmic scaffolding*, *Nature* **445** (2007) 286, [astro-ph/0701594].

[175] DES collaboration, T. Abbott et al., *The dark energy survey*, [astro-ph/0510346].

[176] DES collaboration, M. A. Troxel et al., *Dark Energy Survey Year 1 results: Cosmological constraints from cosmic shear*, *Phys. Rev.* **D98** (2018) 043528, [1708.01538].

[177] DES collaboration, T. M. C. Abbott et al., *Cosmological Constraints from Multiple Probes in the Dark Energy Survey*, [1811.02375].

[178] J. S. Bullock and M. Boylan-Kolchin, *Small-Scale Challenges to the ΛCDM Paradigm*, *Ann. Rev. Astron. Astrophys.* **55** (2017) 343–387, [1707.04256].

[179] V. Springel, J. Wang, M. Vogelsberger, A. Ludlow, A. Jenkins, A. Helmi et al., *The Aquarius Project: the subhalos of galactic halos*, *Mon. Not. Roy. Astron. Soc.* **391** (2008) 1685–1711, [0809.0898].

[180] M. Kuhlen, P. Madau and J. Silk, *Exploring Dark Matter with Milky Way substructure*, *Science* **325** (2009) 970–973, [0907.0005].

[181] J. Stadel, D. Potter, B. Moore, J. Diemand, P. Madau, M. Zemp et al., *Quantifying the heart of darkness with GHALO - a multi-billion particle simulation of our galactic halo*, *Mon. Not. Roy. Astron. Soc.* **398** (2009) L21–L25, [0808.2981].

[182] S. Garrison-Kimmel, M. Boylan-Kolchin, J. Bullock and K. Lee, *ELVIS: Exploring the Local Volume in Simulations*, *Mon. Not. Roy. Astron. Soc.* **438** (2014) 2578–2596, [1310.6746].

[183] B. F. Griffen, A. P. Ji, G. A. Dooley, F. A. Gómez, M. Vogelsberger, B. W. O'Shea et al., *The Caterpillar Project: a Large Suite of Milky way Sized Halos*, *Astrophys. J.* **818** (2016) 10, [1509.01255].

[184] A. A. Klypin, A. V. Kravtsov, O. Valenzuela and F. Prada, *Where are the missing Galactic satellites?*, *Astrophys. J.* **522** (1999) 82–92, [astro-ph/9901240].

[185] B. Moore, S. Ghigna, F. Governato, G. Lake, T. R. Quinn, J. Stadel et al., *Dark matter substructure within galactic halos*, *Astrophys. J.* **524** (1999) L19–L22, [astro-ph/9907411].

[186] R. A. Flores and J. R. Primack, *Observational and theoretical constraints on singular dark matter halos*, *Astrophys. J.* **427** (1994) L1–4, [astro-ph/9402004].

[187] B. Moore, *Evidence against dissipationless dark matter from observations of galaxy haloes*, *Nature* **370** (1994) 629.

[188] M. Boylan-Kolchin, J. S. Bullock and M. Kaplinghat, *Too big to fail? The puzzling darkness of massive Milky Way subhaloes*, *Mon. Not. Roy. Astron. Soc.* **415** (2011) L40, [1103.0007].

[189] A. W. McConnachie, *The Observed Properties of Dwarf Galaxies in and around the Local Group*, *The Astrophysical Journal* **144** (2012) 4, [1204.1562].

[190] J. F. Navarro, A. Ludlow, V. Springel, J. Wang, M. Vogelsberger, S. D. M. White et al., *The Diversity and Similarity of Cold Dark Matter Halos*, *Mon. Not. Roy. Astron. Soc.* **402** (2010) 21, [0810.1522].

[191] S.-H. Oh et al., *High-resolution mass models of dwarf galaxies from LITTLE THINGS*, *Astron. J.* **149** (2015) 180, [1502.01281].

[192] S. M. K. Alam, J. S. Bullock and D. H. Weinberg, *Dark matter properties and halo central densities*, *Astrophys. J.* **572** (2002) 34–40, [astro-ph/0109392].

[193] K. A. Oman et al., *The unexpected diversity of dwarf galaxy rotation curves*, *Mon. Not. Roy. Astron. Soc.* **452** (2015) 3650–3665, [1504.01437].

[194] M. Boylan-Kolchin, J. S. Bullock and M. Kaplinghat, *The Milky Way's bright satellites as an apparent failure of LCDM*, *Mon. Not. Roy. Astron. Soc.* **422** (2012) 1203–1218, [1111.2048].

[195] E. J. Tollerud, M. Boylan-Kolchin and J. S. Bullock, *M31 Satellite Masses Compared to LCDM Subhaloes*, *Mon. Not. Roy. Astron. Soc.* **440** (2014) 3511–3519, [1403.6469].

[196] E. N. Kirby, J. S. Bullock, M. Boylan-Kolchin, M. Kaplinghat and J. G. Cohen, *The dynamics of isolated Local Group galaxies*, *Mon. Not. Roy. Astron. Soc.* **439** (2014) 1015–1027, [1401.1208].

[197] I. Ferrero, M. G. Abadi, J. F. Navarro, L. V. Sales and S. Gurovich, *The dark matter halos of dwarf galaxies: a challenge for the LCDM paradigm?*, *Mon. Not. Roy. Astron. Soc.* **425** (2012) 2817–2823, [1111.6609].

[198] E. Papastergis, R. Giovanelli, M. P. Haynes and F. Shankar, *Is there a "too big to fail" problem in the field?*, *Astron. Astrophys.* **574** (2015) A113, [1407.4665].

[199] D. Anderhalden, A. Schneider, A. V. Maccio, J. Diemand and G. Bertone, *Hints on the Nature of Dark Matter from the Properties of Milky Way Satellites*, *JCAP* **1303** (2013) 014, [1212.2967].

[200] C. Boehm, H. Mathis, J. Devriendt and J. Silk, *Non-linear evolution of suppressed dark matter primordial power spectra*, *Mon. Not. Roy. Astron. Soc.* **360** (2005) 282–287, [astro-ph/0309652].

[201] J. A. Schewtschenko, R. J. Wilkinson, C. M. Baugh, C. Bœhm and S. Pascoli, *Dark matter–radiation interactions: the impact on dark matter haloes*, *Mon. Not. Roy. Astron. Soc.* **449** (2015) 3587–3596, [1412.4905].

[202] J. A. Schewtschenko, C. M. Baugh, R. J. Wilkinson, C. Bœhm, S. Pascoli and T. Sawala, *Dark matter–radiation interactions: the structure of Milky Way satellite galaxies*, *Mon. Not. Roy. Astron. Soc.* **461** (2016) 2282–2287, [1512.06774].

[203] D. N. Spergel and P. J. Steinhardt, *Observational evidence for selfinteracting cold dark matter*, *Phys. Rev. Lett.* **84** (2000) 3760–3763, [astro-ph/9909386].

[204] S. Tulin and H.-B. Yu, *Dark Matter Self-interactions and Small Scale Structure*, *Phys. Rept.* **730** (2018) 1–57, [1705.02358].

[205] M. Vogelsberger, J. Zavala and A. Loeb, *Subhaloes in Self-Interacting Galactic Dark Matter Haloes*, *Mon. Not. Roy. Astron. Soc.* **423** (2012) 3740, [1201.5892].

[206] A. H. G. Peter, M. Rocha, J. S. Bullock and M. Kaplinghat, *Cosmological Simulations with Self-Interacting Dark Matter II: Halo Shapes vs. Observations*, *Mon. Not. Roy. Astron. Soc.* **430** (2013) 105, [1208.3026].

[207] A. B. Fry, F. Governato, A. Pontzen, T. Quinn, M. Tremmel, L. Anderson et al., *All about baryons: revisiting SIDM predictions at small halo masses*, *Mon. Not. Roy. Astron. Soc.* **452** (2015) 1468–1479, [1501.00497].

[208] O. D. Elbert, J. S. Bullock, S. Garrison-Kimmel, M. Rocha, J. Oñorbe and A. H. G. Peter, *Core formation in dwarf haloes with self-interacting dark matter: no fine-tuning necessary*, *Mon. Not. Roy. Astron. Soc.* **453** (2015) 29–37, [1412.1477].

[209] M. Rocha, A. H. G. Peter, J. S. Bullock, M. Kaplinghat, S. Garrison-Kimmel, J. Onorbe et al., *Cosmological Simulations with Self-Interacting Dark Matter I: Constant Density Cores and Substructure*, *Mon. Not. Roy. Astron. Soc.* **430** (2013) 81–104, [1208.3025].

[210] G. Efstathiou, *Suppressing the formation of dwarf galaxies via photoionization*, *Mon. Not. Roy. Astron. Soc.* **256** (1992) 43P–47P.

[211] J. S. Bullock, A. V. Kravtsov and D. H. Weinberg, *Reionization and the abundance of galactic satellites*, *Astrophys. J.* **539** (2000) 517, [astro-ph/0002214].

[212] M. J. Rees and J. P. Ostriker, *Cooling, dynamics and fragmentation of massive gas clouds - Clues to the masses and radii of galaxies and clusters*, *Mon. Not. Roy. Astron. Soc.* **179** (June, 1977) 541–559.

[213] E. J. Tollerud, J. S. Bullock, L. E. Strigari and B. Willman, *Hundreds of Milky Way Satellites? Luminosity Bias in the Satellite Luminosity Function*, *Astrophys. J.* **688** (2008) 277–289, [0806.4381].

[214] J. R. Hargis, B. Willman and A. H. G. Peter, *Too Many, Too Few, or Just Right? The Predicted Number and Distribution of Milky Way Dwarf Galaxies*, *Astrophys. J.* **795** (2014) L13, [1407.4470].

[215] J. F. Navarro, V. R. Eke and C. S. Frenk, *The cores of dwarf galaxy halos*, *Mon. Not. Roy. Astron. Soc.* **283** (1996) L72–L78, [astro-ph/9610187].

[216] O. Y. Gnedin and H. Zhao, *Maximum feedback and dark matter profiles of dwarf galaxies*, *Mon. Not. Roy. Astron. Soc.* **333** (2002) 299, [astro-ph/0108108].

[217] F. Governato, A. Zolotov, A. Pontzen, C. Christensen, S. H. Oh, A. M. Brooks et al., *Cuspy No More: How Outflows Affect the Central Dark Matter and Baryon Distribution in Lambda CDM Galaxies*, *Mon. Not. Roy. Astron. Soc.* **422** (2012) 1231–1240, [1202.0554].

[218] A. Di Cintio, C. B. Brook, A. V. Macciò, G. S. Stinson, A. Knebe, A. A. Dutton et al., *The dependence of dark matter profiles on the stellar-to-halo mass ratio: a prediction for cusps versus cores*, *Mon. Not. Roy. Astron. Soc.* **437** (2014) 415–423, [1306.0898].

[219] A. M. Brooks, M. Kuhlen, A. Zolotov and D. Hooper, *A Baryonic Solution to the Missing Satellites Problem*, *Astrophys. J.* **765** (2013) 22, [1209.5394].

[220] K. S. Arraki, A. Klypin, S. More and S. Trujillo-Gomez, *Effects of baryon removal on the structure of dwarf spheroidal galaxies*, *Mon. Not. Roy. Astron. Soc.* **438** (2014) 1466–1482, [1212.6651].

[221] A. M. Brooks and A. Zolotov, *Why Baryons Matter: The Kinematics of Dwarf Spheroidal Satellites*, *Astrophys. J.* **786** (2014) 87, [1207.2468].

[222] C. B. Brook and A. Di Cintio, *Expanded haloes, abundance matching and too-big-to-fail in the Local Group*, *Mon. Not. Roy. Astron. Soc.* **450** (2015) 3920–3934, [1410.3825].

[223] A. R. Wetzel, P. F. Hopkins, J.-h. Kim, C.-A. Faucher-Giguere, D. Keres and E. Quataert, *Reconciling dwarf galaxies with ΛCDM cosmology: Simulating a realistic population of satellites around a Milky Way-mass galaxy*, *Astrophys. J.* **827** (2016) L23, [1602.05957].

[224] M. Tomozeiu, L. Mayer and T. Quinn, *TIDAL STIRRING OF SATELLITES WITH SHALLOW DENSITY PROFILES PREVENTS THEM FROM BEING TOO BIG TO FAIL*, *The Astrophysical Journal* **827** (aug, 2016) L15.

[225] T. Sawala et al., *The APOSTLE simulations: solutions to the Local Group's cosmic puzzles*, *Mon. Not. Roy. Astron. Soc.* **457** (2016) 1931–1943, [1511.01098].

[226] A. A. Dutton, A. V. Macciò, J. Frings, L. Wang, G. S. Stinson, C. Penzo et al., *NIHAO V: too big does not fail – reconciling the conflict between ΛCDM predictions and the circular velocities of nearby field galaxies*, *Mon. Not. Roy. Astron. Soc.* **457** (2016) L74–L78, [1512.00453].

[227] A. Benitez-Llambay, J. F. Navarro, M. G. Abadi, S. Gottloeber, G. Yepes, Y. Hoffman et al., *Dwarf Galaxies and the Cosmic Web*, *Astrophys. J.* **763** (2013) L41, [1211.0536].

[228] R. Verbeke, E. Papastergis, A. A. Ponomareva, S. Rathi and S. De Rijcke, *A new astrophysical solution to the Too Big To Fail problem*, *Astron. Astrophys.* **607** (2017) A13, [1703.03810].

[229] D. J. Fixsen, E. S. Cheng, J. M. Gales, J. C. Mather, R. A. Shafer and E. L. Wright, *The Cosmic Microwave Background spectrum from the full COBE FIRAS data set*, *Astrophys. J.* **473** (1996) 576, [astro-ph/9605054].

[230] J. Chluba and R. A. Sunyaev, *The evolution of CMB spectral distortions in the early Universe*, *Mon. Not. Roy. Astron. Soc.* **419** (2012) 1294–1314, [1109.6552].

[231] Planck collaboration, N. Aghanim et al., *Planck 2015 results. XI. CMB power spectra, likelihoods, and robustness of parameters*, *Astron. Astrophys.* **594** (2016) A11, [1507.02704].

[232] P. J. E. Peebles and J. T. Yu, *Primeval adiabatic perturbation in an expanding universe*, *Astrophys. J.* **162** (1970) 815–836.

[233] R. A. Sunyaev and Ya. B. Zeldovich, *Small scale fluctuations of relic radiation*, *Astrophys. Space Sci.* **7** (1970) 3–19.

[234] R. K. Sachs and A. M. Wolfe, *Perturbations of a cosmological model and angular variations of the microwave background*, *Astrophys. J.* **147** (1967) 73–90. [Gen. Rel. Grav.39,1929(2007)].

[235] R. G. Crittenden and N. Turok, *Looking for Lambda with the Rees-Sciama effect*, *Phys. Rev. Lett.* **76** (1996) 575, [astro-ph/9510072].

[236] Planck collaboration, P. A. R. Ade et al., *Planck 2015 results. XXI. The integrated Sachs-Wolfe effect*, *Astron. Astrophys.* **594** (2016) A21, [1502.01595].

[237] A. Blanchard and J. Schneider, *Gravitational lensing effect on the fluctuations of the cosmic background radiation*, *Astron. Astrophys.* **184** (Oct., 1987) 1–6.

[238] A. Lewis and A. Challinor, *Weak gravitational lensing of the CMB*, *Phys. Rept.* **429** (2006) 1–65, [astro-ph/0601594].

[239] W. Hu and T. Okamoto, *Mass reconstruction with cmb polarization*, *Astrophys. J.* **574** (2002) 566–574, [astro-ph/0111606].

[240] C. M. Hirata and U. Seljak, *Analyzing weak lensing of the cosmic microwave background using the likelihood function*, *Phys. Rev.* **D67** (2003) 043001, [astro-ph/0209489].

[241] Planck collaboration, N. Aghanim et al., *Planck 2018 results. VIII. Gravitational lensing*, [1807.06210].

[242] W. Hu and M. J. White, *A CMB polarization primer*, *New Astron.* **2** (1997) 323, [astro-ph/9706147].

[243] M. Zaldarriaga and U. Seljak, *An all sky analysis of polarization in the microwave background*, *Phys. Rev.* **D55** (1997) 1830–1840, [astro-ph/9609170].

[244] M. Kamionkowski, A. Kosowsky and A. Stebbins, *A Probe of primordial gravity waves and vorticity*, *Phys. Rev. Lett.* **78** (1997) 2058–2061, [astro-ph/9609132].

[245] J. Kovac, E. M. Leitch, C. Pryke, J. E. Carlstrom, N. W. Halverson and W. L. Holzapfel, *Detection of polarization in the cosmic microwave background using DASI*, *Nature* **420** (2002) 772–787, [astro-ph/0209478].

[246] A. G. Polnarev, *Polarization and Anisotropy Induced in the Microwave Background by Cosmological Gravitational Waves*, *Sov. Astron.* **29** (Dec., 1985) 607–613.

[247] U. Seljak and M. Zaldarriaga, *Signature of gravity waves in polarization of the microwave background*, *Phys. Rev. Lett.* **78** (1997) 2054–2057, [astro-ph/9609169].

[248] M. Zaldarriaga and U. Seljak, *Gravitational lensing effect on cosmic microwave background polarization*, *Phys. Rev.* **D58** (1998) 023003, [astro-ph/9803150].

[249] R. H. Hildebrand, J. L. Dotson, C. D. Dowell, D. A. Schleuning and J. E. Vaillancourt, *The far-infrared polarization spectrum: First results and analysis*, *The Astrophysical Journal* **516** (may, 1999) 834–842.

[250] Planck collaboration, Y. Akrami et al., *Planck 2018 results. XI. Polarized dust foregrounds*, [1801.04945].

[251] BICEP2 collaboration, P. A. R. Ade et al., *Detection of B-Mode Polarization at Degree Angular Scales by BICEP2*, *Phys. Rev. Lett.* **112** (2014) 241101, [1403.3985].

[252] G. Hinshaw, D. Larson, E. Komatsu, D. N. Spergel, C. L. Bennett, J. Dunkley et al., *Nine-year Wilkinson Microwave Anisotropy Probe (WMAP) Observations: Cosmological Parameter Results*, *Astrophys. J.* **208** (Oct, 2013) 19, [1212.5226].

[253] BICEP2, Keck Array collaboration, P. A. R. Ade et al., *BICEP2 / Keck Array x: Constraints on Primordial Gravitational Waves using Planck, WMAP, and New BICEP2/Keck Observations through the 2015 Season*, *Phys. Rev. Lett.* **121** (2018) 221301, [1810.05216].

[254] POLARBEAR collaboration, P. A. R. Ade et al., *A Measurement of the Cosmic Microwave Background B-Mode Polarization Power Spectrum at Sub-Degree Scales from 2 years of POLARBEAR Data*, *Astrophys. J.* **848** (2017) 121, [1705.02907].

[255] Z. Hou et al., *A Comparison of Maps and Power Spectra Determined from South Pole Telescope and Planck Data*, *Astrophys. J.* **853** (2018) 3, [1704.00884].

[256] ACTPol collaboration, T. Louis et al., *The Atacama Cosmology Telescope: Two-Season ACTPol Spectra and Parameters*, *JCAP* **1706** (2017) 031, [1610.02360].

[257] SPT collaboration, J. W. Henning et al., *Measurements of the Temperature and E-Mode Polarization of the CMB from 500 Square Degrees of SPTpol Data*, *Astrophys. J.* **852** (2018) 97, [1707.09353].

[258] S. Riemer-Sørensen and E. S. Jenssen, *Nucleosynthesis Predictions and High-Precision Deuterium Measurements*, *Universe* **3** (2017) 44, [1705.03653].

[259] F. Beutler, C. Blake, M. Colless, D. H. Jones, L. Staveley-Smith, L. Campbell et al., *The 6dF Galaxy Survey: baryon acoustic oscillations and the local Hubble constant*, *Mon. Not. Roy. Astron. Soc.* **416** (Oct, 2011) 3017–3032, [1106.3366].

[260] A. J. Ross, L. Samushia, C. Howlett, W. J. Percival, A. Burden and M. Manera, *The clustering of the SDSS DR7 main Galaxy sample – I. A 4 per cent distance measure at $z = 0.15$*, *Mon. Not. Roy. Astron. Soc.* **449** (2015) 835–847, [1409.3242].

[261] BOSS collaboration, S. Alam et al., *The clustering of galaxies in the completed SDSS-III Baryon Oscillation Spectroscopic Survey: cosmological analysis of the DR12 galaxy sample*, *Mon. Not. Roy. Astron. Soc.* **470** (2017) 2617–2652, [1607.03155].

[262] D. M. Scolnic et al., *The Complete Light-curve Sample of Spectroscopically Confirmed SNe Ia from Pan-STARRS1 and Cosmological Constraints from the Combined Pantheon Sample*, *Astrophys. J.* **859** (2018) 101, [1710.00845].

[263] Y. Y. Y. Wong, *Neutrino mass in cosmology: status and prospects*, *Ann. Rev. Nucl. Part. Sci.* **61** (2011) 69–98, [1111.1436].

[264] C. Dvorkin et al., *Neutrino Mass from Cosmology: Probing Physics Beyond the Standard Model*, [1903.03689].

[265] T. Brinckmann, D. C. Hooper, M. Archidiacono, J. Lesgourgues and T. Sprenger, *The promising future of a robust cosmological neutrino mass measurement*, *JCAP* **1901** (2019) 059, [1808.05955].

[266] DES collaboration, T. M. C. Abbott et al., *Dark Energy Survey year 1 results: Cosmological constraints from galaxy clustering and weak lensing*, *Phys. Rev.* **D98** (2018) 043526, [1708.01530].

[267] E. van Uitert et al., *KiDS+GAMA: cosmology constraints from a joint analysis of cosmic shear, galaxy–galaxy lensing, and angular clustering*, *Mon. Not. Roy. Astron. Soc.* **476** (2018) 4662–4689, [1706.05004].

[268] S. Joudaki et al., *KiDS-450 + 2dFLenS: Cosmological parameter constraints from weak gravitational lensing tomography and overlapping redshift-space galaxy clustering*, *Mon. Not. Roy. Astron. Soc.* **474** (2018) 4894–4924, [1707.06627].

[269] DES collaboration, T. M. C. Abbott et al., *Dark Energy Survey Year 1 Results: A Precise H0 Estimate from DES Y1, BAO, and D/H Data*, *Mon. Not. Roy. Astron. Soc.* **480** (2018) 3879–3888, [1711.00403].

[270] D. N. Spergel, R. Flauger and R. Hložek, *Planck Data Reconsidered*, *Phys. Rev.* **D91** (2015) 023518, [1312.3313].

[271] G. E. Addison, Y. Huang, D. J. Watts, C. L. Bennett, M. Halpern, G. Hinshaw et al., *Quantifying discordance in the 2015 Planck CMB spectrum*, *Astrophys. J.* **818** (2016) 132, [1511.00055].

[272] Planck collaboration, N. Aghanim et al., *Planck intermediate results. LI. Features in the cosmic microwave background temperature power spectrum and shifts in cosmological parameters*, *Astron. Astrophys.* **607** (2017) A95, [1608.02487].

[273] G. Efstathiou, *H0 Revisited*, *Mon. Not. Roy. Astron. Soc.* **440** (2014) 1138–1152, [1311.3461].

[274] W. Cardona, M. Kunz and V. Pettorino, *Determining H_0 with Bayesian hyper-parameters*, *JCAP* **1703** (2017) 056, [1611.06088].

[275] B. R. Zhang, M. J. Childress, T. M. Davis, N. V. Karpenka, C. Lidman, B. P. Schmidt et al., *A blinded determination of H_0 from low-redshift Type Ia supernovae, calibrated by Cepheid variables*, *Mon. Not. Roy. Astron. Soc.* **471** (2017) 2254–2285, [1706.07573].

[276] B. Follin and L. Knox, *Insensitivity of the distance ladder Hubble constant determination to Cepheid calibration modelling choices*, *Mon. Not. Roy. Astron. Soc.* **477** (2018) 4534–4542, [1707.01175].

[277] E. Di Valentino, C. Bøehm, E. Hivon and F. R. Bouchet, *Reducing the H_0 and σ_8 tensions with Dark Matter-neutrino interactions*, *Phys. Rev.* **D97** (2018) 043513, [1710.02559].

[278] V. Poulin, T. L. Smith, T. Karwal and M. Kamionkowski, *Early Dark Energy Can Resolve The Hubble Tension*, [1811.04083].

[279] C. D. Kreisch, F.-Y. Cyr-Racine and O. Doré, *The Neutrino Puzzle: Anomalies, Interactions, and Cosmological Tensions*, [1902.00534].

[280] H. Boehringer, G. Chon and C. A. Collins, *Observational evidence for a local underdensity in the Universe and its effect on the measurement of the Hubble Constant*, [1907.12402].

[281] C. Boehm, P. Fayet and R. Schaeffer, *Constraining dark matter candidates from structure formation*, *Phys. Lett.* **B518** (2001) 8–14, [astro-ph/0012504].

[282] C. Boehm, A. Riazuelo, S. H. Hansen and R. Schaeffer, *Interacting dark matter disguised as warm dark matter*, *Phys. Rev.* **D66** (2002) 083505, [astro-ph/0112522].

[283] C.-P. Ma and E. Bertschinger, *Cosmological perturbation theory in the synchronous and conformal Newtonian gauges*, *Astrophys. J.* **455** (1995) 7–25, [astro-ph/9506072].

[284] E. Lifshitz, *Republication of: On the gravitational stability of the expanding universe*, *J. Phys.(USSR)* **10** (1946) 116. [Gen. Rel. Grav.49,no.2,18(2017)].

[285] R. J. Wilkinson, J. Lesgourgues and C. Boehm, *Using the CMB angular power spectrum to study Dark Matter-photon interactions*, *JCAP* **1404** (2014) 026, [1309.7588].

[286] E. M. Lifshitz and I. M. Khalatnikov, *Investigations in relativistic cosmology*, *Adv. Phys.* **12** (1963) 185–249.

[287] S. Weinberg, *Gravitation and Cosmology*. John Wiley and Sons, New York, 1972.

[288] D. Blas, J. Lesgourgues and T. Tram, *The Cosmic Linear Anisotropy Solving System (CLASS) II: Approximation schemes*, *JCAP* **1107** (2011) 034, [1104.2933].

[289] A. Kosowsky, *Cosmic microwave background polarization*, *Annals Phys.* **246** (1996) 49–85, [astro-ph/9501045].

[290] J. R. Bond and G. Efstathiou, *Cosmic background radiation anisotropies in universes dominated by nonbaryonic dark matter*, *Astrophys. J.* **285** (1984) L45–L48.

[291] G. Mangano, A. Melchiorri, P. Serra, A. Cooray and M. Kamionkowski, *Cosmological bounds on dark matter-neutrino interactions*, *Phys. Rev.* **D74** (2006) 043517, [astro-ph/0606190].

[292] C. Boehm and R. Schaeffer, *Constraints on dark matter interactions from structure formation: Damping lengths*, *Astron. Astrophys.* **438** (2005) 419–442, [astro-ph/0410591].

[293] F.-Y. Cyr-Racine, K. Sigurdson, J. Zavala, T. Bringmann, M. Vogelsberger and C. Pfrommer, *ETHOS—an effective theory of structure formation: From dark particle physics to the matter distribution of the Universe*, *Phys. Rev.* **D93** (2016) 123527, [1512.05344].

[294] R. J. Wilkinson, C. Boehm and J. Lesgourgues, *Constraining Dark Matter-Neutrino Interactions using the CMB and Large-Scale Structure*, *JCAP* **1405** (2014) 011, [1401.7597].

[295] M. Escudero, O. Mena, A. C. Vincent, R. J. Wilkinson and C. Bœhm, *Exploring dark matter microphysics with galaxy surveys*, *JCAP* **1509** (2015) 034, [1505.06735].

[296] A. Olivares-Del Campo, C. Bœhm, S. Palomares-Ruiz and S. Pascoli, *Dark matter-neutrino interactions through the lens of their cosmological implications*, *Phys. Rev.* **D97** (2018) 075039, [1711.05283].

[297] M. Blennow, E. Fernandez-Martinez, A. O.-D. Campo, S. Pascoli, S. Rosauro-Alcaraz and A. V. Titov, *Neutrino Portals to Dark Matter*, [1903.00006].

[298] W. Hu and N. Sugiyama, *Anisotropies in the cosmic microwave background: An Analytic approach*, *Astrophys. J.* **444** (1995) 489–506, [astro-ph/9407093].

[299] A. Lewis and S. Bridle, *Cosmological parameters from CMB and other data: A Monte Carlo approach*, *Phys. Rev.* **D66** (2002) 103511, [astro-ph/0205436].

[300] U. Seljak, *A Two fluid approximation for calculating the cosmic microwave background anisotropies*, *Astrophys. J.* **435** (1994) L87–L90, [astro-ph/9406050].

[301] U. Seljak and M. Zaldarriaga, *A Line of sight integration approach to cosmic microwave background anisotropies*, *Astrophys. J.* **469** (1996) 437–444, [astro-ph/9603033].

[302] J. Lesgourgues and T. Tram, *Fast and accurate CMB computations in non-flat FLRW universes*, *JCAP* **1409** (2014) 032, [1312.2697].

[303] C. Boehm, J. A. Schewtschenko, R. J. Wilkinson, C. M. Baugh and S. Pascoli, *Using the Milky Way satellites to study interactions between cold dark matter and radiation*, *Mon. Not. Roy. Astron. Soc.* **445** (2014) L31–L35, [1404.7012].

[304] F.-Y. Cyr-Racine and K. Sigurdson, *Photons and Baryons before Atoms: Improving the Tight-Coupling Approximation*, *Phys. Rev.* **D83** (2011) 103521, [1012.0569].

[305] Planck collaboration, P. A. R. Ade et al., *Planck 2013 results. I. Overview of products and scientific results*, *Astron. Astrophys.* **571** (2014) A1, [1303.5062].

[306] Y. Ali-Haïmoud, *Spinning Dust Radiation: A Review of the Theory*, *Advances in Astronomy* **2013** (Jan, 2013) 462697, [1211.2748].

[307] Planck collaboration, R. Adam et al., *Planck 2015 results. X. Diffuse component separation: Foreground maps*, *Astron. Astrophys.* **594** (2016) A10, [1502.01588].

[308] R. A. Sunyaev and Y. B. Zeldovich, *Small-Scale Fluctuations of Relic Radiation*, *Astrophys. Space Sci.* **7** (Apr., 1970) 3–19.

[309] R. A. Sunyaev and Ya. B. Zeldovich, *Microwave background radiation as a probe of the contemporary structure and history of the universe*, *Ann. Rev. Astron. Astrophys.* **18** (1980) 537–560.

[310] Planck collaboration, P. A. R. Ade et al., *Planck 2015 results. XXIV. Cosmology from Sunyaev-Zeldovich cluster counts*, *Astron. Astrophys.* **594** (2016) A24, [1502.01597].

[311] C. L. Reichardt et al., *A measurement of secondary cosmic microwave background anisotropies with two years of South Pole Telescope observations*, *Astrophys. J.* **755** (2012) 70, [1111.0932].

[312] Planck collaboration, P. A. R. Ade et al., *Planck 2015 results. XV. Gravitational lensing*, *Astron. Astrophys.* **594** (2016) A15, [1502.01591].

[313] R. Trotta, *Bayes in the sky: Bayesian inference and model selection in cosmology*, *Contemp. Phys.* **49** (2008) 71–104, [0803.4089].

[314] J. A. D. Diacoumis and Y. Y. Wong, *On the prior dependence of cosmological constraints on some dark matter interactions*, *JCAP* **1905** (2019) 025, [1811.11408].

[315] M. Hobson, A. Jaffe, A. Liddle, P. Mukherjee and D. Parkinson, eds., *Bayesian Methods in Cosmology*. Cambridge University Press, 2009, 10.1017/CBO9780511802461.

[316] B. Audren, J. Lesgourgues, K. Benabed and S. Prunet, *Conservative Constraints on Early Cosmology: an illustration of the Monte Python cosmological parameter inference code*, *JCAP* **1302** (2013) 001, [1210.7183].

[317] A. Lewis, *Efficient sampling of fast and slow cosmological parameters*, *Phys. Rev.* **D87** (2013) 103529, [1304.4473].

[318] J. A. D. Diacoumis and Y. Y. Y. Wong, *Trading kinetic energy: how late kinetic decoupling of dark matter changes N_{eff}*, *JCAP* **1901** (2019) 001, [1811.05601].

[319] Y. Ali-Haïmoud, J. Chluba and M. Kamionkowski, *Constraints on Dark Matter Interactions with Standard Model Particles from Cosmic Microwave Background Spectral Distortions*, *Phys. Rev. Lett.* **115** (2015) 071304, [1506.04745].

[320] PRISM collaboration, P. Andre et al., *PRISM (Polarized Radiation Imaging and Spectroscopy Mission): A White Paper on the Ultimate Polarimetric Spectro-Imaging of the Microwave and Far-Infrared Sky*, [1306.2259].

[321] J. A. D. Diacoumis and Y. Y. Y. Wong, *Using CMB spectral distortions to distinguish between dark matter solutions to the small-scale crisis*, *JCAP* **1709** (2017) 011, [1707.07050].

[322] EUCLID collaboration, R. Laureijs et al., *Euclid Definition Study Report*, [1110.3193].

[323] V. Gluscevic et al., *Cosmological Probes of Dark Matter Interactions: The Next Decade*, [1903.05140].

[324] S. Das and K. Sigurdson, *Cosmological Limits on Hidden Sector Dark Matter*, *Phys. Rev.* **D85** (2012) 063510, [1012.4458].

[325] R. Diamanti, S. Ando, S. Gariazzo, O. Mena and C. Weniger, *Cold dark matter plus not-so-clumpy dark relics*, *JCAP* **1706** (2017) 008, [1701.03128].

[326] Z. Chacko, Y. Cui, S. Hong, T. Okui and Y. Tsai, *Partially Acoustic Dark Matter, Interacting Dark Radiation, and Large Scale Structure*, *JHEP* **12** (2016) 108, [1609.03569].

[327] R. Foot and S. Vagnozzi, *Dissipative hidden sector dark matter*, *Phys. Rev.* **D91** (2015) 023512, [1409.7174].

[328] A. Kamada, K. T. Inoue, K. Kohri and T. Takahashi, *Constraints on long-lived electrically charged massive particles from anomalous strong lens systems*, *JCAP* **1711** (2017) 008, [1703.05145].

[329] J. R. Bond, G. Efstathiou and J. Silk, *Massive Neutrinos and the Large Scale Structure of the Universe*, *Phys. Rev. Lett.* **45** (1980) 1980–1984.

[330] W. Hu, D. J. Eisenstein and M. Tegmark, *Weighing neutrinos with galaxy surveys*, *Phys. Rev. Lett.* **80** (1998) 5255–5258, [astro-ph/9712057].

[331] DESI collaboration, A. Aghamousa et al., *The DESI Experiment Part I: Science,Targeting, and Survey Design*, [1611.00036].

[332] J. Schechter and J. W. F. Valle, *Neutrinoless Double beta Decay in SU(2) x U(1) Theories*, *Phys. Rev.* **D25** (1982) 2951.

[333] KATRIN collaboration, J. Angrik et al., *KATRIN design report 2004*, .

[334] Project 8 collaboration, A. Ashtari Esfahani et al., *Determining the neutrino mass with cyclotron radiation emission spectroscopy—Project 8*, *J. Phys.* **G44** (2017) 054004, [1703.02037].

[335] M. Agostini, G. Benato and J. Detwiler, *Discovery probability of next-generation neutrinoless double-β decay experiments*, *Phys. Rev.* **D96** (2017) 053001, [1705.02996].

[336] DESI collaboration, M. Vargas-Magana, D. D. Brooks, M. M. Levi and G. G. Tarle, *Unraveling the Universe with DESI*, [1901.01581].

[337] R. A. Fisher, *The logic of inductive inference*, *Journal of the Royal Statistical Society* **98** (1935) 39–82.

[338] L. Verde, *Statistical methods in cosmology*, *Lect. Notes Phys.* **800** (2010) 147–177, [0911.3105].

[339] D. Coe, *Fisher Matrices and Confidence Ellipses: A Quick-Start Guide and Software*, *arXiv e-prints* (Jun, 2009) arXiv:0906.4123, [0906.4123].

[340] L. Wolz, M. Kilbinger, J. Weller and T. Giannantonio, *On the validity of cosmological Fisher matrix forecasts*, *JCAP* **2012** (Sep, 2012) 009, [1205.3984].

[341] S. Khedekar and S. Majumdar, *Cosmology with the largest galaxy cluster surveys: Going beyond Fisher matrix forecasts*, *JCAP* **1302** (2013) 030, [1210.5586].

[342] M. Tegmark, *Measuring cosmological parameters with galaxy surveys*, *Phys. Rev. Lett.* **79** (1997) 3806–3809, [astro-ph/9706198].

[343] N. Kaiser, *Clustering in real space and in redshift space*, *Mon. Not. Roy. Astron. Soc.* **227** (1987) 1–27.

[344] L. R. Abramo and K. E. Leonard, *Why multi-tracer surveys beat cosmic variance*, *Mon. Not. Roy. Astron. Soc.* **432** (2013) 318, [1302.5444].

[345] L. R. Abramo, *The full Fisher matrix for galaxy surveys*, *Mon. Not. Roy. Astron. Soc.* **420** (Mar, 2012) 2042–2057, [1108.5449].

[346] T. Brinckmann and J. Lesgourgues, *MontePython 3: boosted MCMC sampler and other features*, [1804.07261].

[347] A. Kamada and T. Takahashi, *Dark matter kinetic decoupling with a light particle*, *JCAP* **1801** (2018) 047, [1703.02338].

[348] S. Gariazzo, M. Escudero, R. Diamanti and O. Mena, *Cosmological searches for a noncold dark matter component*, *Phys. Rev.* **D96** (2017) 043501, [1704.02991].

[349] A. Schneider, *Structure formation with suppressed small-scale perturbations*, *Mon. Not. Roy. Astron. Soc.* **451** (2015) 3117–3130, [1412.2133].

[350] A. Schneider, *Astrophysical constraints on resonantly produced sterile neutrino dark matter*, *JCAP* **1604** (2016) 059, [1601.07553].

[351] M. Hazumi et al., *LiteBIRD: A Satellite for the Studies of B-Mode Polarization and Inflation from Cosmic Background Radiation Detection*, *J. Low. Temp. Phys.* **194** (2019) 443–452.

[352] K. Abazajian et al., *CMB-S4 Science Case, Reference Design, and Project Plan*, [1907.04473].